

**Jets**  
**with high transverse momenta**  
**in photoproduction**  
**at HERA**

**Dissertation**  
**zur Erlangung des Doktorgrades**  
**des Fachbereichs Physik**  
**der Universität Hamburg**

vorgelegt von

**Ingo Strauch**

aus Linnich

Hamburg

2004

Gutachterin/Gutachter der Dissertation:	Prof. Dr. F.-W. Büßer Prof. Dr. P. Schleper
Gutachterin/Gutachter der Disputation:	Prof. Dr. B. Naroska Prof. Dr. P. Schleper
Datum der Disputation:	08.12.2004
Vorsitzende/Vorsitzender des Prüfungsausschusses:	Dr. H.D. Rüter
Vorsitzende/Vorsitzender des Promotionsausschusses:	Prof. Dr. G. Huber
Dekanin/Dekan des Fachbereichs Physik:	Prof. Dr. G. Huber

## Abstract

Dijet production in the region of photon virtualities  $Q^2 < 1 \text{ GeV}^2$  and inelasticities  $0.1 < y < 0.9$  is investigated with the H1 detector at the  $ep$  collider HERA. The data sample comprises data collected during the years 1999 and 2000 with an integrated luminosity of  $66.6 \text{ pb}^{-1}$ . Jets are defined using the inclusive  $k_{\perp}$  algorithm with a minimum transverse momentum of the leading jet of 25 GeV. Longitudinal photon momentum fractions of  $0.1 < x_{\gamma} < 1.0$  and longitudinal proton momentum fractions of  $0.05 < x_p < 0.7$  are reached. The data are compared to Monte Carlo event generators based on LO QCD cross sections and NLO QCD parton level calculations. Both yield a good description of the measured cross sections over a wide kinematical range. In the case of the NLO calculations results obtained using different photon and proton parton densities are found to be in good agreement with the data and yield differences of the same size or smaller than both experimental and theoretical uncertainties.

## Zusammenfassung

Die Zwei-Jet-Produktion im Bereich von Photon-Virtualitäten  $Q^2 < 1 \text{ GeV}^2$  und Inelastizitäten  $0.1 < y < 0.9$  wurde mit dem H1 Detektor am  $ep$  Beschleuniger HERA untersucht. Die Daten aus den Jahren 1999 und 2000 entsprechen einer integrierten Luminosität von  $66.6 \text{ pb}^{-1}$ . Jets wurden mittels des inklusiven  $k_{\perp}$  Algorithmus definiert mit einem minimalen Transversalimpuls von 25 GeV des führenden Jets. Damit wurden longitudinale Photon Impulsbruchteile von  $0.1 < x_{\gamma} < 1.0$  und Proton Impulsbruchteile von  $0.05 < x_p < 0.7$  erreicht. Die Daten werden mit Monte Carlo Ereignisgeneratoren verglichen, die auf LO QCD Wirkungsquerschnitten basieren, sowie mit NLO QCD Rechnungen auf Parton-Niveau. Beide ergeben eine gute Beschreibung der gemessenen Wirkungsquerschnitte über einen weiten kinematischen Bereich. Im Falle der NLO Rechnungen zeigt sich, dass Ergebnisse für verschiedene Photon- und Proton-Partondichten die Daten gut beschreiben und zu Unterschieden führen, die gleich groß oder kleiner als die experimentellen und theoretischen Unsicherheiten sind.



# Contents

<b>1</b>	<b>Introduction</b>	<b>1</b>
<b>2</b>	<b>Theory</b>	<b>3</b>
2.1	Perturbative QCD and Asymptotic Freedom . . . . .	3
2.2	Factorisation and Parton Density Functions . . . . .	4
2.2.1	Parton Density Functions of the Photon . . . . .	6
2.2.2	Parton Density Functions of the Proton . . . . .	7
2.3	Photoproduction at HERA . . . . .	8
2.3.1	Basics of electron-proton scattering . . . . .	8
2.3.2	Photon Flux . . . . .	10
2.3.3	Photoproduction in the Parton Model . . . . .	11
2.4	Jet Algorithms and Observables . . . . .	13
2.5	Definition of the Phase Space . . . . .	15
2.6	Fixed order calculations . . . . .	16
2.7	Monte Carlo Models . . . . .	17
2.7.1	PYTHIA and HERWIG . . . . .	18
2.7.2	DJANGO ARIADNE . . . . .	18
<b>3</b>	<b>Experiment</b>	<b>19</b>
3.1	The HERA Collider . . . . .	19
3.2	The H1 Experiment . . . . .	19
3.2.1	Calorimetry . . . . .	21
3.2.2	Tracking . . . . .	23
3.2.3	Muon System . . . . .	23
3.2.4	Luminosity System . . . . .	23
3.2.5	Trigger System . . . . .	24
<b>4</b>	<b>Development of a new object-oriented analysis framework</b>	<b>27</b>
4.1	Why a new framework? . . . . .	27
4.1.1	Homogenous environment . . . . .	27
4.1.2	Increasing demands . . . . .	28
4.1.3	Modern techniques . . . . .	28
4.2	The H1 OO framework . . . . .	28

4.2.1	Data storage . . . . .	29
4.2.2	Main concepts . . . . .	29
<b>5</b>	<b>Data analysis</b>	<b>35</b>
5.1	Data selection . . . . .	35
5.1.1	Analysis setup . . . . .	35
5.1.2	Preselection cuts . . . . .	36
5.1.3	Calibration . . . . .	37
5.1.4	Background studies . . . . .	41
5.1.5	Final event selection . . . . .	45
5.1.6	Selection stability . . . . .	47
5.1.7	Trigger studies . . . . .	47
5.2	Data to Monte Carlo comparison . . . . .	52
5.3	Data unfolding . . . . .	53
5.3.1	Correction for detector effects . . . . .	56
5.3.2	Hadronisation corrections . . . . .	58
5.4	Systematic studies . . . . .	60
5.4.1	Liquid Argon energy scale . . . . .	60
5.4.2	SpaCal energy scale . . . . .	60
5.4.3	Monte Carlo reweighting . . . . .	61
5.5	Pushing towards high $x_p$ . . . . .	62
5.5.1	Extension of the acceptance . . . . .	63
5.5.2	Effect of different reconstruction methods . . . . .	64
5.6	Sensitivity to the gluon density. . . . .	70
5.7	Effects in the NLO calculations . . . . .	71
5.7.1	Centre-of-mass Energy . . . . .	71
5.7.2	Effect of the jet cuts . . . . .	72
5.7.3	Uncertainty from the Proton PDFs . . . . .	73
<b>6</b>	<b>Results</b>	<b>77</b>
6.1	Dijet cross sections . . . . .	78
6.2	Using different PDFs . . . . .	87
<b>7</b>	<b>Conclusions and Outlook</b>	<b>93</b>
<b>A</b>	<b>Summary Tables For Data</b>	<b>95</b>
A.1	Cross sections in data for $p_{t,2nd} > 15$ GeV, $-0.5 < \eta_{jet} < 2.75$ . . . . .	96
A.2	Cross sections in data for $p_{t,2nd} > 15$ GeV, $-0.5 < \eta_{jet} < 2.5$ . . . . .	100
A.3	Cross sections in data for $p_{t,2nd} > 20$ GeV, $-0.5 < \eta_{jet} < 2.75$ . . . . .	104
A.4	Cross sections in data for $p_{t,2nd} > 20$ GeV, $-0.5 < \eta_{jet} < 2.5$ . . . . .	108

<b>B</b>	<b>Summary Tables For NLO Predictions</b>	<b>113</b>
B.1	Cross sections in NLO calculations for $p_{t,2nd} > 15$ GeV, $-0.5 < \eta_{jet} < 2.75$ . . .	113
B.2	Cross sections in NLO calculations for $p_{t,2nd} > 15$ GeV, $-0.5 < \eta_{jet} < 2.5$ . . .	117
B.3	Cross sections in NLO calculations for $p_{t,2nd} > 20$ GeV, $-0.5 < \eta_{jet} < 2.75$ . . .	121
B.4	Cross sections in NLO calculations for $p_{t,2nd} > 20$ GeV, $-0.5 < \eta_{jet} < 2.5$ . . .	125
	<b>List of Figures</b>	<b>129</b>
	<b>List of Tables</b>	<b>132</b>
	<b>Bibliography</b>	<b>133</b>



# Chapter 1

## Introduction

Quantum Chromo Dynamics (QCD) is the generally accepted theory of strong interaction physics. A wide range of phenomena can be successfully described using a perturbative expansion of the calculations in the strong coupling constant. The unique feature of QCD that makes this perturbative ansatz useful is the so-called *asymptotic freedom* which arises from the underlying non-Abelian SU(3) colour symmetry of the theory. As a consequence of renormalisation, the strong coupling constant  $\alpha_s$  is scale-dependent, giving rise to the term *running coupling constant*. For large scales  $Q \gg \Lambda_{QCD} \approx 0.2 \text{ GeV}$  – equivalent to small distances – the coupling constant is small and vanishes as  $Q \rightarrow \infty$ .

To apply results of theoretical calculations in perturbative QCD (pQCD) on partons (quarks and gluons) to the particles observed in high energy experiments (hadrons, electro-weak bosons or new physics particles) a concept called *factorisation* is crucial. The cross section of a process can be factorised into a short-distance part – the hard scatter of partons – and a long-distance part that absorbs singularities encountered in the calculations. The long distance part is process independent (or universal) and has to be determined from experiment. Once measured from one or more different processes these *parton distribution functions* (PDFs) – properties of the initial state particles in a reaction – can be used in calculations of any other process involving those particles. The knowledge of the parton densities is of crucial importance in collisions with hadrons in the initial state for both high precision measurements of standard model processes and searches for new physics, where the background for a potential signal needs to be well known.

The photoproduction of dijets with high transverse momenta is described within pQCD by the hard interaction of real photons with partons inside the proton. Calculations of such cross sections have been carried out in leading (LO) and next-to-leading (NLO) order. The high transverse momentum of jets provides the hard scale to make the perturbative ansatz applicable.

At HERA the largest cross section is due to photoproduction, where the beam electron emits a photon at small virtualities  $Q^2 \approx 0$ . This quasi-real photon then interacts with the proton. Two contributions to the total cross section are distinguished: so-called *direct processes* where the photon itself scatters off a quark or gluon in the proton and *resolved processes* where the photon first fluctuates into partons and one of the resulting partons participates in the hard scatter. For the latter case parton densities are associated to the photon.

Measurements of the parton densities of photon and proton, respectively, have been performed in several processes in  $e^+e^-$ ,  $ep$  and  $p\bar{p}$  collisions. Quark densities in the photon have been determined at  $e^+e^-$  colliders up to longitudinal momentum fractions  $x_\gamma$  of  $0.8 - 1.0$  and scales between  $0.2$  to  $780 \text{ GeV}^2$  by measuring the photon structure function  $F_2^\gamma$ . There gluons don't contribute at leading order, therefore the gluon density of the photon is less constrained from  $e^+e^-$  scattering than the quark densities. The parton densities of the proton are mainly determined from DIS experiments. They are accompanied by Drell-Yan and Tevatron jet data, the latter putting the strongest constraints on the gluon density at high  $x_p$ . While the quark densities have rather small uncertainties over a wide range in  $x_p$  the uncertainty of the gluon density up to  $x_p \approx 0.3$  is about 15% and then increases rapidly for larger  $x_p$  reaching a factor two at  $x_p \approx 0.5$ . To reduce this uncertainty is of much interest for the physics programs of the Tevatron and LHC.

To test both the predictions of perturbative calculations and the current PDF parametrisations, this work investigates dijet production at very small squared four-momentum transfers  $Q^2$  in electron (positron) proton interactions using the H1 detector at HERA. Scales between  $600 \text{ GeV}^2$  and  $6500 \text{ GeV}^2$  are reached. The range of the reconstructed photon momentum fraction is  $0.1 < x_\gamma < 1.0$  and unlike the  $e^+e^-$  data the photoproduction of jets is directly sensitive to the gluon density in the photon. In case of the proton the reconstructed momentum fraction is in the range of  $0.05 < x_p < 0.7$ . Therefore the results of this work can be used to further constrain parton density functions at momentum fractions and scales where currently only few measurements are available. A direct extraction of PDFs however is not possible from this data alone.

This work is outlined as follows. Chapter 2 reviews the theoretical foundations of the photoproduction of jets. The perturbative calculations are discussed and the kinematic variables are introduced as well as the phase space of this analysis. In chapter 3 a short description of the HERA collider and the H1 detector is given. The development of a new object-oriented analysis framework that was developed and utilised in this work is the topic of chapter 4. Chapter 5 will present the measurement procedure of the jet cross sections. It contains the event selection, correction procedure for data and NLO cross sections and the study of systematic effects. The final cross sections are presented in chapter 6. Finally this work is concluded with a summary and outlook. The appendix contains the cross sections as measured in the data as well as calculated by the NLO program in tabulated form.

Throughout the text natural units are used in which  $c = \hbar = 1$ .

# Chapter 2

## Theory

### 2.1 Perturbative QCD and Asymptotic Freedom

Quantum Chromo Dynamics (QCD) is the quantum field theory of strong interactions. With an underlying non-Abelian SU(3) colour symmetry it describes the interactions between quarks and gluons. Cross sections for processes are derived from a Lagrangian using Feynman rules. Fundamental constants of this theory are

- the gauge coupling constant  $g_s$ , or equivalently  $\alpha_s \equiv g_s^2/4\pi$ ;
- the quark masses  $m_i, i = 1, \dots, n_f$ , where  $n_f$  is the number of quark flavours, i.e.  $n_f = 6$ ;
- the SU(3) group structure constants  $C_F (=4/3)$ ,  $C_A (=3)$  and  $T_R (=1/2)$ .

To perform the calculations involved, a power series expansion in the strong coupling constant,  $\alpha_s$ , is done. The so-called leading order (LO) – or Born term – of a process is the simplest configuration that evolves the initial state of the process to its final state. Higher orders in the expansion stem from Feynman diagrams with internal loops where one has to integrate over all possible internal momenta  $P$ . These integrals become divergent as  $P \rightarrow \infty$ . Divergencies of this type are called *ultraviolet* (UV).

To overcome the infinities they are regularised according to a regularisation procedure. There is some freedom in the exact choice of the procedure so that different so-called regularisation schemes exist. Throughout this thesis the widely used  $\overline{\text{MS}}$  scheme [BBDM78] will be employed where not noted otherwise. In this procedure the divergencies are absorbed into the definition of the strong coupling constant. This introduces a new dimensional parameter  $\mu_r$ , the *renormalisation scale*. Both, the strong coupling constant and the perturbative coefficients in the power series for any observable  $R$ , now depend on  $\mu_r$ , i.e.  $\alpha_s = \alpha_s(\mu_r)$  and  $R = R(\mu_r, \alpha_s)$ . Since  $\mu_r$  is an arbitrary parameter, physical quantities as well as the strong coupling constant cannot depend on the actual choice for  $\mu_r$  if they are calculated to all orders. This is expressed by the so-called *renormalisation group equation* (RGE)

$$\mu_r^2 \frac{d}{d\mu_r^2} R(\mu_r, \alpha_s) \equiv \mu_r^2 \frac{\partial R}{\partial \mu_r^2} + \mu_r^2 \frac{\partial \alpha_s}{\partial \mu_r^2} \frac{\partial R}{\partial \alpha_s} = 0. \quad (2.1)$$

The dependence of  $\alpha_s$  on  $\mu_r$  is given by the *beta function*  $\beta(\alpha_s)$  that is a power series in the strong coupling constant:

$$\mu_r^2 \frac{d\alpha_s}{d\mu_r^2} = \alpha_s \beta(\alpha_s) = -\beta_0 \frac{\alpha_s^2}{4\pi} - \beta_1 \frac{\alpha_s^3}{16\pi^2} + \dots \quad (2.2)$$

Here the coefficients  $\beta_0$  and  $\beta_1$  are universal for massless quarks while higher ones depend on the renormalisation scheme. Performing a 1-loop calculation of an arbitrary physical quantity that depends on  $\mu_r$  yields

$$\beta_0 = (11N_c - 2n_f)/3 = 11 - 2n_f/3 \quad (2.3)$$

where  $n_f$  is the number of active quark flavours and  $N_c$  is the number of colours. Setting the coefficients beyond  $\beta_0$  to zero leads to the formula for the so-called *running coupling constant* at leading order:

$$\alpha_s(\mu_r^2) = \frac{\alpha_s(\mu_0^2)}{1 + \beta_0/4\pi \cdot \alpha_s(\mu_0^2) \ln(\mu_r^2/\mu_0^2)} \quad (2.4)$$

This means the value of the strong coupling constant at any scale  $\mu_r$  can be calculated when it is known at some other scale  $\mu_0$ .

The denominator of equation (2.4) can become zero when  $\mu_r \rightarrow \Lambda_{QCD}$ , then the coupling diverges. This leads to the so-called *confinement* of partons inside hadrons. The cut-off scale  $\Lambda_{QCD}$  has to be determined from experiment and is of the order of 200 – 500 MeV, depending on the number of quark flavours  $n_f$ . Using this, the strong coupling constant at leading order can alternatively be written as

$$\alpha_s(\mu_r^2) = \frac{4\pi}{\beta_0 \ln(\mu_r^2/\Lambda_{QCD}^2)}. \quad (2.5)$$

From either equation, (2.4) or (2.5), it is also obvious that for infinitely large  $\mu_f$  the strong coupling constant vanishes. This is the so-called *asymptotic freedom*, one of the key features of perturbative QCD (pQCD) that ensures that for sufficiently large scales (or short distances) the perturbative ansatz is valid and calculations can be carried out. Note that this is different from QED where the electro-magnetic coupling constant increases with increasing scale. This difference comes from the non-Abelian nature of the SU(3) group that manifests itself in self-coupling of the gauge bosons, i.e. the gluons.

## 2.2 Factorisation and Parton Density Functions

Another crucial concept besides asymptotic freedom for the usefulness of the perturbative approach in QCD is *infrared safety*. Calculating simple cross sections – like that of a three-parton final-state in the reaction  $e^+e^- \rightarrow q\bar{q}g$  for example – one often encounters divergencies near the boundaries of the phase space. They are associated with collinear and soft configurations of the partons in momentum space or long-distance interactions in space-time. For some physical

quantities singularities in partonic cross sections cancel with that of other processes contributing to a more inclusive cross section.

However, the number of such intrinsic *infrared safe* (IRS) quantities is rather limited. This number is greatly increased by the property of *factorisation*, the third key concept necessary to perform perturbative calculations based on partons and to apply them to the particles observed in real world applications: cross sections are factorised into a short-distance part – the hard scatter – and a long-distance part which is process independent or *universal*. The hard cross section is calculable in pQCD, the universal *parton density functions* (PDF) have to be determined from experiment and are characteristics of the corresponding hadrons.

Factorisation introduces another scale: the *factorisation scale*  $\mu_f$  that marks the transition between the hard and the soft part of a process. The PDF  $f_{a/b}(\xi, \mu_f)$  can be interpreted as the number density to find a parton  $a$  with a longitudinal momentum fraction  $\xi$  in a particle  $b$ , treating parton emissions with transverse momentum  $p_t < \mu_f$  as part of the structure of the particle while partons emitted with higher  $p_t$  are treated as part of the hard interaction. Similar to the renormalisation procedure factorisation can be performed using different choices of scheme so that the resulting PDFs are only defined within the chosen scheme. As with renormalisation the  $\overline{\text{MS}}$  scheme will be used for factorisation unless noted otherwise.

The dependence of the parton density functions on the factorisation scale can be calculated using the DGLAP evolution equations [Dok77, GL72, AP77]. As an example for the proton they are written as

$$\frac{df_q(\xi, \mu_f)}{d \ln \mu_f^2} = \frac{\alpha_s(\mu_f^2)}{2\pi} \int_{\xi}^1 \frac{dz}{z} \left( P_{qg}(z, \mu_f) f_g\left(\frac{\xi}{z}, \mu_f\right) + P_{qq}(z, \mu_f) f_q\left(\frac{\xi}{z}, \mu_f\right) \right) \quad (2.6a)$$

$$\frac{df_g(\xi, \mu_f)}{d \ln \mu_f^2} = \frac{\alpha_s(\mu_f^2)}{2\pi} \int_{\xi}^1 \frac{dz}{z} \left( P_{gg}(z, \mu_f) f_g\left(\frac{\xi}{z}, \mu_f\right) + \sum_q P_{gq}(z, \mu_f) f_q\left(\frac{\xi}{z}, \mu_f\right) \right). \quad (2.6b)$$

Here the *splitting functions*  $P_{ij}(z, \mu_f)$  are probability densities to obtain a parton  $i$  from parton  $j$  with a momentum fraction  $z$  of the momentum of the parent parton  $j$ . These splitting functions are calculated as perturbative expansion in the strong coupling constant  $\alpha_s$

$$P_{ij}(z, \mu_f) = \frac{\alpha_s(\mu_f^2)}{2\pi} P_{ij}^{(0)}(\xi) + \left( \frac{\alpha_s(\mu_f^2)}{2\pi} \right)^2 P_{ij}^{(1)}(\xi) + \dots \quad (2.7)$$

The  $P_{ij}^{(0)}(\xi)$  are universal, higher order ones depend on the choice of the factorisation scheme. According to the factorisation theorem of QCD cross sections of interacting hadrons can be expressed as a convolution of the hard partonic cross section and the parton density functions, summed over all contributing partons

$$\sigma = \sum_{i,j} \iint d\xi_a f_{i/a}(\xi_a, \mu_a) d\xi_b f_{j/b}(\xi_b, \mu_b) \hat{\sigma}_{ij}(\hat{s}, \mu_a, \mu_b, \alpha_s(\mu_r), \mu_r) \quad (2.8)$$

In this equation  $\hat{s} = \xi_a \xi_b s$  is the squared centre-of-mass energy of the hard subprocess between partons  $i$  and  $j$  that are found with momentum fractions  $\xi_a$  and  $\xi_b$  inside the colliding hadrons  $a$  and  $b$ .  $\hat{\sigma}_{ij}$  is the partonic cross section of the hard subprocess.

### 2.2.1 Parton Density Functions of the Photon

While the photon has no known intrinsic structure, it is able to fluctuate into quark-antiquark pairs due to the Heisenberg uncertainty principle. These quarks may subsequently radiate gluons. Therefore parton density functions describing this kind of fluctuations can be attributed to the photon. In QED the process  $\gamma \rightarrow q\bar{q}$  can be calculated for sufficiently high transverse momenta of the quark-antiquark pair. The result is

$$f_{q/\gamma}(\xi_\gamma, \mu_\gamma) = q_f^2 \frac{\alpha}{2\pi} (\xi_\gamma^2 + (1 - \xi_\gamma)^2) \ln \left( \frac{\mu_\gamma^2 (\xi_\gamma - 1)}{m_q^2 \xi_\gamma} \right). \quad (2.9)$$

Here  $q_f$  is the electric charge of the quark  $q$  and  $m_q$  is the effective mass of the free quark. The scale  $\mu_\gamma$  can be interpreted as the virtuality of the particle probing the photon fluctuations. QCD corrections to eq. (2.9) have been carried out in [Wit77] and yield the so-called *asymptotic* solution

$$f_{q/\gamma}(\xi_\gamma, \mu_\gamma) \approx \alpha F(\xi_\gamma) \ln \left( \frac{\mu_\gamma^2}{\Lambda_{QCD}^2} \right). \quad (2.10)$$

This part of the photon structure is called *point-like* or *anomalous*. It is only valid for  $\mu_\gamma \rightarrow \infty$ . Here  $F(\xi_\gamma)$  is a function that contains the  $\xi_\gamma$  dependence of the solution. In the so-called *hadron-like* part the photon is interpreted as a superposition of vector meson states, bound  $q\bar{q}$  states the photon also couples to which have the same quantum numbers as the photon. This interpretation is also called *Vector Meson Dominance Model* (VDM). Both the point-like part and hadron-like part are solutions of the evolution equations of the photon PDFs

$$\begin{aligned} \frac{df_{q/\gamma}(\xi_\gamma, \mu_\gamma)}{d \ln \mu_\gamma^2} &= \frac{\alpha}{2\pi} q_f^2 P_{q\gamma}(z, \mu_\gamma) + \frac{\alpha_s(\mu_\gamma^2)}{2\pi} \int_{\xi_\gamma}^1 \frac{dz}{z} \left( P_{qg}(z, \mu_\gamma) f_{g/\gamma} \left( \frac{\xi_\gamma}{z}, \mu_\gamma \right) + \right. \\ &\quad \left. P_{qq}(z, \mu_\gamma) f_{q/\gamma} \left( \frac{\xi_\gamma}{z}, \mu_\gamma \right) \right) \end{aligned} \quad (2.11a)$$

$$\begin{aligned} \frac{df_{g/\gamma}(\xi_\gamma, \mu_\gamma)}{d \ln \mu_\gamma^2} &= \frac{\alpha_s(\mu_\gamma^2)}{2\pi} \int_{\xi_\gamma}^1 \frac{dz}{z} \left( P_{gg}(z, \mu_\gamma) f_{g/\gamma} \left( \frac{\xi_\gamma}{z}, \mu_\gamma \right) + \right. \\ &\quad \left. \sum_q P_{gq}(z, \mu_\gamma) f_{q/\gamma} \left( \frac{\xi_\gamma}{z}, \mu_\gamma \right) \right). \end{aligned} \quad (2.11b)$$

The general solution to equations 2.11a and 2.11b can be written as the sum of a particular solution to the full inhomogeneous equations and the general solution of the corresponding homogeneous equations. Then the point-like solutions are a subset of the former. There is, however, an infinite number of solutions to these equations and the separation of the physical photon PDF into point-like and hadron-like parts is ambiguous. By choosing an additional parameter  $\mu_\gamma^0$  defined as the value of the factorisation scale at which the point-like part vanishes the ambiguity is removed and the parton density functions reads

$$f_{q/\gamma}(\xi_\gamma, \mu_\gamma) = f_{q/\gamma}^{PL}(\xi_\gamma, \mu_\gamma, \mu_\gamma^0) + f_{q/\gamma}^{HAD}(\xi_\gamma, \mu_\gamma, \mu_\gamma^0) \quad (2.12)$$

where  $f_{q/\gamma}^{PL}$  is the perturbatively calculable point-like part and  $f_{q/\gamma}^{HAD}$  is the hadron-like part that is not calculable in perturbation theory. Here an increasing value of  $\mu_\gamma^0$  means that less parton emissions are included in the point-like part and are put into the hadron-like part instead.

Parton density functions of the photon have been determined in  $e^+e^-$  collisions where the photon structure function  $F_2^\gamma$  has been measured [Nis00, A<sup>+</sup>02a]. Scales between  $0.2 \text{ GeV}^2$  and  $780 \text{ GeV}^2$  and momentum fractions of  $\xi_\gamma$  between 0.01 and  $0.8 - 1$  have been reached. Higher scales and reduced uncertainties for large values of  $\xi_\gamma$  are reached in  $ep$  collisions [A<sup>+</sup>02b]. Parametrisations of the photon PDFs at next-to-leading order are available from different groups. The two parametrisations used in this analysis are:

- **Glück, Reya and Vogt**

The parametrisation of the GRV group [GRV92] is constructed at an input scale of  $0.3 \text{ GeV}^2$ . There the quark distributions have the same shape as the pion structure function, i.e. the point-like part vanishes at the input scale and is purely generated by the photon evolution equations (2.11a) and (2.11b). The so-called  $DIS_\gamma$  factorisation scheme is used for the NLO evolution equations with massless quarks and  $\Lambda_{QCD} = 200 \text{ MeV}$ . One free parameter fixing the normalisation of the input distributions was fitted to  $F_2^\gamma$  data. This PDF is termed GRV-HO.

- **Aurenche, Fontannaz and Guillet**

A similar strategy to the GRV group is employed by the AFG group [AGF94]. At an input scale of  $0.5 \text{ GeV}^2$  only the hadron-like part is non-zero and assumed to be a coherent sum of vector meson states. The NLO evolution is performed in the  $\overline{\text{MS}}$  scheme with four active quark flavours and  $\Lambda_{QCD} = 200 \text{ MeV}$ . A scale factor can be used to control the hadron-like contribution, it is set to 1 as the default value. This PDF is termed AFG-HO.

## 2.2.2 Parton Density Functions of the Proton

Quark and gluon density functions of the proton are obtained in so-called *global fits* to deeply inelastic scattering (DIS) data as well as jet production,  $W$ ,  $Z$ ,  $\gamma$  production and Drell-Yan processes in  $p\bar{p}$  collisions.

Of the many available proton PDFs this analysis uses sets of the CTEQ and MRS groups for the NLO calculations, namely CTEQ5 [L<sup>+</sup>00] and MRST99 [MRST00] that were also used in the previous H1 analysis of dijets in photoproduction [A<sup>+</sup>02b] plus the newer sets CTEQ6 [P<sup>+</sup>02a]

and MRST2001 [MRST02]. These PDFs are obtained from global fits to parametrisations of the parton densities of the proton with mainly DIS data as input. The most commonly used parametric form is

$$f(\xi_p, \mu_p) = A_0 \xi_p^{A_1} (1 - \xi_p)^{A_2} P(\xi_p) \quad (2.13)$$

where  $P(\xi_p)$  is a smooth function of  $\xi_p$ . The parton flavour label  $i$  and hadron label  $a$  on  $f$ ,  $P(\xi_p)$  and the fit parameters  $A_i$  have been suppressed.

The parametrisations of the different groups differ in the choice of  $P(\xi_p)$ , CTEQ uses  $(1 + A_3 \xi_p^{A_4})$ , MRS uses  $(1 + A_3 \sqrt{\xi_p} + A_4 \xi_p)$ . In addition the groups as well as the different sets within one group differ by the input data used for the fit. Both groups use NLO evolution equations in the  $\overline{\text{MS}}$  scheme,  $\Lambda_{QCD}$  for four active quark flavours is set to 326 MeV and  $\alpha_s(M_Z) = 0.118$  in case of both CTEQ sets, for MRST99  $\Lambda_{QCD} = 300$  MeV and  $\alpha_s(M_Z) = 0.1175$  is used and  $\Lambda_{QCD} = 323$  MeV and  $\alpha_s(M_Z) = 0.119$  for MRST2001.

While quark densities in the proton are well known from DIS data, the gluon density has large uncertainties for  $\xi_p \gtrsim 0.5$ . This is depicted in figure 2.1 where the relative uncertainty of the u-, d- and gluon-density for the CTEQ6 parametrisation is shown. It is clear that the uncertainty of the gluon parton distribution at high  $\xi_p$  needs to be reduced since many signal and background processes at HERA, the Tevatron and the LHC have a gluon in the initial state.

## 2.3 Photoproduction at HERA

### 2.3.1 Basics of electron-proton scattering

In the general case of electron-proton scattering the interaction is mediated by either a photon ( $\gamma$ ),  $Z^0$  or  $W^\pm$  boson. The type of exchanged boson divides the interactions in two classes: *neutral current* (NC) interactions for  $\gamma/Z^0$  and *charged current* (CC) for  $W^\pm$  exchange. This thesis solely concentrates on NC scatterings. Figure 2.2 shows a diagram of such a process. The incoming electron with four-momentum  $k$  scatters off the proton with four-momentum  $p$  by the exchange of a photon. The outgoing electron (neutrino in CC interactions) has four-momentum  $k'$ .  $X$  is an abbreviation for the not specified final state of the reaction.

Several invariant variables describe the reaction, first of all the squared centre-of-mass energy

$$s = (p + k)^2. \quad (2.14)$$

It is common practice to use the *negative* squared four-momentum transfer  $Q^2$  from electron to proton defined by

$$Q^2 = -q^2 = -(k - k')^2. \quad (2.15)$$

The value of  $Q^2$  is used to further divide the interactions into classes. For non-vanishing  $Q^2$  one speaks of *electroproduction*. If the invariant mass of the system  $X$  is much larger than the proton mass the processes are called *deep-inelastic scattering* (DIS). In this case the kinematics of the

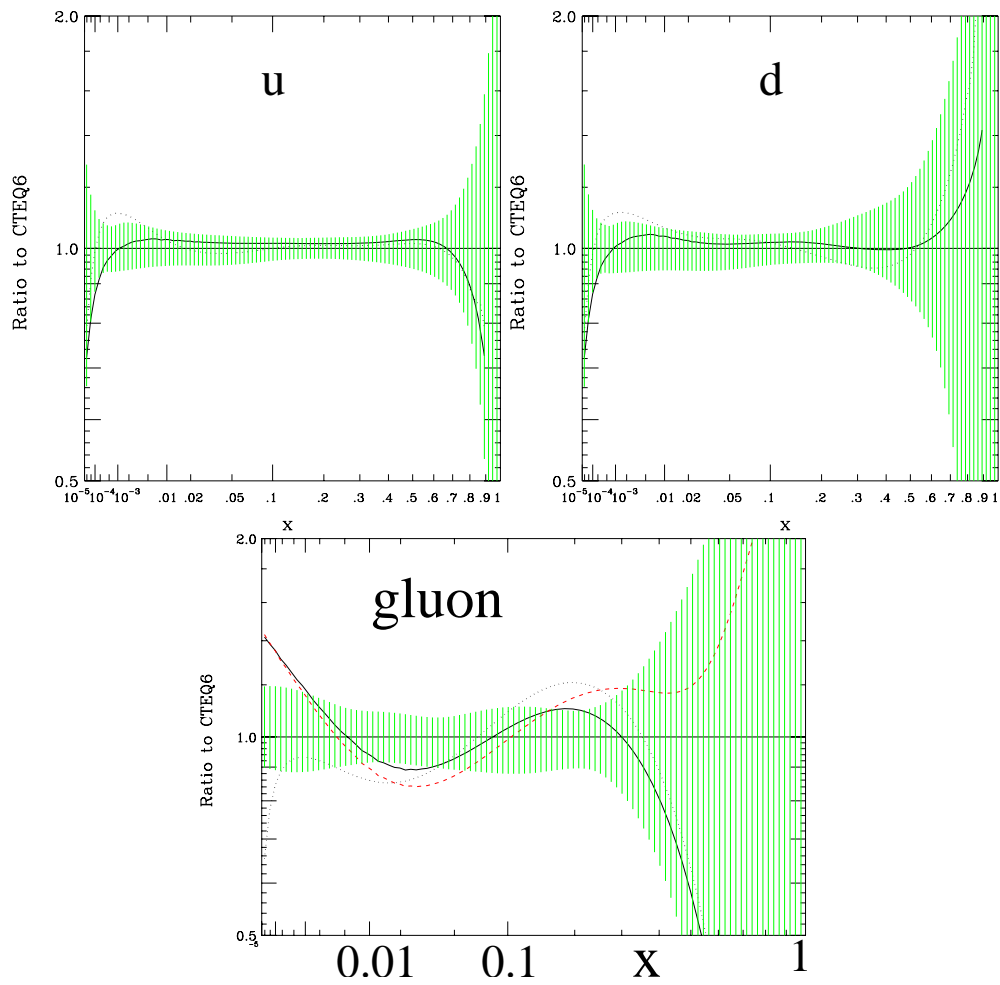


Figure 2.1: Relative CTEQ6 proton PDF uncertainties for the  $u$ -,  $d$ -quark and gluon distributions. The label  $x$  on the axis corresponds to  $\xi_p$  in the text. The lines correspond to CTEQ5M1 (solid), MRST2001 (dotted) and CTEQ5HJ (dashed, only shown in the gluon plot). Figures taken from [P<sup>+</sup>02a].

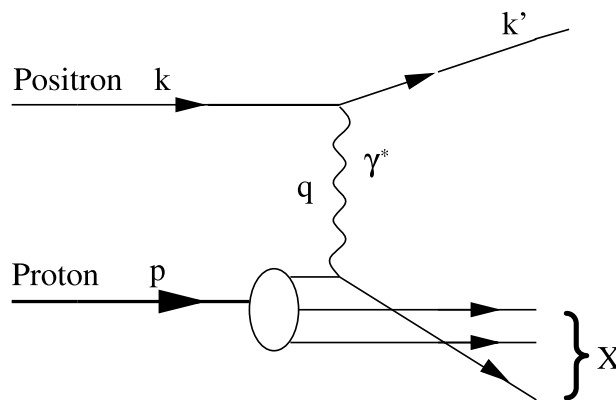


Figure 2.2: Electron-proton scattering.

reaction  $ep \rightarrow eX$  can be fully described by two variables if the centre-of-mass energy is fixed. One possible choice is  $Q^2$  and the so-called *inelasticity*  $y$  defined by

$$y = \frac{p \cdot q}{p \cdot k}. \quad (2.16)$$

In the proton rest frame  $y$  can be interpreted as the fractional energy loss of the scattering lepton. In the so-called parton model the proton is assumed to be made up by partons  $i$  that carry a fraction  $\xi_{p,i}$  of the longitudinal proton momentum  $p$  such that  $\sum_i \xi_{p,i} = 1$ . In this picture the scattering of hadrons is interpreted as a superposition of the scattering of partons. The fraction  $\xi_p$  for an interacting parton of four-momentum  $a$  is given by

$$\xi_p = \frac{q \cdot a}{q \cdot p}. \quad (2.17)$$

In the case of  $Q^2 \approx 0$  one speaks of *photoproduction*. There the processes can be seen as a radiation of a quasi-real photon from the electron and a subsequent scattering of the photon with the proton. These are the dominant processes in electron-proton collisions as the cross section goes roughly like  $\sigma \propto 1/Q^4$ .

### 2.3.2 Photon Flux

The energy of the quasi-real photon can be derived from the Weizsäcker Williams approximation. It yields the longitudinal momentum fraction  $y$  of the incoming electron taken by the photon which is the same variable as the inelasticity for DIS events.  $y$  is directly related to the photon-proton centre-of-mass energy  $W_{\gamma p}$  that is given by

$$W_{\gamma p} = (q + p)^2 \approx \sqrt{s y}. \quad (2.18)$$

In this last equation the approximation becomes equality if the electron and proton masses are neglected.

The Weizsäcker Williams approximation [Kes60, BGMS74, FMNR93] now gives the photon flux  $f_{\gamma,e}(y)$  out of the electron at fixed  $y$  by

$$f_{\gamma,e}(y) = \frac{\alpha}{2\pi} \left[ 2m_e^2 y \left( \frac{1}{Q_{max}^2} - \frac{1-y}{m_e^2 y^2} \right) + \frac{1 + (1-y)^2}{y} \log \frac{Q_{max}^2 (1-y)}{m_e^2 y^2} \right] \quad (2.19)$$

so that the cross section in photoproduction can be written as

$$\sigma_{ep \rightarrow eX} = \int dy f_{\gamma,e}(y) \sigma_{\gamma p}(y). \quad (2.20)$$

This factorisation ansatz is derived using current conservation and the condition that  $Q^2$  is small. The value of  $Q_{max}^2$  is determined from experimental conditions and related to the maximum energy and scattering angle of the electron via

$$Q_{max}^2 = -(k - k')^2 = 2E_e E'_e (1 + \cos \theta'_e). \quad (2.21)$$

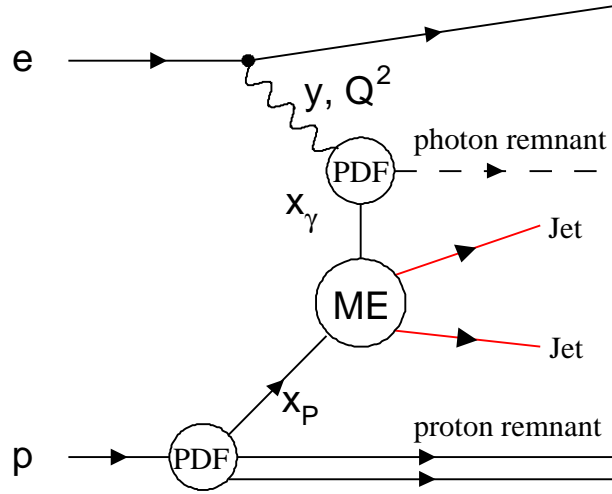


Figure 2.3: Schematic view of dijet production in  $ep$  scattering.  $x_\gamma$  and  $x_p$  in the picture correspond to  $\xi_\gamma$  and  $\xi_p$  in the text.

Here,  $E_e$  is the energy of the incoming,  $E'_e$  the energy and  $\theta'_e$  the polar angle of the outgoing electron. From the experimental setup (details are discussed later in section 3.2) the value of  $Q_{max}^2$  is set to  $1 \text{ GeV}^2$ .

### 2.3.3 Photoproduction in the Parton Model

As illustrated in the previous sections of this chapter, processes involving hadrons in the initial state are factorised into a hard interaction of partons and parton density functions of the participating hadrons. In photoproduction at HERA also the real photon radiated off the beam electron can enter the interaction in two ways. It either couples directly to the parton from the proton or first fluctuates into a quark-antiquark pair or vector meson. Processes where the photon enters the hard scatter without fluctuations are called *direct* interactions in contrast to *resolved* processes where the photon exhibits hadronic structure and one of the resulting partons participates in the hard interaction. Similar to the proton case there is a longitudinal momentum fraction of the interacting parton of momentum  $b$  from the photon side defined as

$$\xi_\gamma = \frac{p \cdot b}{p \cdot q}. \quad (2.22)$$

The production of dijets with high transverse momenta is due to processes that yield at least two final state partons with large transverse momenta. A schematic view of dijet photoproduction is depicted in figure 2.3. For direct interactions the hard processes include  $\gamma q \rightarrow gq$  (QCD-Compton scattering) and  $\gamma g \rightarrow q\bar{q}$  (photon-gluon fusion). The corresponding leading order Feynman diagrams are shown in figure 2.4. For resolved interactions the photon is exchanged with either a quark (antiquark) or gluon. Examples of leading order diagrams for resolved processes are shown in figure 2.5.

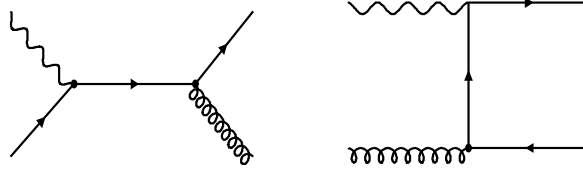


Figure 2.4: LO diagrams for direct photoproduction. Figures taken from [Car02].

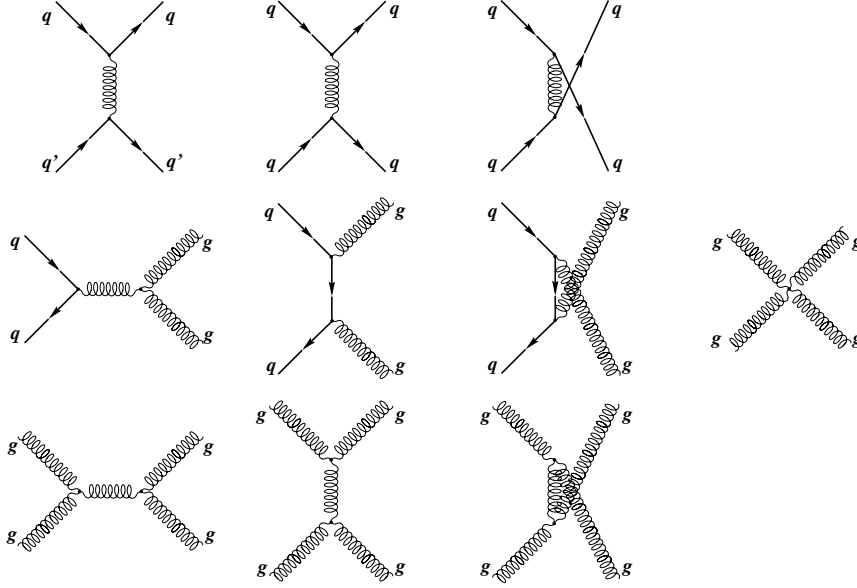


Figure 2.5: LO diagrams for resolved photoproduction. Figure taken from [Car02].

The hadronic photon-proton cross section is obtained using a convolution of the partonic cross sections with the parton density functions of the proton and the photon. It is usually divided into the direct and resolved component

$$\sigma_{\gamma P}^{\text{direct}} = \sum_i \int d\xi_p f_{i/P}(\xi_p, \mu_P) \hat{\sigma}_{i\gamma}(\hat{s}, \mu_\gamma, \mu_p, \alpha_s(\mu_r), \mu_r) \quad (2.23a)$$

$$\sigma_{\gamma P}^{\text{resolved}} = \sum_{j,i} \int d\xi_\gamma f_{j/\gamma}(\xi_\gamma, \mu_\gamma) d\xi_p f_{i/p}(\xi_p, \mu_p) \hat{\sigma}_{ij}(\hat{s}, \mu_\gamma, \mu_p, \alpha_s(\mu_r), \mu_r). \quad (2.23b)$$

Here the squared centre-of-mass energy of the hard subprocess is  $\hat{s} = \xi_p \xi_\gamma y s$ . This distinction is unambiguously defined only in leading order and depends on the photon factorisation scale  $\mu_\gamma$ . The individual components are not physical, only their sum is.

## 2.4 Jet Algorithms and Observables

To compare experimental measurements with theoretical predictions it is important that a common denominator is used. While NLO calculations yield partons, experimentally some “objects” are reconstructed from the detector response to the particles produced in the interactions. To make both comparable, the effects of the detector (efficiencies, acceptance, etc.) need to be corrected for so that the experimental result no longer depends on the apparatus. On the other hand, results on partons from NLO calculations need to be transferred to results on real-world hadrons. This so-called *hadron level* is the common denominator that makes it possible to compare the experimental *detector level* to the theoretical *parton level*. More details follow in the sections about the program used for NLO calculations (2.6), the Monte Carlo event generators (2.7) and the data unfolding procedure used in this analysis (5.3).

This has implications on how jets are defined. The definition has to be applicable to all three levels mentioned above while ensuring good correlations between the levels. Perfect correlation of course is not possible as there can be no exact correspondence between a jet of colourless hadrons and a single parton carrying colour. Any jet algorithm nevertheless should minimise the effect of the hadronisation. A second requirement on jet algorithms is infrared safety that was already discussed in section 2.2. Replacing two collinear input objects (partons, hadrons or detector level objects) with one of the same momentum as the sum of the two or adding soft objects must not affect the result of the algorithm.

Different algorithms have been proposed, tested and optimised in the past, today we are left with two popular algorithms used in collisions involving hadrons: cone algorithm (see e.g. [B<sup>+</sup>00]) and inclusive  $k_{\perp}$  algorithm (e.g. [CDSW93]). One very basic advantage of the inclusive  $k_{\perp}$  algorithm is that it uniquely assigns particles to jets whereas in the cone algorithm particles belonging to more than one overlapping jet need special treatment. Comparisons of jet algorithms in DIS (e.g. [Wob99]) have shown that the hadronisation corrections are smaller for the inclusive  $k_{\perp}$  algorithm than for the cone algorithm. The application of the former has become standard in jet analyses at HERA [A<sup>+</sup>01].

I will describe the inclusive  $k_{\perp}$  algorithm as it was used in this thesis in the following. It is a so-called *clustering algorithm* that iteratively combines particles into jets until all input particles are merged. As a consequence all particles belong to a “jet” at the end of the procedure. An additional hardness requirement is necessary to identify the jets of the hard interaction, typically a minimum transverse energy is required.

The iterative procedure is as follows:

1. For each object  $i$  calculate the distance to the beam axis

$$d_i = p_{t,i}^2 \tag{2.24}$$

and for each combination of objects  $i$  and  $j$  their distance between each other

$$d_{ij} = \min(p_{t,i}^2, p_{t,j}^2) \cdot \Delta R_{ij}^2 / R_0^2 \tag{2.25}$$

where  $\Delta R_{ij}^2$  is the distance of the two objects in the  $\eta - \phi$  plane

$$\Delta R_{ij}^2 = (\Delta\eta_{ij})^2 + (\Delta\phi_{ij})^2 \tag{2.26}$$

and  $R_0$  is a separation parameter (similar to the cone radius in the cone algorithm) of order 1.

Here  $\eta = -\ln(\tan(\theta/2))$  is the pseudorapidity and  $\phi$  is the azimuthal angle of the object.

2. Find the smallest distances  $d_{i,\min}$  and  $d_{ij,\min}$
3. If  $d_{i,\min} < d_{ij,\min}$  remove object  $i$  and add it to the list of jets. Otherwise merge particles  $i$  and  $j$  that correspond to  $d_{ij,\min}$ .
4. Continue at 1. if there are still objects left in the input list.

The merging of two objects is done according to the  $p_t$ -weighted scheme:

$$p_{t,ij} = p_{t,i} + p_{t,j} \quad (2.27a)$$

$$\eta_{ij} = (p_{t,i}\eta_i + p_{t,j}\eta_j)/p_{t,ij} \quad (2.27b)$$

$$\phi_{ij} = (p_{t,i}\phi_i + p_{t,j}\phi_j)/p_{t,ij} \quad (2.27c)$$

The resulting jets are massless and ordered ascendingly in  $p_t$ . And additional cut on the  $p_t$  of those jets yields the final hard jets. The separation parameter  $R_0$  is set to 1 as suggested in [Sey95] and the algorithm is applied in the laboratory frame. A simplified example of the iterative steps for the inclusive  $k_\perp$  algorithm is visualised in figure 2.6.

In this thesis only the two jets with the highest  $p_t$  are considered. They are used to reconstruct the two scaled parton momenta  $\xi_\gamma$  and  $\xi_p$  from photon and proton side, respectively, via

$$x_\gamma = \frac{1}{2yE_e} \cdot \sum_{i=1}^2 p_{t,i} \cdot e^{-\eta_i} \quad (2.28a)$$

$$x_p = \frac{1}{2E_p} \cdot \sum_{i=1}^2 p_{t,i} \cdot e^{+\eta_i} \quad (2.28b)$$

Here  $E_e$  and  $E_p$  are the energies of the electron and proton beam, respectively.  $p_{t,i}$  is the transverse momentum of jet  $i$  and  $\eta_i$  its pseudorapidity. For  $2 \rightarrow 2$  processes with massless partons the observables  $x_\gamma$  and  $x_p$  are equal to to the “true”  $\xi_\gamma$  and  $\xi_p$ . These relations can easily be derived from eq. (2.17) and (2.22) for leading order processes.

Another observable accessible through the measurements of dijets is the angular distribution of the jets in their centre-of-mass system via

$$\cos \theta^* = |\tanh(\eta_1 - \eta_2)/2|. \quad (2.29)$$

The angle  $\theta^*$  is sensitive to the dynamics of jet production, i.e. the matrix element of the hard interaction. The corresponding differential cross section is evaluated for two regions of  $x_\gamma$  to either enhance the contribution of the direct or the resolved component. For direct interactions

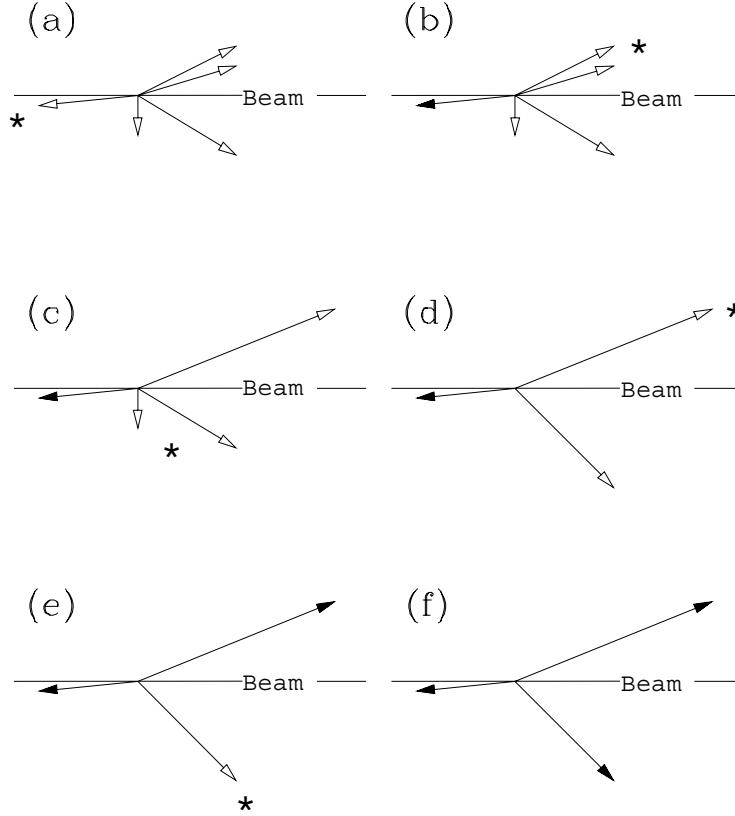


Figure 2.6: *Simplified example of the inclusive  $k_{\perp}$  algorithm. Open arrows represent the objects to be iterated over, solid arrows represent jets removed from the procedure. The asterisk marks the object(s) corresponding to the minimal distance of each step. Figure taken from [B<sup>+</sup>00].*

only quark propagators are possible (c.f. figure 2.4) while for resolved interactions most diagrams in figure 2.5 have a gluon propagator. In the two regions one expects to see a different slope as the quark propagator yields a  $(1 - |\cos \theta^*|)^{-1}$  behaviour while the gluon propagator gives  $(1 - |\cos \theta^*|)^{-2}$ . Cuts in jet transverse momentum lead to phase space effects at high values of  $\cos \theta^*$ . Therefore the differential cross section in  $\cos \theta^*$  is also evaluated with an additional cut in the invariant dijet mass  $M_{JJ}$  which mostly affects the low  $\cos \theta^*$  region.

Other cross sections to be considered are the mean transverse momentum, mean pseudorapidity and invariant dijet mass of the two jets.

## 2.5 Definition of the Phase Space

The phase space of the measured cross section is introduced in this section. Most cuts are due to experimental reasons as will be discussed in section 5.1.

For this thesis jets with high transverse momentum are considered. High values of  $p_t$  provide a natural hard scale to make perturbative QCD calculations feasible. Secondly, at low  $p_t$  the cross section may be dominated by soft physics while the aim of this work is to address the hard

Phase space definition
$Q^2 < 1 \text{ GeV}^2$
$0.1 < y < 0.9$
$p_{t,max} > 25 \text{ GeV}$
$p_{t,2nd} > 15/20 \text{ GeV}$
$-0.5 < \eta_{jet} < 2.5/2.75$

Table 2.1: *Definition of the phase space of the measured cross sections.*

process exclusively.

To avoid regions of the phase space with uncertainties in the NLO dijet calculation (c.f. [FR97]) asymmetric cuts on the two jets with the highest transverse momenta are made. For the leading jet – the jet with the highest  $p_t$  – the cut is  $p_{t,max} > 25 \text{ GeV}$ . To test the effect of the asymmetry of the cuts, two scenarios are considered concerning the cut on the second-leading jet:  $p_{t,2nd} > 15 \text{ GeV}$  and  $p_{t,2nd} > 20 \text{ GeV}$ .

Similarly two scenarios for the pseudorapidity of the jets are investigated:  $-0.5 < \eta_{jet} < 2.75$  and  $-0.5 < \eta_{jet} < 2.5$ . The measured kinematic region was restricted to  $0.1 < y < 0.9$  and  $Q^2 < 1 \text{ GeV}^2$ .

Table 2.1 summarises the kinematic range of the measured cross sections.

## 2.6 Fixed order calculations

The aim of this thesis is to compare the measured cross sections to perturbative QCD calculations at next-to-leading order. The NLO dijet cross sections on parton level were obtained using a program [Fri97, FR97] based on the subtraction method for the cancellation of infrared singularities. In the subtraction method [KS92] an additional term gets added and subtracted in the cross section calculation such that an analytical integration is possible.

For the direct part of the dijet cross sections  $ep$  scattering was calculated whereas for the resolved part,  $\gamma p$  scattering was calculated at eight fixed photon-proton centre-of-mass energies (i.e. bins in  $W_{\gamma p}$ ) and multiplied with the corresponding photon flux. In [Car02] it was found that the uncertainty was below 1% when increasing the number of  $W_{\gamma p}$  bins.

In the calculation of the NLO cross sections a 2-loop  $\alpha_s$  was taken with 5 active quark flavours and value  $\alpha_s(M_Z) = 0.118$ . A value of  $\Lambda_{QCD} = 226 \text{ MeV}$  was chosen as used in the CTEQ proton PDFs. As the main parametrisation CTEQ6M [P<sup>+</sup>02a] was chosen and MRST2001 [MRST02] to test the dependence of the NLO calculation on the proton PDFs at the same value of  $\Lambda_{QCD}$ . CTEQ5M [L<sup>+</sup>00] and MRST99 [MRST00] were included to evaluate the developments from old to new PDF fits and to compare with the previous analysis [A<sup>+</sup>02b]. For the photon the GRV-HO [GRV92] parametrisation is used as the main setting. To test the dependence of the cross sections on the photon PDF AFG-HO [AGF94] was used. Renormalisation scale  $\mu_r$  and factorisation scale  $\mu_f$  have been set to the sum of the transverse momenta of the outgoing partons divided by two on an event-by-event basis.

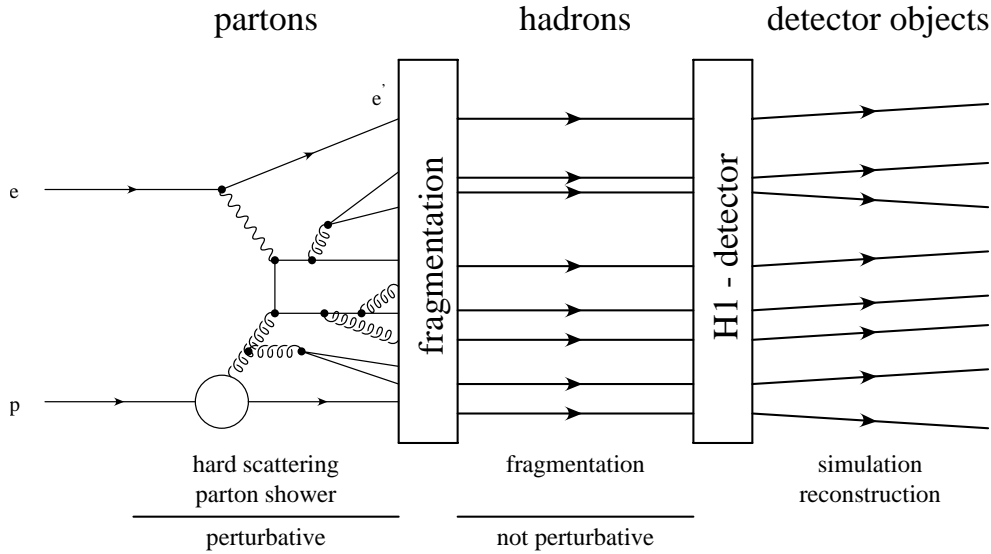


Figure 2.7: Schematic view of scattering process from perturbative over non-perturbative processes to the detector simulation and event reconstruction. Figure taken from [Car02].

Testing the effect of the choice of scale was performed by varying the common scale  $\mu = \mu_r = \mu_f$  by a factor 2 up and down. The uncertainty arising from this procedure was found to vary between a few percent and  $\pm 30\%$ . On average it is slightly higher for the cut on the sub-leading jet of  $p_{t,2nd} > 15$  GeV.

The data are also compared to the NLO calculations after a correction for hadronisation effects. The correction is defined as the cross section ratio with jets reconstructed from hadrons and from partons before hadronisation as determined by Monte Carlo model. More details will be discussed in section 5.3.2.

## 2.7 Monte Carlo Models

As already discussed in section 2.4 about observables the measured data need to be corrected for detector effects in order to compare experimental cross sections with predictions from theoretical calculations. QCD Monte Carlo event generators are used to estimate effects like limited detector acceptance or resolution and the non-perturbative hadronisation for example. The event generators produce artificial events that are passed through a detailed simulation of the detector using the GEANT 3 package [BBM<sup>+</sup>]. Afterwards the artificial events are treated like real data and enter the same reconstruction and analysis steps. The generators consider leading order direct and resolved processes, additional QCD radiation, plus the simulation of the beam remnants and hadronisation. This procedure is depicted schematically in figure 2.7.

### 2.7.1 PYTHIA and HERWIG

PYTHIA [Sjo94, Sjo95, S<sup>+</sup>01] and HERWIG [M<sup>+</sup>92, C<sup>+</sup>01] are powerful event generators developed for a large variety of interactions. Both packages contain the Born level QCD matrix elements of hard processes, regulated by a minimum cut-off in transverse momentum. To simulate direct and resolved photoproduction of jets, version 6.1 of PYTHIA and 6.4 of HERWIG was used with the leading order parametrisations CTEQ5L for the proton PDF and GRV-LO for the photon PDF. The kinematic range of the generated events covers  $Q^2 < 4 \text{ GeV}^2$  and  $0.001 < y < 0.999$ . In case of PYTHIA a 1-loop  $\alpha_s$  with  $\Lambda_{QCD} = 200 \text{ MeV}$  was taken, in case of HERWIG the choice was a 2-loop  $\alpha_s$  with  $\Lambda_{QCD} = 291 \text{ MeV}$ .

Higher order QCD radiation is represented by leading logarithmic parton showers. In this ansatz multiple branchings of partons using splitting functions are performed. This is followed by the hadronisation of the coloured partons into colourless hadrons. PYTHIA uses the Lund String model while HERWIG relies on the cluster model. In the Lund String model a string – a colour field with constant energy per unit length – is stretched between the partons. Gluons are assumed to produce kinks on the otherwise straight strings. At the end of the procedure, the strings break up into hadrons. In the cluster model neighbouring partons are formed into colour-singlet clusters. These clusters decay into hadrons. For more details of the two models see [Sjo94] and [M<sup>+</sup>92].

Both programs allow multiple interactions between the resolved photon and the proton. In PYTHIA they are dealt with by adding additional interactions between spectator partons within the same event by extending the perturbative parton-parton scattering to a low  $p_t$  cut-off. In case of HERWIG multiple interactions are treated by adding so-called *soft underlying event* interactions to a fraction  $P$  of the events. They are modelled on experimental soft hadron-hadron collision results. The fraction  $P$  is set to 35%.

Both generators fail to describe the absolute dijet cross sections as they only contain the leading order  $2 \rightarrow 2$  photoproduction processes. To compare them to data, the results obtained from PYTHIA are scaled up by a factor of 1.2, those from HERWIG are scaled up by 1.55. These factors are obtained by dividing the measured total dijet cross section by the unscaled predictions of PYTHIA and HERWIG, respectively.

### 2.7.2 DJANGO ARIADNE

ARIADNE 4.08 [Lon92] interfaced with DJANGO 6.2 [CSS94] was used to generate neutral current DIS events to estimate the background<sup>1</sup> for the dijet measurement as well as to study the hadronic calibration. MRS (H) [MSR] in the DIS scheme was used as the proton PDF in both cases. Two samples were generated, the first to study the background covers the phase space of  $Q^2 > 60 \text{ GeV}^2$ , the second sample covers the phase space of  $Q^2 > 100 \text{ GeV}^2$ .

---

<sup>1</sup>In [Car02] it was found that high  $Q^2$  neutral current events are the main source of background.

# Chapter 3

## Experiment

### 3.1 The HERA Collider

The HERA collider (*Hadron Elektron Ring Anlage*) at DESY (*Deutsches Elektronen Synchrotron*) is located in Hamburg, Germany. It's the only machine in the world to collide electrons<sup>1</sup> and protons.

In a tunnel 10 m - 20 m below the Volkspark two separate storage rings of 6.3 km circumference for electrons and protons have been constructed between 1984 and 1990. Located at four spots of the tunnel are the two general purpose experiments H1 and Zeus plus the two beam-target experiments Hera-B and Hermes as can be seen in figure 3.1.

The beam energy of the electrons is 27.55 GeV while for the protons energies of 820 GeV (before 1998) and 920 GeV (since 1998) are reached, leading to centre-of-mass energies of approximately 300 GeV and 320 GeV, respectively. To reach these energies, electrons and protons first pass through several pre-accelerators before they enter HERA where the final acceleration is done. The particle beams are bunched with a time distance of 96 ns, corresponding to a 10.4 MHz collision rate.

The right-handed HERA coordinate system is defined such that the  $z$ -direction coincides with the direction of the protons. The  $x$ -axis always points to the centre of the rings and the  $y$ -axis then points upwards.

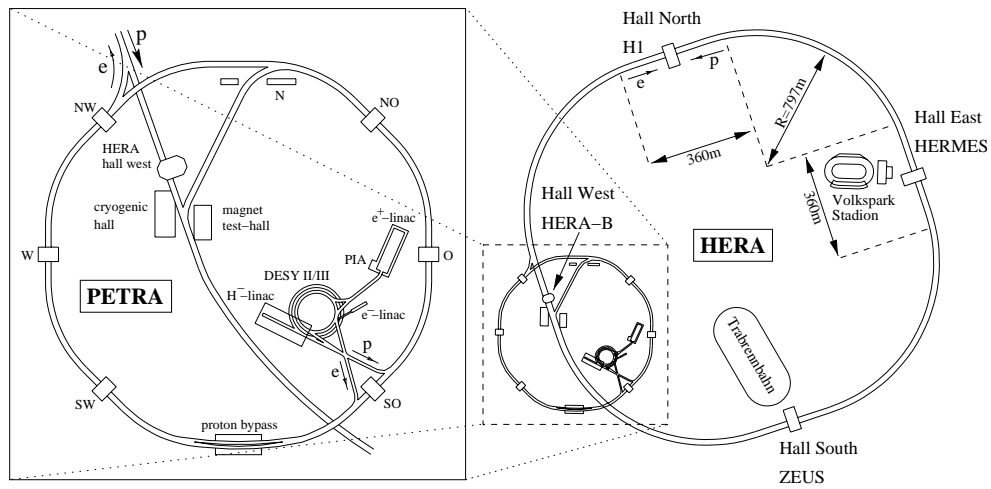
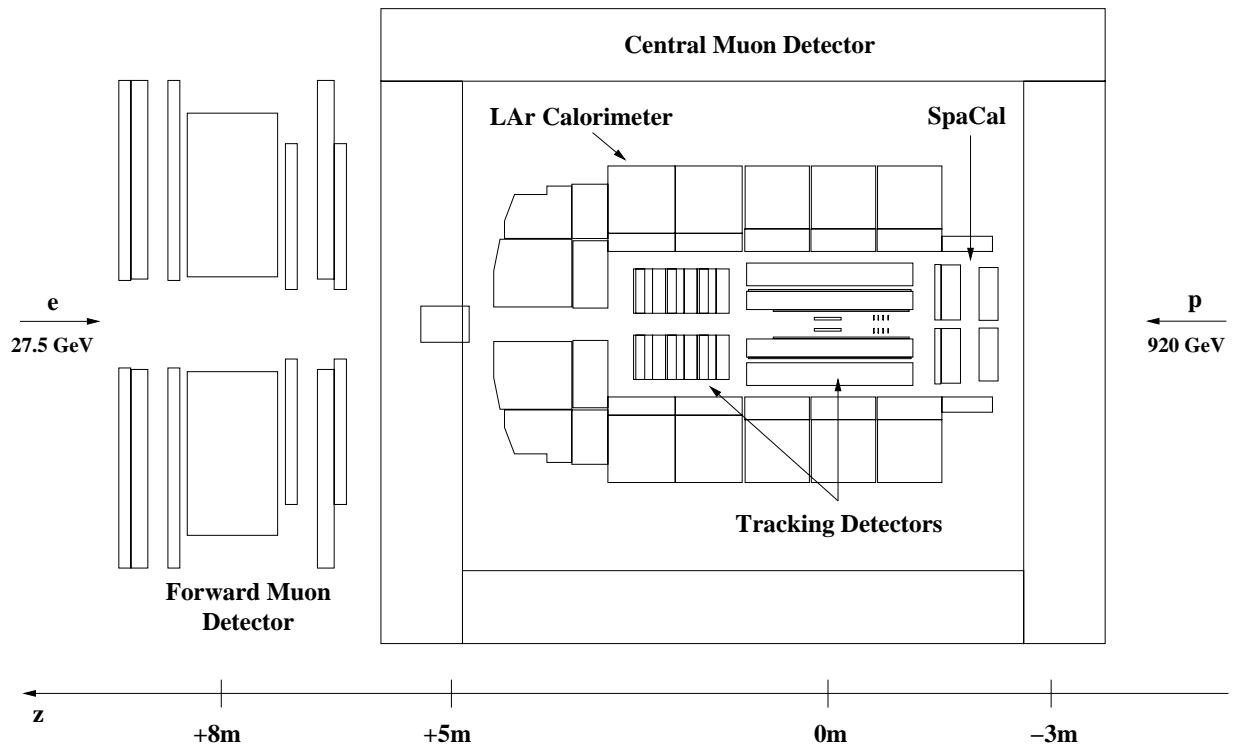
### 3.2 The H1 Experiment

The H1 detector is designed to cover almost the entire solid angle around the interaction point in its centre. Due to the different energies of the electron and proton beams and the resulting boost along the  $z$ -direction the detector is built in an asymmetric fashion. More instrumentation is put into the direction of the outgoing proton, which is also called the *forward region*.

On page 20 a schematic view of the H1 detector is given in figure 3.2. Starting from the interaction point at 0m outgoing particles first pass the tracking detectors made of drift and proportional

---

<sup>1</sup>HERA was operated using electrons or positrons during different data taking periods. Throughout this thesis both are generally referred to as electrons.

Figure 3.1: *HERA and its pre-accelerators.*Figure 3.2: *Schematic view of the H1 detector.*

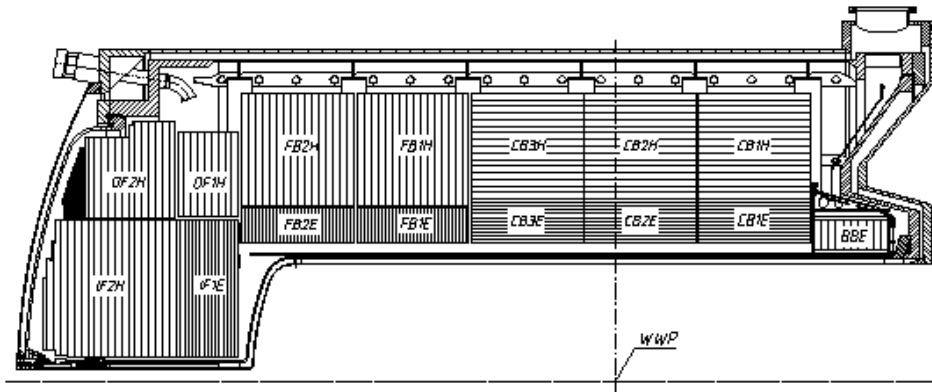


Figure 3.3: Side view of the LAr calorimeter.

chambers and silicon detectors. In the backward direction follows the *spaghetti calorimeter* (SpaCal), a lead scintillating fibre calorimeter, to mainly detect the outgoing electron which is most likely scattered under small angles. Surrounding those components is the main calorimeter, named LAr after liquid argon as the active material. It has an electromagnetic section of lead absorber plates and a hadronic section with steel as absorber.

The so-called *central detector* comprised of aforementioned tracking devices and calorimeters is inside a superconducting coil of 6m in diameter providing a magnetic field of 1.15 T. The iron return yoke of the magnet is instrumented with limited streamer tube detectors to measure hadronic energy leaking out of the main calorimeter. These detectors together with a toroid equipped with drift chambers in the forward direction make up the muon system.

Finally small angle electron and photon detectors at +33.4m and +102.9m from the interaction point complete the H1 detector. Their primary purpose is to measure the luminosity of HERA. Since the detector is described in detail in [A<sup>+</sup>97a, A<sup>+</sup>97b] I will concentrate on the components relevant to this analysis in the following sections.

### 3.2.1 Calorimetry

The calorimetry of the H1 detector is made up from four different components: the liquid argon (LAr) calorimeter, the spaghetti calorimeter (SpaCal), the tail catcher (TC) and the plug calorimeter (PLUG). Tail catcher and plug are not used in this analysis and therefore not described further.

#### Liquid Argon Calorimeter

The LAr calorimeter covers the range  $4^\circ < \theta < 154^\circ$  of the polar angle and has full azimuthal acceptance. It is the main calorimeter to measure the energy of the hadronic final state. In addition, the scattered electron is also detected under those angles for virtualities  $Q^2 \gtrsim 100 \text{ GeV}^2$ .

The LAr is segmented along the beam axis in eight wheels and each wheel azimuthally in

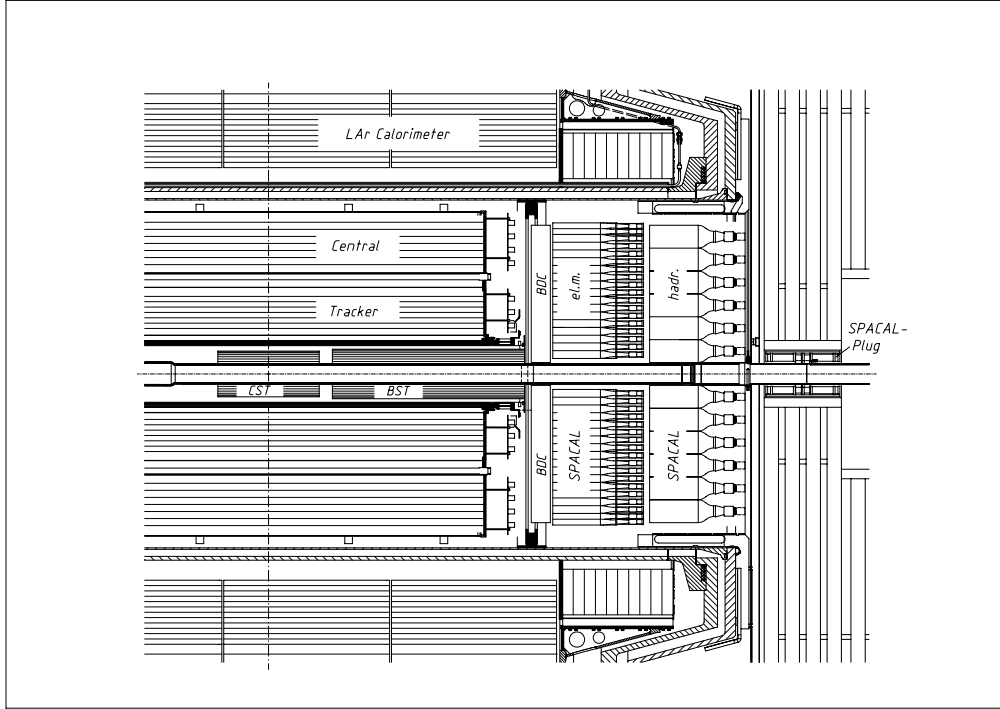


Figure 3.4: *The backward region of the H1 detector also showing the SpaCal.*

eight identical octants. The octants are then divided into an inner electromagnetic and an outer hadronic section except for the most backward wheel (BBE, c.f. figure 3.3) which is purely electromagnetic. In both parts the active material is liquid argon which was chosen because of its good stability, simplicity of calibration, fine transverse granularity and homogeneity of the signal response. The liquid argon is cooled down to  $-183^\circ$  Celsius so that it has to be placed inside a cryostat which in turn sits inside the magnet solenoid. In this way the amount of dead material in front of the main detector components is minimised.

For the electromagnetic sections lead absorber plates are used and stainless steel for the hadronic sections. The total thickness varies between 20 and 30 radiation lengths  $X_0$  for the electromagnetic sections and between 4.7 and 8 nuclear interaction lengths  $\lambda$  for the hadronic sections. The achieved energy resolution as measured in test beams is  $\sigma_{em}(E)/E \approx (11\%/\sqrt{E(\text{GeV})}) + 1\%$  in the electromagnetic and  $\sigma_{had}(E)/E \approx (50\%/\sqrt{E(\text{GeV})}) + 2\%$  in the hadronic part. The LAr is non-compensating, i.e. the response to hadrons is about 30% lower than the response to electrons of the same energy. This is compensated in the reconstruction where an energy dependent reweighting of the hadronic energy scale is performed.

More information about the LAr calorimeter can be found in [H1 93].

### SpaCal

In the backward region of the H1 detector the *spaghetti calorimeter*, SpaCal, covers the angular range of  $153^\circ < \theta < 177.8^\circ$ . It is a lead scintillating fibre calorimeter to precisely measure the

energy and impact point of the scattered electron. It also has an electromagnetic and hadronic section with energy resolution of  $\sigma_{\text{em}}(E)/E \approx (7.1\%/\sqrt{E(\text{GeV})}) + 1\%$  and  $(56.0 \pm 3.0)\%$ , respectively. The hadronic section is needed to measure leakage of electromagnetic showers from the electromagnetic part and hadronic energy flow in the backward region. For electrons with energies around 5 GeV and scattering angles  $175^\circ - 177.8^\circ$  the resulting  $Q^2$  of  $0.5 - 1 \text{ GeV}^2$  gives an upper bound on the  $Q^2$  of this analysis where events are selected in which the scattered electrons are outside the (lower) acceptance of the SpaCal.

More information about the spaghetti calorimeter can be found in [A<sup>+</sup>97c].

### 3.2.2 Tracking

The H1 tracking system is made up from several individual trackers: the two central jet chambers (CJC1 and CJC2), two – inner and outer – trackers dedicated to  $z$ -coordinate measurements (CIZ and COZ), central proportional chambers (CIP and COP), forward (FTD) and backward (BDC) trackers and central and backward silicon trackers (CST and BST). CIZ and BDC were removed during the luminosity upgrade 2001 and a forward silicon microvertex detector (FST) was added. Figure 3.5 shows a side view of the tracking system.

Two concentric cylindrical drift chambers make up the CJC. The wires are parallel to the beam-line, the angular coverage is  $15^\circ < \theta < 165^\circ$ . The resolution of the CJC is  $170\mu\text{m}$  in the  $r - \phi$  plane and  $22\text{cm}$  for the  $z$ -coordinate. Transverse momenta of (charged) tracks can be measured to an accuracy of  $\sigma_{p_t}/p_t = 0.01 \cdot p_t / \text{GeV}$  at high  $p_t$ . An improved  $z$  measurement is provided by CIZ and COZ, two thin drift chambers located at the inner and outer boundary of the CJC1. The accuracy in  $z$  is about  $350\mu\text{m}$  reached by wires perpendicular to the beam direction. Each  $z$  chamber is supported by a proportional chamber (CIP and COP) that provide a fast trigger signal.

### 3.2.3 Muon System

Muon identification was used in this analysis to reduce background events not coming from  $ep$  collisions, i.e. cosmic muons or muons from beam gas reactions. There are two parts of the detector that deal with muon identification: the Central Muon System (as part of the iron yoke of the solenoid) and the Forward Muon spectrometer. Tracks in those parts are used to identify muons by linking them with tracks in the inner trackers.

### 3.2.4 Luminosity System

The main task of the luminosity system is of course the luminosity measurement. Besides this it is also used to provide electron beam monitoring for the HERA crew, to tag photoproduction events by measuring electrons (and their energy) scattered under very small angles and to measure the energy of photons from the initial state radiation. In this work only the luminosity measurement was used.

The luminosity is determined from the rate of Bethe-Heitler reactions  $ep \rightarrow ep\gamma$  that are theoretically well understood. Background of about 10% due to bremsstrahlung on the residual gas in the beam pipe  $eA \rightarrow aA\gamma$  can be subtracted using information from the so-called *electron*

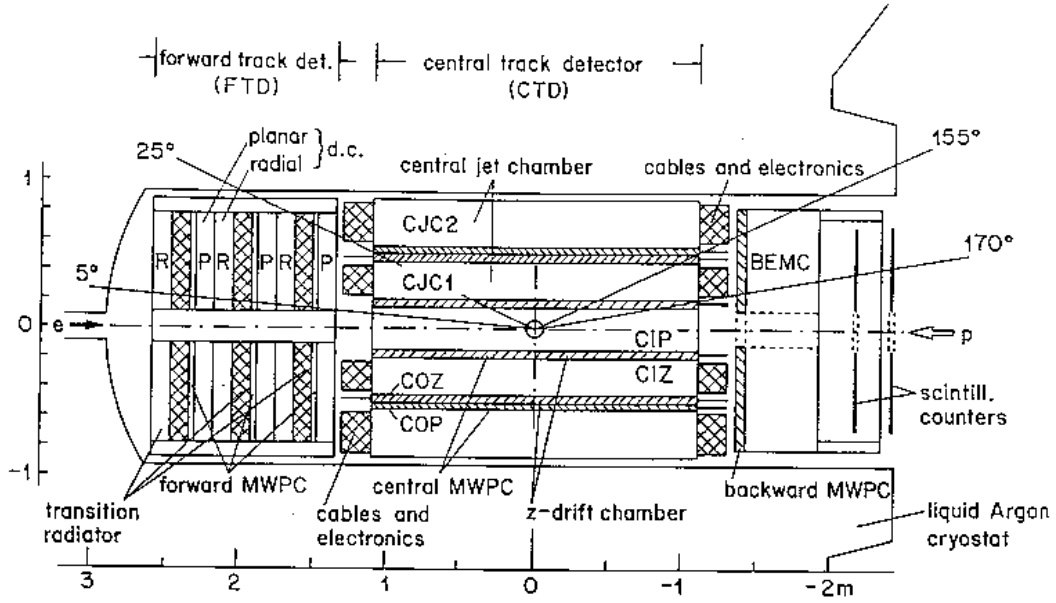


Figure 3.5: *r-z* view of the H1 tracking.

*pilot bunches*. These have no counter-bunches to collide with so that electrons confined in them interact solely with the residual gas. The luminosity is then calculated as

$$L = \frac{R_{tot} - (I_{tot}/I_0)R_0}{\sigma_{vis}}$$

Here  $R_{tot}$  is the total rate of all events registered in the luminosity detector,  $R_0$  is the rate from the pilot bunches,  $I_{tot}$  and  $I_0$  are the corresponding beam currents and  $\sigma_{vis}$  is the visible part of the Bethe-Heitler cross section corrected for trigger efficiency and acceptance of the luminosity detector.

The precision of the luminosity measurement is 1.5% for the years 1999 and 2000 which are relevant for this work. This value enters as a global normalisation uncertainty in the total systematic uncertainty.

### 3.2.5 Trigger System

A trigger system is needed to quickly decide if an event is interesting for physics analysis or a mere background reaction. The rate at which electron and proton bunches collide at the interaction point is 10.4 MHz. Not every bunch collision yields a reaction so that the typical rates of physics events range from 20 – 30 Hz for tagged photoproduction to rare processes at high  $p_t$  that occur only on much larger timescales like once per day or per week. Background rates are about 1kHz. It is clear that not all channels of the detector can be read out at such rates. A four level trigger setup provides a reduction to about 40 Hz in total that gets written to disk. Main objectives are to eliminate background while keeping the interesting events.

The first level – L1 – provides a decision after  $2\mu\text{s}$  without causing dead time. This is achieved by putting the signals of the L1 systems into a pipeline. The smallest piece of information is a so-called *trigger element* TE, e.g. energy measurements above certain thresholds or number of hits in a tracker. The central trigger logic then combines different trigger elements to 128 so-called *subtriggers*. A positive decision to keep the event on this trigger level is reached if at least one subtrigger “fired”. Some of the subtriggers might have too high rates so that all 128 subtrigger rates added up exceed the upper limit allowed for this level. Therefore certain subtriggers get prescaled with a factor  $n$  so that only every  $n$ -th positive decision of this subtrigger gives a keep signal.

The L2 decision is formed by two hardware systems: a topological trigger (L2TT) and a neural network (L2NN). The time to reach a decision is  $20\mu\text{s}$ , the L2 system can evaluate somewhat more complex information than L1 like track multiplicities. The L3 system is not yet in place. It is a software trigger that will include a fast track trigger (FTT) and a jet trigger.

On L4 a full but simplified event reconstruction is performed that is used to verify the L1 decision. Events accepted by L4 are written to disk and later fully reconstructed.

More detailed information on the H1 trigger system can be found in chapter 5 of [A<sup>+</sup>97a]. The triggers used for this thesis are discussed in section 5.1.7.



# Chapter 4

## Development of a new object-oriented analysis framework

### 4.1 Why a new framework?

In 1998 H1 decided to implement a new software framework for general analysis purposes. The motivations to take this step were threefold.

#### 4.1.1 Homogenous environment

First of all there was the aim of a single framework and code reference for all steps of an analysis. Roughly speaking an analysis will consist of batch processing of large data volumes with compiled software, interactive or automated visualisation of the data within a macro environment, and last not least a graphical representation of the detector with its chamber hits, tracks, energy deposits in the calorimeters etc.

So far those three steps were accomplished with different software packages and programming/macro languages. Fortran was used as language for batch processing along with a library of commonly used functions called PHAN (Physics Analysis Package). The display of histograms, functions and the like was done with PAW (Physics Analysis Workstation) which has its own macro language and an interpreter for KUIP, a Fortran inspired language. The event display H1ed then was based on a package called LOOK.

For the new analysis framework it was decided to take ROOT [BR97] as the basis for all three major tasks described above. It uses C++ as both the language for compiled code as well as for interactive macros. To achieve the latter – C++ normally is not an interpreted language – the C++ interpreter CINT is used. The expected benefit is that code developed in later steps of an analysis can more easily be ported to the official software repository and thus become available to everyone. The new event display H1Red then is also implemented within the same framework. This means it can be used just as the macro environment where all selection cuts are directly reflected in the events that get displayed. A sample picture of the new event display is shown in figure 4.1.

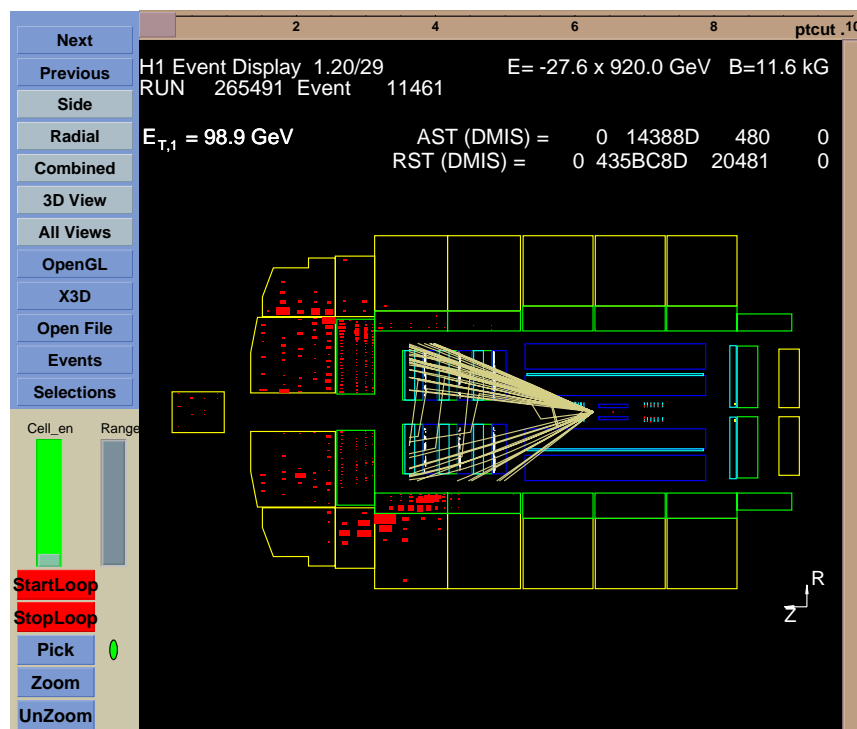


Figure 4.1: A typical H1 event display. Shown is the event with the highest  $p_t$  jet from the final event sample of this analysis.

### 4.1.2 Increasing demands

The second motivation is related to the increasing demands of the software used for analysis. With more efficient data taking and the luminosity upgrade the data volumes to be processed are becoming larger. The capabilities of the ROOT I/O system along with a new data storage model were believed to better match those requirements than the existing model.

### 4.1.3 Modern techniques

In going for a framework based on object orientation and the – with respect to Fortran – more popular programming language C++ it was envisaged that the H1 experiment would become more attractive for new students. Using modern and widely accepted tools and software paradigms will benefit young people beyond their career in the field of high energy physics.

## 4.2 The H1 OO framework

Now follows a description of the basic principles implemented in the H1 OO framework. I will first outline the data storage design because it drives the decisions to be taken for the actual code that makes up the environment.

### 4.2.1 Data storage

The data format produced by the H1 reconstruction software H1Rec are so called DST files (Data Summary Tape). They are written in FPACK format and contain so called BOS banks to represent the data structures. One can imagine those BOS banks as tables where for example each row represents a particle and the columns make up the properties of a single particle. These DST files are centrally stored and are in principle the basis of any analysis performed in H1.

The first step of an analysis in the context of Fortran and PHAN is the production of a so called *ntuple*. This is a file that contains only part of the information of the full DSTs. Firstly because just a subset of all events is put into the ntuple that fulfil certain preselection cuts. And secondly because only quantities that will be used later in the analysis are written out. The reason is to keep the data volume to be processed small in the detailed studies of an analysis. Otherwise the many iterations needed for final results would take too long with the always limited computing resources at hand. In principle not everybody has to create their own ntuple. Typically working groups produce ntuples with file contents and a selection applied that allow more than one analysis to run on them.

A drawback of this approach is that if it turns out that information is missing from the ntuple it has to be recreated completely. This is a time consuming procedure and can't be done too often in the course of an analysis.

The new data model in the H1 OO framework replaced the DST with the so-called *Object Data Store* ODS that contains the same information in object format. For clusters and tracks completely new objects were designed to ease usage in everyday analysis, all other information was still kept in BOS-bank-like objects. In the early stages of the framework ODS was persistently written to disk as files. Nowadays when ODS-like information is accessed the original DST is read in and converted to the ODS format on-the-fly.

New in the data model in H1 OO are the so-called *Micro Object Data Store* (MODS) and *H1 Analysis Tag* (HAT). The MODS contains higher level information like particles reconstructed from tracks and clusters. Particle identification is also performed on this level so that ready-to-use electrons, muons or composed particles like  $D^*$ s are provided. The HAT then contains event summary information like kinematic variables, particle multiplicities, energy sums in different parts of the detector, etc. Based on those quantities (simple numbers instead of objects) a fast event selection can be performed without the need to read large data volumes. The three layers are physically written to different file streams.

So-called *user trees* can be added in parallel to the three official data layers that may contain any kind of information not provided in the standard data layers. Typically these are analysis specific information too time consuming to recompute in each event. The number of user trees parallel to the official data layers is not limited.

### 4.2.2 Main concepts

In the following key features of the implementation are briefly highlighted. Code examples or class names will be written using `this font`. For more detailed descriptions see the H1 OO project document [Pro03a].

## Access to Data

In ROOT data inside a file is organised as a so-called *tree*. A tree can have an arbitrary number of so-called *branches* holding the actual objects or collections of objects to be stored. Random access to individual events is provided by the tree as well as the so-called *partial event reading*, i.e. branches can be read independently of each other. Reading only a subset of the branches for each event can speed up data access significantly.

The parallel access to data of the same event for the three<sup>1</sup> storage layers in H1 OO – ODS, MODS and HAT – cannot be achieved with the features provided by ROOT alone. Therefore the H1Tree was designed to grant transparent and consistent access to all layers present in an analysis program. It is possible to loop over events sequentially forwards and backwards or to directly jump to an event based on its run<sup>2</sup> and event number.

In order to conveniently read objects so-called *branch pointers* were designed. These are smart pointers that load the objects on demand when they are first accessed for an event. On which data layer the actual information is stored is encapsulated in the pointer mechanism. This pointer mechanism also contains a second type of smart pointers that are used to reference between objects of different layers (i.e. files). A typical example is a particle stored on MODS that references its tracks and or clusters that are stored on ODS. Thanks to the H1Tree and the pointer mechanism the user sees only one input stream and need not care about the physical location of the information he wants to access.

A second key feature provided by the H1Tree are selections. The simple form is the so-called *HAT selection* in which an arbitrary logical combination of arithmetic expressions on the variables stored on HAT can be used to select events. To select for example events with at least two jets with the transverse momentum of the leading jet larger than 25 GeV the selection string

```
"NumKtJets > 1 && KtJetPt > 25"
```

is used. A list of more than 200 available HAT variables is provided in the online documentation [Pro03b]. HAT selections are typically performed before the event loop, the sequential reading of events then only reads events matching the criteria of the HAT selection.

The more powerful method to select events uses so-called *event lists*. To fill an event list with entries one has to first create an object of type H1EventList. Looping over the events any selection using information from all available data layers can be applied. If an events matches the selection criteria, it is added to the event list by calling its `Enter()` method. At the end of the event loop the event list can be written to file to be re-used when running on the same data again. When performing a HAT selection, internally a default event list is created. It can be retrieved and treated exactly the same as an event list that was filled on an event-by-event basis.

An H1EventList object also remembers the input files that were loaded while constructing it, so that event lists can also be used to conveniently specify the data input for an analysis program. Otherwise files for each layer to be used need to be specified individually or as file ranges. It is possible to use only the file specification feature of the event lists, i.e. to specify the data input

---

<sup>1</sup>User trees are handled exactly the same as the official data layers, thus the number of parallel layers can be larger than three.

<sup>2</sup>A “run” is a period of data taking with stable conditions. In H1 the maximum length of a run is two hours.

without applying a selection. In this way one can for example conveniently group any number of corresponding MODS and HAT files together to form meaningful data sets.

### Runtime steering

A crucial feature to the success of the new analysis environment was the possibility to steer the behaviour of the software at runtime. This includes for example specifying the data input or setting parameters for physics algorithms. There were two possibilities: either re-use the code that was used in the Fortran world or write new code directly in the new environment. The latter option was chosen to avoid the many additional dependencies a re-use would pull in. Also the Fortran steering reads from standard input, i.e. the keyboard. Since the number of steering option can get large, it is common practice to write all options into a file and then “pipe in” its content to the program. But this closes the standard input stream at the end of the file which makes it unusable for interactive work, contradicting the paradigm that a single framework was to be used for batch jobs as well as interactive sessions.

The newly written steering mechanism is twofold. First, classes are provided to evaluate options given at the command line at program start. They encapsulate the complexity of the low-level functions provided by the standard C library. A class `H1StdCmdLine` can be used to automatically evaluate the most common options like specifying an output file, the number of events to be processed or the name of the steering file containing e.g. the names of the data input files.

Such a steering file is an example of the second kind of runtime steering developed for the H1 OO framework. To stick to the “one framework” idea the syntax of the steering was chosen to be C++-like, somewhat resembling the constructor of a class. The steering file gets parsed and blocks of related steering options identified by keywords. Such blocks then get delegated to classes of the same name as the keywords in the file. Those classes are responsible to evaluate the settings. This way the general mechanism does not need to know about all possible steering options, it uses the so-called *runtime type information* (RTTI) system of ROOT to find the delegates.

A steering example is shown here:

```
// steering of the OO electron finder
H1SteerCreateScatElec ()
{
    fCutElmLow   = 8.5; // default is 8.0
    fCutElmFrac  = 90;  // default is 98
    fCutThetaLow = 100.0; // default is 155.0
}
```

Basic features are the grouping of related options by the same kind of braces (“{” and “}”) used in the C/C++ language and assigning them to a class (here “`H1SteerCreateScatElec`”). Simple assignments are supported where a steering class is responsible to set meaningful default values so that nothing needs to be given if standard settings are to be used. Of course comments (in the C++ notation “//”) are allowed to annotate the options. More features and details can be found in the steering manual [Pro03c].

### Data Structures and their Filling

The definition and the filling of the data structures is separated in the H1 OO framework. This was done to allow different algorithms to fill the same data structures, namely wrapped Fortran code to make real data available in the H1 OO framework before physics algorithms were natively available in C++. The separation also avoids large dependencies on filling code in an environment where data only needs to be read, e.g. on a laptop.

So-called *event classes* define the data structures in memory as well as on disk. They are responsible to allocate the objects and to create corresponding branches on file for writing or connect the branches on file with the objects in memory for reading. In principle there is one event class per data layer with the exception of the ODS, where the sheer amount of objects suggests to split the classes up. The implementation of the event classes is done in a way that only those branches are used in reading that are “known” to the class and are on the file. This ensures that old files can still be read with newer versions of the software if only new objects have been added<sup>3</sup>. Of course when the data format of objects changes it is necessary to use a version that is compatible. On each event before the writing or reading the event classes also clear the data structures in memory.

To each event class corresponds a so-called *filler class* that is responsible to fill the data structure with content. Internally it uses other classes that either convert the input format to the H1 OO data structures or implement physics algorithms like track selection, particle identification, jet algorithms, etc. New physics algorithms can be plugged in at any time by extending the event class and filler class of the corresponding data layer.

Users who want to write and read additional data via user trees just have to provide at least one event and corresponding filler class. Several standard executables are prepared to easily plug in the user code in the form of a shared library.

For more information see chapters 3 and 6 of the H1 OO project document [Pro03a].

### Definition of the Hadronic Final State

Since the jets used in this work are reconstructed from objects of the hadronic final state (HFS) a description of the corresponding algorithm is given in this section.

The HFS algorithm in the H1 OO framework – called HADROO – uses tracks from the central jet chamber CJC and clusters from the SpaCal and LAr calorimeters plus vertex information as input. The input objects are already preselected based on quality criteria described in chapter 5 of [Pro03a] that also contains the detailed description of the HADROO algorithm. Before the actual algorithm is run, tracks and clusters already associated to identified electrons and muons are removed from the input.

The procedure matches track and cluster information in a way that avoids double counting of energies. The resulting objects of this algorithm are called *HFS objects*. Whether to take track or cluster information to construct an HFS object depends on the precision of the momentum

---

<sup>3</sup>Or removed. In this case all other objects can still be read.

measurement of the track and the expected precision in the calorimeter of

$$\left(\frac{dp_t}{p_t}\right)_{calo}^{expected} = \frac{50\%}{\sqrt{E_{track}}}.$$

The algorithm has a parameter  $\alpha$  that influences at which point calorimeter measurements are preferred over track measurements. The default value of 0.05 is taken in this analysis. This means only for low  $p_t$  where the track resolution is much better than the calorimeter resolution the track information is used.

The procedure starts with all tracks and tries to match them with clusters. For tracks with

$$\left(\frac{dp_t}{p_t}\right)_{track}^{measured} < \alpha \cdot \left(\frac{dp_t}{p_t}\right)_{calo}^{expected}$$

the track information is preferred and electromagnetic (hadronic) energy in clusters within a cylinder of 25cm (50cm) around the extrapolated track is discarded until the removed energy is approximately equal to the track energy.

For tracks with

$$\left(\frac{dp_t}{p_t}\right)_{track}^{measured} \geq \alpha \cdot \left(\frac{dp_t}{p_t}\right)_{calo}^{expected}$$

three cases need to be distinguished. If the energy of the track is within  $N\sigma$  of the calorimeter energy in a cylinder behind the extrapolated track, the corresponding clusters are used to construct the HFS object. Similar to  $\alpha$ ,  $N$  is a parameter of the algorithm set to the default value of 2 in this analysis. If the energy measurements are not compatible, i.e. more than  $N\sigma$  apart, the track is simply ignored as mismeasured if  $E_{calo} \ll E_{track}$ . If  $E_{calo} \gg E_{track}$  energy in a cylinder behind the track is discarded in the same fashion as when the track precision is better than the expected calorimeter precision.

After all tracks have been considered, HFS objects are constructed from each cluster left. The jet algorithm is then run on all HFS objects plus electrons and muons that had been excluded for the HFS finding as input except for the scattered electron.



# Chapter 5

## Data analysis

### 5.1 Data selection

The data of this analysis was taken in the years 1999/2000 where electrons of 27.6 GeV were brought to collision inside HERA with protons of 920 GeV, yielding a centre-of-mass energy of  $\approx 320$  GeV. This sample corresponds to a total integrated luminosity of  $66.6 \text{ pb}^{-1}$  corrected for deadtime and vertex restrictions.

This section is outlined as follows. First the general setup of the analysis inside the so-called OO framework is described. Then I will present the general preselection cuts before I come to the selection of the final event sample to be analysed. This is followed by an examination of the background from DIS events. Finally the trigger efficiency is studied.

#### 5.1.1 Analysis setup

In order to produce results in reasonable time the amount of data to run on needs to be reduced from the originally  $\approx 100$  million events that were recorded in the analysed data taking period. The first means to achieve this is a selection on HAT variables. This is quite fast since only few data has to be read from file as compared to reading the complete MODS information. Events that match the criteria of the HAT selection are then stored to new files that are the starting point for further selections. This step is usually done only once or twice in an analysis.

In the next step MODS information is regarded in addition to further reduce the number of events. Also cuts on HAT variables are placed in this step that a-priori were not obvious enough to be included in the first preselection. One example is the cut against the scattered electron which has to be disabled for the data sample to monitor the trigger efficiency (c.f. section 5.1.7). The events selected in this step once again are written out for the final analysis steps to run on. In addition for those events a user tree is written in case of Monte Carlo containing detailed generator level information not available on standard MODS or HAT. This reduces the effective number of events to be repeatedly processed by a factor 5000 in the case of data and a factor 8 for Monte Carlo.

Preselection on HAT
run quality “good” or “medium”
reconstructed central vertex
$p_{t,miss} < 20 \text{ GeV}$
$E_{t,scalar} > 30 \text{ GeV}$
$p_{t,jet,max} > 18 \text{ GeV}$
#jets > 1

Table 5.1: Cuts used in the first preselection step. This is HAT level information only.

### 5.1.2 Preselection cuts

To reduce the amount of data a preselection is performed, which in a first step uses only HAT data and in a second step uses MODS data. For the first preselection step any energy cuts are done without the final state calibration described in section 5.1.3. At that stage there are six quantities to cut on (c.f. table 5.1). The so-called run quality has to be either “good” or “medium”. This excludes data taking periods with unstable running conditions or main detector components not operational. A reconstructed central vertex is required to reduce background events. To exclude charged current events and further background the total  $p_{t,miss}$  has to be below 20 GeV.

Having the final selection in mind, the number of events to be processed in later stages of the analysis can be further reduced by cutting on the scalar  $E_t$  of the event. This is the sum of the transverse energy for all particles in the event. Since the jet selection criteria in the end impose cuts of  $E_{t,max} > 25 \text{ GeV}$  and  $E_{t,second} > 15 \text{ GeV}$ , the scalar  $E_t$  will be at least 40 GeV. So in the preselection we cut on  $E_{t,scalar} > 30 \text{ GeV}$ . Finally the number of jets in the event<sup>1</sup> has to be larger than one with the highest  $p_{t,jet} > 18 \text{ GeV}$ . Cuts on the second highest  $p_{t,jet}$  are not possible at this stage, since that information is not available on HAT level. A summary of the cuts on HAT level for the preselection can be found in table 5.1. Applying those cuts leads to a reduction of the total H1 data sample to 200,000 events.

In the second step also more detailed information from MODS is used. Those quantities are evaluated after the hadronic final state has been calibrated. Only events are kept that have a maximum jet  $p_t > 24 \text{ GeV}$  and a second largest  $p_t > 14 \text{ GeV}$ . The inelasticity calculated from the hadrons – called *Jaquet Blondel* method,  $y_{JB}$  – is restricted to the range  $0.1 < y_{JB} < 0.9$  which also defines the phase space of the measurement.

Also the cut on the photon virtuality as calculated from the scattered electron (labelled  $Q_{el}^2$ ) is done here to remove events with an identified scattered electron. They are excluded by requiring  $Q_{el}^2 = 0 \text{ GeV}^2$ . Background is rejected by requiring the vertex of the event to be reconstructed within  $-35 \text{ cm} < z_{vertex} < 35 \text{ cm}$ . Further background is reduced by using information from the non- $ep$  background finders that will be described in 5.1.4. Events flagged as background by one of the standard algorithms are rejected. Last in this step is the cut on the status of the high-voltage systems. Only events are accepted where the following components of the detector were operational: CJC, CIP/COP, LAr, SpaCal, time of flight and luminosity system. The same sub-

<sup>1</sup>Jets identified by the jet finder as stored on MODS are considered “jets” for  $p_t > 2.5 \text{ GeV}$ .

Preselection on MODS and HAT
CJC, CIP/COP, LAr, SpaCal, ToF, lumi HV on non- $ep$ background finder (bits 0-9 not fired)
$ z_{vertex}  < 35 \text{ cm}$
$Q_{el}^2 = 0 \text{ GeV}^2$
$0.1 < y_{JB} < 0.9$
$p_{t,jet1} > 24 \text{ GeV}, p_{t,jet2} > 14 \text{ GeV}$

Table 5.2: Cuts used in the second preselection step.

systems are required as operational in the calculation of the luminosity of the analysed sample. The cuts of this step are summarised in table 5.2. They define the sample that is used to iterate on. It comprises 20706 events.

### 5.1.3 Calibration

#### Jet ordering

Detailed studies in multi-jet events require some kind of ordering of the jets if they are to be examined individually. Natural choices are the transverse momentum or the pseudorapidity. As it turns out, comparing data to Monte Carlo – using the PYTHIA and HERWIG generators – with  $p_t$  ordered jets leads to an insufficient description of the jet angular distribution. This can be attributed to a slightly imperfect energy calibration. To first order the two jets should be balanced in  $p_t$ . If the calibration is different in different areas of the detector, the second leading jet can be reconstructed as the higher  $p_t$  jet depending on the direction. If this is not well enough described in the simulation, ordering the two jets in transverse momentum should be avoided. The situation can be seen in figure 5.1, where transverse momentum and polar angle of the two jets are shown before any additional calibration is applied. Especially the  $\theta$  distribution of the leading jet is not in good agreement and shows a structure not easily understood. Going to angular ordered jets as in figure 5.2 cures the problem. This is because angles are generally measured better than energies.

For the rest of this thesis, individual jets are always shown in angular ordering if not specified otherwise. They are labelled “forw” for the forward and “backw” for the backward jet. In  $p_t$  ordering the labels are “max” for the leading and “2nd” for the subleading jet. Quantities that don’t depend on any ordering like mean values or  $x_\gamma$  and  $x_p$  are of course not affected by the variable in which the jets are ordered.

#### Hadronic calibration

For a better reconstruction of the jet quantities an additional calibration is applied to the individual jets. The total four-vector of the hadronic final state is then recalculated as well as kinematic quantities like  $y_{JB}$ .

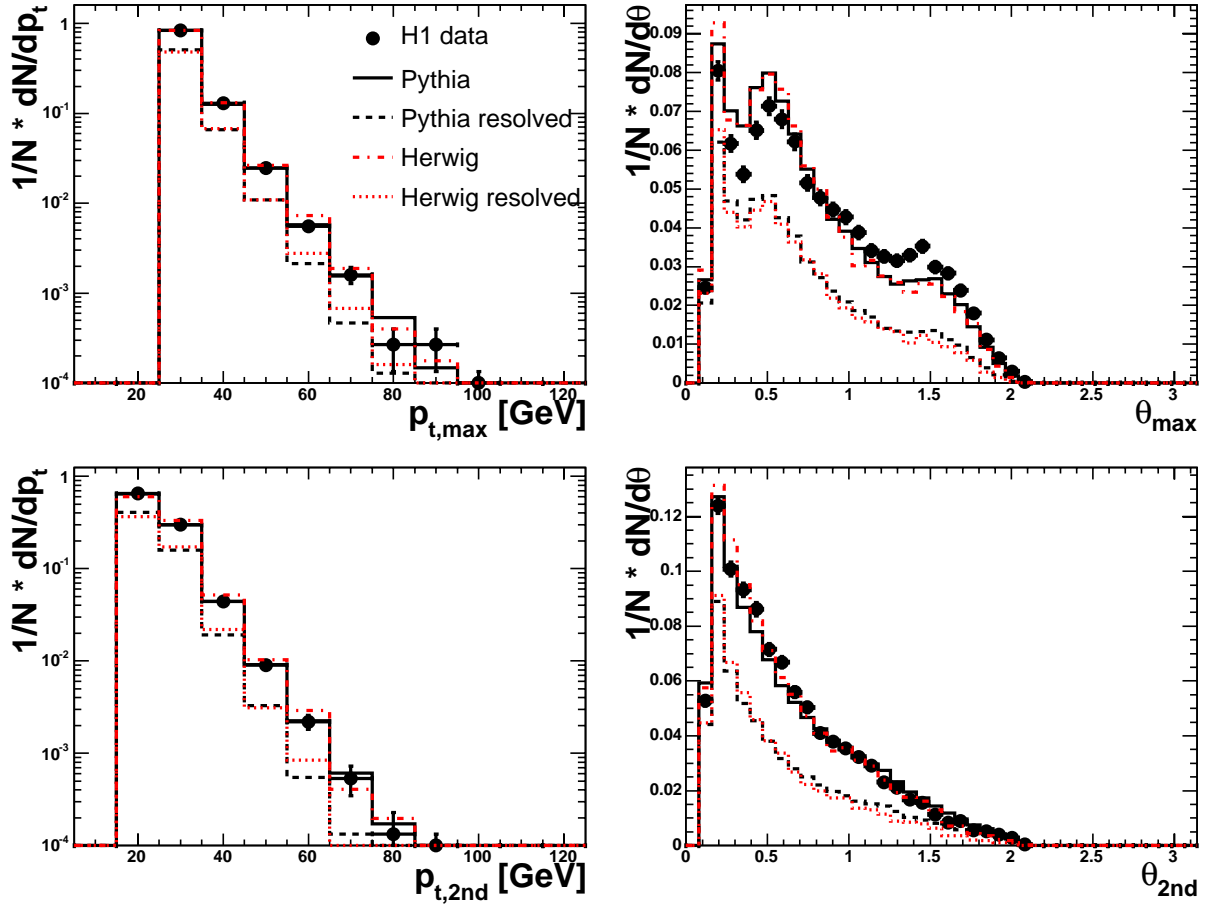


Figure 5.1: Jets in  $p_t$  ordering before additional hadronic calibration. Transverse momentum and polar angle of the jet with the highest  $p_t$  is shown in the upper two figures, the lower two show the second leading jet.

The hadronic calibration makes use of the fact that for neutral current DIS events the transverse momentum of the scattered electron  $p_{t,e}$  and of the hadronic final state  $p_{t,had}$  are balanced. A  $p_t$  dependent absolute calibration of the HFS is performed and applied to both data and Monte Carlo. The relative calibration is performed separately for all wheels of the detector and depends on the pseudorapidity of the jet. It is applied only to data. This study was carried out in [Rau02] and the constants obtained there were applied in this analysis.

To check the effect of the calibration a neutral current DIS sample of the year 2000 data taking period was selected and compared to a DJANGO ARIADNE Monte Carlo. The cuts used for this selection are listed in table 5.3.

Figures 5.3 to 5.6 show the  $p_t$  balance between the scattered electron and the hadronic final state as function of different electron, HFS or jet observables. In general the agreement between data and Monte Carlo improves by applying the calibration. While the balance is not always shifted exactly to unity, the distributions get flatter.

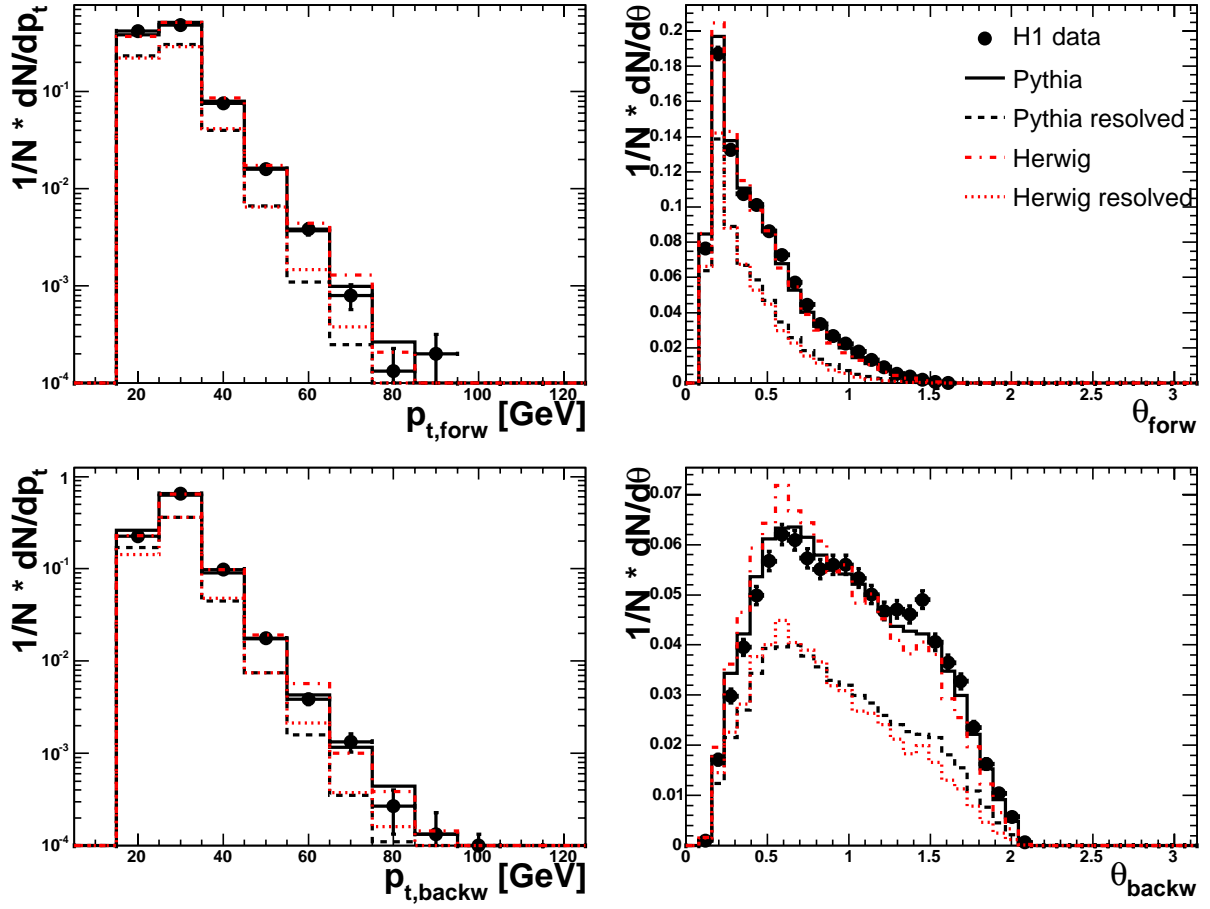


Figure 5.2: Jets in angular ordering before additional hadronic calibration. Transverse momentum and polar angle of the forward jet is shown in the upper two figures, the lower two show the backward jet.

NC DIS selection
$ z_{vertex}  < 35 \text{ cm}$
$Q_{el}^2 > 200 \text{ GeV}^2$
$0.1 < y_{JB} < 0.9$
$45 \text{ GeV} < (E - p_z)_{total} < 65 \text{ GeV}$
$p_{t,miss} < 20 \text{ GeV}$
$E_{elec} > 10 \text{ GeV}$

Table 5.3: Selection cuts for the neutral current DIS sample that was used to check the hadronic calibration.

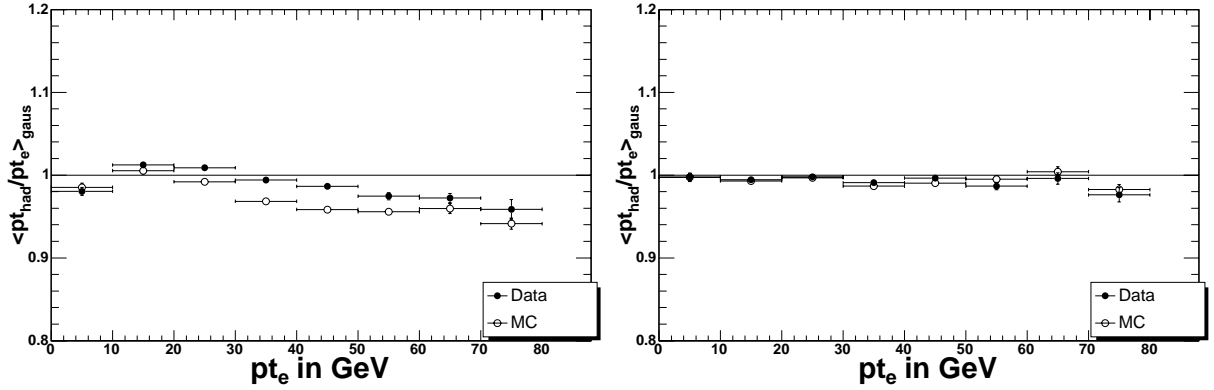


Figure 5.3:  $p_t$  balance between electron and hadrons as function of the electron  $p_t$  before (left) and after (right) calibration.

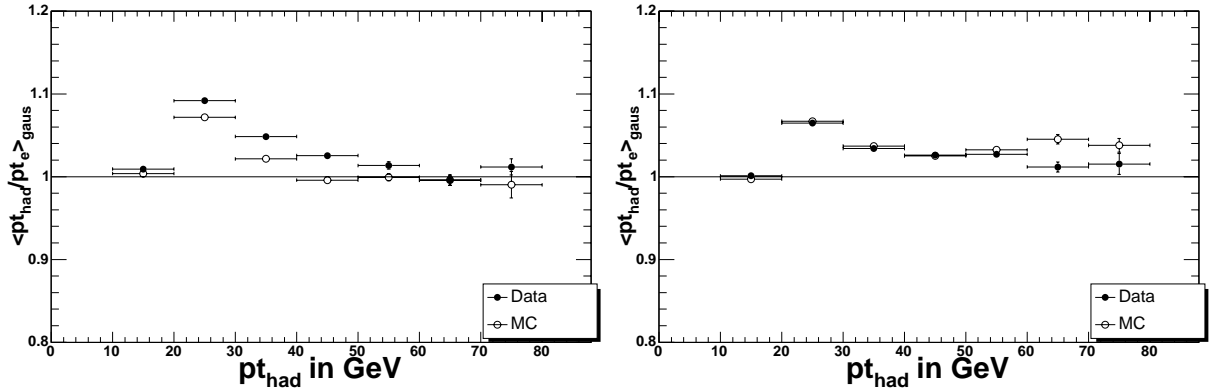


Figure 5.4:  $p_t$  balance between electron and hadrons as function of the hadronic  $p_t$  before (left) and after (right) calibration.

Most important is the balance as function of the jet angle  $\theta$  in figure 5.6. In the backward direction agreement between data and Monte Carlo is within 2% up to  $\theta = 110^\circ$  and both quantities are close to one. The backward cut on the jets in the final selection of  $\eta = -0.5$  corresponds to  $\theta \approx 118^\circ$ . In the forward direction up until  $30^\circ$  the ratio shown is smaller than one. In this region the jet energy is typically reconstructed too low because particles belonging to a jet may escape undetected through the beam pipe. Since the data is well described by Monte Carlo even for small angles the correction for detector effects compensate for these losses in the cross section calculation.

As shown in figures 5.3 to 5.6 data and Monte Carlo agree within 2%. This value is later used in the determination of systematic uncertainties (c.f. section 5.4.1).

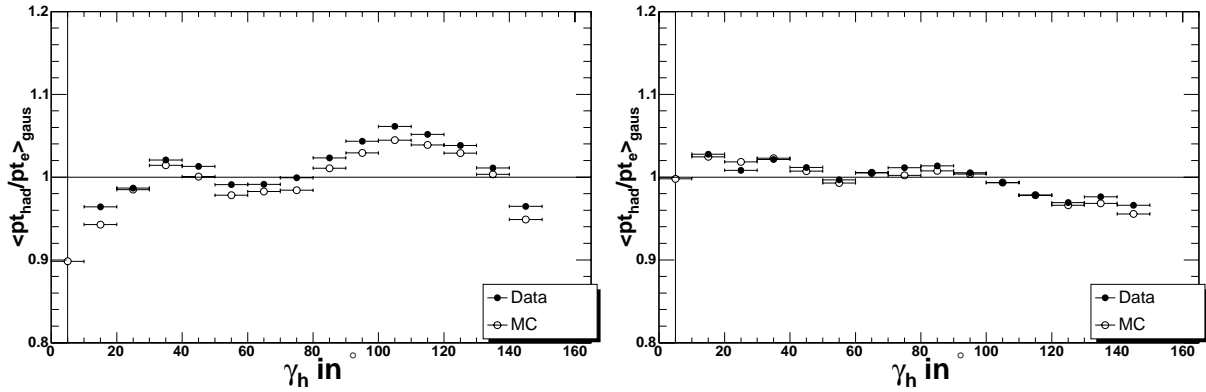


Figure 5.5:  $p_t$  balance between electron and hadrons as function of the hadronic angle before (left) and after (right) calibration.

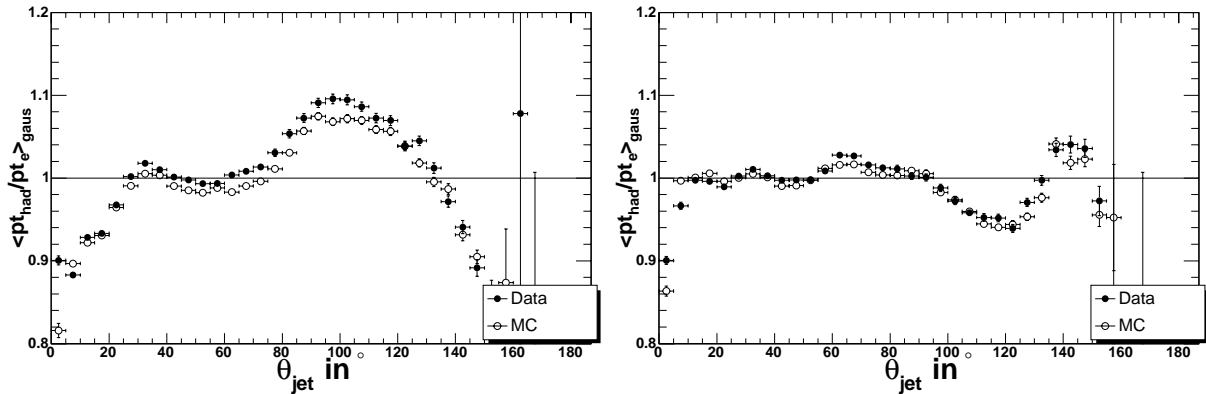


Figure 5.6:  $p_t$  balance between electron and hadrons as function of the jet angle before (left) and after (right) calibration.

### 5.1.4 Background studies

#### Non $ep$ background finders

Several background finder algorithms are used to search for signatures of cosmic muon events where muons are produced when highly energetic cosmic particles hit the earth's atmosphere and halo particles which are coming from interactions of the proton beam with the beam pipe wall or gas molecules inside the beam pipe. The package used<sup>2</sup> consists of several independent algorithms that look for different topologies typical to events that don't come from  $ep$  collisions. There are 10 so-called "safe" algorithms numbered 0 to 9 that ensure minimal inefficiency for  $ep$  physics. Additional discriminating quantities and predefined cuts on them also provided by the package are not considered in this analysis.

Figure 5.9 shows the distribution of the background finder bits after all other cuts of the final

<sup>2</sup>The so-called QBGMAR background finders [C<sup>+</sup>98] were originally written in Fortran and later ported to the OO framework [Vee02].

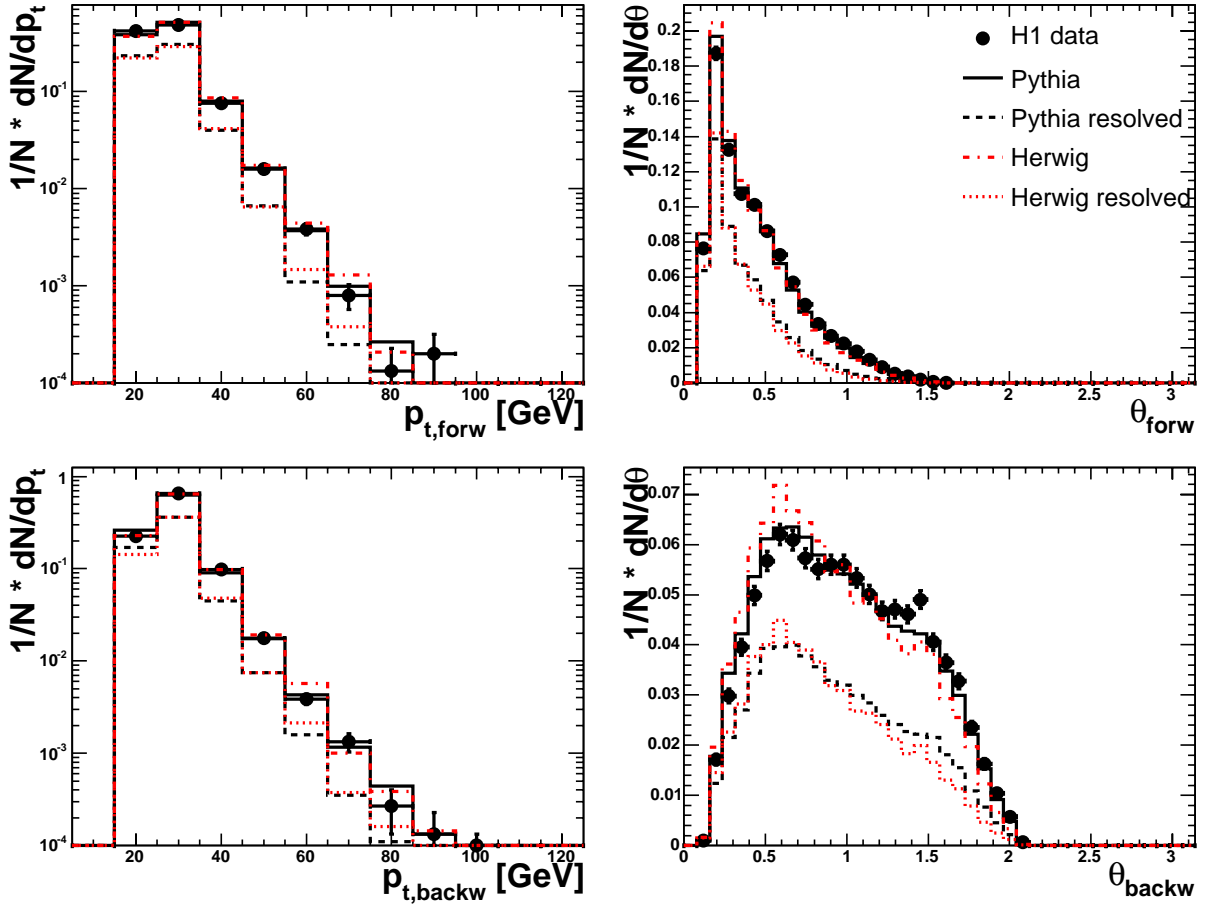


Figure 5.7: Jet comparison between data and Monte Carlo before calibration for  $p_t$  and  $\theta$  of the forward (above) and backward jet (below).

event selection (c.f. table 5.4) have been applied. Less than 1.5 events per inverse picobarn are rejected as background in both data and Monte Carlo. Only the finder algorithm corresponding to bit 7 rejects significantly more events in data than in Monte Carlo. This can be interpreted as the rejection of real cosmics on top of an inefficiency introduced by the algorithms. The inefficiency found in the  $\gamma p$  Monte Carlos is used to correct the data in the unfolding step. Compared with a total of  $\approx 165$  events/ $\text{pb}^{-1}$  in the final sample any uncertainty from this selection step is neglected.

### DIS background

The main handle to remove DIS events from the analysed sample is to require that no candidates for the scattered electron are found in the LAr or SpaCal calorimeter. This then restricts the range in the photon virtuality to  $Q^2 < 1 \text{ GeV}^2$  simply given by the acceptance of the detector. Because the electron finder algorithm is not 100% efficient, the scattered electron can remain unidentified. In this case it is treated as part of the HFS. As a consequence, all kinematics

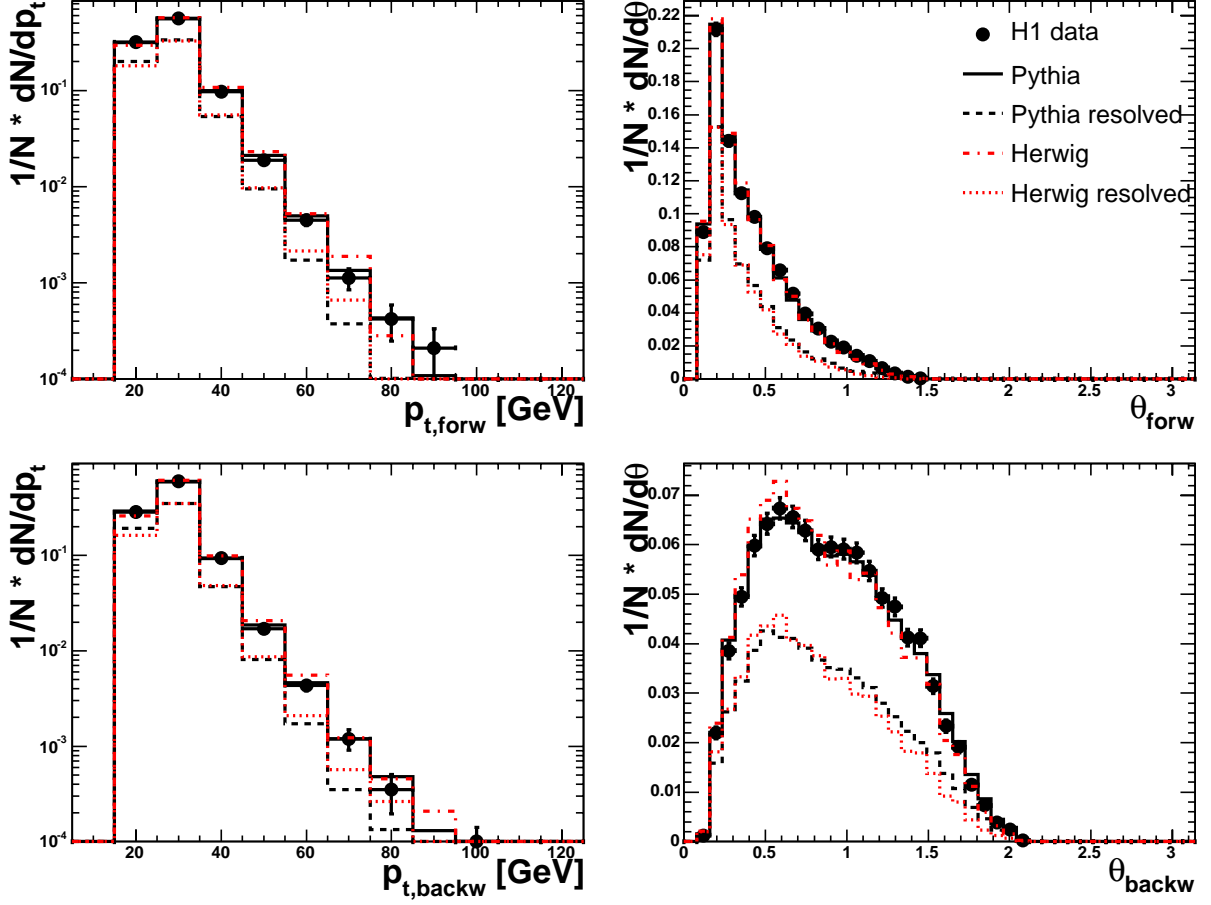


Figure 5.8: Jet comparison between data and Monte Carlo after calibration for  $p_t$  and  $\theta$  of the forward (above) and backward jet (below). Improvements in the description can be clearly seen in the jet angle.

calculated from the hadronic final state are wrong. To reject such events, the total hadronic  $E - P_z$  is considered. This quantity is defined as

$$E - P_z = \sum_i E_i - P_{z,i} \quad (5.1)$$

where the index  $i$  runs over all HFS particles. Looking at energy and momentum conservation this quantity plus the  $E - P_z$  of the scattered electron should sum up to twice the electron beam energy<sup>3</sup>. This means the hadronic component should be smaller than 55.2 GeV. For events where the scattered electron mistakenly is part of the HFS, the hadronic  $E - P_z$  will be close to that value. Therefore a cut is made in  $E - P_z$  at  $0.9 * 2E_{e,beam}$  against such events. Since  $y_{JB}$  and  $E - P_z$  are connected via  $y_{JB} = (E - P_z)/(2E_{e,beam})$  this cut also defines the upper limit of the phase space in  $y$  at 0.9.

<sup>3</sup>For massless incoming electron and proton this can easily be calculated for the initial state.

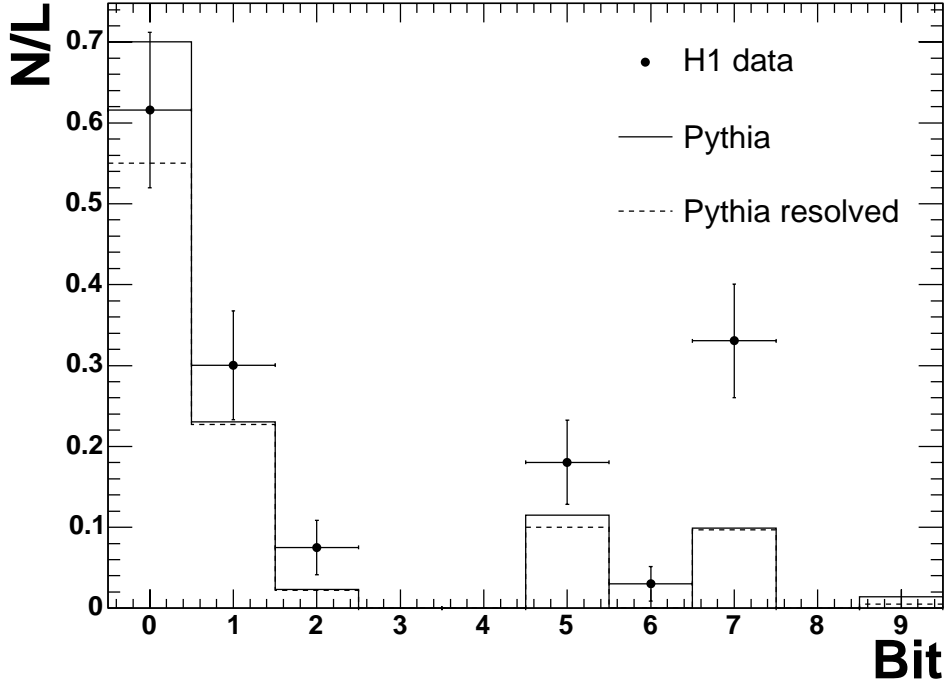


Figure 5.9: *Background finder bits in the final selection. Bits 0 to 4 correspond to halo finders, bits 5 to 9 are used to reject cosmics.*

Still this doesn't remove all neutral current DIS background. Electrons can fake jets or be covered by high transverse momentum jets. Therefore additional jet criteria need to be considered. Events are rejected if they meet one of the following conditions:

- The invariant jet mass for one jet is calculated as:

$$\text{jet mass} = \sqrt{\left(\sum_j p_j\right)^2} \quad (5.2)$$

where  $j$  runs over all particles associated to the jet and  $p_j$  is the four-vector of particle  $j$ . Hadronic jets typically have large values of the jet mass defined in that way. To remove electrons faking jets, events are rejected if one of the two leading jets has a jet mass  $< 2$  GeV.

- Electron reconstruction in regions of  $\phi$  cracks in the LAr is less efficient. If the scattered electron hits those regions it might not be identified as such. All events where one of the leading jets lies within  $\pm 2$  degrees of a phi crack and has a jet size smaller than 0.05 are rejected. The jet size is defined as:

$$\text{jet size} = \frac{\sum_j E_j * \sqrt{(\Delta\phi(\text{jet} - j))^2 + (\Delta\eta(\text{jet} - j))^2}}{E_{\text{jet}}} \quad (5.3)$$

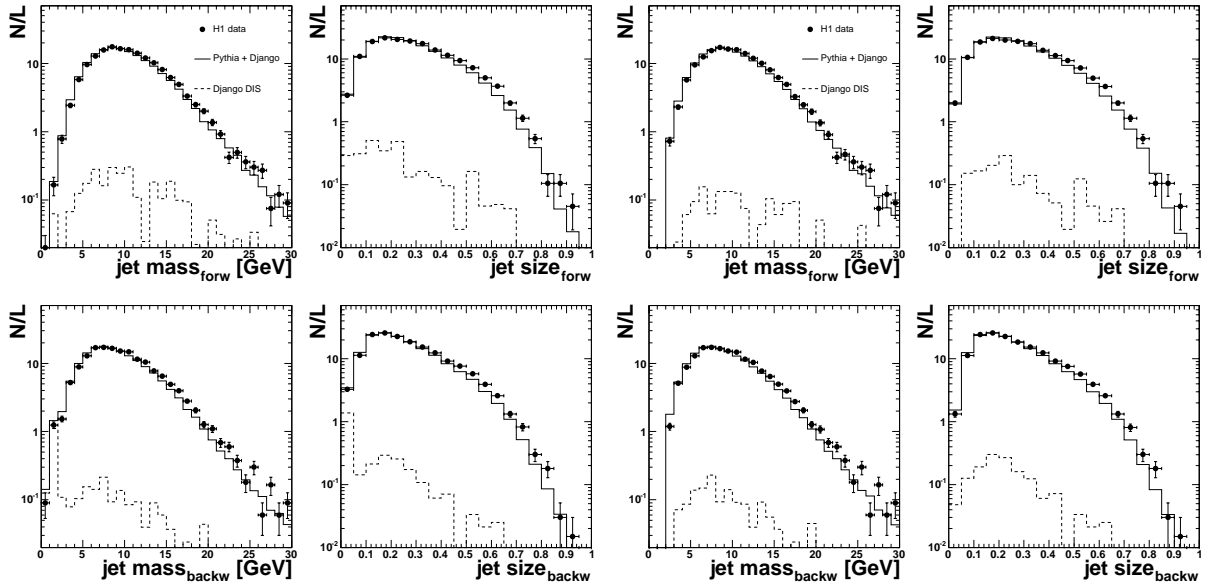


Figure 5.10: Background from DIS events in jet mass and jet size of the forward (upper plots) and the backward (lower plots) jet before (left four plots) and after (right four plots) cuts in those quantities. Shown are luminosity normalised distributions with the PYTHIA Monte Carlo weighted up by a factor 1.2 to match the absolute normalisation of the data.

The jet mass and jet size of both jets before and after those cuts are shown in figure 5.10 as luminosity normalised distributions. Large contributions from DIS events in the regions of small jet mass and jet size are visible, even more pronounced in the backward jet than in the forward jet. After the cuts the DIS background at small jet size is reduced by more than one order of magnitude. Overall this is a small effect as the regions affected by those cuts comprise only 1.6% of the total sample.

Figure 5.11 shows the luminosity normalised distributions of several observables after the cuts described in this section have been applied. The overall background from DIS events is 1.8% of the total sample as derived from Monte Carlo. For the highest  $y$  bin 5% are reached and 13% for  $p_{t,forw} \approx 70$  GeV. This background will be subtracted statistically, assuming an uncertainty of the DIS prediction of 20%.

### 5.1.5 Final event selection

In the last step the pseudorapidity of the jets is restricted. The first condition is that the jets are well contained in the LAr calorimeter. Its acceptance is in the range of  $-1.47 < \eta < 3.35$ . This is further restricted in the forward direction where migrations start to get too high and the jet calibration gets worse. This can be attributed to particle losses outside the calorimeter acceptance for broad jets and dead material in front of the calorimeter. Reasonable values for the upper cut on  $\eta$  are 2.5 to 2.75. Both values will be used for cross section measurements because the NLO calculations show that the acceptance at large  $x_p$  is very sensitive to that cut (cf. section 5.7.2).

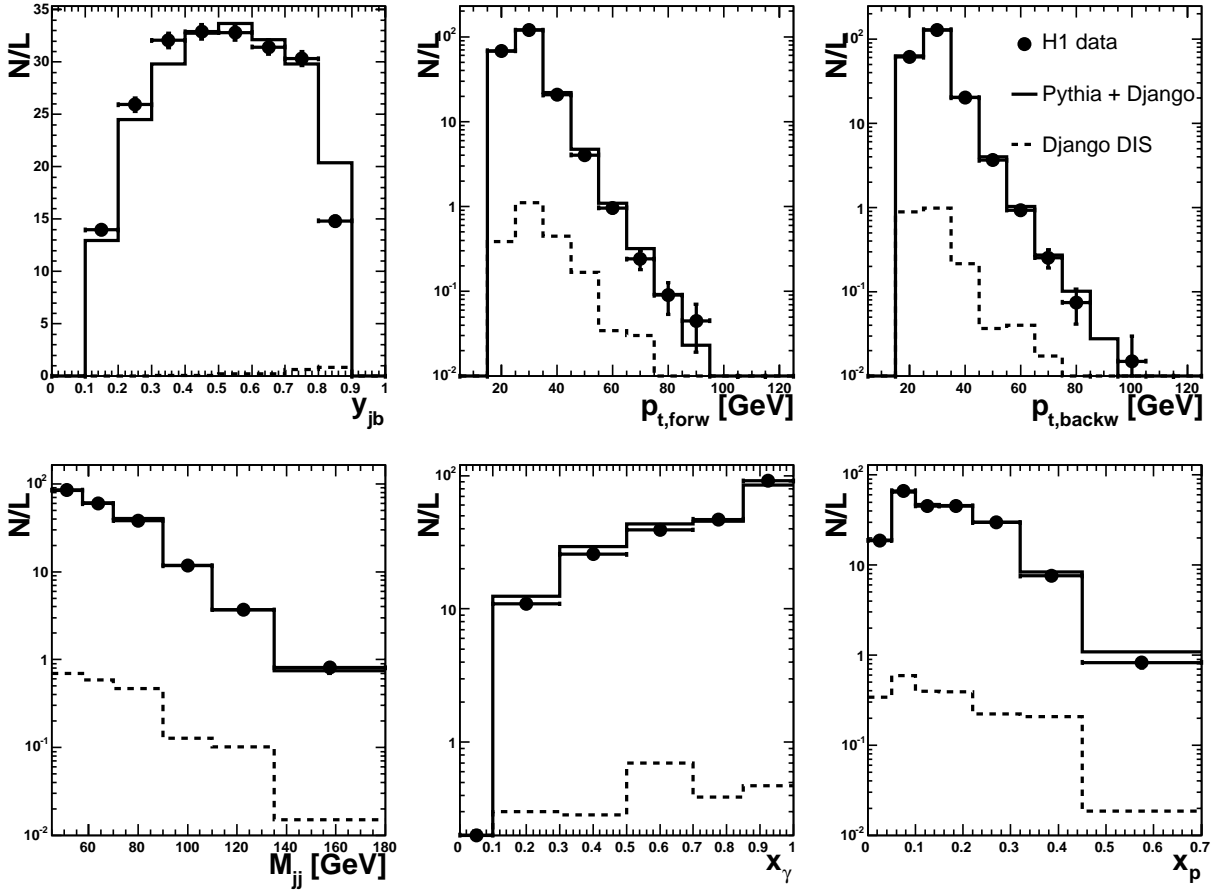


Figure 5.11: Remaining background from DIS events in  $y_{JB}$ ,  $p_t$  of both jets, their invariant dijet mass,  $x_\gamma$  and  $x_p$ . Shown are luminosity normalised distributions with the PYTHIA Monte Carlo weighted up by a factor 1.2 to match the absolute normalisation of the data.

The lower bound on the jet pseudorapidity of  $-0.5$  is chosen mainly because the measurement of hadronic jets is difficult in the SpaCal region. While the SpaCal itself starts at lower values of pseudorapidity, jets of size 1 in  $\eta$  can already overlap with the SpaCal acceptance when the jet-axis is still well outside. The problems on both sides of the  $\eta$ -range can be seen in figure 5.6.

Similar arguments as for the upper cut on  $\eta$  apply to the  $p_t$  cut of the second leading jet. By using 15 GeV or 20 GeV the cross section ratio of data/NLO changes drastically. Both values will be used in comparison of data to NLO calculations.

The final event selection criteria are summarised in table 5.4. After applying these cuts and the hadronic calibration described in 5.1.3 the total number of selected events in case of the  $p_{t,jet2} > 15$  GeV cut is 12755 and 14261 for  $\eta$  cuts at 2.5 and 2.75, respectively. For  $p_{t,jet2} > 20$  GeV the numbers are 9630 and 10848.

Final event selection
run quality “good” or “medium” CJC, CIP/COP, LAr, SpaCal, ToF, lumi HV on
$ z_{vertex}  < 35$ cm $p_{t,miss} < 20$ GeV non- <i>ep</i> background finder (bits 0-9 not fired)
no identified scattered electron jet mass $> 2$ GeV Not ( jet in $\phi$ crack and jet size $< 0.05$ )
$p_{t,jet1} > 25$ GeV $p_{t,jet2} > 15/20$ GeV $-0.5 < \eta_{jet} < 2.5/2.75$
$0.1 < y_{JB} < 0.9$

Table 5.4: Cuts used for the final event selection.

### 5.1.6 Selection stability

The number of selected events per unit luminosity as a function of the run number (i.e. time) is shown in figure 5.12. The selection is stable over the analysed data taking period. The mean over both years of 0.212 selected events per inverse nanobarn is about 40% higher than in the previous analysis [Car02] at lower centre-of-mass energy and smaller angular acceptance.

### 5.1.7 Trigger studies

The trigger setup at H1 was briefly described in section 3.2.5. To determine the amount of events rejected by the trigger system one or several subtriggers need to be found that gave a positive trigger decision for most of the selected events. For those the efficiency is to be determined and applied to data for cross section measurements.

Figure 5.13 shows the subtriggers fired in the events that passed the final selection cuts. L1 actual subtrigger and L4 verified subtrigger bits are shown separately as well as their logical AND which needs to be used in the event selection. A L1 actual subtrigger bit is set when on L1 the event matches the criteria of this subtrigger and is not rejected because of a prescale factor different from one. Without the prescale condition one speaks of L1 raw subtrigger bits. A L4 verified subtrigger bit is set when the corresponding L1 raw bit is set and the event was not rejected by L4. Thus it is clear that the logical AND combination has to be used to take into account the decision on both trigger levels as well as possible rejection based on prescale factors. A single subtrigger is not sufficient, at most 85% of the events would be selected when requiring subtrigger S67. Examining combinations of the triggers with the highest response it turns out that the combination of S64, S67, S75 and S77 results in a yield of 98.5%. All these triggers are LAr calorimeter triggers that require certain energy thresholds with additional vertex and

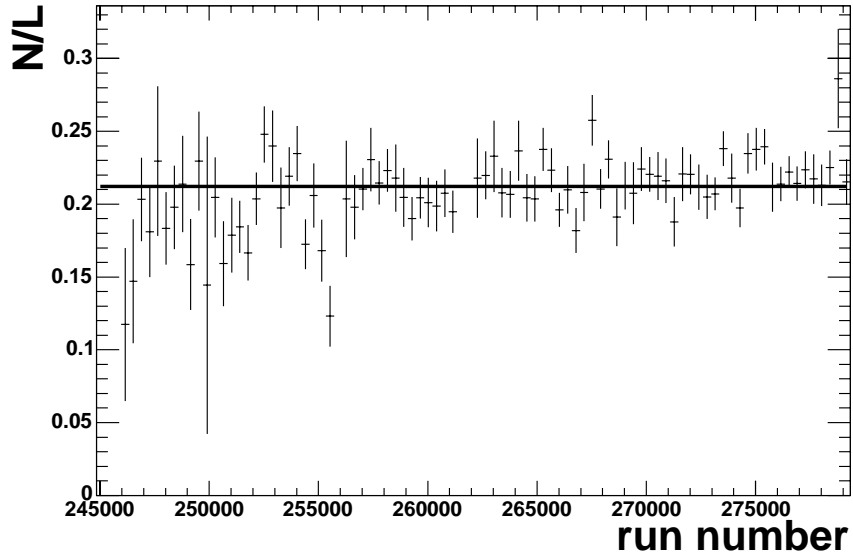


Figure 5.12: *Number of selected events per unit luminosity as a function of time (i.e. run number) without trigger requirements.*

timing conditions. S64 consists of trigger elements for energy deposits in the forward part of the calorimeter plus total transverse energy, S67 and S75 are two electron triggers and S77 is a missing transverse energy trigger. Although those triggers are not specifically optimised for high energetic jets, they also react on events with the desired signatures of this analysis.

The luminosity weighted trigger prescales of the years 1999 and 2000 for aforementioned triggers are shown in figure 5.14. The triggers are unprescaled except for S64 which has a mean prescale of 1.4 in 1999 and 2.4 in 2000. Also shown is S3, the monitor trigger used in the determination of the trigger efficiency. It is a pure SpaCal trigger with energy requirements in the electromagnetic section of the SpaCal and a time-of-flight condition.

The procedure to determine the efficiency is as follows: the efficiency is given by the fraction of events that were triggered by both the signal, S, and the monitor, M, trigger to the events that were triggered by the monitor trigger alone.

$$\text{Efficiency of S} = \frac{\text{number of events triggered by S \& M}}{\text{number of events triggered by M}} \quad (5.4)$$

It is important that the monitor trigger does not share trigger elements with the signal triggers. S64, S67, S75 and S77 are all based on energy thresholds in the LAr calorimeter plus vertex and timing information. A completely independent monitor trigger for high transverse momentum jets in photoproduction is not available. S3 is an electron trigger solely based on SpaCal trigger elements. In order to use it, a data sample needs to be defined without the cut against electrons. The test sample then is made up from events with two high  $p_t$  jets and an electron in the SpaCal. This procedure is only valid if the kinematics of the test sample are similar to the photoproduction sample. That this is the case has been shown in [Bat99].

The trigger efficiency of the signal trigger combination is depicted in figure 5.15 as function of

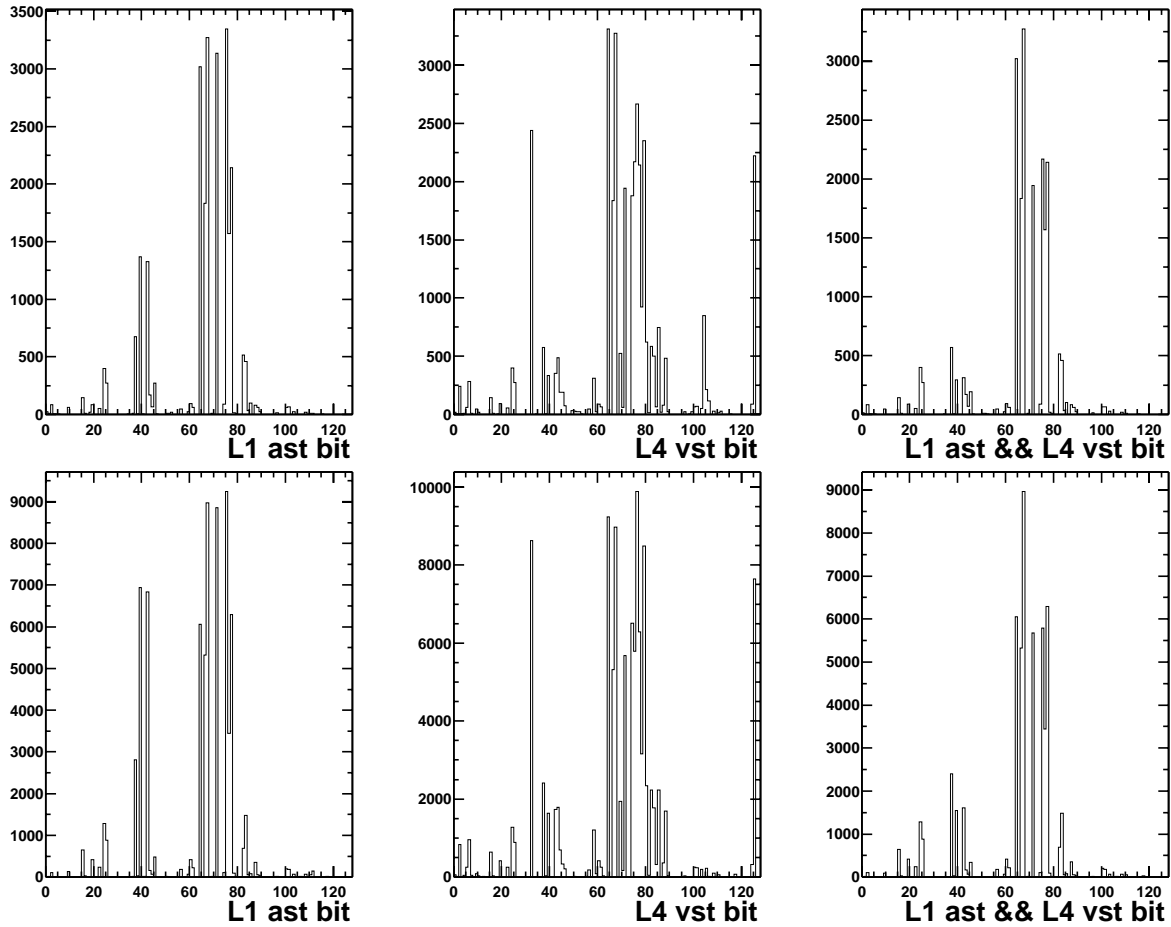


Figure 5.13: *Distribution of subtriggers with the final event selection applied for 1999 (above) and 2000 (below). From left to right the Level 1 actual triggers, the Level 4 verified triggers and the logical AND are shown as the number of events a subtrigger fired in the cut scenario of  $p_{t,jet2} > 15$  GeV,  $\eta < 2.75$ . Relevant for the practical trigger selection is the combination of L1 ast and L4 vst.*

the  $p_t$  and  $\eta$  of the leading jet. For the transverse momentum the efficiency is one for values larger than 30 GeV. In the pseudorapidity deviations from unity are larger and at the very forward  $\eta$  the efficiency drops to 90%.

To correct for this, both distributions were fitted and the results used as a correction to the data. Of the three possible combinations of  $p_t$  and  $\eta$  corrections ( $p_t$ -only,  $\eta$ -only and both) the  $\eta$ -only correction – a polynomial of fifth order – was chosen to be applied to the data. The result is shown in the lower two plots of figure 5.15. The efficiency is brought to one within 2% which is also used as a global contribution to the systematic uncertainty. Applying a  $p_t$  dependent efficiency only does not help at high pseudorapidities and a combined efficiency leads to no worthwhile improvement when compared to a pure  $\eta$  efficiency correction. To see which trigger contributed where the efficiencies are plotted per individual subtrigger in figure 5.16.

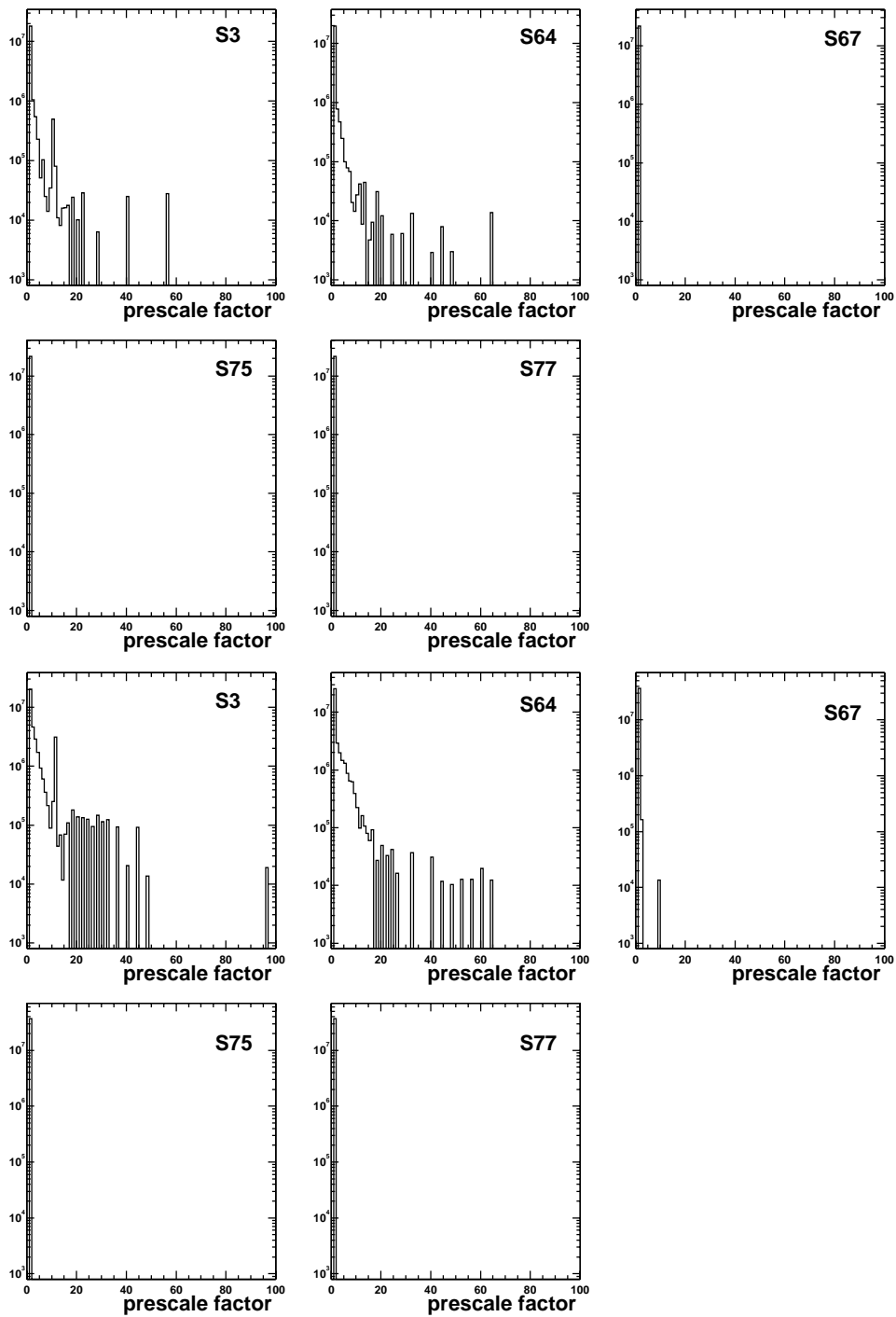


Figure 5.14: *Luminosity weighted trigger prescales for 1999 (upper five figures) and 2000 (lower five figures).*

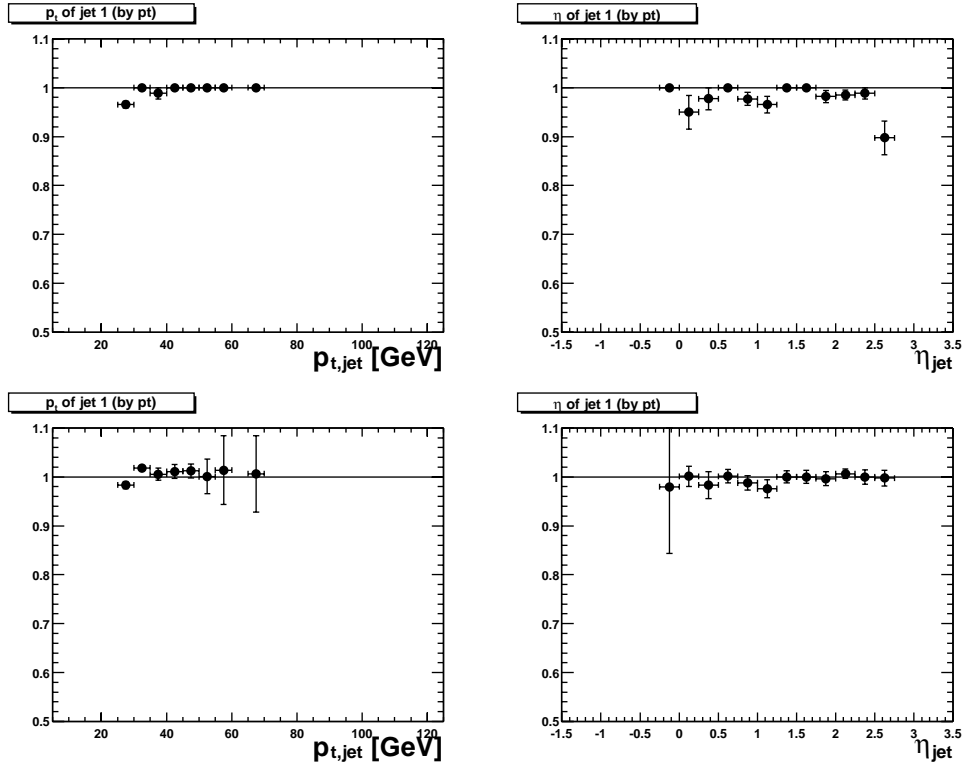


Figure 5.15: Trigger efficiency for the signal trigger combination as a function of  $p_t$  and  $\eta$  of the leading jet before (upper two figures) and after (lower two figures) the  $\eta$  dependent efficiency correction is applied.

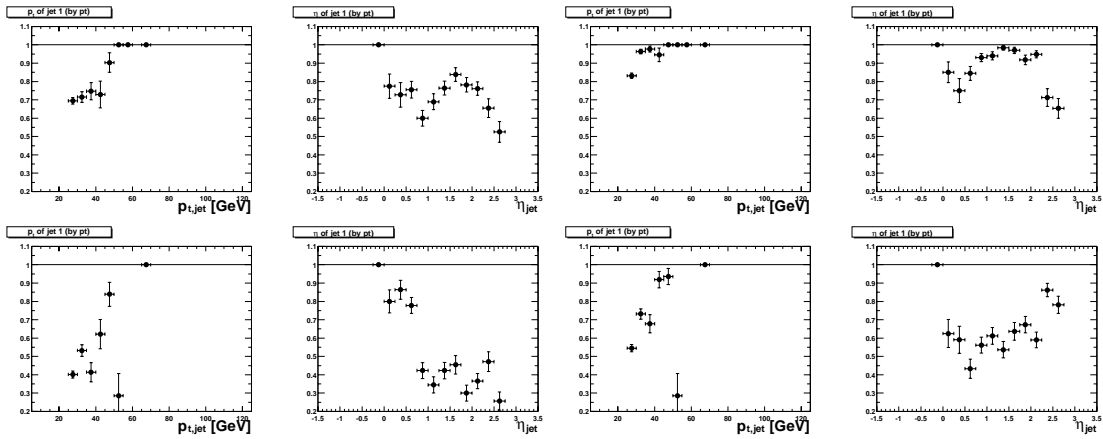


Figure 5.16: Trigger efficiency for the triggers S64 (upper left), S67 (upper right) S75 (lower left) and S77 (lower right) individually.

## 5.2 Data to Monte Carlo comparison

In this section the measured data are compared to Monte Carlo predictions obtained using the PYTHIA and HERWIG generators. If not noted otherwise the distributions are normalised to one to compare the shapes. Quantities calculated from jets or the total hadronic four-vector are presented with the hadronic calibration applied. Only the cut scenario of  $p_{t,jet2} > 15$  GeV and  $\eta_{jet} < 2.75$  is presented in this section.

Figure 5.17 shows quantities not calculated from jets. In the first subpicture the  $z_{vertex}$  distribution is shown after reweighting the  $z_{vertex}$  distribution of the Monte Carlo to the data. The missing transverse energy is shown in the next subpicture. Up to the cut value of 20 GeV the shape is well described by both generators. The rising edge of the scalar transverse energy is not in agreement between data and Monte Carlo but shifted by about 1 GeV. This is more pronounced in the case of HERWIG. The most likely explanation is the hadronic calibration which is not available down to the level of individual particles and thus not for the calculation of  $E_{t,scal}$ . This presents no problem as the cut in  $E_{t,scal}$  is far below the point where both data and prediction die out. Last in this picture is the inelasticity  $y_{JB}$ . The region of high  $y$  is clearly dominated by the resolved component. The description is adequate for both generators with the data near the upper cut clearly below the prediction. For the final cross sections the Monte Carlo will be reweighted to match the data in  $y_{JB}$  described in section 5.4.3. The uncertainty introduced by this procedure will be added to the total systematic uncertainty.

The pseudorapidity  $\eta$  and azimuthal angle  $\phi$  for both jets separately are depicted in figure 5.18. The angular distribution of both jets is well reproduced by the prediction with HERWIG yielding a minimal shift into the forward direction compared to PYTHIA. The azimuthal angle distribution is almost flat as predicted by the models.

Figure 5.19 shows the mean pseudorapidity and the scattering angle in the jet centre-of-mass system in the final binning. The  $\bar{\eta}$  distribution is described very well and exhibits a dominance of the resolved component in the forward direction. The maximum in this distribution is around  $\eta \approx 1.2 - 1.3$  or  $\theta \approx 30^\circ - 34^\circ$ . The small shift into the forward direction of HERWIG with respect to PYTHIA is also observed here. For the absolute cosine of the scattering angle in the jet centre-of-mass system the data show a slightly steeper behaviour than the Monte Carlo. Note that the QCD matrix element does not show a decrease with increasing  $\cos \theta^*$ , the effect here comes from the  $p_t$  cuts on the jets. This is because the transverse component of the energy for jets with fixed energy decreases with increasing  $\cos \theta^*$ . Therefore jets closer to the  $z$ -axis are more likely to be affected by the  $p_t$  cuts. As with  $y_{JB}$  a reweighting of the Monte Carlo will be performed to match the data in  $\cos \theta^*$  with the resulting uncertainty added to the total systematics.

In figure 5.20 the transverse momentum of the individual jets as well as the mean value and the dijet mass is presented. The agreement is good over more than 3 orders of magnitude in  $p_t$  and more than 2 orders of magnitude in  $M_{JJ}$ .

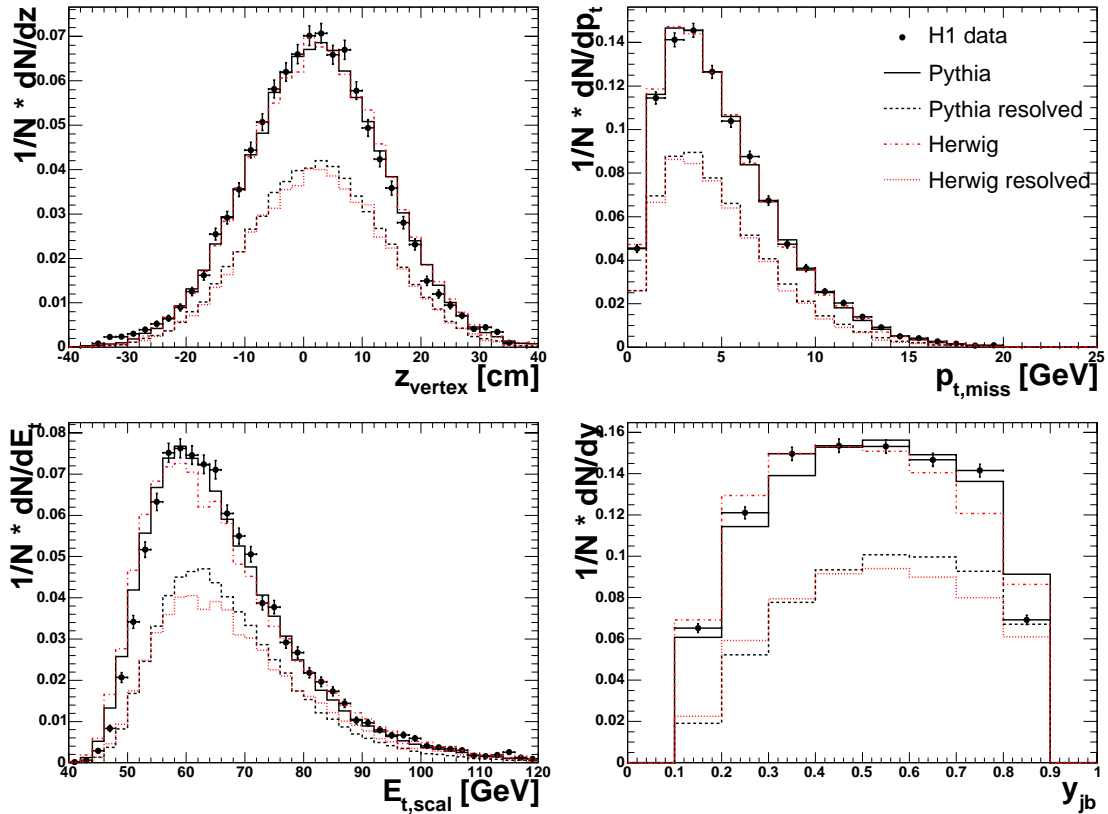


Figure 5.17: Comparison of data with Monte Carlo in the quantities  $z_{vertex}$ ,  $p_{t,miss}$ ,  $E_{t,scal}$  and  $y_{JB}$ . Also shown are the contributions of the resolved parts only.

### 5.3 Data unfolding

In section 5.2 it was shown that the data are described well enough by the Monte Carlo predictions. This is necessary for the bin-to-bin correction method explained below to be applicable. As a common denominator the cross sections need to be given on hadron level. Both next-to-leading order calculations which are only available on parton level and experimental data need to be corrected as will be explained in the next two sections.

The method used in both cases is the so called bin-to-bin correction method, where correlations of a given quantity calculated on two different levels are examined. Ideally the values on both levels would be rather similar, but a good correlation is also sufficient. The bin sizes need to be of similar size as the resolution in the studied quantity, such that migrations between bins are small. As a measure of quality the so called purity and stability are determined. They are defined by the number of events generated *and* reconstructed in one bin divided by the number of events generated (purity) or reconstructed (stability) in this bin:

$$P_i = N_{i,rec \cap gen} / N_{i,gen} \quad (5.5a)$$

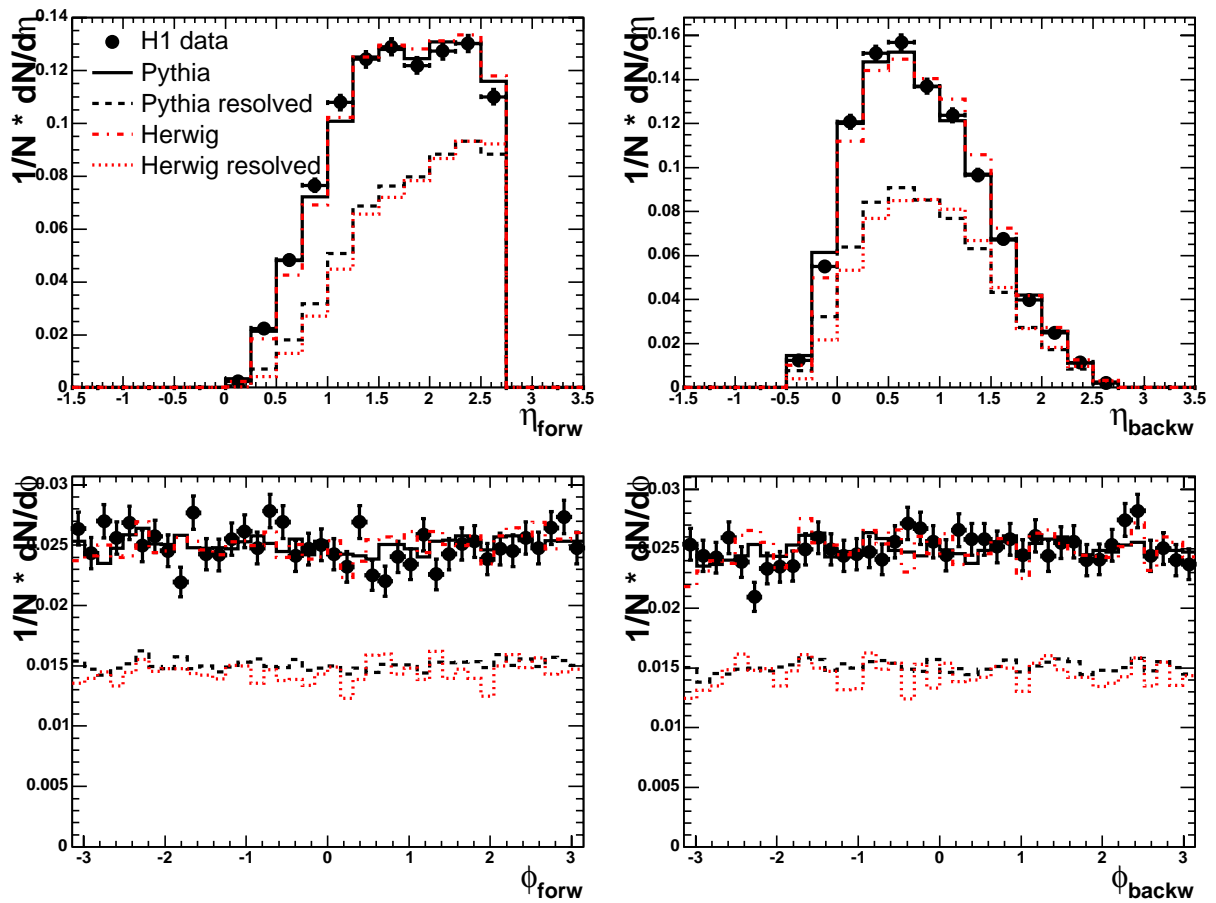


Figure 5.18: Jet pseudorapidity and azimuthal angle for the forward (left) and the backward jet (right). Also shown are the contributions of the resolved parts only.

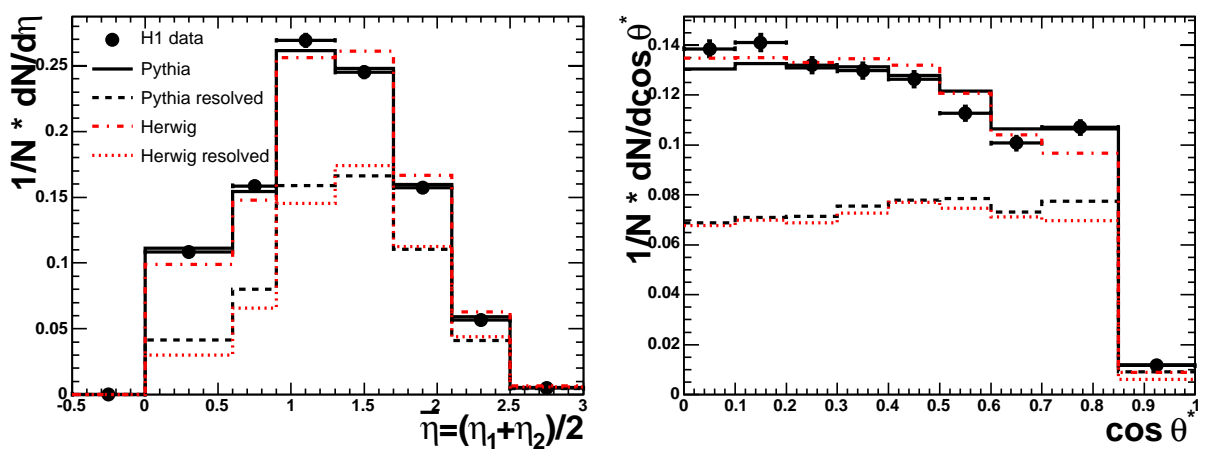


Figure 5.19: Mean jet pseudorapidity (left) and CMS scattering angle (right). Also shown are the contributions of the resolved parts only.

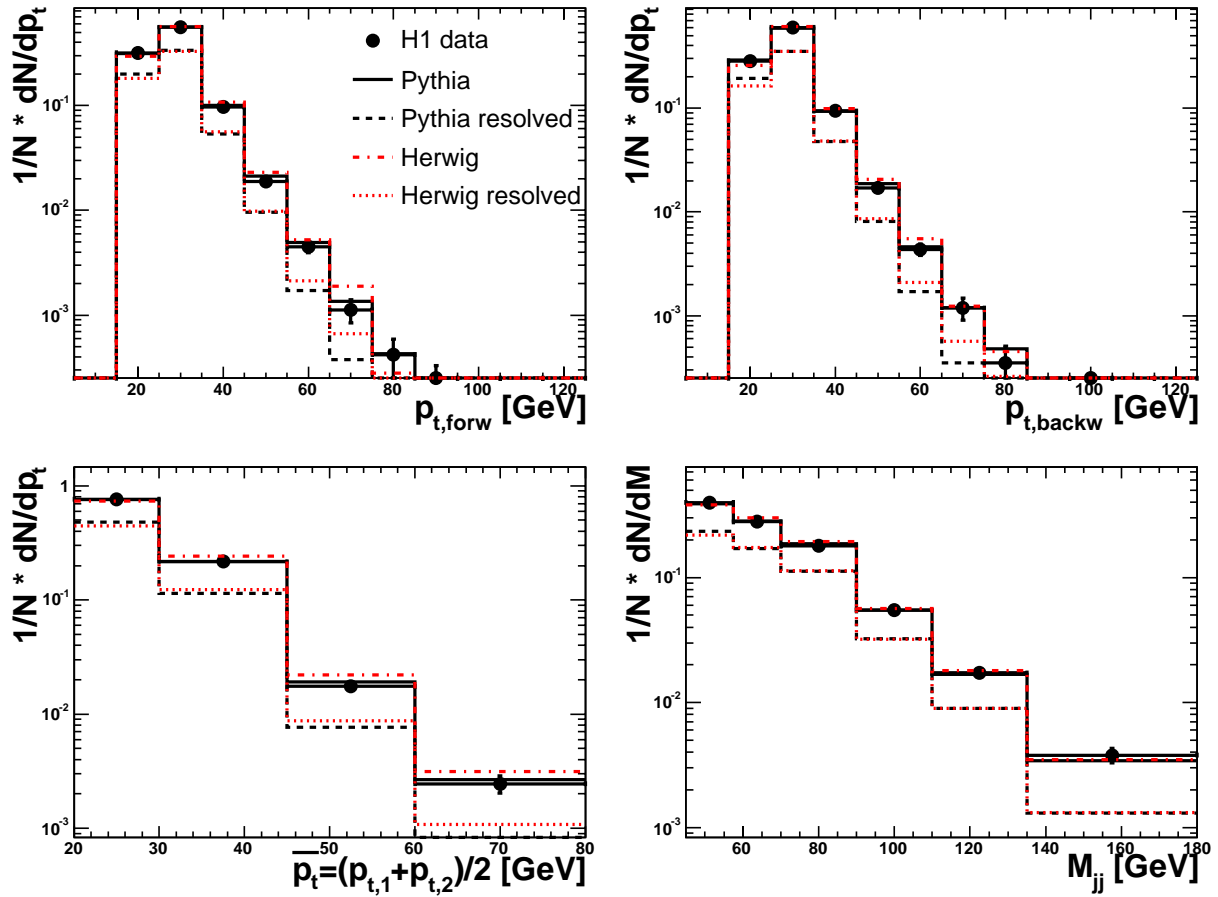


Figure 5.20: Jet  $p_t$  for the forward jet (upper left) and the backward jet (upper right) as well as mean  $p_t$  (lower left) and the dijet mass (lower right). Also shown are the contributions of the resolved parts only.

$$S_i = N_{i,rec \cap gen} / N_{i,rec} \quad (5.5b)$$

In other words (1 - purity) indicates the fraction of events migrating into the bin while (1 - stability) indicated how many events migrate out of the bin. Both, purity and stability, should be as large as possible, the absolute minimum is set to 30%. The correction factor for a given bin is then determined by the ratio of purity and stability in that bin.

Purities, stabilities and correction factors are determined using the PYTHIA and HERWIG predictions. Both give a good description of the data so that the mean correction factors of the two are used for the cross sections in chapter 6. The mean value is computed using the “weighted average” method described in section 32.1.1 of [E<sup>+</sup>04]. This is done to avoid an overestimation of the model uncertainty in the extreme regions of the phase space as the available data sample for the PYTHIA generator is much larger than that of HERWIG.

For  $N$  uncorrelated measurements  $x_i$  with uncertainties  $\pm \delta x_i$  of a quantity  $x$  the weighted average  $\bar{x}$  is calculated as

$$\bar{x} \pm \delta\bar{x} = \frac{\sum w_i x_i}{\sum w_i} \pm \sqrt{\frac{1}{\sum w_i}} \quad (5.6)$$

where the weights  $w_i$  are defined as  $w_i = 1/\delta x_i^2$ . Depending on the quantity

$$\chi^2 = \sum w_i (\bar{x} - x_i)^2 \quad (5.7)$$

the uncertainty  $\delta\bar{x}$  is scaled up by a factor of  $\sqrt{\chi^2/(N-1)}$  if  $\chi^2/(N-1) \gtrsim 1$ . This way it is ensured that deviations beyond statistical uncertainties between the measurements do not result in a too small model uncertainty.

Here the  $x_i$  are the correction factors determined by PYTHIA and HERWIG with  $\delta x_i$  being the statistical uncertainty of the factors, thus  $N = 2$ . Then  $\bar{x}$  is the mean correction factor that will be used in the unfolding procedure and  $\delta\bar{x}$  is the associated model uncertainty.

Note that a normalisation factor of the Monte Carlo predictions with respect to the data is unimportant since the correction factors introduced in the next two sections are ratios of cross sections.

### 5.3.1 Correction for detector effects

To make the cross sections independent of the apparatus they were measured with, the data need to be corrected for detector effects. These include mismeasurements, limited resolution and inefficiencies. To determine the actual correction factors, the hadron level measurements of quantity  $X$  are divided by the detector level measurements<sup>4</sup> to yield bin-wise factors  $C_{Det,i}$ . For the detector level measurements the full selection cuts from table 5.4 are used. They will be abbreviated as  $D$  like detector level cuts. For the hadron level measurement only cuts on the phase space are made. They are abbreviated as  $P$  and summarised in table 2.1 in section 2.5. The detector correction factor for bin  $i$  is then given by:

$$C_{Det,i} = N_{i,Hadron,P}/N_{i,Detector,D} \quad (5.8)$$

where  $N_{i,Hadron,P}$  is the number of events on hadron level in bin  $i$  with cuts  $P$  and  $N_{i,Detector,D}$  is the number of events on detector level in bin  $i$  with cuts  $D$ .

When looking at purities and stabilities only the migrations are of interest so that only events that pass both the detector level cuts  $D$  on the detector level objects as well as the phase space cuts  $P$  on the hadron level objects enter the formulae 5.5a and 5.5b. The same is true when looking at the resolution in the quantity  $X$  as defined by

$$R_{Det,i} = (N_{i,Detector,D\&P} - N_{i,Hadron,D\&P})/N_{i,Hadron,D\&P} \quad (5.9)$$

In this section only the correlations for the PYTHIA generator are shown. Those of HERWIG are of similar quality.

---

<sup>4</sup>The definition of the different levels was given in section 2.4

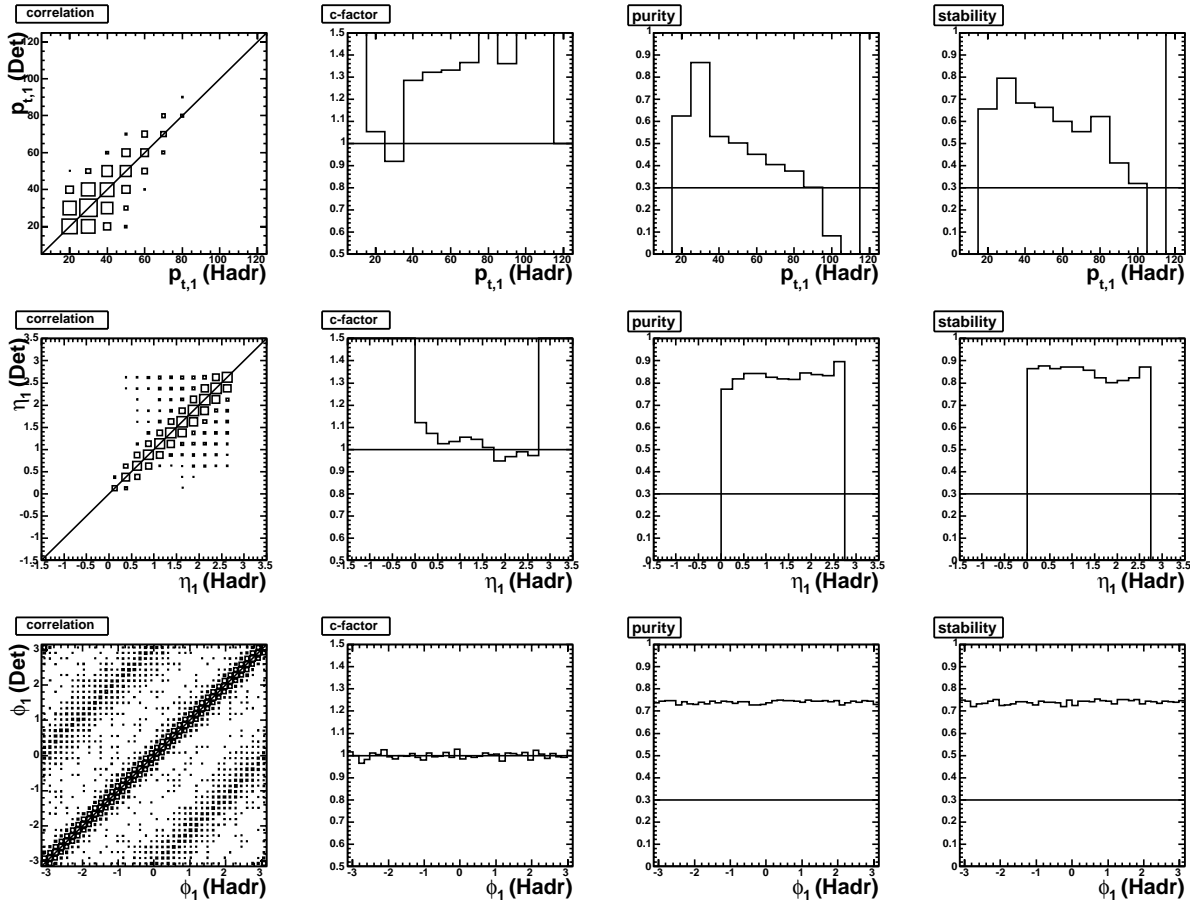


Figure 5.21: Correlations, correction factors, purity and stability for the forward jet. The upper figures show the transverse momentum, the middle figures show the pseudorapidity and the lower show the azimuthal angle. The boxes in the correlation plots are logarithmic.

Figure 5.21 shows the correlations between detector and hadron level of the forward jet in its transverse energy, pseudorapidity and azimuthal angle. The correlations are shown with logarithmic boxes so that differences in the off-diagonal entries are more clearly visible. Good correlation can be seen in all three quantities. From the  $\eta$  and  $\phi$  correlations it can be seen that sometimes forward and backward jet are not properly matched between detector and hadron level. In the more extreme cases this is due to more than two jets in the event where the two jets on detector level are not the same as on hadron level. Purities and stabilities are high except for the larger values of the jet  $p_t$ . This is due to the binning that in this particular case is not optimised to yield minimal migrations as no cross sections will be presented in single jet observables. A very similar picture arises for the backward jet shown in figure 5.22. All correlations are good and low purities and stabilities for high  $p_t$  are attributed to a non-optimised binning.

Individual jets are shown here to illustrate that the measurement of high energetic jets is well under control. For quantities in which cross sections will be given in chapter 6 the correlations

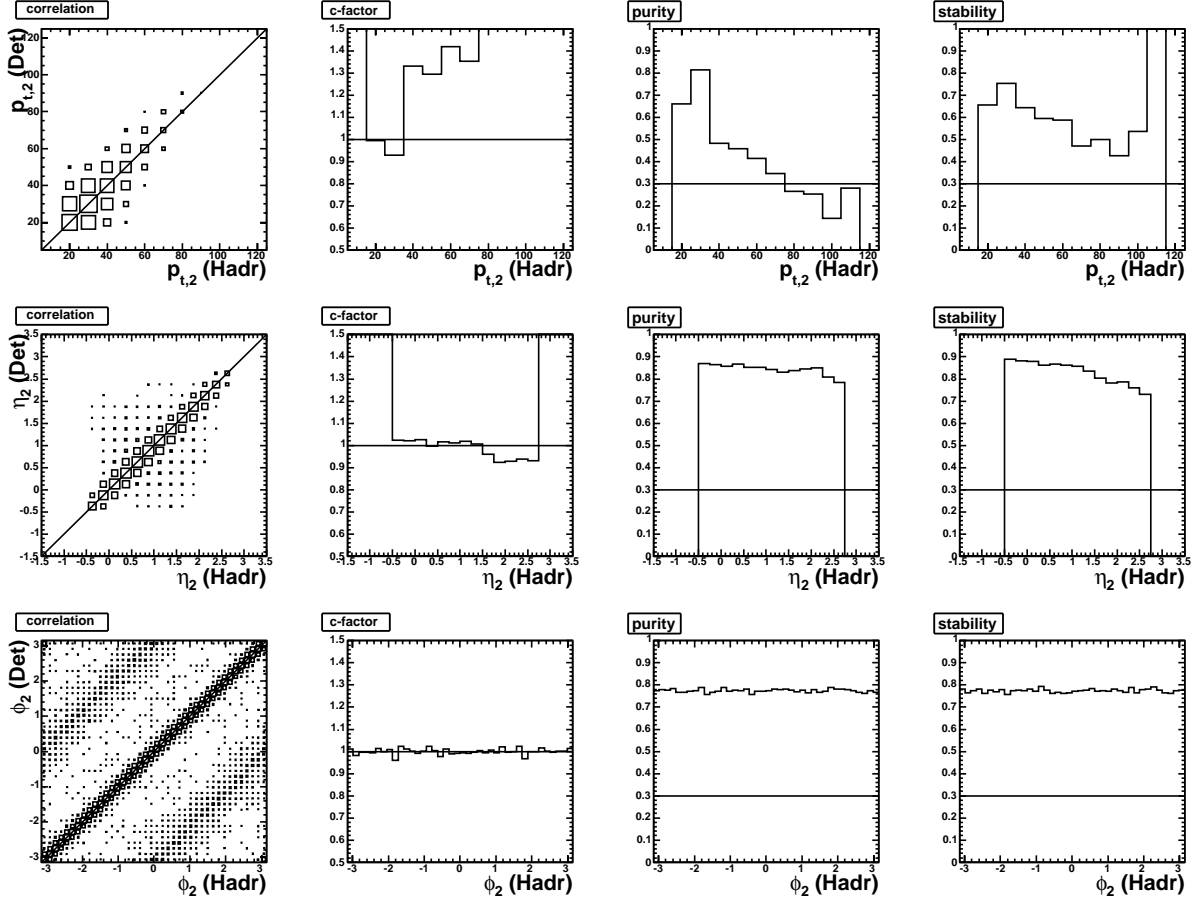


Figure 5.22: Correlations, correction factors, purity and stability for the backward jet. The upper figures show the transverse momentum, the middle figures show the pseudorapidity and the lower show the azimuthal angle. The boxes in the correlation plots are logarithmic.

are equally good or better with purities and stabilities in the final binning of 60% and higher.

### 5.3.2 Hadronisation corrections

Similar to the detector corrections in the previous section the NLO cross section needs to be corrected to the hadron level. In this case the starting point is the parton level which is generated by the NLO program. Since the hadronisation corrections are determined from a leading order Monte Carlo, there is one imprecision involved in this procedure. There is no exact correspondence to the three parton final state of the NLO calculation in the LO programs. One can either use the two partons of the hard scattering process or the partons after the parton shower. Generally the latter option is used as long as no consistent treatment is available. This gives hadronisation factors

$$C_{Had,i} = N_{i,Hadron,P} / N_{i,Parton,P} \quad (5.10)$$

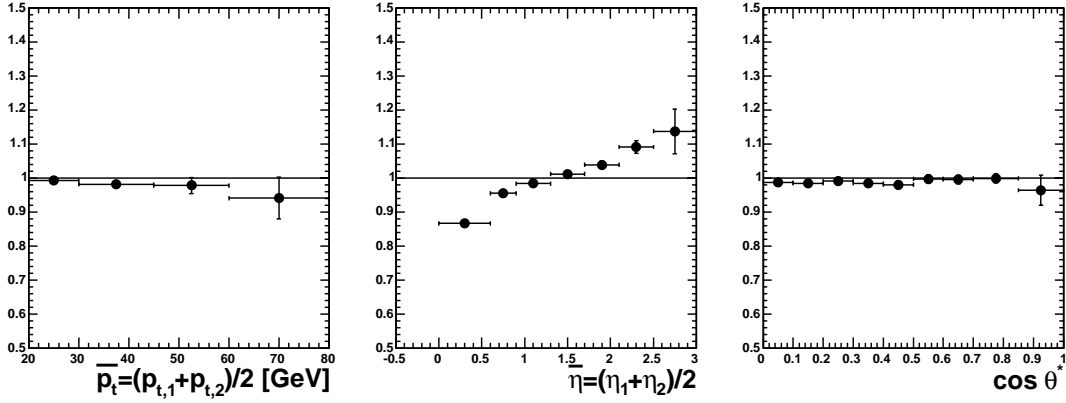


Figure 5.23: Hadronisation correction factors for  $\bar{p}_t$ ,  $\bar{\eta}$  and  $\cos \theta^*$ .

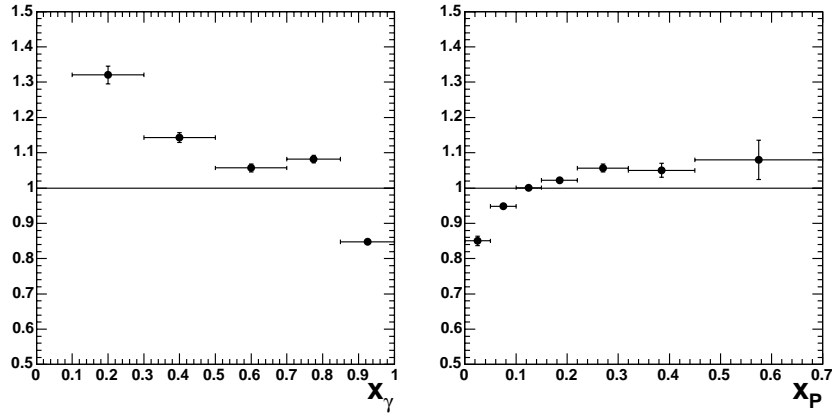


Figure 5.24: Hadronisation correction factors for  $x_\gamma$  and  $x_p$ .

where  $P$  stands for the phase space cuts as described in the previous section. Note that in contrast to the detector corrections for data, the NLO cross sections need to be multiplied with the hadronisation correction factor when using this definition.

Figure 5.23 shows the hadronisation correction factors for the mean transverse momentum, the mean pseudorapidity of the jets in the laboratory system and the angle of the jets with respect to the  $z$ -direction in their centre-of-mass system. For  $\bar{p}_t$  the corrections are small but grow slightly with rising  $\bar{p}_t$  to a value of  $-6\%$ . In  $\bar{\eta}$  there is a much stronger dependence, corrections start at  $-13\%$  at low  $\bar{\eta}$  and rise to  $+14\%$  at highest  $\bar{\eta}$ . The corrections in  $\cos \theta^*$  are all within  $2\%$  and flat over the entire  $\cos \theta^*$  range.

The hadronisation correction factors for  $x_\gamma$  and  $x_p$  are depicted in figure 5.24. In  $x_\gamma$  they are large at the lower end of the spectrum where they reach  $+32\%$ . At the highest values of  $x_\gamma$  the picture changes to a  $-16\%$  correction. For  $x_p$  the corrections are largest at  $x_p < 0.05$  with  $-15\%$ . They change from  $+6\%$  to  $+8\%$  for  $x_p > 0.22$ .

The corrections as presented in this section are then used to calculate NLO cross sections that can be compared to data in chapter 6.

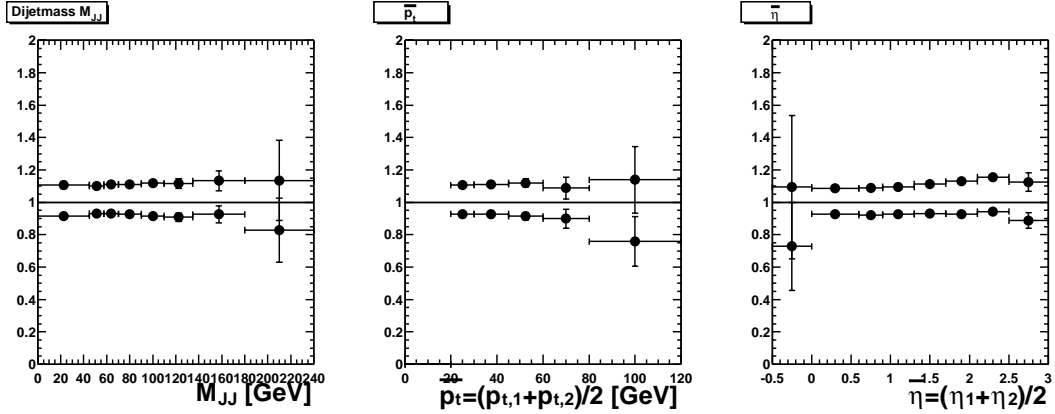


Figure 5.25: Effect of the LAr energy scale variation on the dijet system. Shown are the dijet mass  $M_{JJ}$  (left), mean transverse momentum  $\bar{p}_t$  (middle) and mean pseudorapidity  $\bar{\eta}$  (right) of the two jets.

## 5.4 Systematic studies

### 5.4.1 Liquid Argon energy scale

To estimate the uncertainty arising from the uncertainty of the LAr energy scale all cell energies in the LAr have been varied up and down by 2% in Monte Carlo. Afterwards the standard processing was performed again, including the electron identification, the HFS finder and the jet algorithm. As it turns out, the effect is roughly the same as would result in a direct variation of the jet energies by 2%. For the variation by +2% the overall shift is +10.0%, for -2% the result is -6.6%.

Effects on the dijet system can be seen in figure 5.25. For the dijet mass and the mean transverse momentum the errors on the uncertainties become large in the highest bins. Therefore they will be excluded from the final cross section measurements. The same is true for the lowest bin in the mean pseudorapidity. The resulting uncertainty in  $x_\gamma$  and  $x_p$  is shown in figure 5.26. For  $x_\gamma$  the uncertainty at large values is slightly smaller than 10% and growing to 15% towards smaller values of  $x_\gamma$ . In case of  $x_p < 0.1$  the uncertainty is only reasonably determined for  $x_\gamma > 0.3$ , in case of  $x_p > 0.1$  for  $x_\gamma > 0.1$ . This then restricts the range in  $x_\gamma$  for which cross sections will be presented. In  $x_p$  the uncertainties are smaller at the lower end of the distribution and rise to 20% at the highest bin of  $0.45 < x_p < 0.7$ . There is no significant difference between the two regions of  $x_\gamma$  for which the  $x_p$  distribution is examined.

### 5.4.2 SpaCal energy scale

The SpaCal energy scale uncertainty is determined by a variation of  $\pm 8\%$  in the SpaCal cell energy. Otherwise the same procedure is used as in the previous section. This leads to overall shifts by +0.7% and +2.0%. In this case the downward variation leads to an increased number of events. The effects are much smaller than those of the LAr energy scale since it enters more

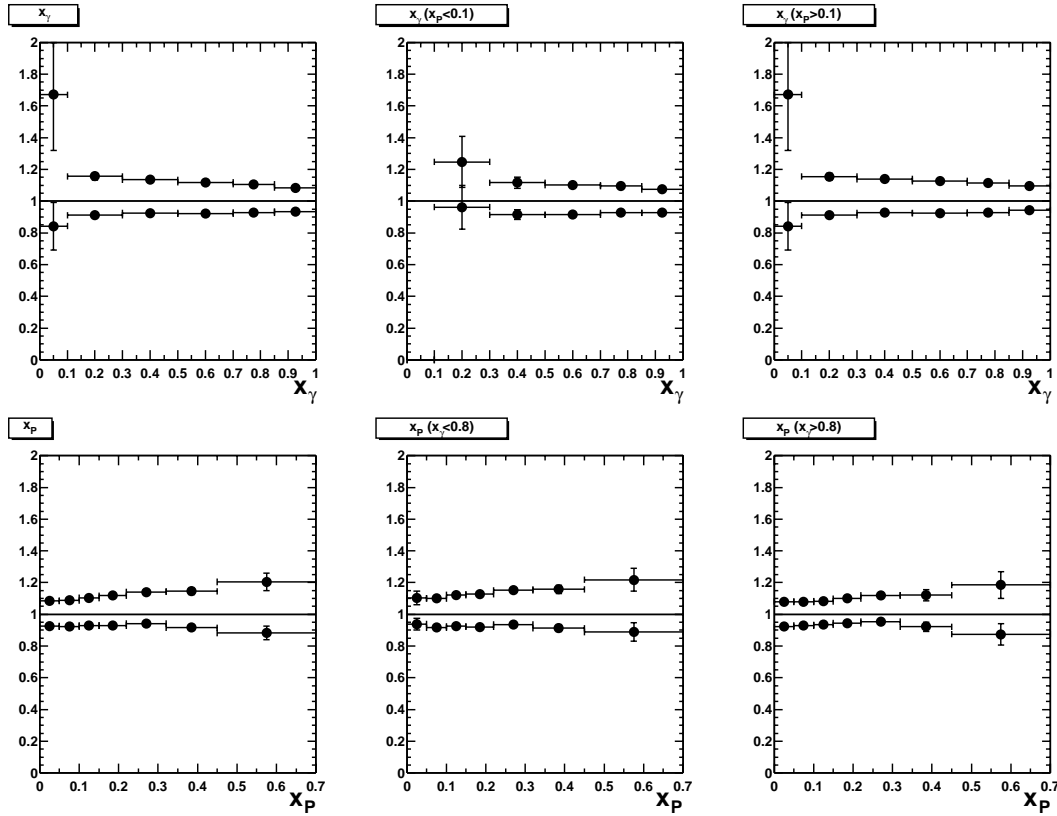


Figure 5.26: Effect of the LAr energy scale variation on the cross section measurement in  $x_\gamma$  (upper three plots) and  $x_p$  (lower three plots).

indirectly. Firstly it affects the  $y_{JB}$  measurement that includes all hadrons of the final state, some of which go into the acceptance of the SpaCal. Secondly electron candidates close to the energy threshold in the electron finder are affected. Finally very backward jets close to the lower  $\eta$  cut of the phase space definition might have some of their particles reaching the SpaCal.

### 5.4.3 Monte Carlo reweighting

The description of the data by Monte Carlo in the  $y_{JB}$  and  $\cos\theta^*$  distributions is not too well (c.f. section 5.2). Since these are rather basic quantities a reweighting has been performed. For each of the two observables the area normalised data distribution has been divided by the corresponding distribution in Monte Carlo. Those ratios then have been simultaneously applied to Monte Carlo as a multiplicative event-by-event weighting factor depending on  $y_{JB}$  and  $\cos\theta^*$  respectively. This procedure only changes the shapes, not the normalisation. The  $y_{JB}$  and  $\cos\theta^*$  distributions after the reweighting procedure are shown in figure 5.27 as well as the resulting uncertainty of the procedure on those observables.

The control distributions have been checked again after the reweighting was done to ensure that the description of other observables is not worsened. For the cross sections in chapter 6 the  $y_{JB}$

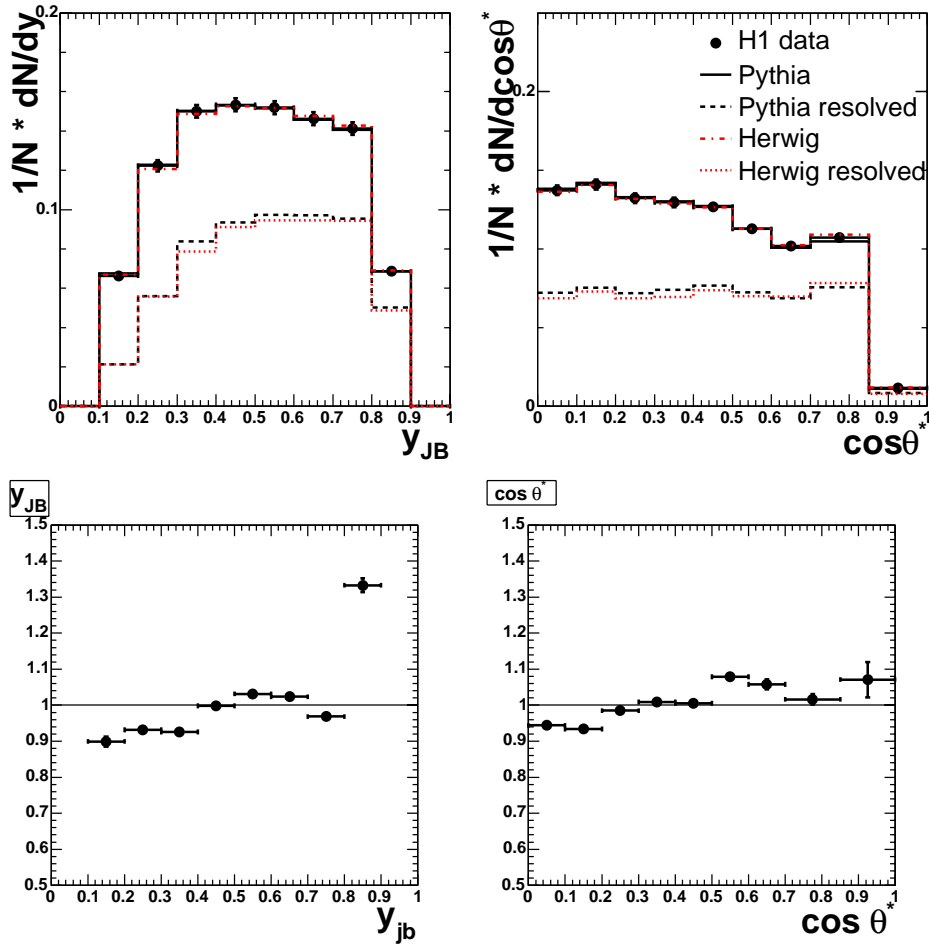


Figure 5.27: *Effect of the simultaneous  $y_{JB}$  and  $\cos \theta^*$  reweighting. The upper two figures show both observables after the reweighting was performed. Also shown are the contributions of the resolved parts only. In the lower two figures the systematic uncertainty of this procedure is depicted.*

and  $\cos \theta^*$  reweighting will be taken into account. The uncertainty of this procedure is given by the relative difference of the cross sections before and after the reweighting. As an example the uncertainty is shown for  $x_\gamma$  and  $x_p$  in figure 5.28.

## 5.5 Pushing towards high $x_p$

In order to have a better handle on high  $x_p$  values, several attempts have been made to either enhance the number of selected events in that region or to find a better way of reconstructing this quantity. In section 5.5.1 an extension of the acceptance to the more forward region is studied while in 5.5.2 other methods to reconstruct  $x_p$  are examined.

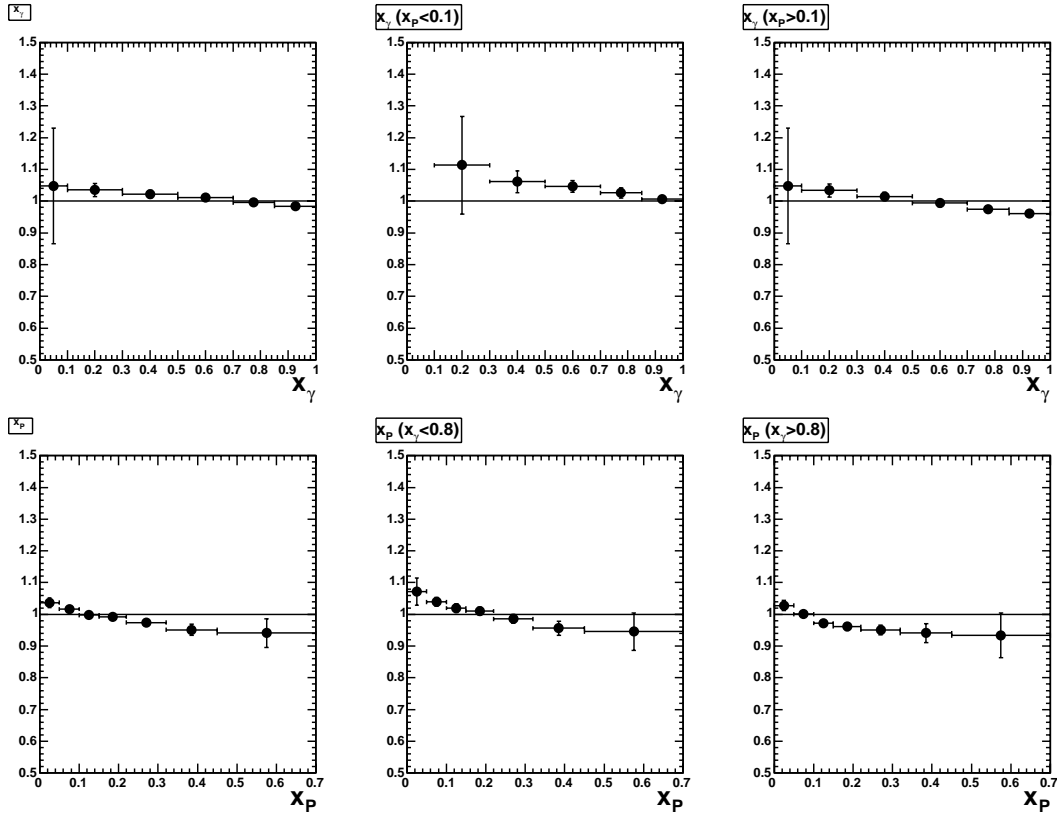


Figure 5.28: Effect of the  $y_{JB}$  and  $\cos\theta^*$  reweighting on the cross section measurement in  $x_\gamma$  (upper three plots) and  $x_p$  (lower three plots).

### 5.5.1 Extension of the acceptance

High values of  $x_p$  mean that more energy from the proton side enters the hard scatter with the effect of the whole event being more boosted into the direction of the proton momentum. This also becomes apparent in the kinematic formula for  $x_p$  (c.f. eq. 2.28b). In previous analyses a value of 2.5 was used as the upper threshold on the jet pseudorapidity.

As the liquid argon calorimeter extends to  $\eta < 3.35$  the otherwise same selection of dijet events was performed using 2.75, 3.0 and 3.25 as the upper limit on the allowed jet pseudorapidity range. The description of data by Monte Carlo was checked for each of the three cases as well as the correlations of the jets between detector and hadron level.

The transverse momentum and pseudorapidity of the two jets is still well described for the cut at  $\eta = 3.0$  as can be seen in figure 5.29. Looking at the correlation between detector and hadron level of the backward jet in figure 5.32 it can be observed that both purity and stability drop off in the additional  $\eta$  bin, in case of the stability by more than 20%. Description and correlations get significantly worse for a cut value of 3.25 (not shown separately). The most important reason to not use 3.0 or even higher values for the pseudorapidity cut is that the jet energy calibration is not well enough described by the Monte Carlo so close to the beam direction (c.f. figure 5.6 in

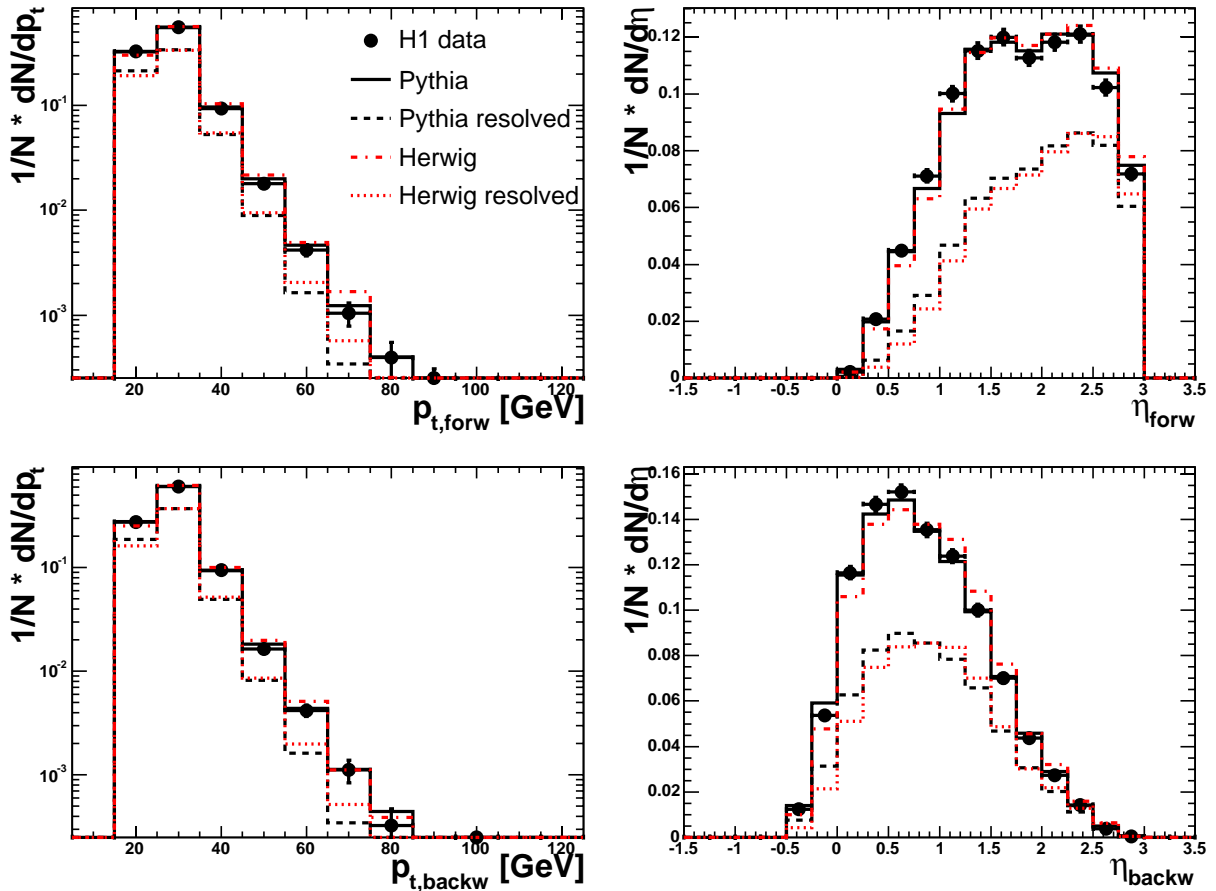


Figure 5.29: Jet reconstruction for  $\eta$  up to 3.0.

section 5.1.3).

As a check of the quality of the measurement at high values of  $x_p$  control distributions are shown again in figures 5.30 and 5.31. Here the jet transverse momentum and pseudorapidities have been compared between data and Monte Carlo for values of  $0.32 < x_p < 0.45$  and  $x_p > 0.45$ , respectively. The agreement is still good enough so that one can be confident in the measurement up to the highest  $x_p$  that can be reached in this analysis.

As a conclusion the cut value of 2.75 in the jet pseudorapidity was found to allow a good measurement while higher values suffer mainly from problems in the jet energy calibration. It will be used in the cross section measurements presented in section 6.1. Differences to the previously used cut of 2.5 will be discussed in section 5.7.2.

## 5.5.2 Effect of different reconstruction methods

To get a better handle on the high  $x_p$  region different reconstruction methods were tried. In this section two new methods are presented. The same comparisons between data and Monte Carlo

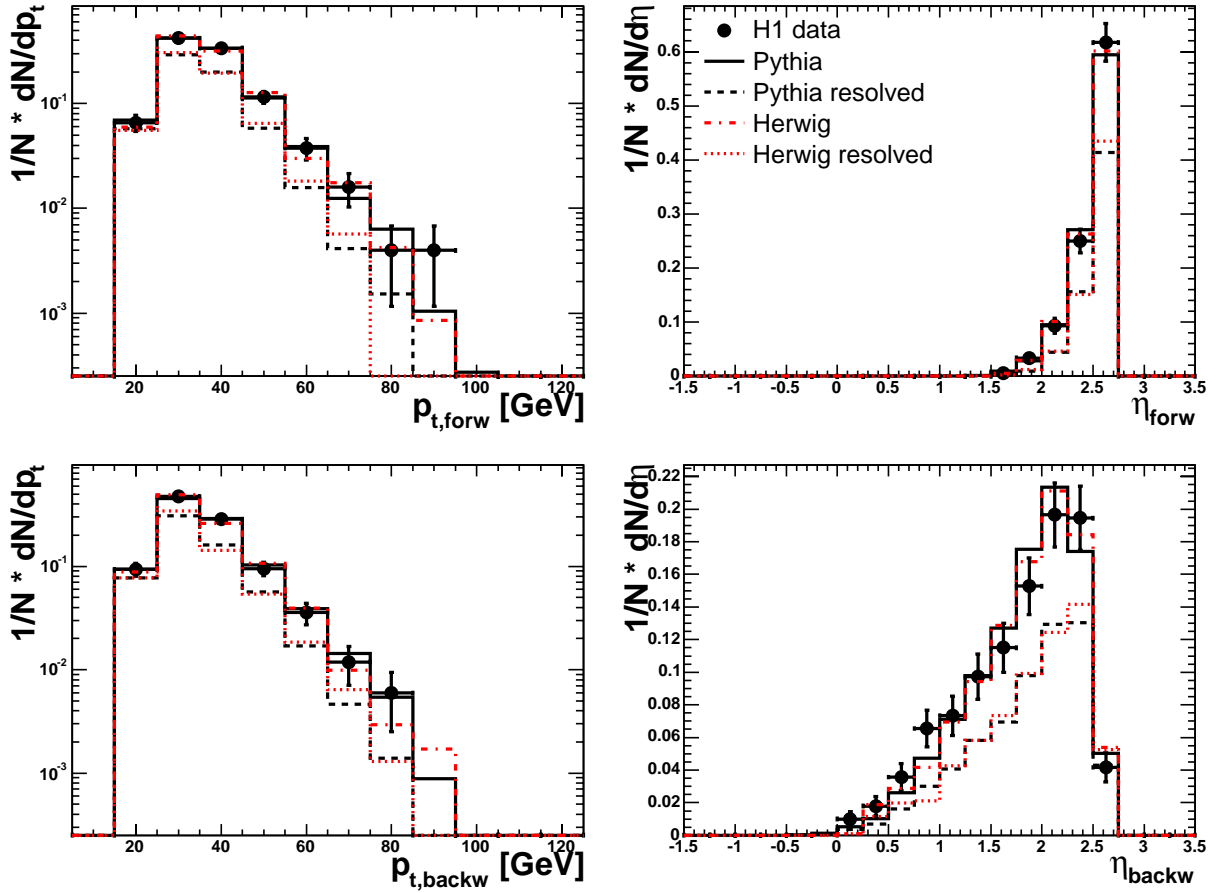


Figure 5.30: Jet reconstruction at  $0.32 < x_p < 0.45$ . Shown are transverse momentum and pseudorapidity of the forward (upper plots) and backward (lower plots) jet for  $\eta$  up to 2.75.

and detector and hadron level are done as with the standard method described in section 2.4. All three methods are then compared with the true value used in the generation of the Monte Carlo data set.

The first new method is characterised by taking all jets above a certain  $p_t$  threshold into account when calculating  $x_p$ . This is motivated by the fact that there is a certain fraction of real three-jet events where energy is “lost” when only two jets are used in the calculation. Additional jets are required to have at least 10 GeV in transverse momentum. So the sum in equation 5.11 below runs over  $n$  jets while in 2.28b on page 14 it was fixed to 2 jets.

$$x_p^{all} = \frac{1}{2E_p} \cdot \sum_{i, p_{t,jet} > 10\text{GeV}}^n p_{t,i} \cdot e^{+\eta_i} \quad (5.11)$$

The second new method is driven by the fact that in leading order the two jets from the hard scatter are balanced in  $p_t$ . The idea is that the backward jet in the more central region of the

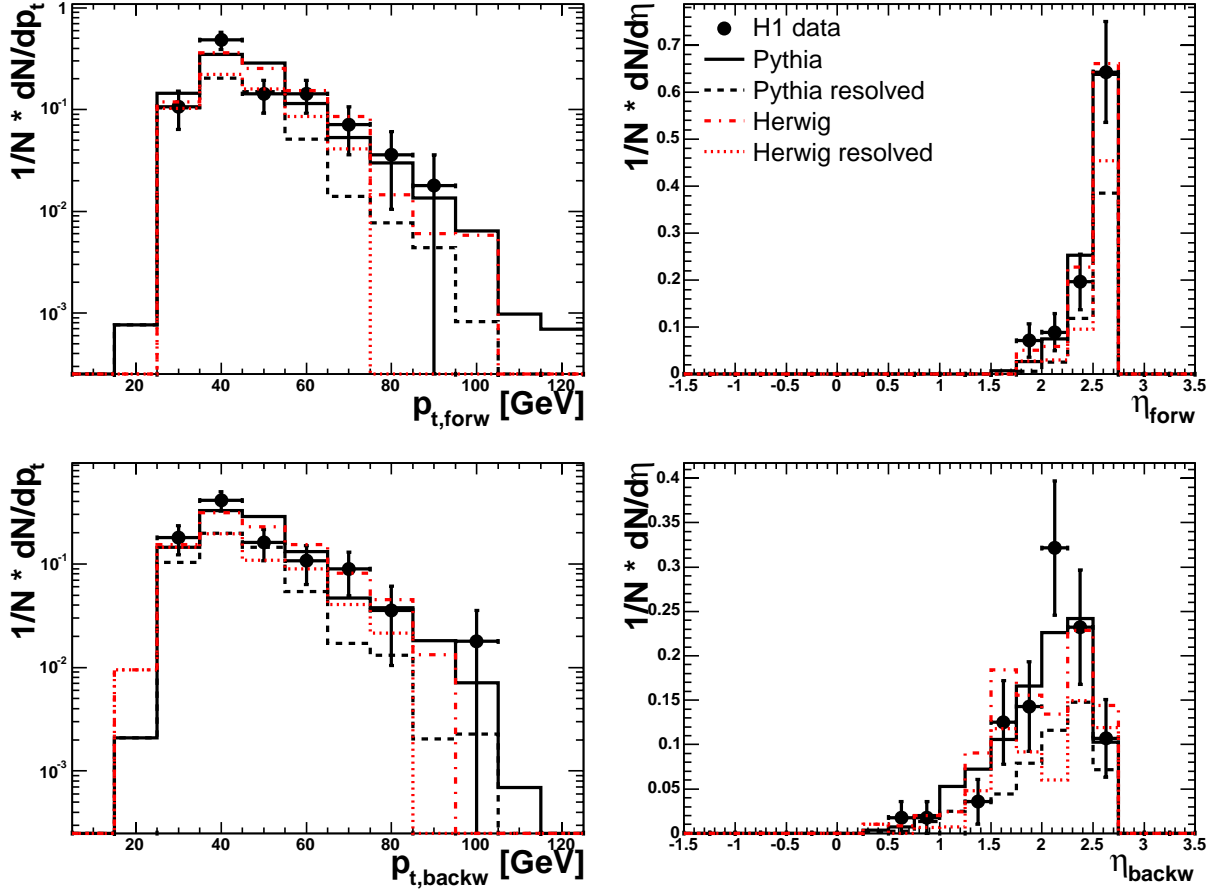


Figure 5.31: Jet reconstruction at  $x_p > 0.45$ . Shown are transverse momentum and pseudorapidity of the forward (upper plots) and backward (lower plots) jet for  $\eta$  up to 2.75.

detector has a better measurement of the transverse momentum than the forward jet which is closer to the acceptance threshold of the calorimeter. Then the  $p_t$  of the backward jet is taken for both jets and only the pseudorapidity is measured individually<sup>5</sup>. Then the formula becomes

$$x_p^{bal} = \frac{p_{t,backw}}{2E_p} \cdot \sum_i^2 e^{+\eta_i} \quad (5.12)$$

Figure 5.33 shows the comparison of  $x_p$  between data and Monte Carlo for the standard plus the two alternative methods. Using more than two jets for the  $x_p$  reconstruction has a similar good description as the standard method while making use of the  $p_t$  balance of the two jets leads to somewhat larger differences between data and expectation at the highest  $x_p$  values. It is also clear that using more than two jets in the sum (5.11) will enhance the large values of  $x_p$  where

<sup>5</sup>Angles are assumed to be more precisely measurable than energies.

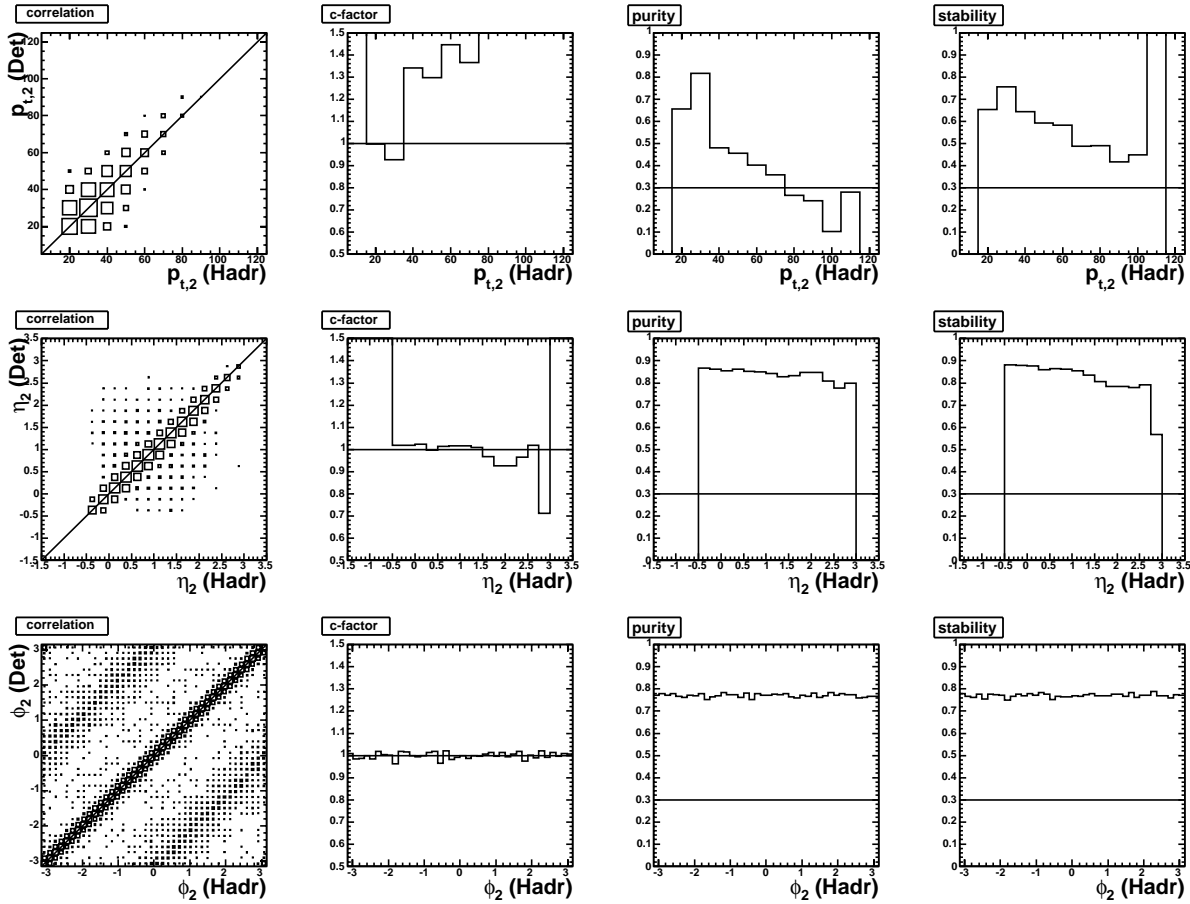


Figure 5.32: Correlations for the backward jet with  $\eta_{jet} < 3.0$ . The upper figures show the transverse momentum, the middle figures show the pseudorapidity and the lower show the azimuthal angle. The boxes in the correlation plots are logarithmic.

more stringent constraints on the PDFs are desired. This effect is larger in the resolved enhanced sample where  $x_\gamma < 0.8$ .

Looking at the worse correlation between detector and hadron level depicted in figure 5.34 the conclusion is that this method picks up jets that do not originate from the hard scattering process. Both alternative methods yield lower purities and stabilities, the resulting corrections are much higher for the “balance method” at highest  $x_p$  and over the entire  $x_p$  range for the “all jet method”. Therefore it was decided to stick to the standard method to reconstruct  $x_p$ .

All three methods are then compared to the true  $x_p$  that was used in the generation of the Monte Carlo events. Figure 5.35 shows the number of events per unit luminosity as a function of  $x_p$  and the ratio of the  $x_p$  distributions for the different reconstruction methods to the distribution of the true value. The general trend is that the reconstructed  $x_p$  is lower than the true one. Less events are found at values larger than 0.3 and subsequently there is an excess below that value. Using the balance method yields values that are closer to the true  $x_p$  than the standard reconstruction

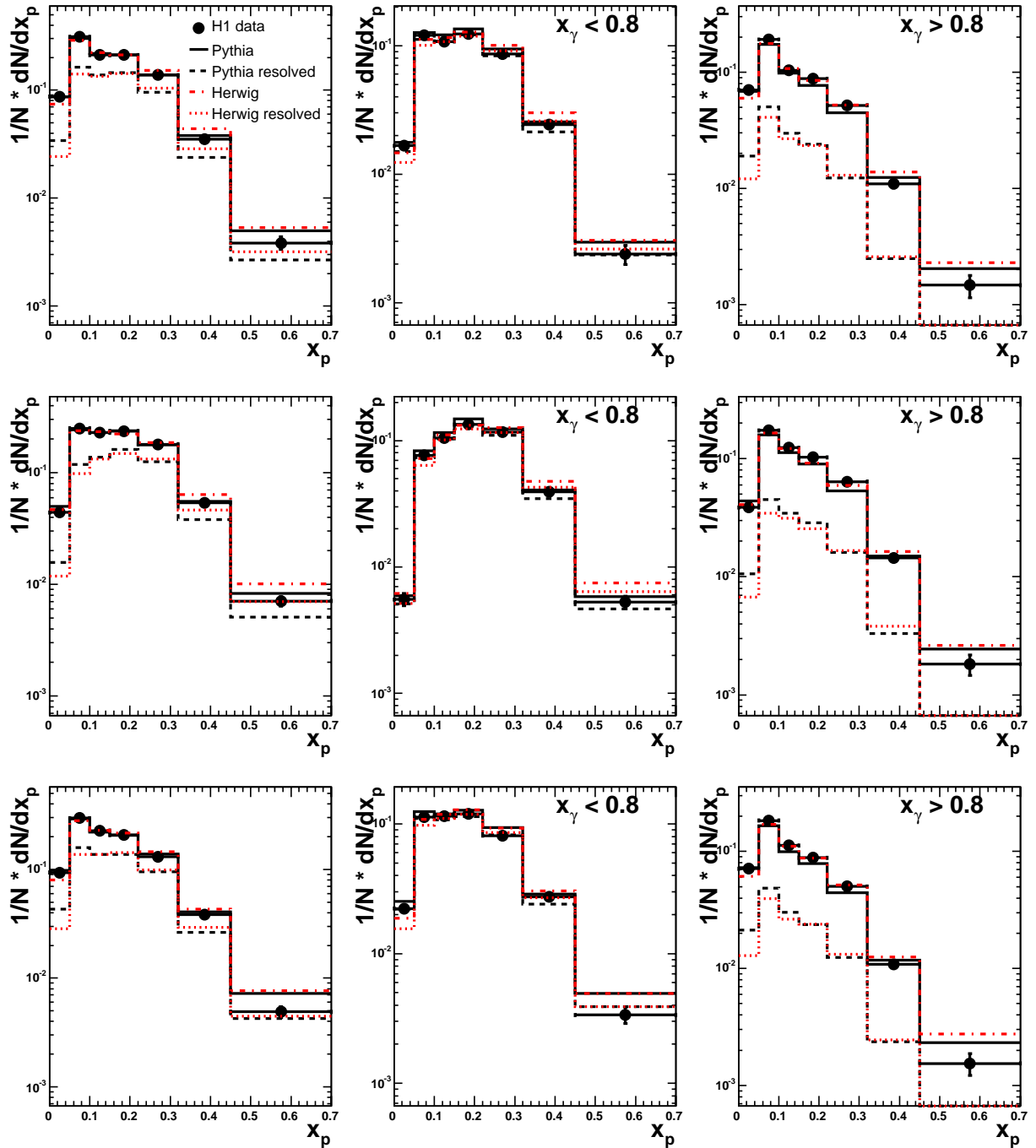


Figure 5.33:  $x_p$  reconstruction for different methods. The top row is the standard method, middle row is the method using all jets and bottom row is the method assuming the two jets to be balanced in  $p_t$ .

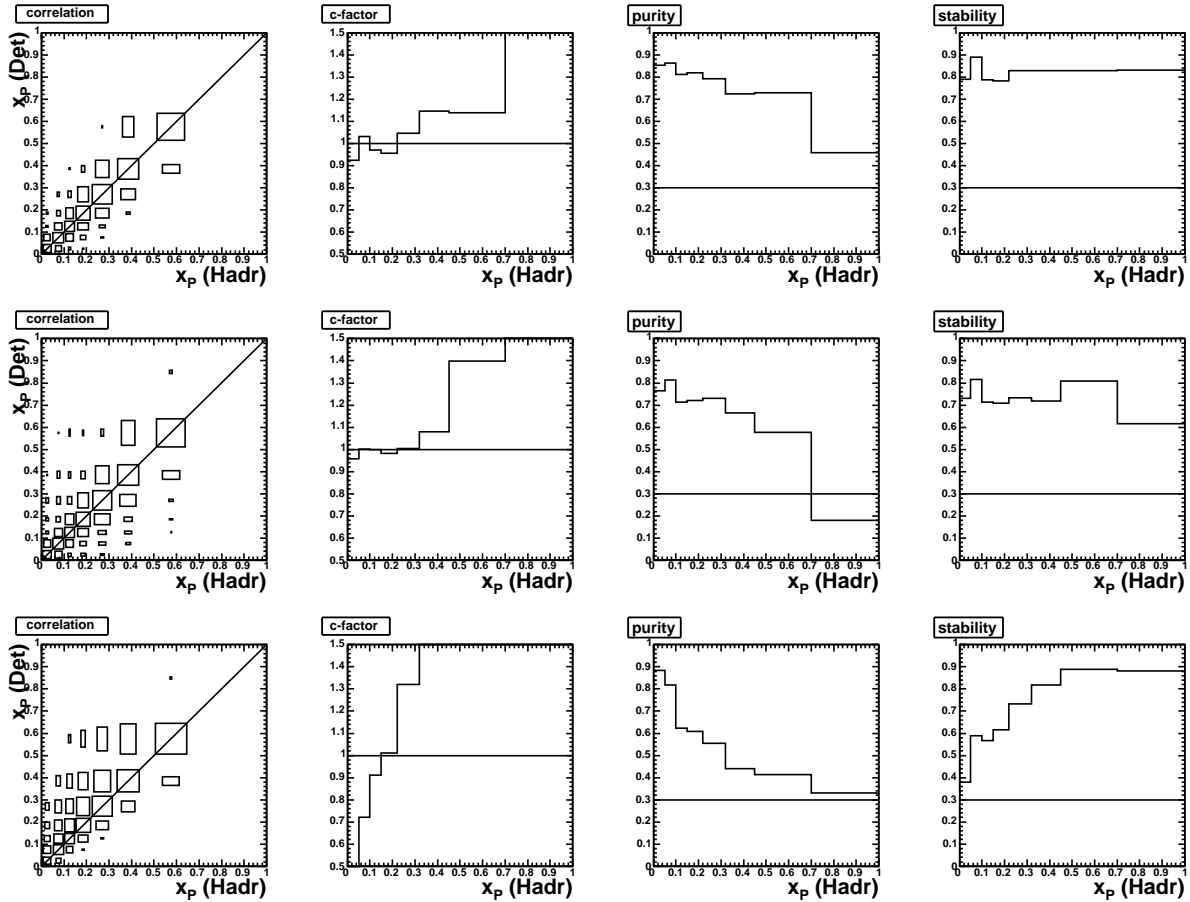


Figure 5.34: Correlations in  $x_p$  for different reconstruction methods. The top row is the standard method, middle row is the method using all jets and bottom row is the method assuming the two jets to be balanced in  $p_t$ .

over the entire  $x_p$  range. For the all jet method this is only true for  $x_p > 0.3$ .

The general message to take away from the fact that all three methods reconstruct smaller momentum fractions for  $x_p > 0.3$  is that in order to put a constraint on large momentum fractions in the PDFs it is not sufficient to look at the medium range of reconstructed  $x_p$  because there the cross section is much larger. Even if the alternative reconstruction methods have less good correlations between detector and hadron level future analyses might be able to find more sophisticated methods without the deficiencies of the two examined in this analysis.

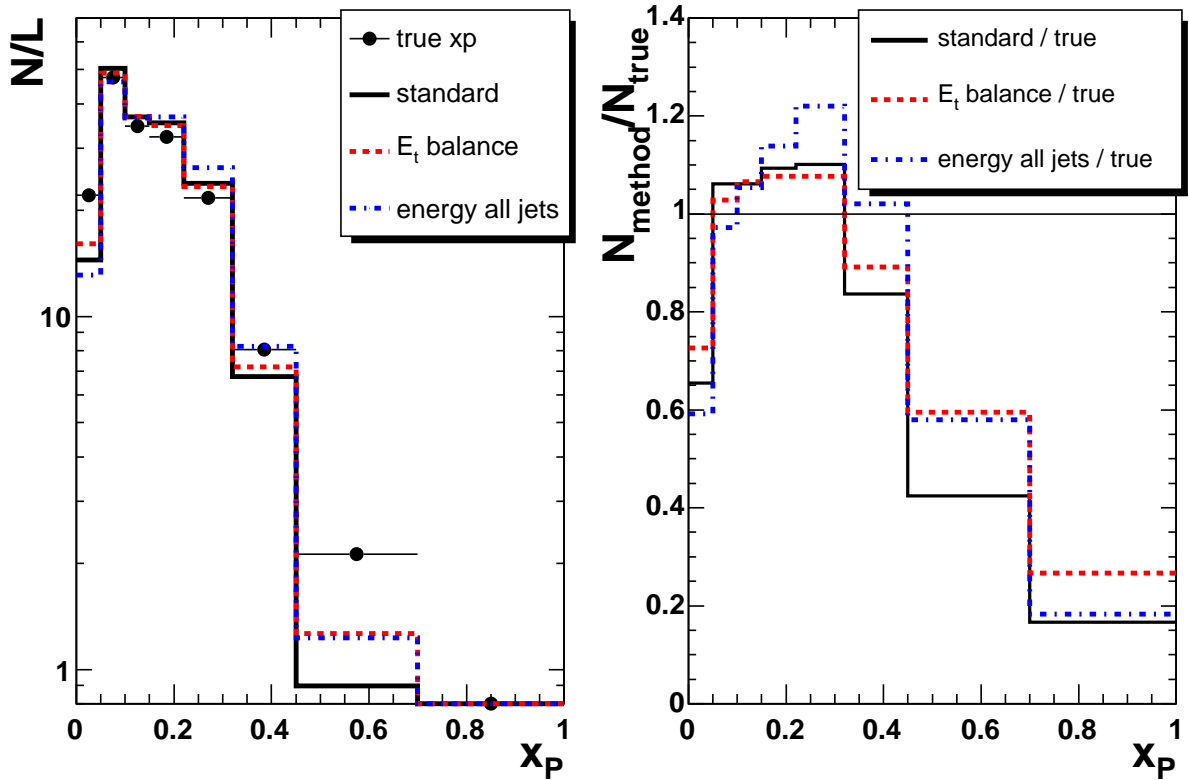


Figure 5.35: In the left plot the distributions of the reconstructed and true  $x_p$  are shown. On the right is the ratio of the reconstructed distributions to the true distribution.

## 5.6 Sensitivity to the gluon density.

Since the gluon density is the PDF with the largest uncertainty today the sensitivity to this quantity was also checked in a Monte Carlo study. The fraction of events induced by a gluon entering the hard scatter from the proton side was examined using the PYTHIA generator. Figure 5.36 shows the number of events per unit luminosity as a function of  $x_p$ , first as the total number of events and second as number of events induced by gluons. From the ratio plot one can see that starting from the lowest  $x_p$  values the gluon fraction drops from 70% to 14% in the highest bin used in this analysis. This means to get a direct handle on the gluon density the uncertainty of the measurement needs to be smaller than those values. Unfortunately the uncertainty from the LAr energy scale uncertainty alone is already larger. Therefore no further effort was made to extract the gluon density in the proton directly. Compared to the previous analysis stronger constraints are shown in this work with smaller statistical uncertainties as well as an additional data point and the extension from 0.6 to 0.7 in the  $x_p$  range.

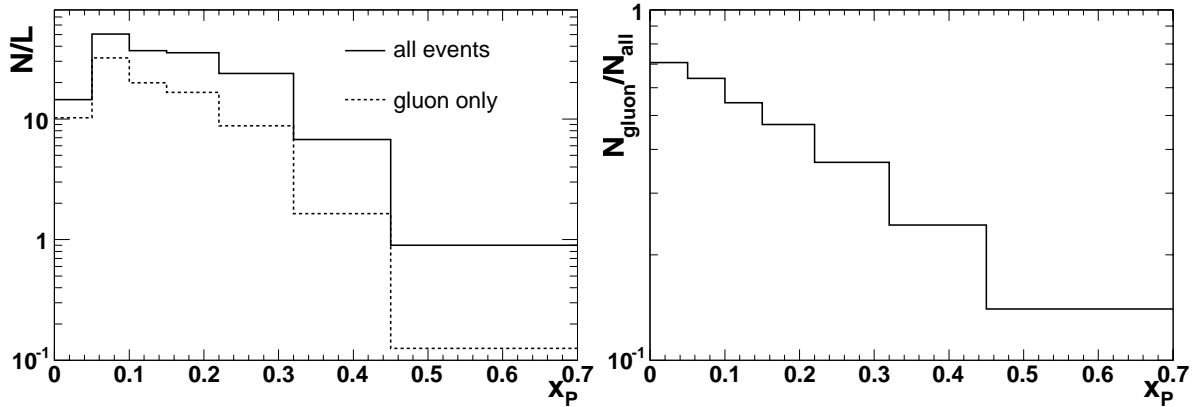


Figure 5.36: The left plots shows the  $x_p$  distribution for all events (solid) and those induced by gluons from the proton side (dashed). The right plots shows the ratio of the two.

## 5.7 Effects in the NLO calculations

In the next two sections the effects of different proton beam energies and different jet cut scenarios on the results of the NLO calculations are examined. For this purpose the NLO calculations have been carried out in different scenarios of centre-of-mass energies and jet cuts. For the energy the two proton beam energies of the years up to and including 1997 (820 GeV) and afterwards (920 GeV) have been used. In case of the jets the upper  $\eta$  cut has been set to 2.5 or 2.75 and the cut on the  $p_t$  of the second jet to 15 GeV or 20 GeV. The NLO results of the previous analysis [A<sup>+</sup>02b] were reproduced when using the same parameters ( $E_{p,beam} = 820$  GeV,  $p_{t,2nd} > 15$  GeV,  $\eta_{jet} < 2.5$ ).

This is followed by a section that describes the procedure to determine uncertainties of the theoretical predictions that arise from the way the theory groups fit their PDFs to the corresponding input data.

### 5.7.1 Centre-of-mass Energy

The previous H1 analysis on dijets in photoproduction [A<sup>+</sup>02b] was performed on data taken with a lower proton beam energy of 820 GeV while this work is done on data taken with a beam energy of 920 GeV. This section highlights the differences that arise in the NLO calculations when going from lower to higher proton beam energy. All results in this section are shown as cross sections without hadronisation corrections applied<sup>6</sup>.

Figure 5.37 shows one sample cross section  $-d\sigma/dx_p$  for the two beam energies with the jet cuts as used in [A<sup>+</sup>02b], i.e.  $p_{t,2nd} > 15$  GeV and  $\eta_{jet} < 2.5$ . In going from  $E_{p,beam} = 820$  GeV to  $E_{p,beam} = 920$  GeV the cross section increases by  $\approx 60\%$  at low  $x_p$  and decreases by  $\approx 25\%$  at high  $x_p$ . This is because for different beam energies a fixed longitudinal momentum fraction results in different boosts along the  $z$ -axis. For the higher beam energy the events at high  $x_p$

<sup>6</sup>The corresponding correction factors were only determined for the proton beam energy of the analysed data.

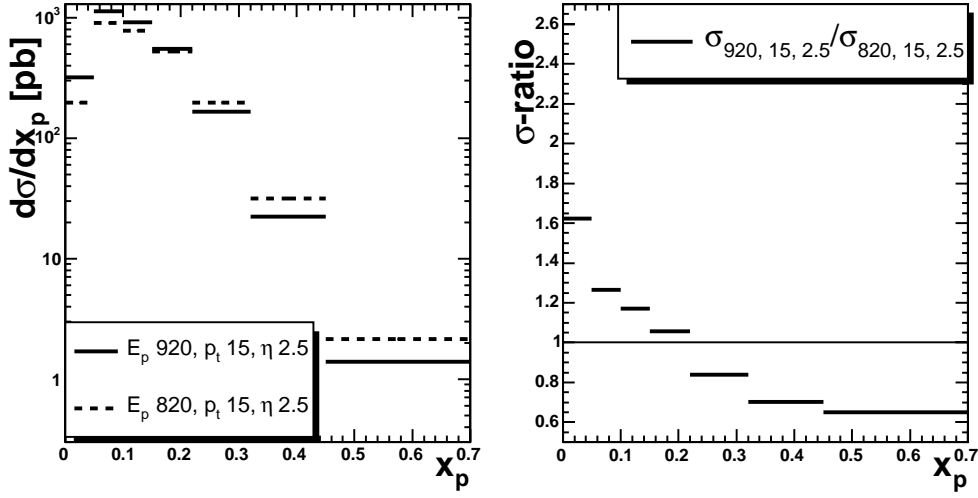


Figure 5.37: NLO cross section as function of  $x_p$  for different proton beam energies. Shown is the cross section before hadronisation corrections for CTEQ6M in the left plot. The right plot shows the cross section ratio between the results obtained for  $E_{p,beam} = 920$  GeV and  $E_{p,beam} = 820$  GeV. In both figures the jet cuts  $p_{t,2nd} > 15$  GeV and  $\eta_{jet} < 2.5$  were used.

are more likely to lie outside the angular acceptance in the forward direction. Similar arguments hold for the low  $x_p$  region: in case of the higher beam energy a small value of  $x_p$  is more likely to lie inside the angular acceptance in the backward direction.

The total cross section increases by  $\approx 15\%$  for this set of jet cuts.

## 5.7.2 Effect of the jet cuts

The effect of varying the cuts in the jet pseudorapidity and transverse momentum of the second leading jet in the NLO predictions of the  $x_p$  cross section are discussed in this section.

In figure 5.38 the ratios of the cross section without hadronisation corrections for the different jet cut scenarios to the setting with  $p_{t,2nd} > 15$  GeV and  $\eta_{jet} < 2.5$  are depicted. The ratios are shown in two regions of  $x_\gamma$ .

The first thing to notice is that the  $p_t$  cut is more important at low  $x_p$  while the  $\eta$  cut has large effects at high  $x_p$ . This can be understood because at high  $x_p$  the event is boosted in the forward direction thus directly related to the forward cut in the pseudo-rapidity. With much energy coming from the proton side the jets typically have large  $p_t$ , therefore the effect of the  $p_t$  cut is small (compare the dashed and dotted lines). For low  $x_p$  there is no such strong boost in the forward direction and the effect of the  $\eta$  cut is negligible. Also with less energy from the proton side the jets will have less  $p_t$  and thus are more sensitive to the cut in the transverse momentum.

Quantitatively the trends between the different cut scenarios vary in size for the two regions of  $x_\gamma$ , the effects being larger in the resolved enhanced sample. Let us first examine the low  $x_p$  regime. Using the higher  $p_t$  cut leads to 40% reduced cross section for the lowest  $x_p$  bin at  $x_\gamma < 0.8$ . At  $x_\gamma > 0.8$  the effect is only a 15% reduced cross section. In both cases this is independent

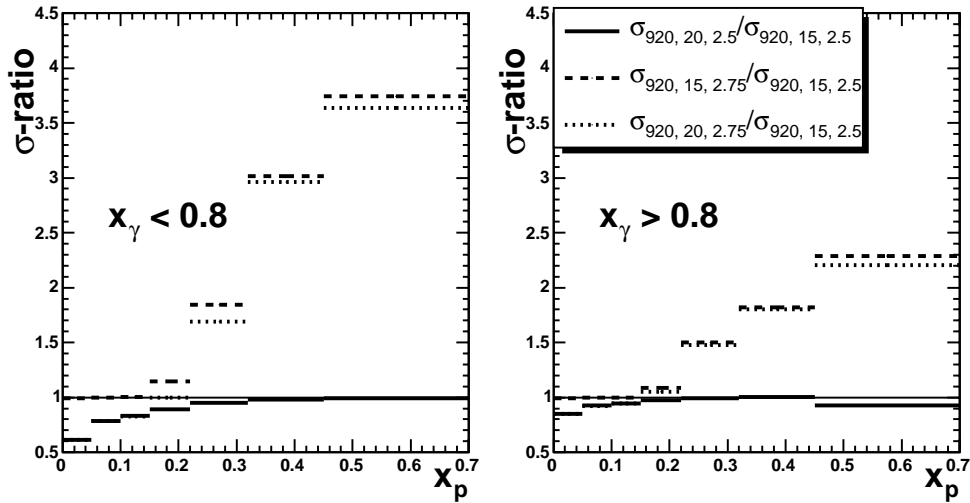


Figure 5.38: Ratio between the NLO cross sections as function of  $x_p$  for different cut scenarios at  $E_{p,beam} = 920$  GeV for two  $x_\gamma$  regions. Shown are ratios without hadronisation corrections applied to the cross sections.

of the  $\eta$  cut used as discussed above. The difference in size of this effect can be explained by the fact that in the resolved enhanced sample less energy from the photon side enters the hard scattering process which leads to smaller transverse momenta of the outgoing particles of the hard interaction.

Looking at the highest  $x_p$  bin and  $x_\gamma < 0.8$  the extension of the acceptance in jet pseudorapidity yields a cross section that is higher by a factor of  $\approx 3.7$ . The effect at  $x_\gamma > 0.8$  is only a factor of  $\approx 2.3$ . To explain this difference the line of reasoning is similar to the low  $x_p$  case. For a fixed value of  $x_p$  less energy from the photon side (i.e. smaller  $x_\gamma$ ) means a stronger boost into the forward direction and therefore a higher sensitivity to the forward boundary in jet pseudorapidity. Since the aim of this analysis is to put constraints on the proton PDF at high values of  $x_p$ , extending the jet angular acceptance in the forward direction is a good means to increase the cross section – thus decreasing the statistical uncertainty – in the mid to high range of the longitudinal momentum fraction coming from the proton side. This also overcompensates the decrease of the cross section at high  $x_p$  to be expected from the higher proton beam energy with respect to the previous analysis.

### 5.7.3 Uncertainty from the Proton PDFs

For newer parton parametrisations the corresponding groups adopted the so-called *Hessian method* to quantify the uncertainties inherent in the fitting method. The “classic” PDFs only represent a best estimate without information on the tolerances in the parameters that would still yield a statistically reasonable fit. The approach is to define an effective global chi-squared function  $\chi_{global}^2$ , fitting the PDFs parameters and find the minimum of  $\chi_{global}^2$ , represented by a particular

set of parameters usually written as  $S_0$ <sup>7</sup>. Then the neighbourhood of this minimum is studied which is defined by

$$\Delta\chi_{global}^2 \leq T^2 \quad (5.13)$$

and a so-called *tolerance parameter*  $T$  which gives the region of “acceptable fits”. There are different estimates on the size of  $T$  from different analyses that typically yield values of  $T \approx 10$  to 15. This is a topic still under study.

The Hessian method now transforms the region given by the tolerance parameter  $T$  from a basis in the original PDFs parameters to an orthonormal eigenvector basis of dimension  $d$ . The so-called “eigenvector sets”  $S_k^\pm$  are determined by a displacement of a standard magnitude  $t$  “up” or “down” along the direction of eigenvector  $k$ . Thus the number of such sets is  $2d$ . When the eigenvectors are expressed in the so-called “ $z$ -representation” using coordinates  $z = (z_1, \dots, z_d)$  the gradient of any observable  $X$  along the direction of one eigenvector is given by

$$\frac{\partial X}{\partial z_k} = \frac{X(S_k^+) - X(S_k^-)}{2t} \quad (5.14)$$

Finally, the uncertainty of observable  $X$  resulting from the eigenvector analysis is

$$\Delta X = \frac{T}{2t} \left( \sum_{k=1}^d [X(S_k^+) - X(S_k^-)]^2 \right)^{1/2} \quad (5.15)$$

Here  $T$  is the tolerance to be used in the analysis and  $t$  is the standard magnitude used in defining the eigenvector sets. For CTEQ6M  $t = 10$  and  $T$  was set equal to  $t$  in this analysis.

More detailed descriptions of this procedure can be found in [PST02, P<sup>+</sup>02b, MRST03].

In figure 5.39 the results of the individual eigenvector sets are shown as a ratio to the best fit for the cross section as function of  $x_p$ . The bulk of the 40 sets is within  $\pm 5\%$ , the largest deviation is 23%, reached in the highest  $x_p$  bin for the resolved enhanced sample. For  $x_p > 0.15$  the set that leads to the biggest change in cross section corresponds to eigenvector 15. This eigenvector is connected to the gluon density of the proton. In [S<sup>+</sup>03] the PDF uncertainties were studied and eigenvector 15 was found to yield the largest variations in  $g(x, Q)$  reaching 50% at  $x_p \approx 0.5$  as can be seen in figure 5.40.

Looking at the resulting uncertainty on the cross section as function of  $x_\gamma$  as calculated by equation 5.15 yields the picture shown in figure 5.41. These uncertainties are much smaller than the scale uncertainties and decrease slightly towards  $x_\gamma = 1$ .

For  $x_p$  the PDF uncertainty is shown in figure 5.42. Up to  $x_p < 0.22$  deviations are around 5% in both  $x_\gamma$  regions. For higher values of  $x_p$  the uncertainties grow up to 19% in the resolved enhanced sample and up to 15% for direct enhanced processes. Compared to the scale uncertainty the size of the deviations is much smaller here for values up to  $x_p < 0.32$  and about equal in the bin  $0.32 < x_p < 0.45$ . At  $0.45 < x_p < 0.7$  the PDF uncertainty is roughly a factor two larger than the scale uncertainty.

---

<sup>7</sup>Which corresponds to the “classic” PDFs.

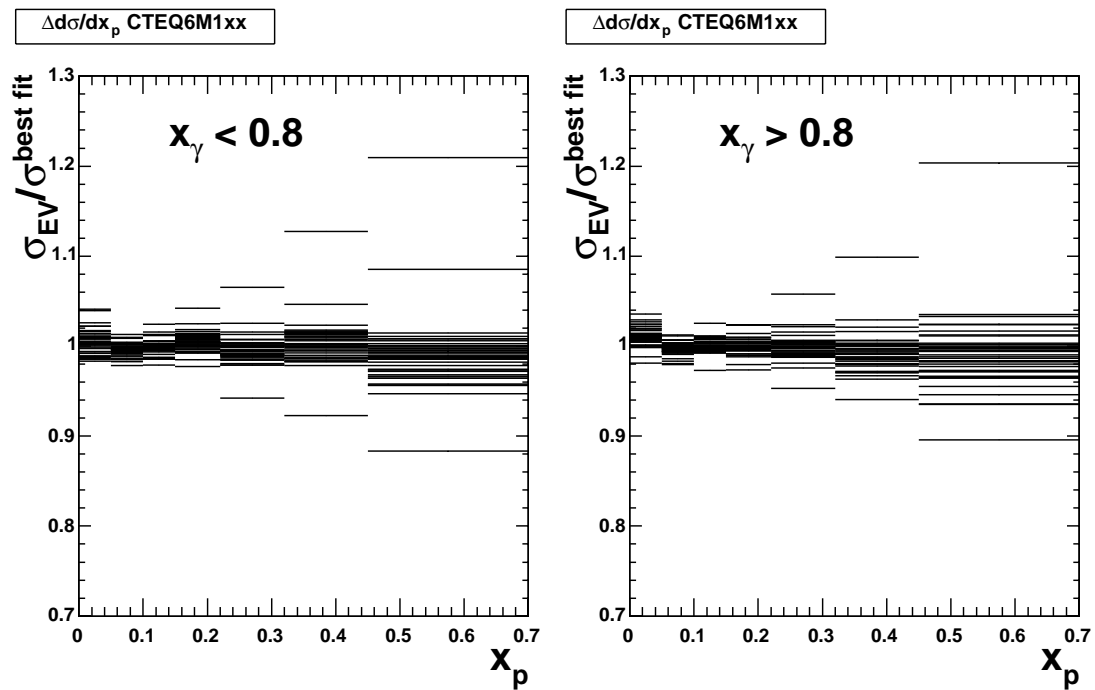


Figure 5.39: Relative deviations of the 40 CTEQ6 eigenvector sets from the central fit value. Largest deviation arises in CTEQ6M130 which corresponds to eigenvector 15.

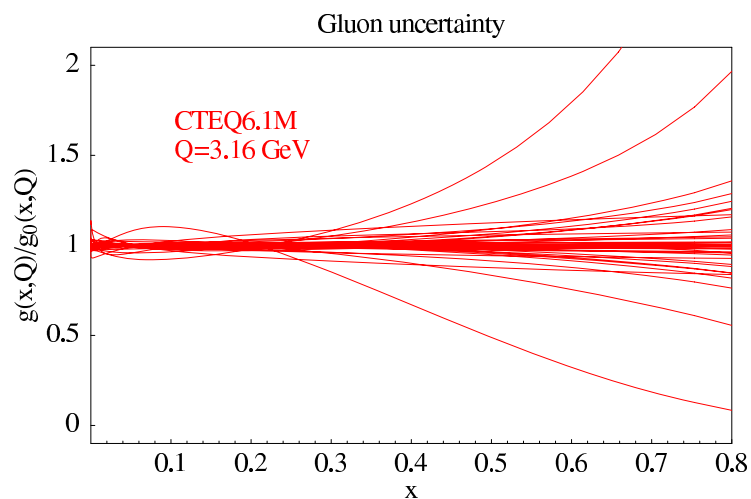


Figure 5.40: Ratio of the gluon density from the CTEQ6.1 eigenvector sets to the best fit. The largest deviation arises from eigenvector 15. Figure taken from [S<sup>+</sup>03].

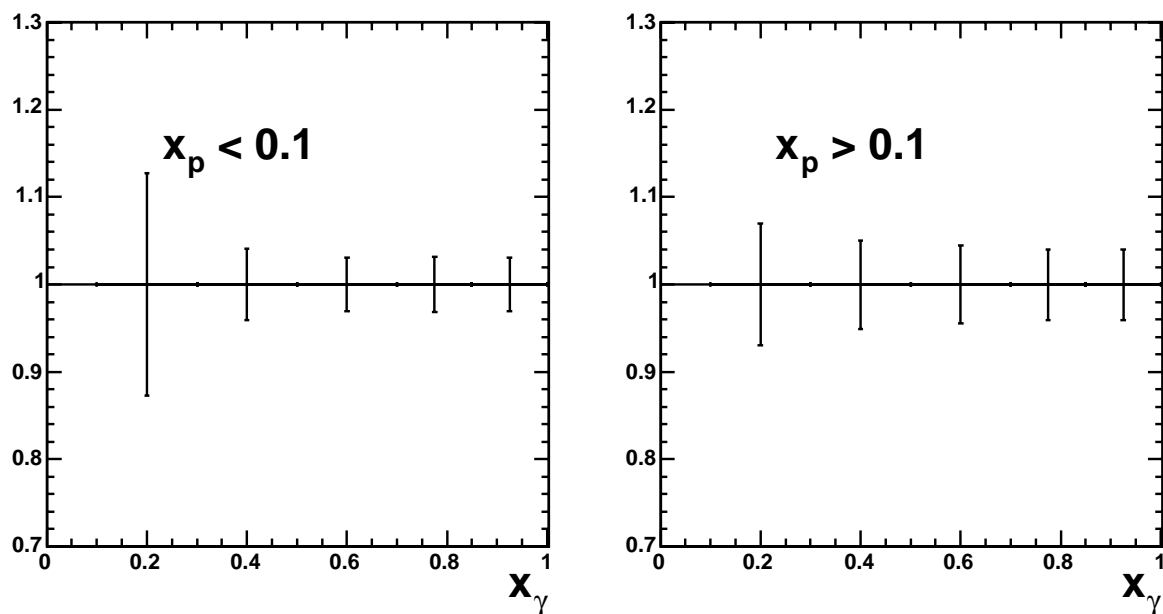


Figure 5.41: Resulting uncertainties of the dijet cross section as a function of  $x_\gamma$  from the CTEQ6M eigenvector sets. The error bars correspond to  $\Delta\sigma/\sigma$  with  $\Delta\sigma$  calculated by eq. 5.15.

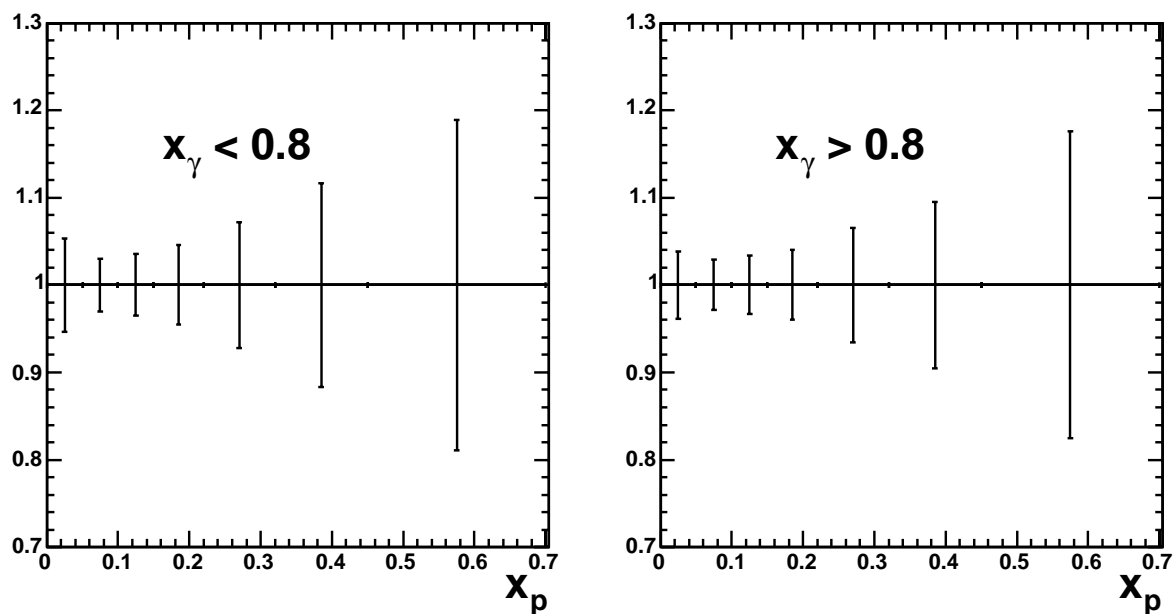


Figure 5.42: Resulting uncertainties of the dijet cross section as a function of  $x_p$  from the CTEQ6M eigenvector sets. The error bars correspond to  $\Delta\sigma/\sigma$  with  $\Delta\sigma$  calculated by eq. 5.15.

# Chapter 6

## Results

In this chapter the measured inclusive dijet cross sections are presented and compared to theoretical predictions at next-to-leading order perturbative QCD in the phase space

$Q^2 < 1 \text{ GeV}^2$ $0.1 < y < 0.9$
$p_{t,max} > 25 \text{ GeV}$ $p_{t,2nd} > 15/20 \text{ GeV}$ $-0.5 < \eta_{jet} < 2.5/2.75$

The data are corrected for detector effects using the mean correction factors obtained by the PYTHIA and HERWIG generators. They are obtained by the ratio of detector level cross sections with all detector cuts applied to hadron level cross sections with only phase space cuts applied. The uncertainty as discussed in section 5.3 is included in the systematic uncertainties of the data cross section as a symmetric uncertainty. Both Monte Carlo results have been reweighted to match the distributions of the inelasticity  $y_{JB}$  and the angle between the two leading jets in their centre-of-mass system  $\cos \theta^*$ . This introduces a one-sided uncertainty to the total systematics. Background from DIS events as estimated by the DJANGO ARIADNE generator was subtracted before the detector corrections were applied. The resulting uncertainty is symmetric. Further systematic effects were estimated by individually varying up and down the energy scale in PYTHIA of the SpaCal and LAr calorimeter by 8% and 2%, respectively. The resulting uncertainties on the data cross section are asymmetric. Finally global uncertainties of 2% from the trigger efficiency correction and 1.5% from the luminosity measurement are included in the total systematic uncertainty of the data cross section. All individual contributions have been added in quadrature.

The NLO calculations have been performed using a program by Frixione and Ridolfi based on the subtraction method to cancel infrared divergencies. As parton density functions GRV-HO was used for the photon and CTEQ6M for the proton. Renormalisation and factorisation scale have been set to half the sum of the transverse momentum of the outgoing partons, the calculations were carried out in the  $\overline{\text{MS}}$  scheme. The NLO cross sections will be shown with and without hadronisation corrections applied. The correction factors are obtained by taking the ratio of

the cross section between hadron level and parton level after parton shower with phase space cuts applied. Similar to the detector corrections the mean factors obtained with PYTHIA and HERWIG are used. The uncertainty of the NLO result is estimated by simultaneously varying up and down the renormalisation and factorisation scale by a factor of two. A second contribution to the uncertainty is added in quadrature by examining the uncertainty arising from the CTEQ6M parametrisation of the proton PDF. For that the NLO cross sections have been recalculated using 40 eigenvector sets to form an uncertainty using the method described in section 5.7.3. Effects of using other parametrisations for the photon and proton will be discussed in section 6.2. Finally the model uncertainty of the hadronisation correction factors is added to the total uncertainty of the NLO calculations.

The analysis was performed in four different cut scenarios. The forward limit of the dijet angular acceptance was set to  $\eta_{jet} < 2.75$  and  $\eta_{jet} < 2.5$ , respectively.  $p_{t,2nd} > 15$  GeV and  $p_{t,2nd} > 20$  GeV were chosen as the two cuts on the transverse momentum of the second leading jet inside the angular acceptance. Only one scenario is discussed in detail in the following section with differences in the other three highlighted at the end. All cross sections and the individual contributions to the uncertainties in a tabulated form for the four cut scenarios in both data and NLO calculation can be found in appendices A and B, respectively.

## 6.1 Dijet cross sections

The measured cross sections of the reaction  $ep \rightarrow e \text{ jet jet } X$  in this section are given for jet cuts of  $p_{t,max} > 25$  GeV,  $p_{t,2nd} > 15$  GeV and  $-0.5 < \eta_{jet} < 2.75$ . In section 5.7.2 a more detailed look is taken at the effects of variations of these cuts. The results are given at the level of stable hadrons. The data were corrected for detector effects and are shown with statistical (inner error bars) and total uncertainty (outer error bars). They are compared with next-to-leading order calculations both before and after hadronisation corrections. The total cross section from the NLO calculation is  $(13.7^{+9.7}_{-13.4})\%$  higher than in data. Here the uncertainty only includes the uncertainty of the data. The data are also compared to the results of the PYTHIA generator with matrix elements at leading order and including parton showers. The cross sections from PYTHIA are scaled up by a factor of 1.2 to match the total cross section with that in data (c.f. 2.7.1).

Figure 6.1 shows the dijet cross section as function of the mean transverse momentum  $\bar{p}_t$  of the two leading jets and the dijet mass  $M_{jj}$ . The mean transverse momentum of the jets can be interpreted as the hard scale of the interaction and the dijet mass corresponds to the centre-of-mass energy of the hard subprocess. Both are essential quantities for any calculation in perturbative QCD.

In the range of 20 GeV – 80 GeV the cross section in  $\bar{p}_t$  drops by almost three orders of magnitude. The total uncertainty of the data cross section is about 12% at low  $\bar{p}_t$  and rises to  $\approx 20\%$  at high  $\bar{p}_t$ . The dominant systematic uncertainty is the LAr energy scale with  $\approx 11\%$  over the entire range. Only at highest  $\bar{p}_t$  the statistical uncertainty plays an important role and amounts to 17%. The NLO calculation is able to describe the measured spectrum over the entire range. Hadronisation corrections are between 1% in the lowest and 6% in the highest bin. Their model uncertainty is below 3% at low  $\bar{p}_t$  and 6% at highest  $\bar{p}_t$ . The scale uncertainty is much larger

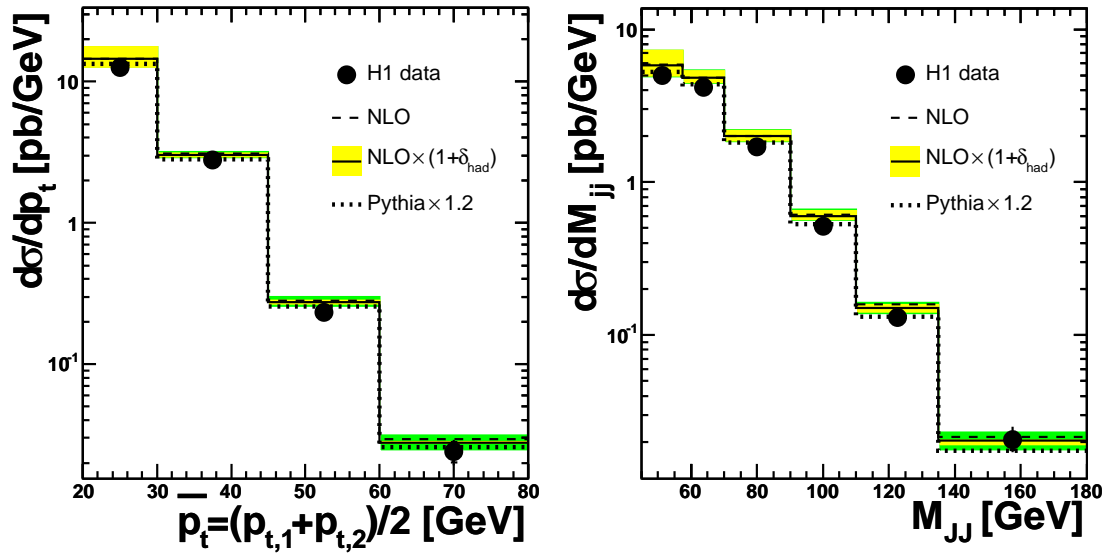


Figure 6.1: Cross sections in mean  $p_t$  (left) and invariant dijet mass (right) for data (points), NLO with (solid line) and without (dashed) hadronisation corrections  $\delta_{had}$  and for the PYTHIA LO generator (dotted) scaled by a factor of 1.2. The inner bar of the data points is the statistical, the outer the total uncertainty. The inner band of the  $NLO \times (1 + \delta_{had})$  result is the scale uncertainty, the outer band is the total uncertainty.

in the lowest bin (21%) than in all others ( $< 6\%$ ). The opposite is the case for the PDF uncertainty which is 3% at low and 11% at high  $\bar{p}_t$ . A similar picture results for the dijet mass. The description of the data by the NLO calculation is good over three orders of magnitude in the range 45 GeV – 180 GeV. As in the case of the mean transverse momentum of the two leading jets the total uncertainty of the cross section as function of the invariant dijet mass grows with increasing values of  $M_{JJ}$ : it starts at 11% and rises to 23%. Dominating again is the energy scale uncertainty of the LAr calorimeter. At the highest  $M_{JJ}$  the statistical uncertainty gets large and with 14% is of almost equal size as the energy scale uncertainty. The two Monte Carlo models and the reweighting of the Monte Carlo to data in the  $y_{JB}$  and  $\cos\theta^*$  distributions account for medium sized uncertainties (6% to 8%) compared to the other contributions at  $M_{JJ} > 90$  GeV. The same is true for the model uncertainty ranging between 5% and 6% at highest  $M_{JJ}$ . Except for the lowest bin the scale uncertainty of the NLO prediction is about or less than 10%. For 45 GeV  $< M_{JJ} < 58$  GeV it reaches 25%. At 135 GeV  $< M_{JJ} < 180$  GeV the PDF uncertainty is 12% and thus slightly larger than the energy scale uncertainty. For lower values of the dijet mass it varies between 3% and 7%. Hadronisation corrections lie between about 1% and 6%. Their model uncertainty is below 3% with the exception of 5% at highest  $M_{JJ}$ .

The agreement between data and NLO for these two basic dijet quantities is good over a wide range and several orders of magnitude. It is noted that the leading order prediction plus parton shower gives similar results as the next-to-leading order calculations plus hadronisation corrections. This means the k-factor between LO and NLO is rather small, thus one can assume the

k-factor in going from NLO to NNLO will be small as well.

In figure 6.2 the cross section as function of the mean pseudorapidity  $\bar{\eta}$  is depicted in four different regions of inelasticity  $y$  and maximum jet transverse energy  $p_{t,max}$ . Dividing into  $y$  regions corresponds to different centre-of-mass energies in the photon-proton system while the two different  $p_{t,max}$  regions correspond to a scale variation. The mean pseudorapidity itself depends on the longitudinal boost which in turn depends on the momentum fractions of the interacting partons taken from the beam particles. Thus  $\bar{\eta}$  depends on the ratio  $x_p/y \cdot x_\gamma$ .

Data and NLO agree within uncertainties over the entire  $\bar{\eta}$  range in all four regions with the exception of four bins that agree within  $\approx 1.5\sigma$ . The statistical uncertainty is below 5% except for high transverse momentum and high inelasticity. There it varies between 5% and 9%. Dominating is the LAr energy scale uncertainty that varies between 7% (low  $\bar{\eta}$ ) and 16% (high  $\bar{\eta}$ ). Sizeable contributions from the model and reweighting procedure uncertainty enter with values mostly between 4% and 7%. The model uncertainty at low  $\bar{\eta}$  gets dominant at high  $p_{t,max}$  and  $y_{JB}$  with a value of 19%. The resulting total uncertainty in data ranges between 10% and 27%, being largest at  $2.1 < \bar{\eta} < 2.5$ . For the NLO predictions the scale uncertainty is a factor of 3 to 5 larger than the PDF uncertainty except for the highest values of  $\bar{\eta}$  where it is still dominant. The scale uncertainty varies between 14% and 24%, the PDF uncertainty between 3% and 13%. Similar to the data the model uncertainty can get large at very forward or backward angles. It is the dominant source of uncertainty at lowest  $\bar{\eta}$  in the region of high  $p_{t,max}$  and high  $y_{JB}$ . In all four regions of  $p_{t,max}$  and  $y_{JB}$  the resolved component of the PYTHIA generator<sup>1</sup> rises from slightly above 20% at low values of  $\bar{\eta}$  to 60% – 70% in case of low  $y$  and almost to 100% in case of high  $y$ . The rise is stronger for low  $p_{t,max}$ . This is to be expected because for the same  $p_{t,max}$  and  $\bar{\eta}$  the product  $y \cdot x_\gamma$  must be constant and therefore resolved events ( $x_\gamma < 1$ ) correspond to high values of  $y$ .

In measuring  $\bar{\eta}$  in two different regions of  $p_{t,max}$  the scale dependence of the cross section is tested. In the NLO calculations  $\alpha_s$  and the parton density functions of the photon and proton are the scale-dependent quantities. Since there is good agreement between data and NLO in both regions of  $p_{t,max}$ , this is an indication that the scale dependence of above quantities as implemented in the NLO calculation is confirmed by the data. As  $\bar{\eta}$  at fixed inelasticity depends on  $x_p/x_\gamma$ , also the  $x$ -dependence of both PDFs is verified by this measurement.

The dijet cross section as function of  $\cos\theta^*$  is shown in figure 6.3.  $\cos\theta^*$  is sensitive to the dynamics of the dijet production, i.e. the matrix element of the hard interaction. Here the measurement is presented separately for  $x_\gamma < 0.8$  and  $x_\gamma > 0.8$  to enrich the resolved or direct component, respectively.

For low  $x_\gamma$  the uncertainties are larger for both data and the NLO prediction. Still they agree within uncertainties. Without the cut on the invariant dijet mass  $M_{JJ}$  the statistical uncertainty of the data is around 4%. With the cut it is 4% to 10% in the resolved enhanced sample and 4% to 7% in the direct enhanced case. Again the LAr energy scale uncertainty is the dominant contribution to the total uncertainty: around 10% and slightly lower for  $x_\gamma > 0.8$ , between 11% and 15% for  $x_\gamma < 0.8$ . In the highest bin  $-0.70 < \cos\theta^* < 0.85$  – the model uncertainty also plays an important role with  $\lesssim 10\%$ . The hadronisation corrections are about the same

---

<sup>1</sup>The same is true for HERWIG.

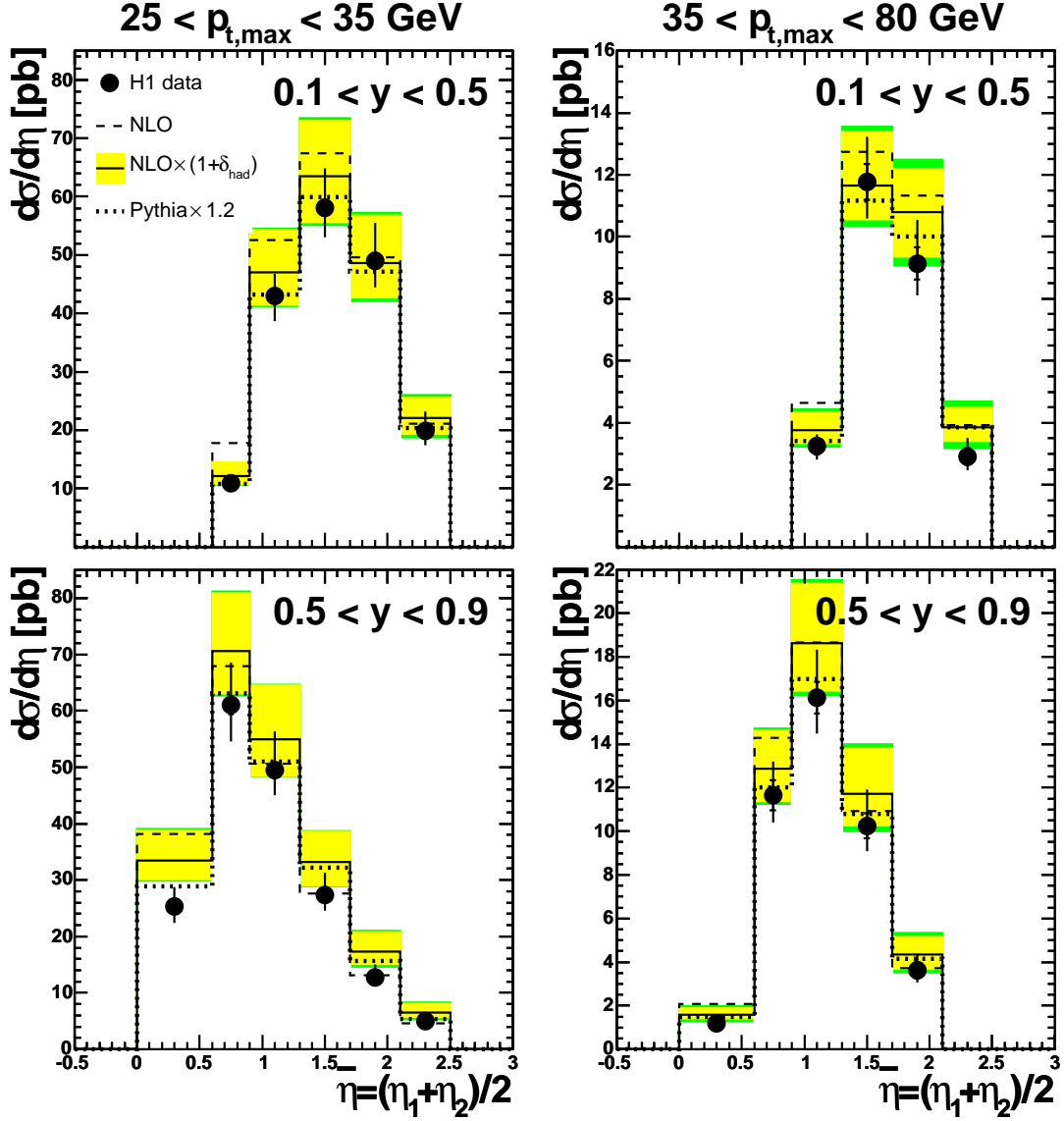


Figure 6.2: Cross sections in mean pseudorapidity of the two leading jets for data (points), NLO with (solid line) and without (dashed) hadronisation corrections  $\delta_{had}$  and for the PYTHIA LO generator (dotted) scaled by a factor of 1.2. The inner bar of the data points is the statistical, the outer the total uncertainty. The inner band of the  $NLO \times (1 + \delta_{had})$  result is the scale uncertainty, the outer band is the total uncertainty. The cross section is shown for two regions in transverse momentum of the leading jet and two regions in the inelasticity.

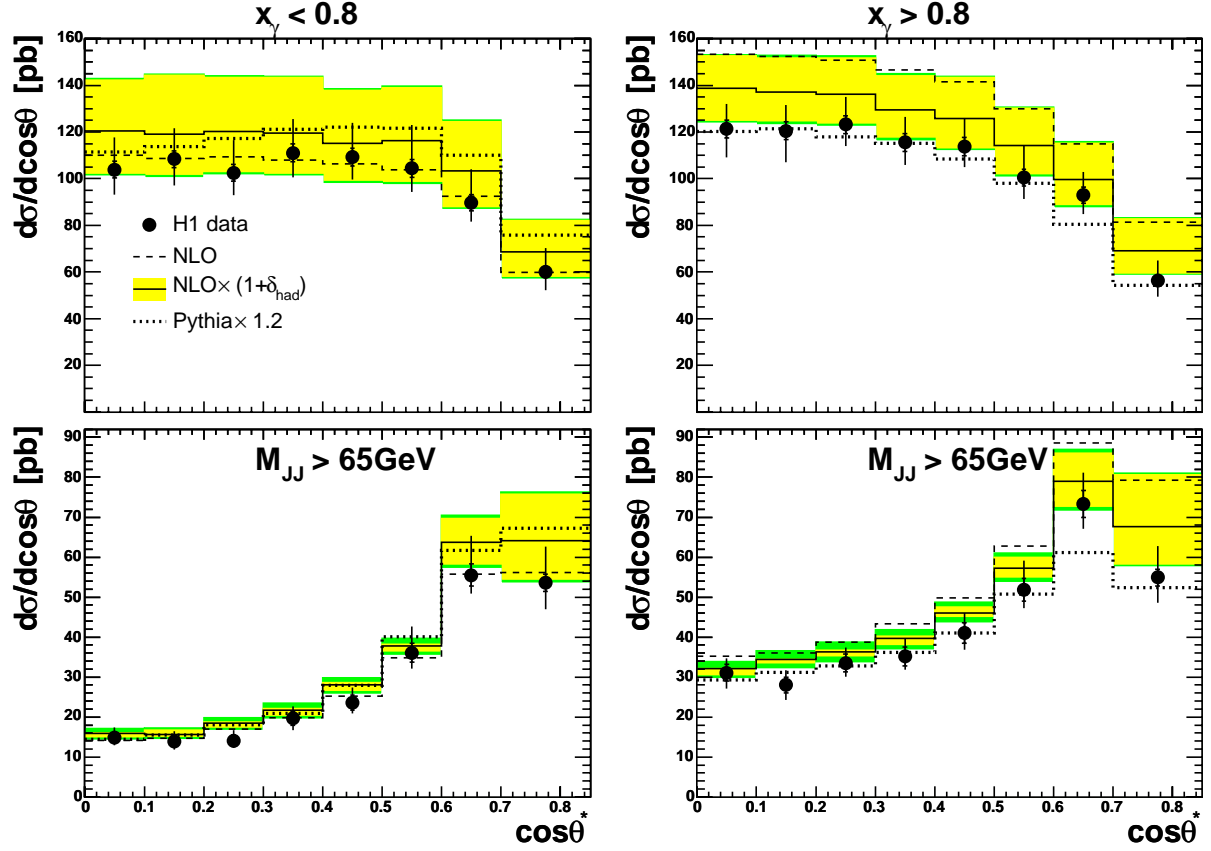


Figure 6.3: Cross sections in  $\cos\theta^*$  for data (points), NLO with (solid line) and without (dashed) hadronisation corrections  $\delta_{had}$  and for the PYTHIA LO generator (dotted) scaled by a factor of 1.2. The inner bar of the data points is the statistical, the outer the total uncertainty. The inner band of the  $NLO \times (1 + \delta_{had})$  result is the scale uncertainty, the outer band is the total uncertainty. The cross section is shown for two regions in  $x_\gamma$  enhancing the resolved (left) or direct (right) contribution and again with an additional cut on the invariant dijet mass applied.

size in both  $x_\gamma$  regions (10% at low and 15% at high  $\cos\theta^*$ ) but of opposite sign. Their model uncertainty is 4% or less, without increasing in the highest  $\cos\theta^*$  bin as in the case of the detector corrections. In the resolved enhanced case the corrections are upwards while for direct they are downwards. For  $x_\gamma < 0.8$  the drop of the cross section with decreasing angle between the jets and the  $\pm z$  direction in their centre-of-mass system starts later in Monte Carlo than in data, for the lowest values of  $\cos\theta^*$  (i.e. at angles between  $90^\circ$  and  $\approx 66^\circ$ ) the cross section even rises slightly.

The general shape of this cross section is different from what is to be expected by the matrix element. This is due to the cut in transverse jet momentum that plays a more important role the closer the jets get to the  $\pm z$  direction. In order to reduce this effect the cross section is also given with an additional cut on the dijet mass of  $M_{JJ} > 65$  GeV. Then the shape of the distributions is shifted to the expected form of the QCD matrix element revealing the different dominating

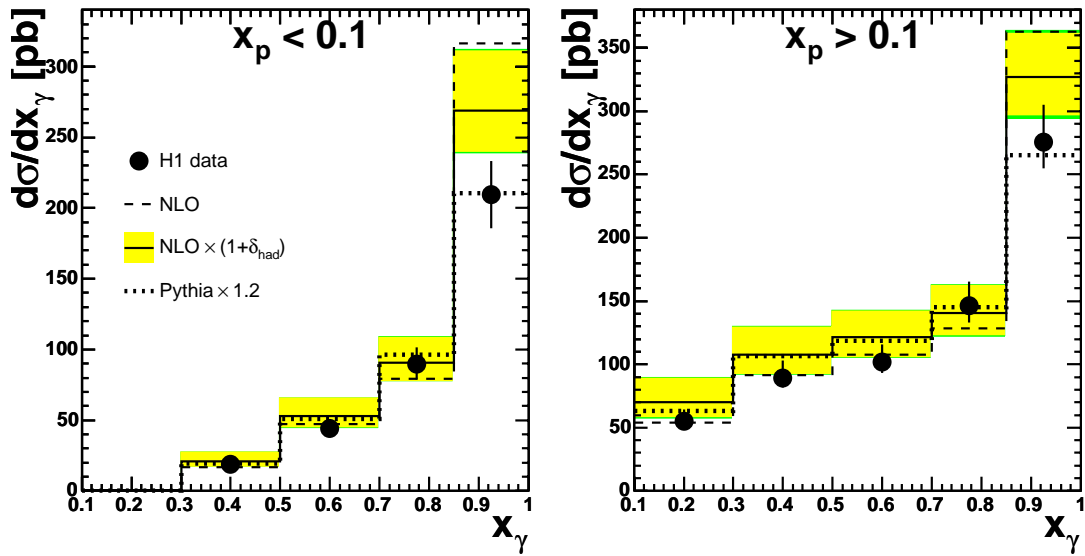


Figure 6.4: Cross sections in  $x_\gamma$  for data (points), NLO with (solid line) and without (dashed) hadronisation corrections  $\delta_{had}$  and for the PYTHIA LO generator (dotted) scaled by a factor of 1.2. The inner bar of the data points is the statistical, the outer the total uncertainty. The inner band of the  $NLO \times (1 + \delta_{had})$  result is the scale uncertainty, the outer band is the total uncertainty. The cross section is shown for two regions in  $x_p$ .

propagator for direct (quark propagator) and resolved (gluon propagator) events (c.f. figures 2.4 and 2.5). The hadronisation corrections stay the same after the  $M_{jj}$  cut but the uncertainties become smaller. In the region of low  $x_\gamma$  data to NLO agreement is outside one standard deviation for  $0.2 < \cos \theta^* < 0.3$  with  $1.3\sigma$ , in case of high  $x_\gamma$  it is  $1.2\sigma$  for  $0.1 < \cos \theta^* < 0.2$ . The rise at low to medium  $\cos \theta^*$  is steeper in NLO than in data. At high  $\cos \theta^*$  the rise is turned into a drop in the direct enhanced case. In the resolved enhanced case this turnover is not present in data and only hinted at in the NLO calculation. This can be interpreted as the  $M_{jj}$  cut being better suited in reducing the jet  $p_t$  cut effect at low  $x_\gamma$ .

The measurement of the dijet cross section as function of  $\cos \theta^*$  shows that the data reproduce the NLO predictions in two regions of  $x_\gamma$ . After the application of a cut on the invariant dijet mass, the different dynamics in the direct and resolved enhanced cases are distinguished.

Figure 6.4 shows the cross section as function of  $x_\gamma$  in two regions of  $x_p$ . For  $x_p < 0.1$  the fraction of events induced by gluons from the proton side is  $\gtrsim 70\%$  (c.f. figure 5.36). It decreases to 14% at the highest  $x_p$  reached in this analysis. Thus the two regions roughly distinguish between photon-gluon ( $x_p < 0.1$ ) and photon-quark ( $x_p > 0.1$ ) scattering.

The highest  $x_\gamma$  bin is dominated by direct processes, there the NLO predictions slightly overshoot the data for both  $x_p$  regions. At lower  $x_\gamma$  data and NLO are in perfect agreement for  $x_p < 0.1$  while for  $x_p > 0.1$  the data is still below the NLO result by up to 20% although within the given uncertainties except for the lowest  $x_\gamma$  where the agreement is within  $1.3\sigma$ . For the low  $x_p$  range the energy scale uncertainty of the LAr calorimeter is around 10%. The model uncertainty for

$0.5 < x_\gamma < 1.0$  is somewhat smaller in that regime. For  $x_p > 0.1$  the total uncertainty is mostly given by the LAr energy scale uncertainty alone. It decreases from 16% at low  $x_\gamma$  to 10% at  $0.85 < x_\gamma < 1.0$ . The uncertainty of the NLO prediction varies strongly between the low and the high end of the  $x_\gamma$  range. The scale uncertainty reaches 30% in the lowest  $x_\gamma$  bin for  $x_p < 0.1$  and 26% in the lowest  $x_\gamma$  bin for  $x_p > 0.1$ . The size of this uncertainty approximately halves for  $x_\gamma$  close to one. The PDF uncertainty is between 3% and 4% in the case of low  $x_p$  and between 4% and 7% for high  $x_p$ , reaching the largest value at  $0.1 < x_\gamma < 0.3$ . The model uncertainty of the hadronisation corrections is up to 4% for  $x_p < 0.1$  and up to 5% for  $x_p > 0.1$ , i.e. of comparable size to the PDF uncertainty. The leading order Monte Carlo predictions are similar to the NLO results except for the highest  $x_\gamma$  bin where they clearly below but agree better with the data.

Over the entire range in  $x_\gamma$  and in both regions of  $x_p$  NLO and data agree within uncertainties which are slightly larger for low  $x_p$ . There the proton structure is well determined from other processes<sup>2</sup> so that the resulting uncertainty from the proton PDFs is almost a factor of two smaller than for  $x_p > 0.1$ . But at low  $x_p$  the experimental uncertainties as well as the scale uncertainty of the NLO calculations are larger than at high  $x_p$ . To test the photon structure it is thus necessary to cover a wide range in  $x_p$  as done in this work. Note that the data point at  $0.3 < x_\gamma < 0.5$  for low  $x_p$  is new with respect to the analysis on the data taken in the years 1995 - 1997 [Car02].

The cross section as function of  $x_p$  is depicted in figure 6.5. Here the measurement is divided into two regions of  $x_\gamma$  corresponding to a division into resolved and direct enhanced samples. For  $x_\gamma > 0.8$  the photon enters the hard subprocess directly while for  $x_\gamma < 0.8$  mainly quarks enter the hard subprocess from the photon side as the gluon density of the resolved photon is small.

In both regions the agreement between data and NLO is within 10% at low  $x_p$  and thus clearly inside the given uncertainties, which are dominated by the uncertainty of the LAr energy scale which grows from slightly below 10% at low  $x_p$  to somewhat above 20% at high  $x_p$ . They are larger in the resolved enhanced sample. The two other significant contributions to the total uncertainty are the model uncertainty (5%) in the lowest  $x_p$  bin and the statistical uncertainty ( $\approx 20\%$ ) in the highest  $x_p$  bin. For the theoretical prediction the scale uncertainty is larger at low compared to high  $x_p$ . It reaches 23% in the resolved enhanced sample and 15% in the direct enhanced sample at  $0.05 < x_p < 0.10$ . For  $0.22 < x_p < 0.70$  it varies between 11% and 16% for the resolved events and between 7% and 9% for direct events. As expected the PDF uncertainty gets large at high  $x_p$ , reaching  $\approx 19\%$  at  $0.45 < x_p < 0.70$ . It is significantly larger than the scale uncertainty in that region. The model uncertainty is small –  $\lesssim 3\%$  – except for the highest values of  $x_p$ . It gets large – up to 12% – in the range of  $0.32 < x_p < 0.70$  for  $x_\gamma > 0.8$  and up to 7% for  $x_\gamma < 0.8$ . For  $x_p > 0.32$  discrepancies between data and NLO get larger than for low  $x_p$ , reaching a 40% difference at highest  $x_p$  which corresponds to  $1.08\sigma$  in the direct enhanced case and  $1.8\sigma$  in the resolved enhanced case. This region is very sensitive to the jet cuts (discussed in section 5.7.2) and of course the parametrisation of the proton PDF which will be discussed in more detail in section 6.2.

The region of  $x_\gamma > 0.8$  where the photon interacts directly with the proton is an ideal facility

---

<sup>2</sup>Like the HERA  $F_2$  proton structure function measurements for example.

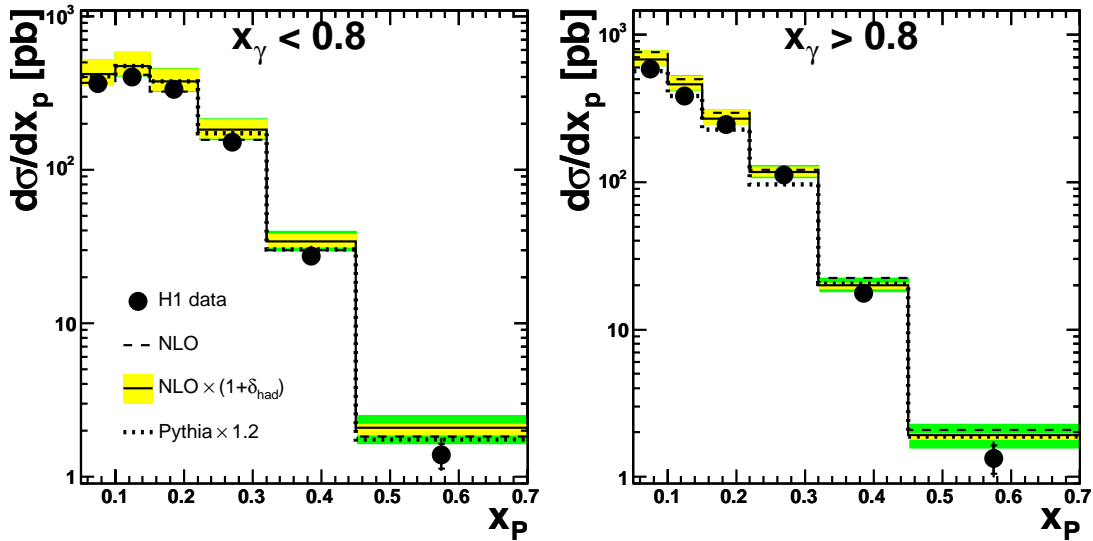


Figure 6.5: Cross sections in  $x_p$  for data (points), NLO with (solid line) and without (dashed) hadronisation corrections  $\delta_{had}$  and for the PYTHIA LO generator (dotted) scaled by a factor of 1.2. The inner bar of the data points is the statistical, the outer the total uncertainty. The inner band of the  $NLO \times (1 + \delta_{had})$  result is the scale uncertainty, the outer band is the total uncertainty. The cross section is shown for two regions in  $x_\gamma$  enhancing the resolved (left) or direct (right) contribution.

to test the proton structure as the photon structure plays no role here. Also the experimental uncertainties and the NLO scale uncertainty are smaller in this regime, yielding more stringent constraints on the proton PDFs than in the resolved enhanced sample. Only at high  $x_p$  the model uncertainty of the hadronisation corrections leads to total NLO uncertainties of similar size in both regions of  $x_\gamma$ . Clearly, going to higher orders will decrease the uncertainties at low  $x_p$  – with smaller scale uncertainties for NNLO perturbative QCD predictions of dijet cross sections – and high  $x_p$  – with smaller model uncertainties of the hadronisation corrections for MC@NLO. Note that this analysis introduces an additional data point at high  $x_p$  with respect to the previous analysis. While this new data point is statistically limited, the uncertainty of the second highest data point in this analysis is comparable to that of the analysis on 1995 - 1997 data but at half the bin width.

The same cross section is shown again in figure 6.6 as the ratio of the cross section in data over the cross section from the NLO calculations including hadronisation corrections. The relative uncertainty of the ratio is the sum of the total systematic uncertainty of the data cross section and the scale uncertainty of the NLO prediction. Again the cross section is divided into the two regions of  $x_\gamma$ . All four cut scenarios are represented, results corresponding to a cut of  $p_{t,2nd} > 15$  GeV are the black and  $p_{t,2nd} > 20$  GeV the grey points. The distinction in the  $\eta$  cut is presented as full circles for  $\eta_{jet} < 2.75$  and open circles for  $\eta_{jet} < 2.5$ .

For the resolved enhanced sample with the jet  $p_t$  cut at 15 GeV the ratio is closer to unity for low

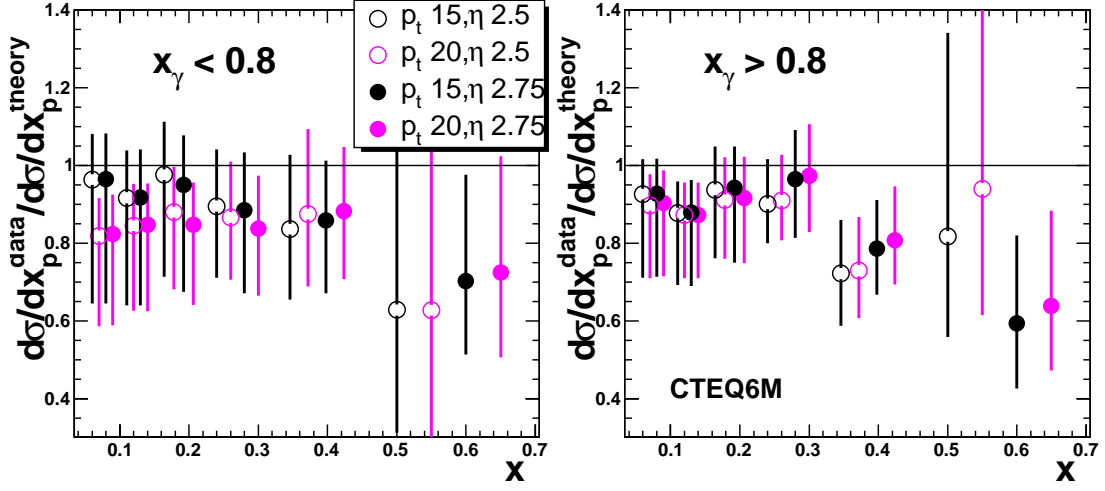


Figure 6.6: Ratio of the dijet cross section as function of  $x_p$  between Data and NLO for the different cut scenarios including uncertainties. Shown is the ratio obtained using the CTEQ6M proton PDF.

to medium values of  $x_p$ . At the highest  $x_p$  the higher cuts in pseudorapidity perform better. The uncertainties are of about the same size between both  $\eta$  cut values for  $x_p$  up to 0.32, while for larger values the uncertainties are smaller for  $\eta_{jet} < 2.75$ . This is due to the significantly smaller statistical uncertainty for the larger angular acceptance at highest  $x_p$ . The ratio is compatible with one within one sigma for  $x_p < 0.32$  and the  $p_{t,2nd} > 15$  GeV scenarios. For  $x_p > 0.45$  all four scenarios are compatible with one except for the  $p_{t,2nd} > 15$  GeV,  $\eta_{jet} < 2.75$  scenario that is slightly outside with  $1.1\sigma$ .

In the direct enhanced sample the spread between the results of all four jet cut scenarios is significantly smaller than in the resolved enhanced sample for  $x_p$  up to 0.22. For larger values of  $x_p$  an identical  $\eta$  cut yields a roughly identical cross section ratio of data to NLO predictions, where the agreement is better for the higher jet pseudorapidity cut except in the highest bin. Similar to the resolved enhanced sample the uncertainties are about the same for all scenarios. The only exception – again – is the bin at  $0.45 < x_p < 0.7$  where the uncertainties of the  $\eta_{jet} < 2.75$  scenarios are significantly smaller leading to a  $1.8\sigma$  and  $1.4\sigma$  deviation from one. There the  $\eta_{jet} < 2.5$  scenarios yield a ratio closer to unity. For the bin  $0.32 < x_p < 0.45$  the two  $\eta_{jet} < 2.75$  scenarios are slightly favoured but all four data to NLO ratios fail to lie within one sigma to unity with the largest deviation being  $2\sigma$  for the  $p_{t,2nd} > 15$  GeV,  $\eta_{jet} < 2.5$  combination. In the range of  $x_p < 0.32$  the data/NLO ratio is closest to one and agreement is reached for all scenarios except for the bin at  $0.1 < x_p < 0.15$  where all scenarios are within  $\approx 1.5\sigma$ .

The conclusion of this examination is that all four cut scenarios yield similar agreement between data and theory at better statistical precision than in the previous analysis, even more so in the case of extended angular acceptance which results in a higher cross section at largest values of  $x_p$ .

## 6.2 Using different PDFs

There are other PDFs on the market besides CTEQ6M, e.g. the older CTEQ5M [L<sup>+</sup>00] of the same group or the 1999 [MRST00] and 2001 [MRST02] parametrisations by the MRST group (c.f. section 2.2). The results obtained by those three proton PDFs as a function of  $x_p$  are depicted in figure 6.7 as a cross section ratio to the results from CTEQ6M that were shown in the previous section. Since the cross section derived from CTEQ6M slightly overshoots the data, ratios smaller than one in figure 6.7 mean better agreement with the measured cross section. First the cut scenario with  $p_{t,2nd} > 15$  GeV and  $\eta_{jet} < 2.75$  is discussed in detail (the uppermost two figures in 6.7). Differences in the other three scenarios will be highlighted afterwards.

For  $x_\gamma < 0.8$  results for all three PDFs are higher than those obtained using CTEQ6M in the range of  $x_p < 0.22$ . The largest deviation – when using CTEQ5M – is 7% which is much smaller than the scale uncertainty of around 20% in that region. Results from MRST1999c are closest to those of CTEQ6M here. Overall CTEQ5M yields the highest cross sections for  $x_p > 0.15$  compared to both MRST results. Except for the highest bin it is also larger than CTEQ6M. Deviations from CTEQ6M reach 15% at  $x_p > 0.45$  in case of MRST1999c. This is about the same size as the scale uncertainty in that bin but somewhat smaller than the PDF uncertainty of 19%.

A similar picture arises in the  $x_\gamma > 0.8$  case, the overall trends are comparable except at the highest  $x_p$ . There the result obtained by using CTEQ5M is closer to that of the two MRST parametrisations. They lie a bit closer to the CTEQ6M result than in the resolved enhanced case. In the direct enhanced sample the scale uncertainties are smaller – between 14% and 7% – and some of the results lie outside this range.

Looking at all jet cut scenarios the variations in the ratio for a given PDF are minimal for  $x_p$  values up to 0.22. That means all four cross sections calculated using the different PDFs exhibit a similar dependency on the jet cuts in that range of  $x_p$ . Above 0.22 the variations get larger and a maximum spread is reached in the highest bin. There CTEQ5M shows the highest variations: for  $p_{t,2nd} > 20$  GeV and  $\eta_{jet} < 2.5$  the ratio to CTEQ6M is  $\approx 1$ . while it is 0.83 in case of  $p_{t,2nd} > 15$  GeV and  $\eta_{jet} < 2.5$ .

Figure 6.8 shows again the ratio of the cross section in data over the cross section from the NLO calculations including hadronisation corrections, now for all proton PDFs used in this thesis. In the low  $x_p$  range up to values of 0.32 the newer fit by the CTEQ group means an improvement in the agreement between the theory cross section and the cross section measured in this analysis over their older fit. For  $x_p > 0.32$  differences between CTEQ6M and CTEQ5M are small except for the scenario of  $p_{t,2nd} > 15$  GeV and  $\eta_{jet} < 2.5$  in the direct enhanced sample where the ratio varies between 0.8 and 1.1. There also the uncertainties are largest.

The results of MRST2001c are rather similar to CTEQ5M for  $x_p < 0.22$ , while for the highest two bins in  $x_p$  they yield a slightly better agreement with data than both CTEQ parametrisations. There they are similar to the results obtained using MRST1999c which in turn perform minimally better in the range of  $x_p < 0.32$

It is noted that the differences in cross sections due to different proton PDFs are  $\lesssim 10\%$  and smaller than the experimental uncertainties. Therefore to summarise the studies of the proton PDFs it can be said that there is neither a parametrisation that is clearly favoured by the data over

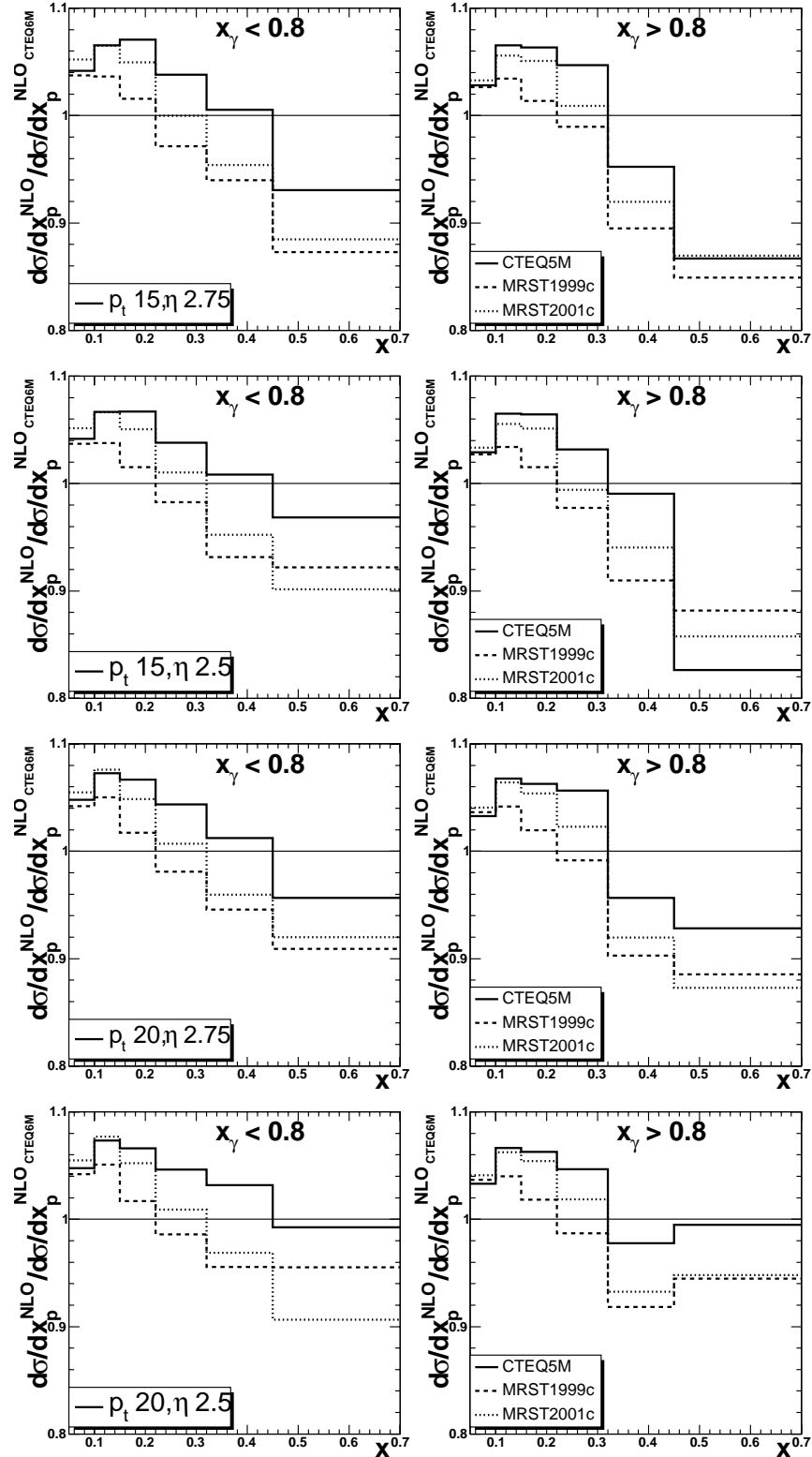


Figure 6.7: Ratio of the  $x_p$  NLO cross section between other PDFs and CTEQ6. Shown are CTEQ5M (solid), MRST1999c (dashed) and MRST2001c (dotted) for all four jet cut scenarios in two regions of  $x_\gamma$ .

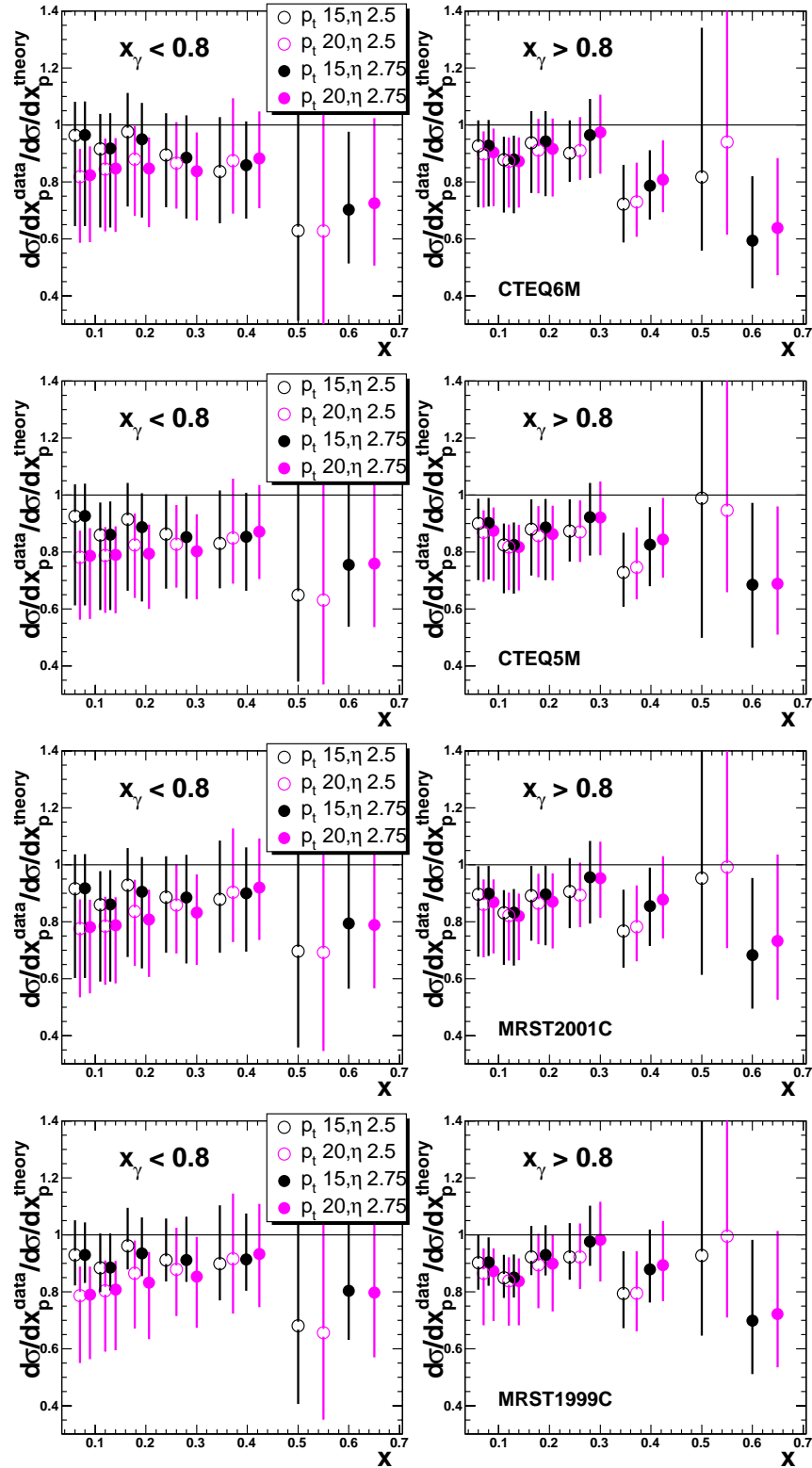


Figure 6.8: Ratio of Data to NLO in  $x_p$  for the different cut scenarios including uncertainties using (from top to bottom) the CTEQ6M, CTEQ5M, MRST2001c and MRST1999c proton PDFs.

the entire range of  $x_p$  nor is there a jet cut scenario that minimises the differences between data and NLO cross sections for all values of  $x_p$  and the two  $x_\gamma$  regions. The MRST parametrisations are slightly favoured at high  $x_p$  while at low  $x_p$  CTEQ6M performs best. In the medium range of  $0.22 < x_p < 0.32$  MRST1999c gives the overall best agreement to the data. For the different combinations of cuts on jet pseudorapidity and transverse momentum of the second leading jet the scenarios with  $p_{t,2nd} > 15$  GeV are favoured at low  $x_p$  and low  $x_\gamma$ . At the very high values of  $x_p$  the  $\eta_{jet} < 2.75$  scenarios agree slightly better with data for the resolved enhanced sample while the  $\eta_{jet} < 2.5$  scenarios are favoured for  $x_\gamma > 0.8$ .

Like in the case of the proton, also for the photon exist different parametrisations besides GRV-HO that is used as the default photon PDF in this analysis (c.f. section 2.2.1). As an additional parametrisation AFG-HO is chosen.

The ratio of the dijet cross section as a function of  $x_\gamma$  between AFG-HO and GRV-HO in all four cut scenarios and two regions of  $x_p$  is shown in figure 6.9. In all cases the results obtained using AFG-HO yield a higher cross section at  $x_\gamma > 0.85$  and a lower at  $x_\gamma < 0.85$ . The rise in cross section in the highest  $x_\gamma$  bin is of the order of 12% for small  $x_p$  and 14% at high  $x_p$  with the exception of the  $p_{t,2nd} > 15$  GeV,  $\eta_{jet} < 2.5$  scenario. There the difference is only 2%. For  $0.7 < x_\gamma < 0.85$  the AFG-HO cross section is less than  $\approx 10\%$  smaller than that using GRV-HO. In the range  $0.1 < x_\gamma < 0.7$  the ratios are between 0.8 and 0.9. For any given cut scenario the difference in the ratios between low and high  $x_p$  at each bin in  $x_\gamma$  are within  $\approx 6\%$  and less over the entire range. Note that the results in the two  $p_{t,2nd} > 20$  GeV scenarios are almost identical. Using AFG-HO instead of GRV-HO as photon PDFs yields differences in the theoretical predictions that are about the same size as the experimental uncertainties but somewhat smaller than the theoretical uncertainties.

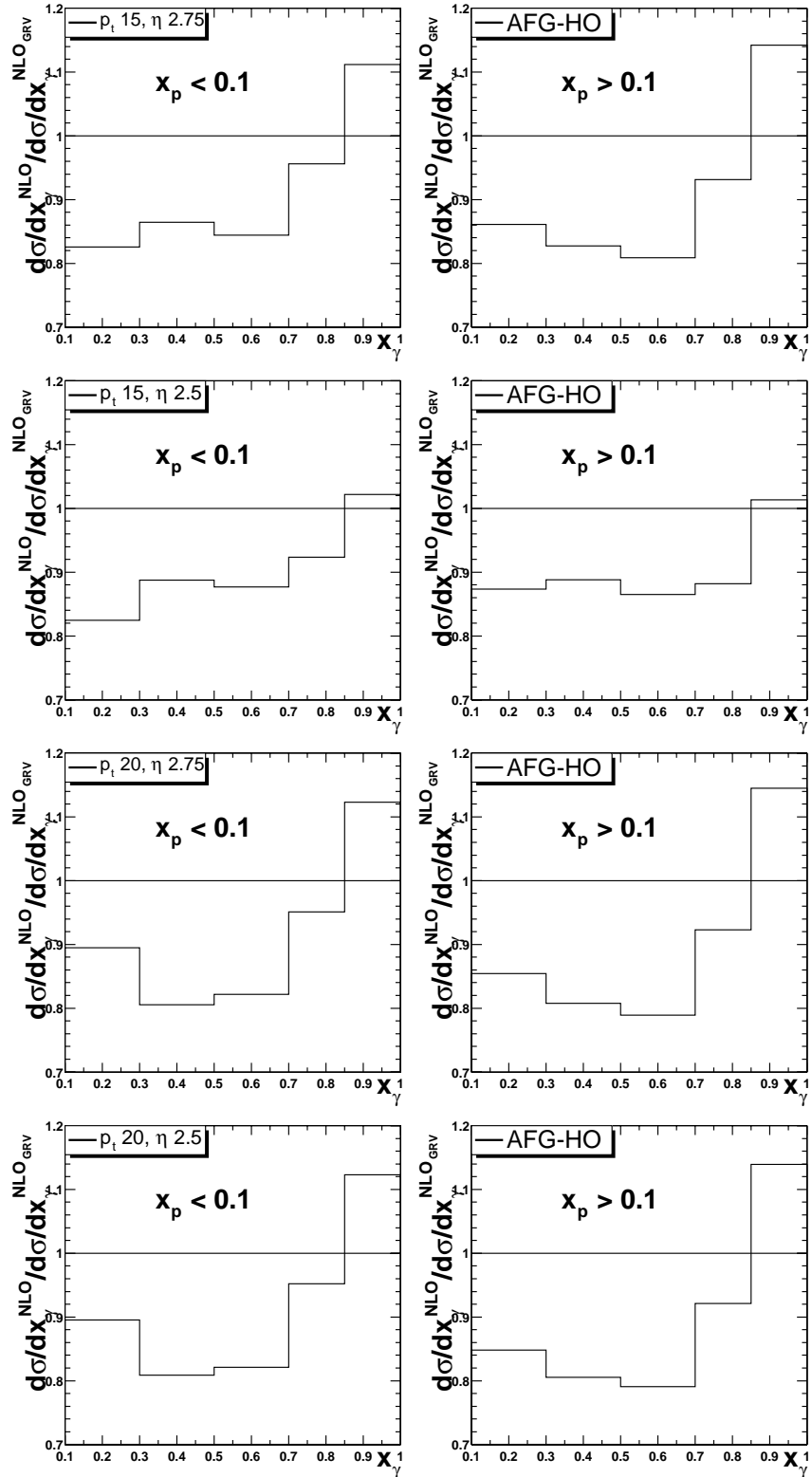


Figure 6.9: Ratio of the  $x_\gamma$  NLO cross section between AFG-HO and GRV-HO. Shown are all four jet cut scenarios in two regions of  $x_p$ .



# Chapter 7

## Conclusions and Outlook

### Summary

Differential cross section measurements of dijet production at high transverse momenta in photo-production were presented for various observables. The data in the phase space of  $Q^2 < 1 \text{ GeV}^2$  and  $0.1 < y < 0.9$  were compared to NLO pQCD calculations for two different ranges of jet angular acceptance and two choices of jet  $p_t$  cuts.

Invariant dijet masses up to 180 GeV and transverse momenta up to 80 GeV have been reached. The range covered in the reconstructed longitudinal momentum fraction entering the hard scatter from photon and proton side, respectively, are  $0.1 < x_\gamma < 1$  and  $0.05 < x_p < 0.7$ . Comparing the data to the NLO predictions shows good agreement in all measured cross sections over a wide kinematical range. This illustrates the strength of the factorisation property: even though the photon PDFs used in the theoretical calculations have been obtained from data at lower scales and in a different process, their QCD evolution to high scales is able to reproduce the data analysed in this work. The same is true for the proton PDFs that are mostly determined from entirely different measurements but still yield a good description of the data.

Compared to a previous H1 measurement this work profits from a factor two in statistics which is particularly helpful to reduce uncertainties in the boundary regions of the phase space such as high transverse momenta or high  $x_p$ . The dominant systematic uncertainty is still the energy scale of the main calorimeter that could not be reduced. Overall the total uncertainty of the measured cross sections is below that of the previous analysis and a more detailed record of the systematic effects is given. The cross section measurement as function of  $x_\gamma$  and  $x_p$  is extended towards lower  $x_\gamma$  and larger  $x_p$  due to the increased statistics. For the updated proton PDFs published by the CTEQ group, uncertainties of the theoretical predictions arising from the range of acceptable fits were estimated in addition to the scale uncertainty of the calculations. These PDF uncertainties were found to dominate at high jet transverse momenta and invariant dijet masses as well as at high  $x_p$ .

Differences between the results obtained from different PDF parametrisations are of the order of 20% in case of the photon PDFs and of the order of 10% in case of the proton PDF. These variations are within the experimental uncertainties so the data of this analysis does not clearly

(dis-)favour one parametrisation. Nevertheless these data are useful to further constrain the proton densities at high  $x_p$ .

### **Outlook**

Although the proton PDF parametrisations of different authors are steadily improving, the gluon density is poorly known for values of  $x_p \gtrsim 0.5$ . A better knowledge is clearly needed for the physics programs of the hadron colliders Tevatron and LHC. To put stronger constraints on the parton densities with the measurement of dijet cross sections with the H1 detector the uncertainties in both the measured data as well as the theoretical predictions need to be reduced. The statistical uncertainty of the data will decrease with the new data taken after the luminosity upgrade of the HERA accelerator. In the 2004 running period the integrated luminosity delivered by the collider is somewhat larger than that of the year 2000 running. With two more years to come the total data sample taken at 920 GeV proton beam energy will significantly lower the uncertainty at the highest values of  $x_p$  reached in this analysis.

Furthermore the systematic uncertainties need to be reduced. An improved algorithm to reconstruct the hadronic final state as well as a better hadronic calibration is being worked on that is expected to improve on the calorimeter energy scale, the dominant contribution to the systematic uncertainty.

From the theoretical side a new parametrisation [CJK04] of the parton distributions of the real photon is certainly of interest. A full next-to-next-to-leading (NNLO) order calculation of dijet cross sections is essential to decrease the scale uncertainty.

# Appendix A

## Summary Tables For Data

In the next four sections – one for each jet cut scenario – the data cross sections together with their uncertainties are presented in tabulated form. The individual contributions to the total uncertainty  $\delta_{tot}$  and their column labels are:

- $\delta_{stat}$ : statistical error of the data
- $\delta_{lar}$ : energy scale uncertainty of the LAr calorimeter
- $\delta_{spac}$ : energy scale uncertainty of the SpaCal calorimeter
- $\delta_{mod}$ : Monte Carlo model uncertainty of the corrections for detector effects
- $\delta_{rew}$ : uncertainty of the reweighting procedure in  $y_{JB}$  and  $\cos \theta^*$
- $\delta_{DIS}$ : uncertainty from the DIS background subtraction

Global contributions from the trigger efficiency correction (2%) and the luminosity measurement (1.5%) are also included in the total uncertainty. All individual contributions are added up in quadrature.

### A.1 Cross sections in data for $p_{t,2nd} > 15 \text{ GeV}$ , $-0.5 < \eta_{jet} < 2.75$

$\bar{p}_t$ [GeV]	$\frac{d\sigma}{d\bar{p}_t}$ [pb/GeV]	$\delta_{stat}$ [%]	$\delta_{tot}$ [%]	$\delta_{lar}$ [%]	$\delta_{spac}$ [%]	$\delta_{mod}$ [%]	$\delta_{rew}$ [%]	$\delta_{DIS}$ [%]
20-30	12.517	1.0	11.6/8.4	10.5/7.1	2.1/0.0	3.5	0.0/0.2	0.2
30-45	2.775	1.9	11.8/8.0	11.2/7.3	2.1/0.0	1.2	0.2/0.0	0.3
45-60	0.231	6.7	14.3/11.4	11.9/8.6	0.9/0.0	2.3	2.2/0.0	0.6
60-80	0.024	16.9	21.1/20.4	10.0/9.3	2.4/0.0	6.1	3.6/0.0	0.0

Table A.1: Data points and uncertainties for  $d\sigma/d\bar{p}_t$  in the  $p_{t,2nd} > 15 \text{ GeV}$ ,  $-0.5 < \eta_{jet} < 2.75$  cut scenario. Where two numbers are given per column they are to be read as  $+\delta/-\delta$ . A 2% uncertainty from the trigger efficiency correction plus 1.5% uncertainty from the luminosity measurement are also included in  $\delta_{tot}$ .

$M_{JJ}$ [GeV]	$\frac{d\sigma}{dM_{JJ}}$ [pb/GeV]	$\delta_{stat}$ [%]	$\delta_{tot}$ [%]	$\delta_{lar}$ [%]	$\delta_{spac}$ [%]	$\delta_{mod}$ [%]	$\delta_{rew}$ [%]	$\delta_{DIS}$ [%]
45-58	4.965	1.4	10.8/8.3	9.9/7.0	1.7/0.0	2.9	0.0/1.7	0.2
58-70	4.176	1.6	11.9/7.9	11.0/6.9	2.4/0.0	2.2	0.9/0.0	0.2
70-90	1.706	2.0	12.4/8.3	11.3/7.2	2.6/0.0	2.4	1.8/0.0	0.2
90-110	0.511	3.7	14.5/10.4	12.3/8.3	2.3/0.0	4.3	3.7/0.0	0.2
110-135	0.131	6.7	15.7/12.7	11.1/8.6	1.6/0.0	6.0	5.8/0.0	0.5
135-180	0.021	14.0	23.0/16.5	14.9/6.6	2.9/0.0	5.2	8.4/0.0	0.4

Table A.2: Data points and uncertainties for  $d\sigma/dM_{JJ}$  in the  $p_{t,2nd} > 15 \text{ GeV}$ ,  $-0.5 < \eta_{jet} < 2.75$  cut scenario. Where two numbers are given per column they are to be read as  $+\delta/-\delta$ . A 2% uncertainty from the trigger efficiency correction plus 1.5% uncertainty from the luminosity measurement are also included in  $\delta_{tot}$ .

$\bar{\eta}$	$\frac{d\sigma}{d\bar{\eta}}$ [pb]	$\delta_{stat}$ [%]	$\delta_{tot}$ [%]	$\delta_{lar}$ [%]	$\delta_{spac}$ [%]	$\delta_{mod}$ [%]	$\delta_{rew}$ [%]	$\delta_{DIS}$ [%]
$25 < p_{t,max} < 35 \text{ GeV}$ and $0.1 < y < 0.5$								
0.6-0.9	10.938	4.9	10.3/10.8	7.2/7.5	0.0/0.9	4.9	0.0/2.6	0.0
0.9-1.3	43.008	2.5	8.8/10.0	7.0/7.3	1.2/0.0	3.8	0.0/4.4	0.0
1.3-1.7	58.093	2.3	11.6/8.7	10.7/5.9	2.5/0.0	1.1	0.0/5.3	0.0
1.7-2.1	49.030	2.7	13.2/9.4	11.9/6.1	3.6/0.0	2.0	0.0/5.7	0.0
2.1-2.5	19.816	4.3	17.2/11.9	15.2/5.2	5.6/0.0	3.0	0.0/8.9	0.1
$35 < p_{t,max} < 80 \text{ GeV}$ and $0.1 < y < 0.5$								
0.9-1.3	3.244	8.1	12.0/13.6	7.3/9.1	0.0/0.9	4.3	0.0/3.2	0.0
1.3-1.7	11.764	4.9	12.5/10.1	10.8/7.0	2.4/0.0	2.0	0.0/4.4	0.0
1.7-2.1	9.140	5.6	15.4/11.3	13.4/7.0	3.4/0.0	3.0	0.0/5.7	0.1
2.1-2.5	2.916	9.3	20.1/15.3	16.8/7.2	3.8/0.0	3.5	0.0/9.0	0.0
$25 < p_{t,max} < 35 \text{ GeV}$ and $0.5 < y < 0.9$								
0.0-0.6	25.349	2.8	13.3/11.5	8.1/6.6	0.9/0.3	8.7	4.5/0.0	0.4
0.6-0.9	60.992	2.6	12.3/10.6	9.3/8.3	0.9/0.6	5.4	4.7/0.0	0.2
0.9-1.3	49.474	2.6	13.9/9.0	11.5/7.1	2.3/0.0	4.1	5.2/0.0	0.1
1.3-1.7	27.294	3.6	14.8/10.1	12.2/8.2	1.6/0.0	4.1	5.7/0.0	0.3
1.7-2.1	12.784	5.7	17.1/11.5	14.1/9.3	2.6/0.0	2.4	6.4/0.0	0.4
2.1-2.5	4.943	9.9	24.6/15.4	20.4/8.4	3.9/0.0	7.8	2.6/0.0	0.5
$35 < p_{t,max} < 80 \text{ GeV}$ and $0.5 < y < 0.9$								
0.0-0.6	1.178	11.4	27.3/24.6	10.3/10.6	0.4/0.7	18.8	12.1/0.0	1.2
0.6-0.9	11.656	6.0	13.3/10.8	8.9/7.7	0.6/0.2	3.6	6.5/0.0	0.7
0.9-1.3	16.132	4.5	13.7/10.1	10.4/7.6	1.6/0.0	4.3	5.5/0.0	0.5
1.3-1.7	10.254	5.6	16.1/11.3	13.2/9.1	2.5/0.0	2.9	5.7/0.0	0.5
1.7-2.1	3.619	10.0	21.4/15.6	16.4/10.0	3.1/0.0	6.1	5.9/0.0	1.4

Table A.3: Data points and uncertainties for  $d\sigma/\bar{\eta}$  in the  $p_{t,2nd} > 15 \text{ GeV}$ ,  $-0.5 < \eta_{jet} < 2.75$  cut scenario. Where two numbers are given per column they are to be read as  $+\delta/ - \delta$ . A 2% uncertainty from the trigger efficiency correction plus 1.5% uncertainty from the luminosity measurement are also included in  $\delta_{tot}$ .

$\cos \theta^*$	$\frac{d\sigma}{d\cos\theta^*}$ [pb]	$\delta_{stat}$ [%]	$\delta_{tot}$ [%]	$\delta_{lar}$ [%]	$\delta_{spac}$ [%]	$\delta_{mod}$ [%]	$\delta_{rew}$ [%]	$\delta_{DIS}$ [%]
$x_\gamma < 0.8$								
0.00-0.10	103.90	3.4	13.2/10.3	12.1/8.0	2.4/0.0	1.5	0.0/4.8	0.4
0.10-0.20	108.33	3.3	12.4/10.5	11.4/7.4	1.4/0.0	1.8	0.0/5.9	0.3
0.20-0.30	102.51	3.5	13.6/9.4	12.2/7.8	3.1/0.0	2.8	0.0/0.7	0.3
0.30-0.40	111.05	3.5	13.0/9.5	11.9/8.4	2.0/0.0	1.6	1.8/0.0	0.3
0.40-0.50	109.24	3.5	13.5/8.8	12.3/7.6	3.0/0.0	1.7	1.6/0.0	0.2
0.50-0.60	104.39	3.7	17.9/9.8	13.9/8.0	3.2/0.0	3.4	9.2/0.0	0.3
0.60-0.70	89.71	3.9	16.0/8.9	12.7/7.1	3.3/0.0	2.9	7.4/0.0	0.3
0.70-0.85	60.12	3.8	17.0/13.1	12.4/7.7	3.5/0.0	9.5	3.4/0.0	0.4
$x_\gamma > 0.8$								
0.00-0.10	121.28	3.1	8.8/10.1	7.7/6.6	0.8/0.0	1.3	0.0/6.3	0.1
0.10-0.20	120.51	3.1	9.2/11.2	8.2/7.4	0.9/0.0	1.3	0.0/7.3	0.0
0.20-0.30	123.15	3.1	9.7/7.5	8.7/5.8	1.3/0.0	1.3	0.0/2.3	0.0
0.30-0.40	115.56	3.3	9.5/8.3	8.2/6.9	1.1/0.2	2.1	0.0/0.1	0.1
0.40-0.50	113.72	3.4	10.9/7.7	9.8/6.2	1.7/0.0	1.4	0.0/0.7	0.2
0.50-0.60	100.45	3.6	13.7/9.2	9.9/6.2	2.0/0.0	5.3	6.2/0.0	0.1
0.60-0.70	92.86	3.8	10.9/8.6	8.6/6.7	1.3/0.0	2.9	3.6/0.0	0.2
0.70-0.85	56.40	3.7	15.3/12.4	10.8/6.7	3.0/0.0	9.4	0.0/0.7	0.2
$x_\gamma < 0.8$ and $M_{JJ} > 65$ GeV								
0.00-0.10	14.89	9.4	17.2/13.2	13.3/6.9	3.4/0.0	3.6	0.0/4.4	0.5
0.10-0.20	13.86	9.8	18.7/14.0	15.1/7.5	2.6/0.0	3.5	0.0/4.8	0.6
0.20-0.30	14.05	10.1	18.8/12.4	14.6/6.0	4.8/0.0	3.3	0.3/0.0	0.7
0.30-0.40	19.64	9.0	15.5/14.9	10.7/10.6	2.1/0.2	4.9	2.9/0.0	0.8
0.40-0.50	23.60	7.8	15.8/11.6	12.5/7.8	3.5/0.0	2.7	2.5/0.0	0.4
0.50-0.60	36.10	6.5	18.2/11.1	13.2/8.3	2.5/0.0	2.2	10.0/0.0	0.4
0.60-0.70	55.55	5.1	17.6/8.4	13.9/5.9	4.0/0.0	2.0	7.9/0.0	0.2
0.70-0.85	53.56	4.0	16.9/12.3	12.6/7.1	3.7/0.0	8.8	3.6/0.0	0.4
$x_\gamma > 0.8$ and $M_{JJ} > 65$ GeV								
0.00-0.10	31.07	6.7	11.8/12.6	9.0/8.4	0.6/0.0	2.6	0.0/5.5	0.0
0.10-0.20	28.00	6.9	13.1/13.5	9.3/7.6	0.6/0.0	5.4	0.0/6.3	0.1
0.20-0.30	33.51	6.7	11.7/10.3	8.9/6.8	1.1/0.0	2.5	0.0/1.5	0.0
0.30-0.40	35.17	6.6	12.4/9.6	9.7/6.1	2.0/0.0	2.3	1.0/0.0	0.2
0.40-0.50	41.04	6.2	12.3/10.2	9.9/7.3	1.4/0.0	2.2	0.0/0.0	0.4
0.50-0.60	51.84	5.5	14.0/8.9	9.9/6.2	2.8/0.0	2.1	6.9/0.0	0.1
0.60-0.70	73.31	4.6	10.6/8.5	8.2/6.4	0.7/0.4	1.9	3.8/0.0	0.1
0.70-0.85	54.91	3.9	14.4/11.4	10.7/6.8	3.0/0.0	7.9	0.0/0.6	0.2

Table A.4: Data points and uncertainties for  $d\sigma/\cos\theta^*$  in the  $p_{t,2nd} > 15$  GeV,  $-0.5 < \eta_{jet} < 2.75$  cut scenario. Where two numbers are given per column they are to be read as  $+\delta/ -\delta$ . A 2% uncertainty from the trigger efficiency correction plus 1.5% uncertainty from the luminosity measurement are also included in  $\delta_{tot}$ .

$x_\gamma$	$\frac{d\sigma}{dx_\gamma}$ [pb]	$\delta_{stat}$ [%]	$\delta_{tot}$ [%]	$\delta_{lar}$ [%]	$\delta_{spac}$ [%]	$\delta_{mod}$ [%]	$\delta_{rew}$ [%]	$\delta_{DIS}$ [%]
$x_p < 0.1$								
0.30-0.50	18.70	5.8	14.3/10.9	10.7/8.1	0.0/1.8	3.2	6.2/0.0	0.3
0.50-0.70	43.99	3.5	13.6/12.2	9.5/8.7	1.5/1.3	7.2	4.6/0.0	0.4
0.70-0.85	89.50	2.9	12.2/10.3	9.4/7.5	1.5/0.6	6.0	2.6/0.0	0.3
0.85-1.00	209.41	1.8	9.7/9.6	7.3/7.3	0.2/0.3	5.5	0.6/0.0	0.1
$x_p > 0.1$								
0.10-0.30	54.92	4.0	17.4/10.7	16.0/9.4	3.2/0.0	1.7	3.4/0.0	0.6
0.30-0.50	89.17	2.8	15.1/8.3	13.8/6.9	4.0/0.0	2.5	1.5/0.0	0.2
0.50-0.70	102.14	2.5	13.2/8.7	12.1/7.6	3.4/0.0	1.9	0.0/0.6	0.3
0.70-0.85	146.27	2.4	12.8/8.7	11.9/7.3	2.4/0.0	2.1	0.0/2.6	0.1
0.85-1.00	275.69	1.9	10.7/7.5	9.9/5.6	2.4/0.0	0.7	0.0/3.9	0.1

Table A.5: Data points and uncertainties for  $d\sigma/dx_\gamma$  in the  $p_{t,2nd} > 15 \text{ GeV}$ ,  $-0.5 < \eta_{jet} < 2.75$  cut scenario. Where two numbers are given per column they are to be read as  $+\delta/ - \delta$ . A 2% uncertainty from the trigger efficiency correction plus 1.5% uncertainty from the luminosity measurement are also included in  $\delta_{tot}$ .

$x_p$	$\frac{d\sigma}{dx_p}$ [pb]	$\delta_{stat}$ [%]	$\delta_{tot}$ [%]	$\delta_{lar}$ [%]	$\delta_{spac}$ [%]	$\delta_{mod}$ [%]	$\delta_{rew}$ [%]	$\delta_{DIS}$ [%]
$x_\gamma < 0.8$								
0.05-0.10	363.07	2.5	12.1/10.7	9.5/8.6	0.8/1.3	5.2	3.9/0.0	0.3
0.10-0.15	400.65	2.6	13.5/9.1	12.0/7.5	2.6/0.0	3.8	2.0/0.0	0.2
0.15-0.22	335.20	2.5	13.5/8.6	12.5/7.8	3.2/0.0	1.1	1.0/0.0	0.3
0.22-0.32	151.89	2.9	16.7/8.3	15.5/6.8	4.3/0.0	2.4	0.0/1.4	0.2
0.32-0.45	27.27	5.8	17.5/12.3	15.8/9.2	3.4/0.0	2.2	0.0/4.4	0.8
0.45-0.70	1.38	18.1	30.4/22.4	22.5/9.8	6.4/0.0	6.4	0.0/5.4	0.7
$x_\gamma > 0.8$								
0.05-0.10	583.43	1.9	9.6/9.2	7.7/7.2	0.5/0.2	4.8	0.1/0.0	0.1
0.10-0.15	383.75	2.6	9.6/8.3	8.5/6.5	1.3/0.0	2.2	0.0/2.8	0.1
0.15-0.22	247.13	2.9	11.2/7.8	10.1/5.5	2.8/0.0	1.2	0.0/3.8	0.1
0.22-0.32	111.90	3.7	12.9/8.6	11.6/5.1	2.9/0.0	2.1	0.0/4.9	0.1
0.32-0.45	17.57	8.1	15.3/13.2	11.8/7.8	3.8/0.0	2.9	0.0/5.9	0.0
0.45-0.70	1.34	21.8	30.4/26.8	19.8/12.1	1.9/0.7	6.9	0.0/6.6	0.0

Table A.6: Data points and uncertainties for  $d\sigma/dx_p$  in the  $p_{t,2nd} > 15 \text{ GeV}$ ,  $-0.5 < \eta_{jet} < 2.75$  cut scenario. Where two numbers are given per column they are to be read as  $+\delta/ - \delta$ . A 2% uncertainty from the trigger efficiency correction plus 1.5% uncertainty from the luminosity measurement are also included in  $\delta_{tot}$ .

## A.2 Cross sections in data for $p_{t,2nd} > 15 \text{ GeV}$ , $-0.5 < \eta_{jet} < 2.5$

$\bar{p}_t$ [GeV]	$\frac{d\sigma}{d\bar{p}_t}$ [pb/GeV]	$\delta_{stat}$ [%]	$\delta_{tot}$ [%]	$\delta_{lar}$ [%]	$\delta_{spac}$ [%]	$\delta_{mod}$ [%]	$\delta_{rew}$ [%]	$\delta_{DIS}$ [%]
20-30	11.158	1.0	11.2/8.4	10.1/7.0	1.9/0.0	3.8	0.0/0.2	0.2
30-45	2.471	2.0	11.3/7.8	10.6/7.1	2.0/0.0	0.8	0.2/0.0	0.3
45-60	0.220	6.8	14.3/10.9	11.9/7.7	1.4/0.0	2.3	1.8/0.0	0.7
60-80	0.025	17.2	21.5/20.4	10.0/8.8	3.5/0.0	6.2	2.9/0.0	0.0

Table A.7: Data points and uncertainties for  $d\sigma/d\bar{p}_t$  in the  $p_{t,2nd} > 15 \text{ GeV}$ ,  $-0.5 < \eta_{jet} < 2.5$  cut scenario. Where two numbers are given per column they are to be read as  $+\delta/-\delta$ . A 2% uncertainty from the trigger efficiency correction plus 1.5% uncertainty from the luminosity measurement are also included in  $\delta_{tot}$ .

$M_{JJ}$ [GeV]	$\frac{d\sigma}{dM_{JJ}}$ [pb/GeV]	$\delta_{stat}$ [%]	$\delta_{tot}$ [%]	$\delta_{lar}$ [%]	$\delta_{spac}$ [%]	$\delta_{mod}$ [%]	$\delta_{rew}$ [%]	$\delta_{DIS}$ [%]
45-58	4.651	1.4	10.8/8.4	9.6/6.9	1.7/0.0	3.4	0.0/1.8	0.2
58-70	3.758	1.7	11.3/7.9	10.4/6.9	2.2/0.0	2.2	1.1/0.0	0.2
70-90	1.433	2.2	12.0/8.3	10.6/7.1	2.5/0.0	2.6	2.4/0.0	0.2
90-110	0.394	4.3	14.7/10.0	12.4/7.8	2.7/0.0	3.7	4.1/0.0	0.2
110-135	0.092	8.4	16.0/10.9	11.3/5.6	1.9/0.0	2.9	6.1/0.0	0.8
135-180	0.014	16.4	23.5/18.8	12.5/6.2	4.8/0.0	6.1	7.7/0.0	0.0

Table A.8: Data points and uncertainties for  $d\sigma/dM_{JJ}$  in the  $p_{t,2nd} > 15 \text{ GeV}$ ,  $-0.5 < \eta_{jet} < 2.5$  cut scenario. Where two numbers are given per column they are to be read as  $+\delta/-\delta$ . A 2% uncertainty from the trigger efficiency correction plus 1.5% uncertainty from the luminosity measurement are also included in  $\delta_{tot}$ .

$\bar{\eta}$	$\frac{d\sigma}{d\bar{\eta}}$ [pb]	$\delta_{stat}$ [%]	$\delta_{tot}$ [%]	$\delta_{lar}$ [%]	$\delta_{spac}$ [%]	$\delta_{mod}$ [%]	$\delta_{rew}$ [%]	$\delta_{DIS}$ [%]
$25 < p_{t,max} < 35 \text{ GeV}$ and $0.1 < y < 0.5$								
0.6-0.9	10.960	4.9	10.3/11.1	7.0/7.5	0.0/0.6	5.3	0.0/3.1	0.0
0.9-1.3	42.791	2.5	8.9/10.1	7.0/7.1	1.1/0.3	4.1	0.0/4.7	0.0
1.3-1.7	53.781	2.4	11.3/8.5	10.4/5.7	2.4/0.0	1.1	0.0/5.0	0.0
1.7-2.1	37.950	3.1	13.0/9.8	11.6/5.8	3.8/0.0	2.4	0.0/6.4	0.0
2.1-2.5	9.918	6.2	18.0/13.7	14.3/5.0	7.4/0.0	4.6	0.0/9.9	0.0
$35 < p_{t,max} < 80 \text{ GeV}$ and $0.1 < y < 0.5$								
0.9-1.3	3.281	8.1	12.1/13.9	7.1/9.0	0.0/1.3	5.0	0.0/3.7	0.0
1.3-1.7	11.375	5.0	11.8/10.5	10.0/7.2	2.3/0.0	2.0	0.0/4.7	0.1
1.7-2.1	7.146	6.3	15.4/12.2	13.3/7.4	2.9/0.0	2.3	0.0/6.6	0.1
2.1-2.5	1.440	13.4	19.5/18.3	12.7/5.5	3.3/0.0	4.9	0.0/9.8	0.0
$25 < p_{t,max} < 35 \text{ GeV}$ and $0.5 < y < 0.9$								
0.0-0.6	25.344	2.8	13.0/11.4	8.2/6.8	0.7/0.3	8.4	3.9/0.0	0.4
0.6-0.9	60.952	2.6	12.0/10.4	9.1/8.2	1.1/0.4	5.2	4.4/0.0	0.2
0.9-1.3	47.863	2.6	13.8/8.7	11.5/7.1	2.3/0.0	3.5	5.2/0.0	0.1
1.3-1.7	22.703	4.0	15.6/10.2	13.1/8.1	1.8/0.0	4.0	5.5/0.0	0.2
1.7-2.1	9.672	6.9	17.6/11.1	15.1/7.8	2.6/0.0	2.8	3.9/0.0	0.5
2.1-2.5	2.375	14.8	26.1/16.7	19.0/1.0	6.5/0.0	7.2	0.0/0.0	0.6
$35 < p_{t,max} < 80 \text{ GeV}$ and $0.5 < y < 0.9$								
0.0-0.6	1.220	11.4	25.0/22.8	9.7/10.6	0.6/0.9	16.4	11.2/0.0	1.2
0.6-0.9	11.803	5.9	12.8/10.6	8.6/7.6	0.2/0.0	3.6	5.9/0.0	0.7
0.9-1.3	16.275	4.5	13.1/9.8	10.3/7.6	1.8/0.0	3.4	5.1/0.0	0.5
1.3-1.7	9.029	6.1	16.4/10.7	13.4/8.0	3.1/0.0	2.5	5.4/0.0	0.6
1.7-2.1	2.725	11.8	23.3/14.4	18.8/6.8	3.7/0.0	4.0	3.5/0.0	1.4

Table A.9: Data points and uncertainties for  $d\sigma/\bar{\eta}$  in the  $p_{t,2nd} > 15 \text{ GeV}$ ,  $-0.5 < \eta_{jet} < 2.5$  cut scenario. Where two numbers are given per column they are to be read as  $+\delta/ - \delta$ . A 2% uncertainty from the trigger efficiency correction plus 1.5% uncertainty from the luminosity measurement are also included in  $\delta_{tot}$ .

$\cos \theta^*$	$\frac{d\sigma}{d\cos\theta^*}$ [pb]	$\delta_{stat}$ [%]	$\delta_{tot}$ [%]	$\delta_{lar}$ [%]	$\delta_{spac}$ [%]	$\delta_{mod}$ [%]	$\delta_{rew}$ [%]	$\delta_{DIS}$ [%]
$x_\gamma < 0.8$								
0.00-0.10	100.52	3.5	13.3/10.1	12.2/7.5	2.4/0.0	1.6	0.0/5.0	0.4
0.10-0.20	100.55	3.5	11.5/10.6	10.3/8.2	2.2/0.4	1.8	0.0/4.8	0.3
0.20-0.30	93.84	3.7	13.0/9.0	11.8/7.5	2.4/0.0	2.2	0.0/0.9	0.3
0.30-0.40	99.51	3.6	12.4/10.0	11.1/8.9	1.6/0.0	1.6	2.1/0.0	0.4
0.40-0.50	93.78	3.7	12.8/9.1	11.5/7.6	2.5/0.0	2.1	1.7/0.0	0.3
0.50-0.60	88.21	4.0	17.5/9.3	13.4/7.0	3.1/0.0	3.9	8.8/0.0	0.3
0.60-0.70	71.43	4.5	17.4/9.0	13.0/6.9	3.6/0.0	2.5	9.4/0.0	0.3
0.70-0.85	39.60	4.8	19.4/14.8	12.9/7.3	4.5/0.0	11.7	4.8/0.0	0.4
$x_\gamma > 0.8$								
0.00-0.10	120.46	3.1	8.8/10.4	7.7/6.7	0.8/0.0	1.3	0.0/6.7	0.1
0.10-0.20	120.97	3.1	8.8/10.4	7.7/7.1	1.1/0.0	1.3	0.0/6.4	0.0
0.20-0.30	119.30	3.2	9.6/7.5	8.6/5.6	0.8/0.0	1.4	0.0/2.6	0.0
0.30-0.40	109.00	3.4	9.3/8.4	7.9/6.8	0.5/0.0	2.5	0.1/0.0	0.1
0.40-0.50	104.87	3.5	10.9/7.6	9.6/5.9	1.6/0.0	2.0	0.0/0.7	0.2
0.50-0.60	90.95	3.7	14.1/9.9	10.2/6.2	1.6/0.0	6.3	5.6/0.0	0.1
0.60-0.70	81.64	4.0	11.5/8.4	8.2/6.1	1.4/0.0	3.3	5.4/0.0	0.2
0.70-0.85	44.18	4.3	16.9/14.2	10.5/6.3	3.4/0.0	11.7	1.0/0.0	0.2
$x_\gamma < 0.8$ and $M_{JJ} > 65$ GeV								
0.00-0.10	15.13	9.5	17.0/13.5	12.9/7.0	3.5/0.0	3.7	0.0/4.6	0.3
0.10-0.20	12.49	10.6	17.8/14.1	13.2/7.3	3.1/0.0	3.6	0.0/3.6	0.7
0.20-0.30	12.00	11.1	18.7/13.5	13.7/6.2	4.2/0.0	3.4	0.0/0.0	0.8
0.30-0.40	18.42	9.4	14.8/15.5	8.7/10.5	1.8/0.3	5.7	3.3/0.0	0.9
0.40-0.50	20.19	8.4	14.8/11.7	10.8/7.1	3.0/0.0	2.9	2.6/0.0	0.4
0.50-0.60	30.61	7.1	18.5/11.2	13.1/7.9	3.8/0.0	2.5	9.7/0.0	0.3
0.60-0.70	42.68	5.9	18.9/8.5	13.6/5.0	4.3/0.0	2.3	10.2/0.0	0.2
0.70-0.85	35.74	5.1	18.8/13.3	12.9/6.5	5.3/0.0	10.1	5.1/0.0	0.4
$x_\gamma > 0.8$ and $M_{JJ} > 65$ GeV								
0.00-0.10	30.69	6.8	11.8/12.9	8.9/8.5	0.2/0.1	2.6	0.0/5.9	0.0
0.10-0.20	27.89	7.0	12.2/12.5	8.5/7.2	0.7/0.0	4.5	0.0/5.4	0.1
0.20-0.30	32.89	6.7	11.7/9.8	8.8/5.9	1.2/0.0	2.5	0.0/1.8	0.0
0.30-0.40	34.09	6.7	11.8/9.9	8.9/6.5	1.5/0.0	2.4	1.3/0.0	0.2
0.40-0.50	37.13	6.5	12.5/10.1	10.1/6.9	1.4/0.0	2.3	0.2/0.0	0.4
0.50-0.60	45.86	5.8	14.3/9.2	10.4/5.8	2.3/0.0	3.3	6.4/0.0	0.1
0.60-0.70	63.20	5.0	11.5/8.5	8.1/6.1	0.5/0.0	2.0	5.7/0.0	0.1
0.70-0.85	42.49	4.4	15.5/12.8	10.2/6.4	3.6/0.0	9.9	1.1/0.0	0.2

Table A.10: Data points and uncertainties for  $d\sigma/\cos\theta^*$  in the  $p_{t,2nd} > 15$  GeV,  $-0.5 < \eta_{jet} < 2.5$  cut scenario. Where two numbers are given per column they are to be read as  $+\delta/-\delta$ . A 2% uncertainty from the trigger efficiency correction plus 1.5% uncertainty from the luminosity measurement are also included in  $\delta_{tot}$ .

$x_\gamma$	$\frac{d\sigma}{dx_\gamma}$ [pb]	$\delta_{stat}$ [%]	$\delta_{tot}$ [%]	$\delta_{lar}$ [%]	$\delta_{spac}$ [%]	$\delta_{mod}$ [%]	$\delta_{rew}$ [%]	$\delta_{DIS}$ [%]
$x_p < 0.1$								
0.30-0.50	18.52	5.7	14.5/11.2	11.2/8.3	0.0/2.0	3.8	5.5/0.0	0.2
0.50-0.70	44.20	3.5	13.3/11.9	9.8/8.8	1.5/1.2	6.6	4.1/0.0	0.4
0.70-0.85	90.40	2.9	12.0/10.4	9.4/7.7	1.6/0.6	5.7	2.1/0.0	0.3
0.85-1.00	208.88	1.8	9.6/9.6	7.3/7.2	0.1/0.3	5.5	0.2/0.0	0.1
$x_p > 0.1$								
0.10-0.30	39.71	4.9	17.5/9.8	16.0/7.8	2.6/0.0	2.1	2.9/0.0	0.6
0.30-0.50	73.97	3.1	15.2/8.2	13.9/6.9	4.0/0.0	1.9	1.2/0.0	0.2
0.50-0.70	84.97	2.8	13.2/8.8	12.0/7.7	3.9/0.0	1.7	0.0/0.4	0.3
0.70-0.85	123.28	2.6	12.1/8.7	11.1/7.3	2.5/0.0	2.3	0.0/2.1	0.1
0.85-1.00	241.17	2.0	10.3/6.9	9.5/5.0	2.2/0.0	0.8	0.0/3.5	0.1

Table A.11: Data points and uncertainties for  $d\sigma/dx_\gamma$  in the  $p_{t,2nd} > 15 \text{ GeV}$ ,  $-0.5 < \eta_{jet} < 2.5$  cut scenario. Where two numbers are given per column they are to be read as  $+\delta/ - \delta$ . A 2% uncertainty from the trigger efficiency correction plus 1.5% uncertainty from the luminosity measurement are also included in  $\delta_{tot}$ .

$x_p$	$\frac{d\sigma}{dx_p}$ [pb]	$\delta_{stat}$ [%]	$\delta_{tot}$ [%]	$\delta_{lar}$ [%]	$\delta_{spac}$ [%]	$\delta_{mod}$ [%]	$\delta_{rew}$ [%]	$\delta_{DIS}$ [%]
$x_\gamma < 0.8$								
0.05-0.10	364.52	2.5	12.1/10.6	9.8/8.5	1.0/1.2	5.1	3.4/0.0	0.3
0.10-0.15	401.91	2.6	13.3/9.0	11.9/7.5	2.7/0.0	3.5	1.7/0.0	0.3
0.15-0.22	303.67	2.6	13.9/8.6	13.0/7.7	3.3/0.0	1.2	0.4/0.0	0.2
0.22-0.32	83.26	3.9	16.1/8.5	14.4/6.3	5.1/0.0	1.6	0.0/2.8	0.2
0.32-0.45	8.72	10.9	21.8/14.4	17.7/7.0	4.1/0.0	3.8	0.0/4.1	1.5
0.45-0.70	0.33	37.8	46.4/41.8	22.5/12.2	8.2/0.0	11.9	0.0/4.8	0.0
$x_\gamma > 0.8$								
0.05-0.10	583.30	1.9	9.6/9.2	7.7/7.1	0.4/0.2	4.8	0.0/0.3	0.1
0.10-0.15	384.01	2.6	9.2/7.9	8.1/6.2	1.1/0.0	2.2	0.0/2.6	0.1
0.15-0.22	229.13	3.0	11.8/7.1	10.6/4.7	3.1/0.0	1.2	0.0/3.4	0.1
0.22-0.32	70.29	4.7	12.6/8.5	10.9/4.2	3.1/0.0	1.8	0.0/4.8	0.0
0.32-0.45	8.51	11.2	18.1/15.8	12.9/8.5	3.8/0.0	3.8	0.0/5.7	0.0
0.45-0.70	0.80	27.7	36.8/31.7	20.9/9.7	6.8/0.0	10.0	0.0/5.9	0.0

Table A.12: Data points and uncertainties for  $d\sigma/dx_p$  in the  $p_{t,2nd} > 15 \text{ GeV}$ ,  $-0.5 < \eta_{jet} < 2.5$  cut scenario. Where two numbers are given per column they are to be read as  $+\delta/ - \delta$ . A 2% uncertainty from the trigger efficiency correction plus 1.5% uncertainty from the luminosity measurement are also included in  $\delta_{tot}$ .

### A.3 Cross sections in data for $p_{t,2nd} > 20 \text{ GeV}$ , $-0.5 < \eta_{jet} < 2.75$

$\bar{p}_t$ [GeV]	$\frac{d\sigma}{d\bar{p}_t}$ [pb/GeV]	$\delta_{stat}$ [%]	$\delta_{tot}$ [%]	$\delta_{lar}$ [%]	$\delta_{spac}$ [%]	$\delta_{mod}$ [%]	$\delta_{rew}$ [%]	$\delta_{DIS}$ [%]
20-30	10.137	1.2	11.1/7.2	10.1/6.0	2.4/0.0	2.8	0.0/0.4	0.1
30-45	2.792	1.9	11.8/7.6	11.0/6.8	2.4/0.0	1.4	0.6/0.0	0.3
45-60	0.236	6.7	14.5/10.8	11.9/7.8	2.1/0.0	2.3	2.8/0.0	0.6
60-80	0.024	16.9	21.4/21.2	9.8/10.9	3.1/0.0	6.3	4.6/0.0	0.0

Table A.13: Data points and uncertainties for  $d\sigma/d\bar{p}_t$  in the  $p_{t,2nd} > 20 \text{ GeV}$ ,  $-0.5 < \eta_{jet} < 2.75$  cut scenario. Where two numbers are given per column they are to be read as  $+\delta/-\delta$ . A 2% uncertainty from the trigger efficiency correction plus 1.5% uncertainty from the luminosity measurement are also included in  $\delta_{tot}$ .

$M_{JJ}$ [GeV]	$\frac{d\sigma}{dM_{JJ}}$ [pb/GeV]	$\delta_{stat}$ [%]	$\delta_{tot}$ [%]	$\delta_{lar}$ [%]	$\delta_{spac}$ [%]	$\delta_{mod}$ [%]	$\delta_{rew}$ [%]	$\delta_{DIS}$ [%]
45-58	4.103	1.6	10.1/7.0	9.2/5.8	2.0/0.0	2.1	0.0/1.5	0.1
58-70	3.902	1.7	11.7/7.4	10.7/6.3	2.7/0.0	2.3	1.1/0.0	0.2
70-90	1.624	2.1	12.1/7.7	11.1/6.5	2.6/0.0	2.3	0.3/0.0	0.2
90-110	0.492	3.8	13.3/9.2	11.9/7.5	2.8/0.0	2.8	0.4/0.0	0.2
110-135	0.130	6.7	15.3/12.3	11.9/8.3	2.0/0.0	5.5	2.5/0.0	0.5
135-180	0.020	14.0	21.8/17.0	14.2/7.6	3.1/0.0	5.4	5.8/0.0	0.4

Table A.14: Data points and uncertainties for  $d\sigma/dM_{JJ}$  in the  $p_{t,2nd} > 20 \text{ GeV}$ ,  $-0.5 < \eta_{jet} < 2.75$  cut scenario. Where two numbers are given per column they are to be read as  $+\delta/-\delta$ . A 2% uncertainty from the trigger efficiency correction plus 1.5% uncertainty from the luminosity measurement are also included in  $\delta_{tot}$ .

$\bar{\eta}$	$\frac{d\sigma}{d\bar{\eta}}$ [pb]	$\delta_{stat}$ [%]	$\delta_{tot}$ [%]	$\delta_{lar}$ [%]	$\delta_{spac}$ [%]	$\delta_{mod}$ [%]	$\delta_{rew}$ [%]	$\delta_{DIS}$ [%]
$25 < p_{t,max} < 35$ GeV and $0.1 < y < 0.5$								
0.6-0.9	8.943	6.4	9.1/10.6	5.2/7.4	0.0/1.1	2.9	0.5/0.0	0.0
0.9-1.3	37.479	3.0	9.0/8.4	7.3/5.9	1.2/0.0	3.3	0.0/3.1	0.0
1.3-1.7	50.486	2.7	11.1/7.5	10.1/4.7	2.3/0.0	1.2	0.0/4.5	0.0
1.7-2.1	42.244	3.0	13.4/7.5	12.1/4.8	4.0/0.0	1.2	0.0/4.0	0.0
2.1-2.5	17.386	4.8	16.7/9.9	14.6/4.6	5.8/0.0	2.1	0.0/6.7	0.0
$35 < p_{t,max} < 80$ GeV and $0.1 < y < 0.5$								
0.9-1.3	3.086	8.4	13.6/15.7	6.5/10.0	0.0/1.7	8.1	0.0/0.7	0.0
1.3-1.7	11.687	5.0	12.3/9.3	10.4/6.4	2.9/0.0	2.1	0.0/3.3	0.1
1.7-2.1	8.931	5.7	16.5/9.9	14.5/6.2	4.3/0.0	2.2	0.0/3.8	0.1
2.1-2.5	2.994	9.3	19.4/13.4	15.5/5.9	5.7/0.0	3.6	0.0/6.3	0.0
$25 < p_{t,max} < 35$ GeV and $0.5 < y < 0.9$								
0.0-0.6	21.728	3.5	11.7/9.0	7.6/5.9	0.9/0.0	5.2	5.7/0.0	0.3
0.6-0.9	52.057	3.1	11.1/9.2	8.5/6.9	1.4/0.0	4.5	3.6/0.0	0.1
0.9-1.3	39.668	3.1	12.9/9.0	11.3/7.3	2.3/0.0	3.5	2.3/0.0	0.1
1.3-1.7	21.149	4.2	13.3/9.4	11.1/7.2	2.9/0.0	3.7	2.5/0.0	0.2
1.7-2.1	9.412	6.7	16.5/9.6	13.0/5.7	4.6/0.0	2.7	4.8/0.0	0.3
2.1-2.5	3.570	12.2	22.7/13.6	17.5/3.5	4.9/0.0	4.2	3.3/0.0	0.4
$35 < p_{t,max} < 80$ GeV and $0.5 < y < 0.9$								
0.0-0.6	1.073	12.6	29.3/25.5	9.2/9.4	0.2/0.0	19.9	14.6/0.0	1.4
0.6-0.9	11.433	6.1	14.0/11.2	9.1/8.0	0.3/0.7	3.9	7.2/0.0	0.7
0.9-1.3	15.803	4.6	13.3/9.6	10.3/6.7	2.0/0.0	4.6	4.4/0.0	0.4
1.3-1.7	10.297	5.7	14.3/11.2	11.9/9.1	2.7/0.0	2.2	3.4/0.0	0.5
1.7-2.1	3.495	10.1	21.9/16.6	16.3/9.4	2.6/0.0	8.7	4.6/0.0	1.3

Table A.15: Data points and uncertainties for  $d\sigma/\bar{\eta}$  in the  $p_{t,2nd} > 20$  GeV,  $-0.5 < \eta_{jet} < 2.75$  cut scenario. Where two numbers are given per column they are to be read as  $+\delta/ - \delta$ . A 2% uncertainty from the trigger efficiency correction plus 1.5% uncertainty from the luminosity measurement are also included in  $\delta_{tot}$ .

$\cos \theta^*$	$\frac{d\sigma}{d\cos\theta^*}$ [pb]	$\delta_{stat}$ [%]	$\delta_{tot}$ [%]	$\delta_{lar}$ [%]	$\delta_{spac}$ [%]	$\delta_{mod}$ [%]	$\delta_{rew}$ [%]	$\delta_{DIS}$ [%]
$x_\gamma < 0.8$								
0.00-0.10	83.48	4.0	13.7/9.4	12.4/7.1	2.9/0.0	1.6	0.0/3.6	0.3
0.10-0.20	87.63	3.9	14.4/9.3	12.7/6.5	4.0/0.0	2.7	0.0/3.9	0.3
0.20-0.30	84.55	4.1	13.4/8.8	11.8/6.7	3.2/0.0	2.9	0.0/0.4	0.3
0.30-0.40	86.47	4.2	13.0/9.2	10.8/7.7	2.0/0.0	1.5	4.6/0.0	0.4
0.40-0.50	86.53	4.1	14.4/7.9	12.3/6.1	3.4/0.0	1.5	4.3/0.0	0.2
0.50-0.60	79.24	4.4	16.4/9.5	12.6/7.2	3.1/0.0	3.5	7.9/0.0	0.3
0.60-0.70	67.95	4.7	14.3/8.2	12.0/6.0	3.5/0.0	1.7	4.3/0.0	0.2
0.70-0.85	41.00	4.7	16.0/11.2	12.5/6.3	4.1/0.0	7.4	0.0/2.1	0.3
$x_\gamma > 0.8$								
0.00-0.10	115.45	3.4	9.3/9.0	8.0/6.1	1.1/0.0	1.8	0.0/4.7	0.1
0.10-0.20	115.47	3.4	8.8/9.5	7.6/6.5	0.9/0.0	1.4	0.0/5.2	0.0
0.20-0.30	115.92	3.5	10.0/7.1	8.8/5.2	1.6/0.0	1.4	0.0/1.9	0.0
0.30-0.40	112.36	3.6	10.4/7.3	8.6/5.4	1.7/0.0	2.0	2.8/0.0	0.1
0.40-0.50	107.94	3.8	10.8/7.4	9.2/5.7	2.1/0.0	1.5	2.0/0.0	0.2
0.50-0.60	93.32	3.9	12.9/8.8	9.7/6.1	2.0/0.0	4.4	5.2/0.0	0.0
0.60-0.70	85.60	4.2	11.6/8.1	10.1/6.1	1.6/0.0	2.1	1.1/0.0	0.1
0.70-0.85	51.30	4.1	13.6/11.7	10.6/6.1	3.2/0.0	6.1	0.0/6.2	0.2
$x_\gamma < 0.8$ and $M_{JJ} > 65$ GeV								
0.00-0.10	15.08	9.4	18.4/12.6	14.6/6.4	4.0/0.0	3.8	0.0/2.9	0.5
0.10-0.20	14.11	9.8	18.8/13.3	14.9/7.2	4.0/0.0	3.6	0.0/2.8	0.6
0.20-0.30	14.01	10.1	19.5/12.8	15.2/6.6	5.1/0.0	3.4	0.5/0.0	0.7
0.30-0.40	19.99	9.0	15.7/15.1	10.1/11.0	2.8/0.0	4.4	5.6/0.0	0.8
0.40-0.50	24.51	7.8	16.6/10.9	12.9/6.6	2.9/0.0	2.7	5.0/0.0	0.4
0.50-0.60	35.88	6.5	16.3/10.9	11.6/8.1	2.5/0.0	2.3	8.4/0.0	0.4
0.60-0.70	53.99	5.2	15.4/8.8	12.8/6.4	3.9/0.0	1.9	4.6/0.0	0.2
0.70-0.85	40.47	4.7	15.8/11.2	12.3/6.4	4.1/0.0	7.2	0.0/2.0	0.3
$x_\gamma > 0.8$ and $M_{JJ} > 65$ GeV								
0.00-0.10	31.02	6.7	12.6/10.9	10.0/6.6	0.9/0.0	2.7	0.0/3.8	0.0
0.10-0.20	28.98	6.9	13.7/11.9	10.3/6.7	1.3/0.0	5.0	0.0/4.1	0.1
0.20-0.30	33.74	6.7	11.5/10.0	8.5/6.5	1.4/0.0	2.6	0.0/1.1	0.0
0.30-0.40	35.84	6.6	13.2/9.2	9.9/5.3	2.3/0.0	2.7	4.0/0.0	0.2
0.40-0.50	42.47	6.2	11.9/10.2	9.0/7.3	1.1/0.0	2.3	2.8/0.0	0.4
0.50-0.60	51.85	5.5	13.8/9.0	10.5/6.3	2.4/0.0	2.1	5.8/0.0	0.1
0.60-0.70	72.37	4.6	11.0/8.2	9.3/6.0	1.0/0.3	1.9	1.2/0.0	0.1
0.70-0.85	51.36	4.1	13.6/11.6	10.8/6.1	3.2/0.0	6.0	0.0/6.2	0.2

Table A.16: Data points and uncertainties for  $d\sigma/\cos\theta^*$  in the  $p_{t,2nd} > 20$  GeV,  $-0.5 < \eta_{jet} < 2.75$  cut scenario. Where two numbers are given per column they are to be read as  $+\delta/-\delta$ . A 2% uncertainty from the trigger efficiency correction plus 1.5% uncertainty from the luminosity measurement are also included in  $\delta_{tot}$ .

$x_\gamma$	$\frac{d\sigma}{dx_\gamma}$ [pb]	$\delta_{stat}$ [%]	$\delta_{tot}$ [%]	$\delta_{lar}$ [%]	$\delta_{spac}$ [%]	$\delta_{mod}$ [%]	$\delta_{rew}$ [%]	$\delta_{DIS}$ [%]
$x_p < 0.1$								
0.30-0.50	10.86	8.7	15.1/15.1	7.5/10.8	0.0/4.3	3.4	8.7/0.0	0.0
0.50-0.70	29.64	4.7	15.4/12.5	10.2/7.9	2.1/0.8	8.1	6.0/0.0	0.3
0.70-0.85	68.62	3.7	11.2/8.5	8.9/6.6	1.7/0.0	3.0	3.8/0.0	0.3
0.85-1.00	194.87	2.1	9.2/8.8	7.0/6.7	0.4/0.3	4.7	1.6/0.0	0.1
$x_p > 0.1$								
0.10-0.30	38.26	5.0	17.7/9.3	15.6/7.2	4.3/0.0	1.7	4.0/0.0	0.5
0.30-0.50	71.03	3.2	14.9/7.8	13.3/6.3	4.4/0.0	2.1	1.8/0.0	0.2
0.50-0.70	87.49	2.8	13.3/8.0	11.9/6.6	3.9/0.0	2.4	0.0/0.7	0.3
0.70-0.85	129.35	2.6	12.4/8.1	11.4/6.5	2.7/0.0	1.9	0.0/2.8	0.0
0.85-1.00	270.49	1.9	11.1/6.9	10.3/5.1	2.6/0.0	0.8	0.0/3.3	0.1

Table A.17: Data points and uncertainties for  $d\sigma/dx_\gamma$  in the  $p_{t,2nd} > 20 \text{ GeV}$ ,  $-0.5 < \eta_{jet} < 2.75$  cut scenario. Where two numbers are given per column they are to be read as  $+\delta/-\delta$ . A 2% uncertainty from the trigger efficiency correction plus 1.5% uncertainty from the luminosity measurement are also included in  $\delta_{tot}$ .

$x_p$	$\frac{d\sigma}{dx_p}$ [pb]	$\delta_{stat}$ [%]	$\delta_{tot}$ [%]	$\delta_{lar}$ [%]	$\delta_{spac}$ [%]	$\delta_{mod}$ [%]	$\delta_{rew}$ [%]	$\delta_{DIS}$ [%]
$x_\gamma < 0.8$								
0.05-0.10	249.64	3.3	12.3/10.2	9.1/7.9	1.2/0.8	4.8	5.2/0.0	0.3
0.10-0.15	307.94	3.1	12.5/8.6	10.8/6.8	2.5/0.0	3.5	2.2/0.0	0.2
0.15-0.22	264.02	2.9	12.8/7.4	11.7/6.2	3.5/0.0	1.1	0.5/0.0	0.3
0.22-0.32	131.10	3.2	16.1/7.8	14.5/6.1	5.0/0.0	2.5	0.0/1.0	0.2
0.32-0.45	27.25	5.9	18.4/10.9	16.6/7.9	3.9/0.0	2.3	0.0/2.9	0.7
0.45-0.70	1.40	18.1	30.6/22.5	22.3/10.5	7.5/0.0	6.7	0.0/3.8	0.7
$x_\gamma > 0.8$								
0.05-0.10	542.09	2.2	9.2/8.8	7.4/7.0	0.3/0.3	4.2	1.0/0.0	0.1
0.10-0.15	370.10	2.8	9.6/7.8	8.5/6.2	1.3/0.0	1.9	0.0/2.3	0.1
0.15-0.22	236.42	3.0	11.6/7.2	10.4/4.6	3.0/0.0	1.2	0.0/3.7	0.1
0.22-0.32	111.63	3.8	13.5/7.8	12.1/4.3	3.5/0.0	1.5	0.0/4.5	0.1
0.32-0.45	17.75	8.1	16.7/12.2	13.2/7.1	4.9/0.0	2.9	0.0/4.3	0.0
0.45-0.70	1.37	21.8	30.4/26.0	19.5/11.0	2.4/0.0	7.2	0.0/4.5	0.0

Table A.18: Data points and uncertainties for  $d\sigma/dx_p$  in the  $p_{t,2nd} > 20 \text{ GeV}$ ,  $-0.5 < \eta_{jet} < 2.75$  cut scenario. Where two numbers are given per column they are to be read as  $+\delta/-\delta$ . A 2% uncertainty from the trigger efficiency correction plus 1.5% uncertainty from the luminosity measurement are also included in  $\delta_{tot}$ .

### A.4 Cross sections in data for $p_{t,2nd} > 20 \text{ GeV}$ , $-0.5 < \eta_{jet} < 2.5$

$\bar{p}_t$ [GeV]	$\frac{d\sigma}{d\bar{p}_t}$ [pb/GeV]	$\delta_{stat}$ [%]	$\delta_{tot}$ [%]	$\delta_{lar}$ [%]	$\delta_{spac}$ [%]	$\delta_{mod}$ [%]	$\delta_{rew}$ [%]	$\delta_{DIS}$ [%]
20-30	8.997	1.2	10.8/7.1	9.7/5.8	2.2/0.0	3.0	0.0/0.4	0.1
30-45	2.468	2.0	11.2/7.4	10.4/6.5	2.3/0.0	1.4	0.6/0.0	0.3
45-60	0.223	6.8	14.4/11.0	11.7/7.9	2.0/0.0	2.4	2.3/0.0	0.7
60-80	0.025	17.2	21.9/20.9	10.2/9.7	4.5/0.0	6.4	3.9/0.0	0.0

Table A.19: Data points and uncertainties for  $d\sigma/d\bar{p}_t$  in the  $p_{t,2nd} > 20 \text{ GeV}$ ,  $-0.5 < \eta_{jet} < 2.5$  cut scenario. Where two numbers are given per column they are to be read as  $+\delta/-\delta$ . A 2% uncertainty from the trigger efficiency correction plus 1.5% uncertainty from the luminosity measurement are also included in  $\delta_{tot}$ .

$M_{JJ}$ [GeV]	$\frac{d\sigma}{dM_{JJ}}$ [pb/GeV]	$\delta_{stat}$ [%]	$\delta_{tot}$ [%]	$\delta_{lar}$ [%]	$\delta_{spac}$ [%]	$\delta_{mod}$ [%]	$\delta_{rew}$ [%]	$\delta_{DIS}$ [%]
45-58	3.827	1.7	9.9/7.2	8.8/5.7	1.8/0.0	2.6	0.0/1.9	0.1
58-70	3.534	1.8	11.2/7.2	10.2/6.1	2.4/0.0	2.2	1.0/0.0	0.2
70-90	1.372	2.3	11.8/7.7	10.6/6.4	2.7/0.0	2.5	1.0/0.0	0.2
90-110	0.380	4.4	14.1/9.1	12.3/6.8	3.2/0.0	3.5	1.5/0.0	0.3
110-135	0.092	8.4	15.2/11.6	11.0/6.8	2.5/0.0	3.0	4.0/0.0	0.8
135-180	0.014	16.4	23.2/19.6	12.5/8.2	4.8/0.0	6.3	6.4/0.0	0.0

Table A.20: Data points and uncertainties for  $d\sigma/dM_{JJ}$  in the  $p_{t,2nd} > 20 \text{ GeV}$ ,  $-0.5 < \eta_{jet} < 2.5$  cut scenario. Where two numbers are given per column they are to be read as  $+\delta/-\delta$ . A 2% uncertainty from the trigger efficiency correction plus 1.5% uncertainty from the luminosity measurement are also included in  $\delta_{tot}$ .

$\bar{\eta}$	$\frac{d\sigma}{d\bar{\eta}}$ [pb]	$\delta_{stat}$ [%]	$\delta_{tot}$ [%]	$\delta_{lar}$ [%]	$\delta_{spac}$ [%]	$\delta_{mod}$ [%]	$\delta_{rew}$ [%]	$\delta_{DIS}$ [%]
$25 < p_{t,max} < 35$ GeV and $0.1 < y < 0.5$								
0.6-0.9	8.796	6.4	8.8/10.9	4.7/7.8	0.0/1.4	2.9	0.0/0.2	0.0
0.9-1.3	36.987	3.0	8.9/8.8	7.0/6.0	1.2/0.0	3.5	0.0/3.8	0.0
1.3-1.7	46.737	2.8	11.2/7.1	10.1/4.4	2.6/0.0	1.4	0.0/3.9	0.0
1.7-2.1	32.341	3.5	13.0/7.9	11.6/4.6	3.9/0.0	1.4	0.0/4.5	0.1
2.1-2.5	8.358	6.8	18.2/12.4	14.5/4.3	7.7/0.0	2.7	0.0/8.7	0.0
$35 < p_{t,max} < 80$ GeV and $0.1 < y < 0.5$								
0.9-1.3	36.987	3.0	8.9/8.8	7.0/6.0	1.2/0.0	3.5	0.0/3.8	0.0
1.3-1.7	46.737	2.8	11.2/7.1	10.1/4.4	2.6/0.0	1.4	0.0/3.9	0.0
1.7-2.1	32.341	3.5	13.0/7.9	11.6/4.6	3.9/0.0	1.4	0.0/4.5	0.1
2.1-2.5	8.358	6.8	18.2/12.4	14.5/4.3	7.7/0.0	2.7	0.0/8.7	0.0
$25 < p_{t,max} < 35$ GeV and $0.5 < y < 0.9$								
0.0-0.6	21.655	3.5	11.1/8.5	7.7/5.7	0.7/0.2	4.8	4.8/0.0	0.3
0.6-0.9	51.631	3.1	10.8/8.9	8.4/6.7	1.4/0.1	4.4	3.0/0.0	0.1
0.9-1.3	38.591	3.1	12.8/8.6	11.3/7.0	2.3/0.0	3.1	2.3/0.0	0.1
1.3-1.7	17.617	4.7	13.8/9.0	11.6/6.6	2.4/0.0	2.9	3.6/0.0	0.2
1.7-2.1	6.935	8.2	18.0/10.2	14.4/4.9	4.8/0.0	2.8	3.5/0.0	0.4
2.1-2.5	1.553	19.8	29.1/21.0	18.6/0.0	7.7/0.0	6.4	0.0/0.2	1.1
$35 < p_{t,max} < 80$ GeV and $0.5 < y < 0.9$								
0.0-0.6	1.076	12.6	29.9/27.0	9.3/10.4	1.2/0.0	21.3	13.6/0.0	1.4
0.6-0.9	11.455	6.1	13.3/10.7	8.9/7.6	0.2/0.7	3.5	6.4/0.0	0.7
0.9-1.3	15.708	4.6	13.1/9.4	10.2/6.6	2.3/0.0	4.3	3.9/0.0	0.4
1.3-1.7	8.843	6.2	14.7/11.2	11.9/8.7	3.5/0.0	2.3	3.8/0.0	0.6
1.7-2.1	2.681	12.1	22.7/15.7	17.5/8.3	4.7/0.0	4.8	3.6/0.0	1.5

Table A.21: Data points and uncertainties for  $d\sigma/\bar{\eta}$  in the  $p_{t,2nd} > 20$  GeV,  $-0.5 < \eta_{jet} < 2.5$  cut scenario. Where two numbers are given per column they are to be read as  $+\delta/ - \delta$ . A 2% uncertainty from the trigger efficiency correction plus 1.5% uncertainty from the luminosity measurement are also included in  $\delta_{tot}$ .

$\cos \theta^*$	$\frac{d\sigma}{d\cos\theta^*}$ [pb]	$\delta_{stat}$ [%]	$\delta_{tot}$ [%]	$\delta_{lar}$ [%]	$\delta_{spac}$ [%]	$\delta_{mod}$ [%]	$\delta_{rew}$ [%]	$\delta_{DIS}$ [%]
$x_\gamma < 0.8$								
0.00-0.10	80.01	4.1	13.5/9.8	12.2/7.0	2.9/0.0	1.6	0.0/4.6	0.3
0.10-0.20	79.34	4.1	14.6/9.0	12.8/6.4	4.0/0.0	2.8	0.0/3.0	0.3
0.20-0.30	75.73	4.3	12.9/8.6	11.3/6.5	2.6/0.0	2.7	0.0/0.7	0.3
0.30-0.40	76.46	4.4	11.9/9.7	9.6/8.1	1.1/0.7	1.6	4.5/0.0	0.5
0.40-0.50	73.02	4.5	13.7/8.2	11.6/6.0	3.1/0.0	2.4	3.7/0.0	0.2
0.50-0.60	66.13	4.8	16.2/9.3	12.6/6.6	3.5/0.0	3.4	7.1/0.0	0.3
0.60-0.70	53.43	5.5	15.9/8.3	11.6/5.3	4.0/0.0	1.9	7.9/0.0	0.2
0.70-0.85	26.47	6.0	16.3/11.3	12.3/5.6	4.4/0.0	7.3	0.0/0.4	0.3
$x_\gamma > 0.8$								
0.00-0.10	114.04	3.4	8.9/9.8	7.6/6.3	1.1/0.0	1.4	0.0/5.9	0.1
0.10-0.20	114.74	3.4	8.9/9.2	7.7/6.6	0.6/0.0	1.4	0.0/4.6	0.0
0.20-0.30	110.57	3.5	9.8/7.3	8.4/5.1	1.2/0.0	2.1	0.0/2.3	0.0
0.30-0.40	103.58	3.7	10.4/7.6	8.3/5.4	1.7/0.0	3.1	2.7/0.0	0.1
0.40-0.50	98.54	3.9	10.8/7.2	9.2/5.3	2.2/0.0	1.5	1.4/0.0	0.2
0.50-0.60	84.02	4.1	12.2/9.1	8.9/5.9	1.9/0.0	5.1	4.2/0.0	0.0
0.60-0.70	75.14	4.5	11.6/7.9	9.2/5.6	1.6/0.0	2.2	4.0/0.0	0.1
0.70-0.85	39.41	4.8	15.2/12.2	11.0/5.5	3.8/0.0	8.1	0.0/4.9	0.2
$x_\gamma < 0.8$ and $M_{JJ} > 65$ GeV								
0.00-0.10	14.98	9.5	17.3/13.6	13.4/7.6	2.7/0.0	3.9	0.0/3.9	0.3
0.10-0.20	12.80	10.6	18.8/13.8	14.2/7.3	4.2/0.0	3.8	0.0/1.8	0.7
0.20-0.30	11.75	11.2	18.8/13.3	13.5/5.5	5.1/0.0	3.6	0.2/0.0	0.8
0.30-0.40	18.49	9.4	15.7/15.1	9.6/10.4	2.2/0.2	4.9	5.6/0.0	0.9
0.40-0.50	20.29	8.5	15.9/11.6	11.7/6.8	3.4/0.0	2.9	4.3/0.0	0.4
0.50-0.60	30.36	7.1	16.7/11.1	12.0/7.7	3.7/0.0	2.5	7.7/0.0	0.3
0.60-0.70	41.92	6.1	17.5/9.0	12.8/5.6	5.1/0.0	2.2	8.3/0.0	0.2
0.70-0.85	25.95	6.1	16.2/11.3	12.1/5.8	4.5/0.0	7.1	0.0/0.4	0.3
$x_\gamma > 0.8$ and $M_{JJ} > 65$ GeV								
0.00-0.10	30.62	6.8	12.3/11.4	9.5/6.7	0.8/0.0	2.7	0.0/5.0	0.0
0.10-0.20	28.16	7.0	13.0/12.0	9.1/6.8	0.4/0.0	5.6	0.0/3.5	0.1
0.20-0.30	32.53	6.7	11.6/9.6	8.7/5.7	1.0/0.0	2.6	0.0/1.4	0.0
0.30-0.40	34.39	6.7	12.8/9.3	9.2/5.2	2.4/0.0	2.9	3.8/0.0	0.2
0.40-0.50	37.91	6.5	12.1/9.8	9.1/6.4	1.8/0.0	2.4	2.2/0.0	0.4
0.50-0.60	45.68	5.8	13.3/9.3	9.7/5.8	2.7/0.0	3.5	4.7/0.0	0.1
0.60-0.70	62.67	5.1	11.2/8.1	8.5/5.5	0.8/0.2	2.0	4.1/0.0	0.1
0.70-0.85	39.48	4.8	15.2/12.1	11.1/5.5	3.7/0.0	8.0	0.0/4.9	0.2

Table A.22: Data points and uncertainties for  $d\sigma/\cos\theta^*$  in the  $p_{t,2nd} > 20$  GeV,  $-0.5 < \eta_{jet} < 2.5$  cut scenario. Where two numbers are given per column they are to be read as  $+\delta/ -\delta$ . A 2% uncertainty from the trigger efficiency correction plus 1.5% uncertainty from the luminosity measurement are also included in  $\delta_{tot}$ .

$x_\gamma$	$\frac{d\sigma}{dx_\gamma}$ [pb]	$\delta_{stat}$ [%]	$\delta_{tot}$ [%]	$\delta_{lar}$ [%]	$\delta_{spac}$ [%]	$\delta_{mod}$ [%]	$\delta_{rew}$ [%]	$\delta_{DIS}$ [%]
$x_p < 0.1$								
0.30-0.50	10.92	8.7	14.6/15.0	7.6/10.8	0.0/3.8	3.4	7.8/0.0	0.0
0.50-0.70	29.40	4.7	14.9/12.2	10.1/7.6	2.0/0.7	7.9	5.1/0.0	0.3
0.70-0.85	68.22	3.7	10.9/8.3	8.9/6.4	1.8/0.3	2.8	3.1/0.0	0.3
0.85-1.00	193.12	2.1	8.9/8.7	6.8/6.6	0.2/0.3	4.7	0.9/0.0	0.1
$x_p > 0.1$								
0.10-0.30	25.78	6.3	18.6/9.8	16.1/6.6	4.7/0.0	2.1	3.8/0.0	0.8
0.30-0.50	59.52	3.6	14.3/7.5	12.8/5.9	4.0/0.0	1.4	1.7/0.0	0.2
0.50-0.70	73.13	3.1	13.6/7.6	12.2/6.1	4.0/0.0	2.1	0.0/0.2	0.3
0.70-0.85	108.78	2.8	12.1/8.2	10.9/6.5	2.8/0.0	2.3	0.0/2.3	0.1
0.85-1.00	234.59	2.1	10.8/6.6	9.9/4.7	2.7/0.0	1.0	0.0/3.0	0.1

Table A.23: Data points and uncertainties for  $d\sigma/dx_\gamma$  in the  $p_{t,2nd} > 20$  GeV,  $-0.5 < \eta_{jet} < 2.5$  cut scenario. Where two numbers are given per column they are to be read as  $+\delta/ - \delta$ . A 2% uncertainty from the trigger efficiency correction plus 1.5% uncertainty from the luminosity measurement are also included in  $\delta_{tot}$ .

$x_p$	$\frac{d\sigma}{dx_p}$ [pb]	$\delta_{stat}$ [%]	$\delta_{tot}$ [%]	$\delta_{lar}$ [%]	$\delta_{spac}$ [%]	$\delta_{mod}$ [%]	$\delta_{rew}$ [%]	$\delta_{DIS}$ [%]
$x_\gamma < 0.8$								
0.05-0.10	246.85	3.3	11.8/10.1	8.8/7.8	1.0/0.8	4.9	4.4/0.0	0.3
0.10-0.15	308.32	3.1	12.7/8.2	11.2/6.5	2.6/0.0	3.1	1.7/0.0	0.2
0.15-0.22	246.19	3.0	13.2/7.4	12.1/6.2	3.6/0.0	1.1	0.4/0.0	0.2
0.22-0.32	75.82	4.2	16.4/7.7	14.6/5.5	5.5/0.0	1.6	0.0/1.6	0.3
0.32-0.45	8.66	10.9	23.8/14.1	19.8/7.0	5.8/0.0	3.9	0.0/2.8	1.5
0.45-0.70	0.31	37.8	44.1/42.2	18.4/13.3	3.7/0.0	12.5	0.0/3.5	0.0
$x_\gamma > 0.8$								
0.05-0.10	538.36	2.2	9.0/8.7	7.2/6.9	0.3/0.4	4.1	0.3/0.0	0.1
0.10-0.15	368.88	2.8	9.6/7.7	8.4/5.8	1.3/0.0	2.4	0.0/2.4	0.1
0.15-0.22	219.67	3.1	12.0/6.8	10.7/4.2	3.5/0.0	1.2	0.0/3.2	0.1
0.22-0.32	68.99	4.7	12.8/7.8	10.8/3.7	3.9/0.0	1.8	0.0/4.0	0.0
0.32-0.45	8.58	11.2	17.9/15.1	12.5/8.0	4.0/0.0	3.9	0.0/4.3	0.0
0.45-0.70	0.75	27.7	43.1/30.3	29.9/4.2	9.0/0.0	10.4	0.0/4.4	0.0

Table A.24: Data points and uncertainties for  $d\sigma/dx_p$  in the  $p_{t,2nd} > 20$  GeV,  $-0.5 < \eta_{jet} < 2.5$  cut scenario. Where two numbers are given per column they are to be read as  $+\delta/ - \delta$ . A 2% uncertainty from the trigger efficiency correction plus 1.5% uncertainty from the luminosity measurement are also included in  $\delta_{tot}$ .



# Appendix B

## Summary Tables For NLO Predictions

In the next four sections – one for each jet cut scenario – the NLO cross sections together with their uncertainties are presented in tabulated form for the choice of GRV-HO for the photon PDF and CTEQ6M for the proton PDF. The cross sections are given with (“ $\times C_{had}$ ”) and without (no extra label) hadronisation corrections applied. The individual contributions to the total uncertainty  $\delta_{tot}$  and their column labels are:

- $\delta_{scale}$ : uncertainty from simultaneous variation of the renormalisation and factorisation scales up and down by a factor of two
- $\delta_{pdf}$ : uncertainty estimated by using the CTEQ6 eigenvector PDF sets of the proton
- $\delta_{mod}$ : Monte Carlo model uncertainty of the hadronisation corrections

The individual contributions are added up in quadrature.

### B.1 Cross sections in NLO calculations for $p_{t,2nd} > 15 \text{ GeV}$ , $-0.5 < \eta_{jet} < 2.75$

$\bar{p}_t$ [GeV]	$\frac{d\sigma}{d\bar{p}_t} \times C_{had} [\frac{\text{pb}}{\text{GeV}}]$	$\frac{d\sigma}{d\bar{p}_t} [\frac{\text{pb}}{\text{GeV}}]$	$\delta_{tot}$ [%]	$\delta_{scale}$ [%]	$\delta_{pdf}$ [%]	$\delta_{mod}$ [%]
20-30	14.394	14.558	21.079/15.169	20.888/14.903	2.792	0.470
30-45	3.001	3.089	4.360/7.222	2.660/6.342	3.385	0.690
45-60	0.268	0.282	7.581/9.728	1.370/6.248	7.104	2.266
60-80	0.027	0.029	12.571/12.862	1.070/2.922	10.943	6.093

Table B.1: Data points and uncertainties for  $d\sigma/d\bar{p}_t$  in the  $p_{t,2nd} > 15 \text{ GeV}$ ,  $-0.5 < \eta_{jet} < 2.75$  cut scenario. Where two numbers are given per column they are to be read as  $+\delta/ -\delta$ .

$M_{JJ}$ [GeV]	$\frac{d\sigma}{dM_{JJ}} \times C_{had} [\frac{\text{pb}}{\text{GeV}}]$	$\frac{d\sigma}{dM_{JJ}} [\frac{\text{pb}}{\text{GeV}}]$	$\delta_{tot}$ [%]	$\delta_{scale}$ [%]	$\delta_{pdf}$ [%]	$\delta_{mod}$ [%]
45-58	5.747	5.892	24.927/17.462	24.774/17.244	2.672	0.659
58-70	4.793	4.820	11.237/10.025	10.893/9.637	2.678	0.678
70-90	2.002	2.005	9.289/9.693	8.628/9.061	3.342	0.823
90-110	0.599	0.613	9.488/9.072	7.955/7.455	4.944	1.516
110-135	0.153	0.158	8.456/10.483	4.426/7.615	6.733	2.564
135-180	0.020	0.022	13.105/15.458	0.000/8.198	12.134	4.949

Table B.2: Data points and uncertainties for  $d\sigma/dM_{JJ}$  in the  $p_{t,2nd} > 15$  GeV,  $-0.5 < \eta_{jet} < 2.75$  cut scenario. Where two numbers are given per column they are to be read as  $+\delta/-\delta$ .

$\bar{\eta}$	$\frac{d\sigma}{d\bar{\eta}} \times C_{had}$ [pb]	$\frac{d\sigma}{d\bar{\eta}}$ [pb]	$\delta_{tot}$ [%]	$\delta_{scale}$ [%]	$\delta_{pdf}$ [%]	$\delta_{mod}$ [%]
$25 < p_{t,max} < 35$ GeV and $0.1 < y < 0.5$						
0.6-0.9	12.162	17.817	19.052/15.055	18.518/14.373	3.628	2.625
0.9-1.3	46.925	52.554	15.957/13.026	15.605/12.591	3.117	1.190
1.3-1.7	65.668	67.442	15.647/13.801	14.976/13.035	3.945	2.232
1.7-2.1	50.080	49.597	17.688/14.000	16.854/12.931	4.970	2.022
2.1-2.5	22.267	21.105	18.177/16.361	15.791/13.662	8.800	1.898
$35 < p_{t,max} < 80$ GeV and $0.1 < y < 0.5$						
0.9-1.3	3.381	4.645	17.985/15.941	15.356/12.902	5.829	7.328
1.3-1.7	11.207	12.742	16.309/11.663	15.061/9.841	5.720	2.541
1.7-2.1	10.543	11.337	15.636/16.501	12.905/13.941	8.547	2.214
2.1-2.5	3.566	3.915	21.578/19.312	16.184/13.011	13.150	5.545
$25 < p_{t,max} < 35$ GeV and $0.5 < y < 0.9$						
0.0-0.6	32.246	38.097	16.754/11.895	16.115/10.977	3.947	2.326
0.6-0.9	70.321	67.961	14.901/11.736	14.547/11.285	2.983	1.226
0.9-1.3	56.114	50.592	17.487/12.902	17.166/12.463	3.059	1.329
1.3-1.7	32.641	27.615	16.568/14.248	16.120/13.725	3.456	1.645
1.7-2.1	16.002	13.078	22.017/17.062	20.297/14.776	6.031	6.034
2.1-2.5	5.629	4.648	27.763/22.287	24.041/17.432	7.587	11.630
$35 < p_{t,max} < 80$ GeV and $0.5 < y < 0.9$						
0.0-0.6	1.247	2.088	26.084/24.224	18.267/15.496	5.979	17.633
0.6-0.9	12.172	14.291	14.468/13.218	13.665/12.335	2.901	3.764
0.9-1.3	17.720	18.660	15.573/13.302	14.597/12.144	4.253	3.373
1.3-1.7	11.017	10.931	19.393/15.346	17.675/13.108	6.776	4.215
1.7-2.1	4.043	3.726	22.731/21.436	19.223/17.672	11.168	4.739

Table B.3: Data points and uncertainties for  $d\sigma/\bar{\eta}$  in the  $p_{t,2nd} > 15$  GeV,  $-0.5 < \eta_{jet} < 2.75$  cut scenario. Where two numbers are given per column they are to be read as  $+\delta/-\delta$ .

B.1. CROSS SECTIONS IN NLO CALCULATIONS FOR  $P_{T,2ND} > 15 \text{ GEV}$ ,  $-0.5 < \eta_{JET} < 2.75$

$\cos \theta^*$	$\frac{d\sigma}{d\cos\theta^*} \times C_{had}$ [pb]	$\frac{d\sigma}{d\cos\theta^*}$ [pb]	$\delta_{tot}$ [%]	$\delta_{scale}$ [%]	$\delta_{pdf}$ [%]	$\delta_{mod}$ [%]
$x_\gamma < 0.8$						
0.00-0.10	118.57	110.08	18.61/16.28	18.04/15.63	4.29	1.59
0.10-0.20	119.88	108.66	21.68/15.59	21.26/14.99	3.98	1.58
0.20-0.30	120.11	109.44	19.80/15.59	19.21/14.84	4.53	1.58
0.30-0.40	121.24	107.94	20.42/15.43	20.03/14.91	3.64	1.62
0.40-0.50	120.74	106.45	20.40/15.08	19.79/14.24	3.85	3.12
0.50-0.60	114.93	103.75	20.19/16.29	19.57/15.52	4.65	1.67
0.60-0.70	106.68	92.53	20.97/16.22	20.39/15.47	4.37	2.16
0.70-0.85	71.27	59.86	20.47/17.06	19.77/16.23	4.57	2.64
$x_\gamma > 0.8$						
0.00-0.10	135.32	153.34	10.43/10.76	10.03/10.37	2.35	1.63
0.10-0.20	134.51	152.41	11.48/10.35	10.66/9.42	4.07	1.30
0.20-0.30	131.75	150.66	12.09/10.13	11.54/9.47	2.85	2.19
0.30-0.40	124.10	146.67	11.96/10.30	11.26/9.48	2.81	2.88
0.40-0.50	123.89	141.60	14.43/10.91	14.01/10.35	3.15	1.41
0.50-0.60	111.04	129.92	14.47/11.84	13.93/11.18	3.43	1.89
0.60-0.70	100.50	114.89	16.29/12.41	15.60/11.48	4.40	1.65
0.70-0.85	69.64	81.39	20.38/15.35	19.86/14.66	4.21	1.74
$x_\gamma < 0.8$ and $M_{JJ} > 65 \text{ GeV}$						
0.00-0.10	16.13	14.22	7.75/10.80	1.23/7.62	6.62	3.84
0.10-0.20	15.06	14.68	10.24/8.38	7.53/4.69	5.90	3.66
0.20-0.30	18.43	17.02	6.83/10.40	1.17/7.93	5.79	3.43
0.30-0.40	23.24	19.89	7.91/10.68	1.93/7.43	6.65	3.82
0.40-0.50	29.10	25.29	6.25/8.54	2.14/6.20	5.17	2.78
0.50-0.60	38.10	34.79	5.23/6.53	1.07/4.05	4.58	2.29
0.60-0.70	65.46	55.80	10.47/10.35	9.23/9.10	4.50	2.04
0.70-0.85	66.69	56.15	18.99/16.56	18.19/15.64	4.75	2.64
$x_\gamma > 0.8$ and $M_{JJ} > 65 \text{ GeV}$						
0.00-0.10	31.66	35.17	5.18/8.02	0.00/6.13	4.50	2.56
0.10-0.20	32.58	36.08	6.24/7.19	0.00/3.57	4.99	3.76
0.20-0.30	35.22	38.74	6.84/7.69	1.27/3.74	6.27	2.43
0.30-0.40	37.63	43.35	5.72/7.22	1.67/4.71	4.11	3.61
0.40-0.50	45.88	49.76	5.80/5.56	3.15/2.69	4.35	2.18
0.50-0.60	55.53	62.76	6.69/6.33	4.91/4.41	4.10	1.97
0.60-0.70	78.72	88.52	9.98/9.58	8.82/8.37	4.31	1.81
0.70-0.85	68.32	79.25	19.80/15.00	19.26/14.28	4.25	1.74

Table B.4: Data points and uncertainties for  $d\sigma/\cos\theta^*$  in the  $p_{t,2nd} > 15 \text{ GeV}$ ,  $-0.5 < \eta_{jet} < 2.75$  cut scenario. Where two numbers are given per column they are to be read as  $+\delta/-\delta$ .

$x_\gamma$	$\frac{d\sigma}{dx_\gamma} \times C_{had}$ [pb]	$\frac{d\sigma}{dx_\gamma}$ [pb]	$\delta_{tot}$ [%]	$\delta_{scale}$ [%]	$\delta_{pdf}$ [%]	$\delta_{mod}$ [%]
$x_p < 0.1$						
0.30-0.50	18.92	16.80	30.54/21.01	30.11/20.38	4.06	3.12
0.50-0.70	51.95	47.46	23.49/17.31	23.21/16.94	3.08	1.81
0.70-0.85	82.76	79.26	20.35/15.96	19.76/15.19	3.20	3.71
0.85-1.00	253.99	316.46	15.89/11.70	15.57/11.27	3.03	0.87
$x_p > 0.1$						
0.10-0.30	66.73	53.99	27.13/20.66	25.68/18.71	6.98	5.30
0.30-0.50	103.78	91.56	20.93/15.60	20.27/14.71	5.07	1.24
0.50-0.70	119.47	107.73	17.61/14.62	16.70/13.50	4.49	3.34
0.70-0.85	136.92	128.24	15.67/14.02	15.10/13.38	4.04	1.15
0.85-1.00	317.23	362.63	11.22/10.41	10.44/9.56	4.04	0.72

Table B.5: Data points and uncertainties for  $d\sigma/dx_\gamma$  in the  $p_{t,2nd} > 15$  GeV,  $-0.5 < \eta_{jet} < 2.75$  cut scenario. Where two numbers are given per column they are to be read as  $+\delta/-\delta$ .

$x_p$	$\frac{d\sigma}{dx_p} \times C_{had}$ [pb]	$\frac{d\sigma}{dx_p}$ [pb]	$\delta_{tot}$ [%]	$\delta_{scale}$ [%]	$\delta_{pdf}$ [%]	$\delta_{mod}$ [%]
$x_\gamma < 0.8$						
0.05-0.10	402.39	369.52	22.77/17.05	22.53/16.73	3.02	1.27
0.10-0.15	460.98	414.76	21.47/16.03	21.14/15.59	3.53	1.20
0.15-0.22	365.17	322.71	20.91/15.81	20.37/15.10	4.55	1.15
0.22-0.32	180.53	156.18	17.54/15.85	15.93/14.04	7.23	1.32
0.32-0.45	33.86	29.89	15.40/15.97	9.77/10.65	11.67	2.35
0.45-0.70	2.05	1.82	20.86/23.55	5.30/12.14	18.92	7.02
$x_\gamma > 0.8$						
0.05-0.10	646.11	760.80	14.36/11.55	13.96/11.05	2.89	1.76
0.10-0.15	441.90	498.89	13.70/11.05	13.23/10.47	3.35	1.09
0.15-0.22	262.53	295.61	13.27/11.40	12.60/10.61	3.99	1.16
0.22-0.32	113.32	120.63	9.79/10.97	7.13/8.68	6.55	1.44
0.32-0.45	20.03	22.40	12.30/14.36	2.01/7.68	9.55	7.49
0.45-0.70	1.89	2.08	21.37/23.01	1.32/8.62	17.57	12.09

Table B.6: Data points and uncertainties for  $d\sigma/dx_p$  in the  $p_{t,2nd} > 15$  GeV,  $-0.5 < \eta_{jet} < 2.75$  cut scenario. Where two numbers are given per column they are to be read as  $+\delta/-\delta$ .

B.2. CROSS SECTIONS IN NLO CALCULATIONS FOR  $P_{T,2ND} > 15 \text{ GeV}$ ,  $-0.5 < \eta_{JET} < 2.5117$

## B.2 Cross sections in NLO calculations for $p_{t,2nd} > 15 \text{ GeV}$ , $-0.5 < \eta_{jet} < 2.5$

$\bar{p}_t$ [GeV]	$\frac{d\sigma}{d\bar{p}_t} \times C_{had} [\frac{\text{pb}}{\text{GeV}}]$	$\frac{d\sigma}{d\bar{p}_t} [\frac{\text{pb}}{\text{GeV}}]$	$\delta_{tot}$ [%]	$\delta_{scale}$ [%]	$\delta_{pdf}$ [%]	$\delta_{mod}$ [%]
20-30	12.763	13.062	20.789/14.897	20.613/14.650	2.655	0.491
30-45	2.697	2.783	4.125/6.869	2.731/6.134	3.005	0.724
45-60	0.247	0.262	7.018/9.299	1.191/6.216	6.443	2.515
60-80	0.026	0.028	12.234/12.461	0.826/2.509	10.537	6.160

Table B.7: Data points and uncertainties for  $d\sigma/d\bar{p}_t$  in the  $p_{t,2nd} > 15 \text{ GeV}$ ,  $-0.5 < \eta_{jet} < 2.5$  cut scenario. Where two numbers are given per column they are to be read as  $+\delta/ - \delta$ .

$M_{JJ}$ [GeV]	$\frac{d\sigma}{dM_{JJ}} \times C_{had} [\frac{\text{pb}}{\text{GeV}}]$	$\frac{d\sigma}{dM_{JJ}} [\frac{\text{pb}}{\text{GeV}}]$	$\delta_{tot}$ [%]	$\delta_{scale}$ [%]	$\delta_{pdf}$ [%]	$\delta_{mod}$ [%]
45-58	5.379	5.560	24.341/17.202	24.186/16.982	2.631	0.785
58-70	4.300	4.362	10.708/9.537	10.384/9.171	2.517	0.706
70-90	1.697	1.716	8.546/8.708	7.970/8.144	2.956	0.876
90-110	0.463	0.479	7.953/8.220	6.366/6.696	4.471	1.654
110-135	0.107	0.112	7.717/10.492	2.015/7.389	6.861	2.902
135-180	0.013	0.014	12.663/14.248	0.000/6.532	11.219	5.872

Table B.8: Data points and uncertainties for  $d\sigma/dM_{JJ}$  in the  $p_{t,2nd} > 15 \text{ GeV}$ ,  $-0.5 < \eta_{jet} < 2.5$  cut scenario. Where two numbers are given per column they are to be read as  $+\delta/ - \delta$ .

$\bar{\eta}$	$\frac{d\sigma}{d\bar{\eta}} \times C_{had}$ [pb]	$\frac{d\sigma}{d\bar{\eta}}$ [pb]	$\delta_{tot}$ [%]	$\delta_{scale}$ [%]	$\delta_{pdf}$ [%]	$\delta_{mod}$ [%]
$25 < p_{t,max} < 35$ GeV and $0.1 < y < 0.5$						
0.6-0.9	12.281	17.897	19.284/15.017	18.758/14.335	3.609	2.644
0.9-1.3	47.065	52.633	15.989/13.049	15.643/12.622	3.090	1.188
1.3-1.7	60.493	62.166	15.557/13.266	14.952/12.551	3.721	2.146
1.7-2.1	38.561	38.269	16.793/13.474	16.110/12.612	4.349	1.888
2.1-2.5	11.002	10.501	17.109/16.546	14.472/13.802	8.714	2.705
$35 < p_{t,max} < 80$ GeV and $0.1 < y < 0.5$						
0.9-1.3	3.458	4.714	18.279/15.946	15.821/13.057	5.809	7.075
1.3-1.7	10.968	12.427	16.278/11.494	15.054/9.683	5.595	2.651
1.7-2.1	8.610	9.164	16.333/15.326	13.757/12.545	8.457	2.445
2.1-2.5	1.929	2.023	22.146/20.186	15.651/12.727	14.839	5.029
$25 < p_{t,max} < 35$ GeV and $0.5 < y < 0.9$						
0.0-0.6	32.346	38.236	16.795/11.932	16.179/11.048	3.932	2.202
0.6-0.9	70.452	68.146	14.976/11.768	14.630/11.323	2.966	1.214
0.9-1.3	53.650	48.121	17.155/12.657	16.800/12.171	3.167	1.425
1.3-1.7	26.670	22.485	17.130/15.038	16.448/14.256	3.511	3.251
1.7-2.1	11.360	9.389	22.585/16.823	20.865/14.431	5.632	6.561
2.1-2.5	2.710	2.152	29.017/22.332	24.906/16.644	8.176	12.444
$35 < p_{t,max} < 80$ GeV and $0.5 < y < 0.9$						
0.0-0.6	1.297	2.142	26.076/23.974	19.004/15.999	5.817	16.881
0.6-0.9	12.311	14.418	14.783/13.464	13.897/12.484	2.897	4.128
0.9-1.3	17.685	18.606	15.801/13.328	14.824/12.154	4.260	3.431
1.3-1.7	9.730	9.581	16.760/15.232	14.808/13.053	6.516	4.377
1.7-2.1	2.953	2.762	22.710/21.460	19.219/17.725	10.354	6.258

Table B.9: Data points and uncertainties for  $d\sigma/\bar{\eta}$  in the  $p_{t,2nd} > 15$  GeV,  $-0.5 < \eta_{jet} < 2.5$  cut scenario. Where two numbers are given per column they are to be read as  $+\delta/ -\delta$ .

B.2. CROSS SECTIONS IN NLO CALCULATIONS FOR  $P_{T,2ND} > 15 \text{ GEV}$ ,  $-0.5 < \eta_{JET} < 2.5119$

$\cos \theta^*$	$\frac{d\sigma}{d\cos\theta^*} \times C_{had} \text{ [pb]}$	$\frac{d\sigma}{d\cos\theta^*} \text{ [pb]}$	$\delta_{tot} \text{ [%]}$	$\delta_{scale} \text{ [%]}$	$\delta_{pdf} \text{ [%]}$	$\delta_{mod} \text{ [%]}$
$x_\gamma < 0.8$						
0.00-0.10	111.53	103.64	18.35/16.27	17.87/15.72	3.86	1.62
0.10-0.20	109.55	99.99	21.50/15.21	21.14/14.70	3.53	1.66
0.20-0.30	107.30	98.61	19.46/15.36	18.93/14.68	4.20	1.62
0.30-0.40	107.02	94.93	20.28/15.27	19.92/14.80	3.39	1.70
0.40-0.50	104.62	91.95	20.38/14.45	19.81/13.64	3.43	3.34
0.50-0.60	96.00	86.68	19.33/16.23	18.79/15.58	4.14	1.83
0.60-0.70	83.95	71.99	21.57/16.20	20.91/15.31	4.37	2.98
0.70-0.85	47.35	38.86	21.15/16.63	20.67/16.01	3.81	2.36
$x_\gamma > 0.8$						
0.00-0.10	134.84	153.41	10.45/10.88	10.02/10.46	2.35	1.84
0.10-0.20	133.46	151.41	11.70/10.36	10.90/9.45	4.04	1.30
0.20-0.30	129.13	147.64	12.34/10.00	11.85/9.40	2.89	1.83
0.30-0.40	118.97	141.10	12.33/10.22	11.72/9.47	2.61	2.80
0.40-0.50	115.49	132.88	14.74/11.34	14.30/10.77	3.26	1.45
0.50-0.60	102.50	120.85	14.69/11.78	14.12/11.06	3.37	2.24
0.60-0.70	89.90	104.01	16.64/12.44	15.92/11.46	4.51	1.73
0.70-0.85	58.01	67.01	20.56/14.92	20.18/14.39	3.42	1.95
$x_\gamma < 0.8$ and $M_{JJ} > 65 \text{ GeV}$						
0.00-0.10	15.31	13.47	7.23/10.57	1.13/7.79	5.98	3.90
0.10-0.20	14.16	13.54	10.17/7.79	7.82/4.29	5.29	3.78
0.20-0.30	16.39	15.52	6.37/10.06	1.11/7.87	5.15	3.58
0.30-0.40	21.27	17.68	8.06/10.65	2.13/7.28	5.93	5.02
0.40-0.50	25.09	21.52	6.65/8.08	2.92/5.43	5.17	3.01
0.50-0.60	31.17	28.17	4.92/6.00	0.88/3.56	4.13	2.53
0.60-0.70	49.63	42.40	10.79/10.32	9.46/8.92	4.52	2.57
0.70-0.85	44.30	36.03	19.44/16.11	18.80/15.33	4.05	2.86
$x_\gamma > 0.8$ and $M_{JJ} > 65 \text{ GeV}$						
0.00-0.10	31.36	34.76	4.97/7.95	0.00/6.21	4.25	2.57
0.10-0.20	31.90	35.05	5.47/6.51	0.00/3.53	4.39	3.27
0.20-0.30	33.85	37.02	6.58/7.52	1.16/3.81	5.99	2.48
0.30-0.40	35.90	41.10	5.25/6.94	1.45/4.76	4.06	2.99
0.40-0.50	42.90	46.64	5.96/5.43	3.51/2.52	4.25	2.25
0.50-0.60	50.86	58.00	6.71/6.36	4.79/4.28	3.92	2.61
0.60-0.70	69.66	79.03	10.19/9.43	8.98/8.11	4.41	1.91
0.70-0.85	56.71	65.02	19.90/14.54	19.50/13.99	3.44	1.94

Table B.10: Data points and uncertainties for  $d\sigma / \cos \theta^*$  in the  $p_{t,2nd} > 15 \text{ GeV}$ ,  $-0.5 < \eta_{jet} < 2.5$  cut scenario. Where two numbers are given per column they are to be read as  $+\delta / -\delta$ .

$x_\gamma$	$\frac{d\sigma}{dx_\gamma} \times C_{had}$ [pb]	$\frac{d\sigma}{dx_\gamma}$ [pb]	$\delta_{tot}$ [%]	$\delta_{scale}$ [%]	$\delta_{pdf}$ [%]	$\delta_{mod}$ [%]
$x_p < 0.1$						
0.30-0.50	18.70	16.90	30.55/21.12	30.08/20.43	4.02	3.55
0.50-0.70	52.02	47.71	23.58/17.37	23.31/17.00	3.08	1.80
0.70-0.85	83.80	79.59	20.40/15.88	19.88/15.22	3.16	3.27
0.85-1.00	254.49	318.01	16.01/11.78	15.71/11.36	3.00	0.84
$x_p > 0.1$						
0.10-0.30	46.34	37.51	27.42/20.90	25.80/18.74	6.01	7.05
0.30-0.50	83.78	73.58	20.73/15.00	20.20/14.27	4.44	1.36
0.50-0.70	97.82	88.19	16.89/14.14	16.05/13.11	4.09	3.34
0.70-0.85	115.20	107.68	15.23/13.62	14.72/13.04	3.72	1.24
0.85-1.00	281.55	321.13	10.74/9.93	10.07/9.21	3.64	0.76

Table B.11: Data points and uncertainties for  $d\sigma/dx_\gamma$  in the  $p_{t,2nd} > 15$  GeV,  $-0.5 < \eta_{jet} < 2.5$  cut scenario. Where two numbers are given per column they are to be read as  $+\delta/ -\delta$ .

$x_p$	$\frac{d\sigma}{dx_p} \times C_{had}$ [pb]	$\frac{d\sigma}{dx_p}$ [pb]	$\delta_{tot}$ [%]	$\delta_{scale}$ [%]	$\delta_{pdf}$ [%]	$\delta_{mod}$ [%]
$x_\gamma < 0.8$						
0.05-0.10	404.16	371.33	22.85/17.09	22.61/16.77	3.01	1.25
0.10-0.15	464.57	414.24	21.49/16.01	21.17/15.57	3.53	1.20
0.15-0.22	319.98	281.94	18.93/14.68	18.38/13.96	4.40	1.18
0.22-0.32	96.88	84.75	14.20/14.22	12.17/12.19	7.12	1.73
0.32-0.45	10.77	9.91	14.27/15.51	8.32/10.30	10.88	4.00
0.45-0.70	0.74	0.49	24.07/24.82	8.60/10.54	18.19	13.21
$x_\gamma > 0.8$						
0.05-0.10	649.03	764.19	14.47/11.60	14.10/11.13	2.87	1.56
0.10-0.15	442.47	499.41	13.74/11.07	13.27/10.49	3.38	1.12
0.15-0.22	243.34	271.73	12.38/10.56	11.76/9.82	3.70	1.19
0.22-0.32	75.98	80.37	6.93/9.98	2.85/7.72	6.08	1.73
0.32-0.45	10.80	12.32	13.40/14.21	2.84/5.52	11.50	6.26
0.45-0.70	0.84	0.91	21.05/21.86	0.00/5.90	18.62	9.81

Table B.12: Data points and uncertainties for  $d\sigma/dx_p$  in the  $p_{t,2nd} > 15$  GeV,  $-0.5 < \eta_{jet} < 2.5$  cut scenario. Where two numbers are given per column they are to be read as  $+\delta/ -\delta$ .

B.3. CROSS SECTIONS IN NLO CALCULATIONS FOR  $P_{T,2ND} > 20 \text{ GeV}$ ,  $-0.5 < \eta_{JET} < 2.75121$

**B.3 Cross sections in NLO calculations for  $p_{t,2nd} > 20 \text{ GeV}$ ,  
 $-0.5 < \eta_{jet} < 2.75$**

$\bar{p}_t$ [GeV]	$\frac{d\sigma}{d\bar{p}_t} \times C_{had} [\frac{\text{pb}}{\text{GeV}}]$	$\frac{d\sigma}{d\bar{p}_t} [\frac{\text{pb}}{\text{GeV}}]$	$\delta_{tot}$ [%]	$\delta_{scale}$ [%]	$\delta_{pdf}$ [%]	$\delta_{mod}$ [%]
20-30	12.926	12.609	17.453/13.679	17.218/13.378	2.546	1.296
30-45	3.020	3.086	4.715/6.703	3.017/5.639	3.553	0.716
45-60	0.266	0.281	7.417/9.180	2.284/5.872	6.582	2.544
60-80	0.028	0.029	12.212/12.784	0.000/3.783	10.457	6.307

Table B.13: Data points and uncertainties for  $d\sigma/d\bar{p}_t$  in the  $p_{t,2nd} > 20 \text{ GeV}$ ,  $-0.5 < \eta_{jet} < 2.75$  cut scenario. Where two numbers are given per column they are to be read as  $+\delta/ - \delta$ .

$M_{JJ}$ [GeV]	$\frac{d\sigma}{dM_{JJ}} \times C_{had} [\frac{\text{pb}}{\text{GeV}}]$	$\frac{d\sigma}{dM_{JJ}} [\frac{\text{pb}}{\text{GeV}}]$	$\delta_{tot}$ [%]	$\delta_{scale}$ [%]	$\delta_{pdf}$ [%]	$\delta_{mod}$ [%]
45-58	5.252	5.117	22.274/16.117	22.100/15.876	2.331	1.511
58-70	4.595	4.587	9.499/9.356	9.097/8.947	2.651	0.670
70-90	1.945	1.935	8.089/8.868	7.310/8.164	3.367	0.810
90-110	0.591	0.603	7.777/9.231	5.769/7.616	5.005	1.467
110-135	0.155	0.158	8.405/9.969	4.558/7.036	6.581	2.560
135-180	0.019	0.021	13.072/13.469	3.795/4.993	11.398	5.155

Table B.14: Data points and uncertainties for  $d\sigma/dM_{JJ}$  in the  $p_{t,2nd} > 20 \text{ GeV}$ ,  $-0.5 < \eta_{jet} < 2.75$  cut scenario. Where two numbers are given per column they are to be read as  $+\delta/ - \delta$ .

$\bar{\eta}$	$\frac{d\sigma}{d\bar{\eta}} \times C_{had}$ [pb]	$\frac{d\sigma}{d\bar{\eta}}$ [pb]	$\delta_{tot}$ [%]	$\delta_{scale}$ [%]	$\delta_{pdf}$ [%]	$\delta_{mod}$ [%]
$25 < p_{t,max} < 35$ GeV and $0.1 < y < 0.5$						
0.6-0.9	10.811	15.151	14.206/12.485	13.317/11.463	4.036	2.863
0.9-1.3	43.323	46.903	13.659/10.772	13.251/10.249	2.926	1.555
1.3-1.7	60.698	60.469	13.530/11.714	12.747/10.800	3.425	2.974
1.7-2.1	46.911	44.796	14.698/12.517	13.431/11.001	5.265	2.816
2.1-2.5	20.919	19.186	14.879/14.849	12.248/12.211	8.243	1.852
$35 < p_{t,max} < 80$ GeV and $0.1 < y < 0.5$						
0.9-1.3	3.285	4.496	16.546/13.692	14.338/10.922	4.026	7.209
1.3-1.7	11.622	12.873	14.195/13.769	12.621/12.141	6.116	2.187
1.7-2.1	10.560	11.163	16.710/15.278	13.903/12.144	8.971	2.335
2.1-2.5	3.583	3.786	23.600/16.387	19.388/9.352	12.679	4.511
$25 < p_{t,max} < 35$ GeV and $0.5 < y < 0.9$						
0.0-0.6	30.105	34.011	12.558/11.558	11.849/10.784	3.969	1.245
0.6-0.9	64.027	60.978	12.729/10.655	12.186/10.000	3.474	1.215
0.9-1.3	49.269	43.444	13.592/11.438	13.144/10.902	3.231	1.240
1.3-1.7	28.083	23.281	12.570/12.253	11.663/11.321	4.397	1.623
1.7-2.1	13.699	10.791	15.576/14.294	13.865/12.408	5.815	4.067
2.1-2.5	4.814	3.886	19.899/20.421	14.803/15.498	9.473	9.333
$35 < p_{t,max} < 80$ GeV and $0.5 < y < 0.9$						
0.0-0.6	1.246	1.931	20.949/13.792	18.733/10.114	4.473	8.241
0.6-0.9	12.304	14.194	12.264/13.216	11.553/12.559	2.765	3.048
0.9-1.3	17.976	18.620	13.685/12.346	13.000/11.582	3.348	2.659
1.3-1.7	11.216	10.823	18.047/14.273	16.603/12.398	6.683	2.314
1.7-2.1	4.014	3.659	22.662/19.682	19.934/16.468	9.398	5.280

Table B.15: Data points and uncertainties for  $d\sigma/\bar{\eta}$  in the  $p_{t,2nd} > 20$  GeV,  $-0.5 < \eta_{jet} < 2.75$  cut scenario. Where two numbers are given per column they are to be read as  $+\delta/ -\delta$ .

B.3. CROSS SECTIONS IN NLO CALCULATIONS FOR  $P_{T,2ND} > 20 \text{ GeV}$ ,  $-0.5 < \eta_{JET} < 2.75123$

$\cos \theta^*$	$\frac{d\sigma}{d\cos\theta^*} \times C_{had}$ [pb]	$\frac{d\sigma}{d\cos\theta^*}$ [pb]	$\delta_{tot}$ [%]	$\delta_{scale}$ [%]	$\delta_{pdf}$ [%]	$\delta_{mod}$ [%]
$x_\gamma < 0.8$						
0.00-0.10	107.41	94.79	16.69/14.44	16.26/13.94	3.41	1.65
0.10-0.20	105.17	94.18	17.84/14.28	17.18/13.45	4.52	1.64
0.20-0.30	107.79	94.57	15.89/14.23	15.48/13.76	3.19	1.66
0.30-0.40	107.03	92.86	16.53/13.23	15.96/12.52	3.96	1.62
0.40-0.50	107.53	90.68	18.31/13.19	17.60/12.19	3.72	3.38
0.50-0.60	100.84	88.56	13.63/14.62	12.85/13.89	4.27	1.64
0.60-0.70	92.61	77.19	17.93/14.09	17.15/13.09	4.21	3.10
0.70-0.85	57.33	48.51	18.92/14.91	18.05/13.79	5.37	1.81
$x_\gamma > 0.8$						
0.00-0.10	131.11	144.37	9.23/8.71	8.74/8.19	2.61	1.38
0.10-0.20	130.50	141.79	8.57/8.57	8.11/8.10	2.41	1.37
0.20-0.30	131.91	144.42	8.33/10.03	8.00/9.76	1.86	1.39
0.30-0.40	123.46	139.15	10.52/8.63	10.03/8.03	2.84	1.40
0.40-0.50	122.86	134.28	10.78/10.84	10.22/10.28	3.12	1.45
0.50-0.60	107.69	121.08	12.89/10.30	12.36/9.63	3.32	1.54
0.60-0.70	97.49	106.83	14.88/10.52	14.43/9.87	3.22	1.69
0.70-0.85	67.31	74.27	17.24/14.12	16.84/13.63	3.29	1.72
$x_\gamma < 0.8$ and $M_{JJ} > 65 \text{ GeV}$						
0.00-0.10	16.27	14.33	8.11/10.64	2.53/7.33	6.58	4.01
0.10-0.20	15.73	15.00	8.49/10.98	3.39/7.75	6.78	3.82
0.20-0.30	18.23	16.81	6.83/9.76	2.17/7.30	5.40	3.58
0.30-0.40	22.57	19.53	7.87/8.32	3.56/4.47	5.95	3.72
0.40-0.50	29.90	25.54	6.39/8.77	2.79/6.62	4.66	3.35
0.50-0.60	38.30	34.63	5.53/7.27	0.00/4.72	4.99	2.40
0.60-0.70	64.79	54.81	9.93/9.32	8.72/8.02	4.27	2.10
0.70-0.85	57.19	48.33	18.81/14.90	17.94/13.77	5.38	1.82
$x_\gamma > 0.8$ and $M_{JJ} > 65 \text{ GeV}$						
0.00-0.10	31.57	35.19	4.67/6.06	1.22/4.04	3.65	2.66
0.10-0.20	32.87	35.97	5.22/6.90	0.00/4.50	3.84	3.54
0.20-0.30	35.38	38.64	5.72/5.85	3.13/3.37	4.06	2.53
0.30-0.40	37.70	43.43	5.79/6.59	0.00/3.13	4.26	3.93
0.40-0.50	47.88	51.62	4.42/7.78	1.85/6.67	3.32	2.25
0.50-0.60	55.24	62.27	6.02/6.21	3.91/4.20	4.11	2.03
0.60-0.70	79.57	88.05	9.77/8.09	9.09/7.26	3.05	1.85
0.70-0.85	67.16	74.15	17.21/14.11	16.80/13.61	3.29	1.72

Table B.16: Data points and uncertainties for  $d\sigma / \cos \theta^*$  in the  $p_{t,2nd} > 20 \text{ GeV}$ ,  $-0.5 < \eta_{jet} < 2.75$  cut scenario. Where two numbers are given per column they are to be read as  $+\delta / -\delta$ .

$x_\gamma$	$\frac{d\sigma}{dx_\gamma} \times C_{had}$ [pb]	$\frac{d\sigma}{dx_\gamma}$ [pb]	$\delta_{tot}$ [%]	$\delta_{scale}$ [%]	$\delta_{pdf}$ [%]	$\delta_{mod}$ [%]
$x_p < 0.1$						
0.30-0.50	13.76	11.17	26.86/19.52	25.88/18.13	4.42	5.71
0.50-0.70	40.84	36.60	18.59/15.51	18.24/15.08	3.04	1.95
0.70-0.85	75.48	66.12	17.44/13.80	17.12/13.41	2.90	1.53
0.85-1.00	246.09	289.45	12.69/10.93	12.19/10.35	3.41	0.85
$x_p > 0.1$						
0.10-0.30	56.36	43.30	22.75/18.84	21.09/16.80	7.47	4.13
0.30-0.50	93.10	79.37	17.23/14.11	16.47/13.16	4.92	1.22
0.50-0.70	108.92	96.72	14.30/13.01	13.15/11.74	4.49	3.38
0.70-0.85	129.73	118.21	14.55/12.65	13.88/11.88	4.06	1.56
0.85-1.00	316.15	350.67	9.94/9.36	9.12/8.49	3.89	0.73

Table B.17: Data points and uncertainties for  $d\sigma/dx_\gamma$  in the  $p_{t,2nd} > 20$  GeV,  $-0.5 < \eta_{jet} < 2.75$  cut scenario. Where two numbers are given per column they are to be read as  $+\delta/-\delta$ .

$x_p$	$\frac{d\sigma}{dx_p} \times C_{had}$ [pb]	$\frac{d\sigma}{dx_p}$ [pb]	$\delta_{tot}$ [%]	$\delta_{scale}$ [%]	$\delta_{pdf}$ [%]	$\delta_{mod}$ [%]
$x_\gamma < 0.8$						
0.05-0.10	330.92	291.17	18.66/14.89	18.37/14.53	2.95	1.35
0.10-0.15	393.58	343.44	18.04/13.85	17.65/13.34	3.27	1.79
0.15-0.22	326.19	281.27	17.69/14.48	17.02/13.66	4.64	1.29
0.22-0.32	166.87	143.24	14.89/14.41	12.82/12.26	7.38	1.73
0.32-0.45	33.61	29.35	14.59/15.46	9.15/10.47	11.06	2.61
0.45-0.70	2.01	1.77	22.13/22.44	8.64/9.40	18.99	7.38
$x_\gamma > 0.8$						
0.05-0.10	627.82	705.21	12.63/10.33	12.12/9.69	3.45	0.91
0.10-0.15	433.84	471.91	11.27/9.80	10.83/9.28	2.93	1.08
0.15-0.22	260.76	285.40	11.88/10.66	11.14/9.83	3.95	1.18
0.22-0.32	115.59	118.91	9.77/10.11	7.04/7.51	6.60	1.50
0.32-0.45	19.87	22.20	13.66/14.67	1.87/5.67	10.28	8.81
0.45-0.70	1.84	2.01	18.98/19.41	0.12/4.05	15.24	11.31

Table B.18: Data points and uncertainties for  $d\sigma/dx_p$  in the  $p_{t,2nd} > 20$  GeV,  $-0.5 < \eta_{jet} < 2.75$  cut scenario. Where two numbers are given per column they are to be read as  $+\delta/-\delta$ .

B.4. CROSS SECTIONS IN NLO CALCULATIONS FOR  $P_{T,2ND} > 20 \text{ GeV}$ ,  $-0.5 < \eta_{JET} < 2.5125$

**B.4 Cross sections in NLO calculations for  $p_{t,2nd} > 20 \text{ GeV}$ ,  
 $-0.5 < \eta_{jet} < 2.5$**

$\bar{p}_t$ [GeV]	$\frac{d\sigma}{d\bar{p}_t} \times C_{had} [\frac{\text{pb}}{\text{GeV}}]$	$\frac{d\sigma}{d\bar{p}_t} [\frac{\text{pb}}{\text{GeV}}]$	$\delta_{tot}$ [%]	$\delta_{scale}$ [%]	$\delta_{pdf}$ [%]	$\delta_{mod}$ [%]
20-30	11.472	11.301	17.030/13.476	16.811/13.198	2.404	1.279
30-45	2.701	2.779	4.502/6.457	3.131/5.588	3.146	0.754
45-60	0.245	0.260	6.616/8.325	2.052/5.454	5.796	2.444
60-80	0.026	0.028	11.723/12.274	0.000/3.633	9.836	6.379

Table B.19: Data points and uncertainties for  $d\sigma/d\bar{p}_t$  in the  $p_{t,2nd} > 20 \text{ GeV}$ ,  $-0.5 < \eta_{jet} < 2.5$  cut scenario. Where two numbers are given per column they are to be read as  $+\delta/ - \delta$ .

$M_{JJ}$ [GeV]	$\frac{d\sigma}{dM_{JJ}} \times C_{had} [\frac{\text{pb}}{\text{GeV}}]$	$\frac{d\sigma}{dM_{JJ}} [\frac{\text{pb}}{\text{GeV}}]$	$\delta_{tot}$ [%]	$\delta_{scale}$ [%]	$\delta_{pdf}$ [%]	$\delta_{mod}$ [%]
45-58	4.920	4.838	21.614/15.850	21.440/15.611	2.256	1.559
58-70	4.153	4.168	8.950/9.061	8.537/8.654	2.592	0.703
70-90	1.658	1.673	7.286/8.406	6.603/7.822	2.953	0.870
90-110	0.457	0.474	6.889/8.153	5.152/6.750	4.267	1.647
110-135	0.106	0.111	8.966/9.791	4.921/6.299	6.864	3.012
135-180	0.013	0.014	11.634/12.540	1.080/4.803	9.856	6.087

Table B.20: Data points and uncertainties for  $d\sigma/dM_{JJ}$  in the  $p_{t,2nd} > 20 \text{ GeV}$ ,  $-0.5 < \eta_{jet} < 2.5$  cut scenario. Where two numbers are given per column they are to be read as  $+\delta/ - \delta$ .

$\bar{\eta}$	$\frac{d\sigma}{d\bar{\eta}} \times C_{had}$ [pb]	$\frac{d\sigma}{d\bar{\eta}}$ [pb]	$\delta_{tot}$ [%]	$\delta_{scale}$ [%]	$\delta_{pdf}$ [%]	$\delta_{mod}$ [%]
$25 < p_{t,max} < 35$ GeV and $0.1 < y < 0.5$						
0.6-0.9	10.884	15.161	14.259/12.521	13.349/11.474	4.018	2.996
0.9-1.3	43.582	46.901	13.726/10.830	13.284/10.263	2.918	1.857
1.3-1.7	55.790	55.856	13.189/11.266	12.531/10.487	3.283	2.480
1.7-2.1	36.555	34.659	13.647/12.473	12.317/11.001	4.975	3.129
2.1-2.5	10.236	9.535	14.187/14.300	11.825/11.960	7.385	2.628
$35 < p_{t,max} < 80$ GeV and $0.1 < y < 0.5$						
0.9-1.3	3.259	4.513	17.012/13.996	14.626/10.972	4.000	7.714
1.3-1.7	11.217	12.500	13.872/13.506	12.412/12.001	5.786	2.215
1.7-2.1	8.646	9.085	15.154/14.984	12.221/12.009	8.581	2.583
2.1-2.5	1.844	1.990	22.489/18.656	16.780/11.129	13.998	5.313
$25 < p_{t,max} < 35$ GeV and $0.5 < y < 0.9$						
0.0-0.6	30.091	34.038	12.580/11.569	11.873/10.797	3.966	1.245
0.6-0.9	63.670	61.032	12.739/10.667	12.198/10.014	3.468	1.214
0.9-1.3	47.227	41.315	13.617/11.232	13.138/10.647	3.233	1.534
1.3-1.7	22.835	18.843	12.334/12.356	11.597/11.620	3.798	1.793
1.7-2.1	9.717	7.798	15.834/14.965	13.460/12.426	5.693	6.094
2.1-2.5	2.474	1.824	18.393/20.744	14.975/17.784	8.584	6.353
$35 < p_{t,max} < 80$ GeV and $0.5 < y < 0.9$						
0.0-0.6	1.283	1.946	20.899/14.159	18.537/10.360	4.428	8.576
0.6-0.9	12.275	14.240	12.421/13.270	11.687/12.585	2.755	3.179
0.9-1.3	17.894	18.517	13.674/12.425	12.953/11.626	3.345	2.831
1.3-1.7	9.766	9.446	18.421/13.849	17.090/12.023	6.337	2.664
1.7-2.1	2.994	2.684	23.045/18.759	20.657/15.734	8.023	6.323

Table B.21: Data points and uncertainties for  $d\sigma/\bar{\eta}$  in the  $p_{t,2nd} > 20$  GeV,  $-0.5 < \eta_{jet} < 2.5$  cut scenario. Where two numbers are given per column they are to be read as  $+\delta/ - \delta$ .

B.4. CROSS SECTIONS IN NLO CALCULATIONS FOR  $P_{T,2ND} > 20 \text{ GEV}$ ,  $-0.5 < \eta_{JET} < 2.5127$

$\cos \theta^*$	$\frac{d\sigma}{d\cos\theta^*} \times C_{had}$ [pb]	$\frac{d\sigma}{d\cos\theta^*}$ [pb]	$\delta_{tot}$ [%]	$\delta_{scale}$ [%]	$\delta_{pdf}$ [%]	$\delta_{mod}$ [%]
$x_\gamma < 0.8$						
0.00-0.10	100.23	88.77	16.41/14.21	16.03/13.77	3.05	1.70
0.10-0.20	95.89	86.28	17.50/13.92	16.95/13.21	4.03	1.70
0.20-0.30	96.00	84.68	15.60/14.07	15.27/13.70	2.68	1.71
0.30-0.40	93.71	81.31	16.24/12.76	15.84/12.24	3.16	1.72
0.40-0.50	93.12	78.17	17.75/13.11	16.95/12.00	3.62	3.83
0.50-0.60	82.54	73.26	13.52/14.35	12.81/13.69	3.92	1.80
0.60-0.70	71.10	59.39	18.45/13.66	17.83/12.80	3.42	3.31
0.70-0.85	37.85	31.36	19.13/15.55	18.48/14.74	4.39	2.27
$x_\gamma > 0.8$						
0.00-0.10	131.03	143.99	9.22/8.65	8.75/8.15	2.56	1.38
0.10-0.20	129.00	140.63	8.70/8.57	8.22/8.08	2.50	1.38
0.20-0.30	128.23	141.10	8.63/10.21	8.32/9.94	1.84	1.41
0.30-0.40	117.30	133.24	10.40/8.76	9.80/8.04	2.99	1.78
0.40-0.50	114.98	125.62	10.77/11.00	10.22/10.45	3.07	1.50
0.50-0.60	99.22	112.42	12.23/10.67	11.62/9.97	3.44	1.60
0.60-0.70	87.44	96.00	15.43/10.37	15.02/9.74	3.03	1.87
0.70-0.85	55.57	60.69	17.41/14.27	16.94/13.70	3.15	2.46
$x_\gamma < 0.8$ and $M_{JJ} > 65 \text{ GeV}$						
0.00-0.10	15.34	13.56	7.68/10.10	2.64/7.07	5.95	4.08
0.10-0.20	14.47	13.87	7.90/10.51	3.14/7.60	6.09	3.95
0.20-0.30	16.43	15.30	6.44/9.49	1.89/7.23	4.88	3.74
0.30-0.40	20.54	17.37	7.81/8.22	3.46/4.30	5.17	4.73
0.40-0.50	25.44	21.93	5.86/8.28	2.56/6.39	4.21	3.18
0.50-0.60	30.82	27.91	5.41/7.14	0.00/4.66	4.72	2.65
0.60-0.70	49.06	41.50	10.76/8.77	9.92/7.72	3.45	2.33
0.70-0.85	37.78	31.21	19.01/15.53	18.35/14.72	4.39	2.28
$x_\gamma > 0.8$ and $M_{JJ} > 65 \text{ GeV}$						
0.00-0.10	30.93	34.77	4.50/5.84	1.07/3.88	3.45	2.68
0.10-0.20	31.84	35.00	5.48/6.86	0.00/4.13	4.34	3.33
0.20-0.30	33.61	36.94	5.75/5.85	3.47/3.63	3.79	2.58
0.30-0.40	35.83	41.02	5.83/6.57	0.00/3.04	4.37	3.86
0.40-0.50	44.58	48.36	4.50/7.89	1.80/6.72	3.41	2.33
0.50-0.60	50.62	57.76	5.89/6.77	3.00/4.47	4.33	2.65
0.60-0.70	70.48	78.28	10.24/7.77	9.65/6.98	2.80	1.95
0.70-0.85	55.43	60.58	17.36/14.25	16.90/13.69	3.15	2.42

Table B.22: Data points and uncertainties for  $d\sigma/\cos\theta^*$  in the  $p_{t,2nd} > 20 \text{ GeV}$ ,  $-0.5 < \eta_{jet} < 2.5$  cut scenario. Where two numbers are given per column they are to be read as  $+\delta/ -\delta$ .

$x_\gamma$	$\frac{d\sigma}{dx_\gamma} \times C_{had}$ [pb]	$\frac{d\sigma}{dx_\gamma}$ [pb]	$\delta_{tot}$ [%]	$\delta_{scale}$ [%]	$\delta_{pdf}$ [%]	$\delta_{mod}$ [%]
$x_p < 0.1$						
0.30-0.50	13.82	11.18	26.72/19.29	25.90/18.13	4.41	4.89
0.50-0.70	40.59	36.64	18.63/15.52	18.28/15.10	3.03	1.94
0.70-0.85	75.58	66.19	17.46/13.81	17.15/13.42	2.89	1.53
0.85-1.00	246.01	289.79	12.71/10.95	12.22/10.38	3.40	0.85
$x_p > 0.1$						
0.10-0.30	38.68	29.56	23.07/18.68	21.40/16.58	6.33	5.83
0.30-0.50	75.11	63.88	16.76/13.61	16.18/12.89	4.16	1.36
0.50-0.70	90.28	79.69	14.20/12.78	13.15/11.60	3.97	3.61
0.70-0.85	108.82	99.51	14.40/12.16	13.94/11.61	3.38	1.28
0.85-1.00	279.79	311.06	9.17/9.15	8.41/8.38	3.59	0.77

Table B.23: Data points and uncertainties for  $d\sigma/dx_\gamma$  in the  $p_{t,2nd} > 20$  GeV,  $-0.5 < \eta_{jet} < 2.5$  cut scenario. Where two numbers are given per column they are to be read as  $+\delta/-\delta$ .

$x_p$	$\frac{d\sigma}{dx_p} \times C_{had}$ [pb]	$\frac{d\sigma}{dx_p}$ [pb]	$\delta_{tot}$ [%]	$\delta_{scale}$ [%]	$\delta_{pdf}$ [%]	$\delta_{mod}$ [%]
$x_\gamma < 0.8$						
0.05-0.10	329.11	291.49	18.68/14.90	18.40/14.54	2.94	1.35
0.10-0.15	395.86	343.89	18.10/13.91	17.68/13.36	3.28	2.07
0.15-0.22	292.40	251.97	15.86/13.81	15.22/13.07	4.28	1.25
0.22-0.32	92.35	80.53	13.12/13.13	10.89/10.92	7.11	1.69
0.32-0.45	10.83	9.73	14.26/14.34	8.23/8.37	10.86	4.19
0.45-0.70	0.70	0.48	23.93/23.17	10.11/8.16	16.90	13.59
$x_\gamma > 0.8$						
0.05-0.10	629.09	706.12	12.66/10.35	12.15/9.72	3.43	0.90
0.10-0.15	431.83	472.49	11.31/9.81	10.87/9.30	2.93	1.08
0.15-0.22	244.58	264.87	10.73/10.09	9.93/9.24	3.88	1.21
0.22-0.32	76.73	79.61	7.40/9.18	3.45/6.43	6.30	1.79
0.32-0.45	10.86	12.39	12.53/14.16	1.60/6.77	10.95	5.88
0.45-0.70	0.72	0.84	21.59/21.15	4.37/0.00	18.27	10.66

Table B.24: Data points and uncertainties for  $d\sigma/dx_p$  in the  $p_{t,2nd} > 20$  GeV,  $-0.5 < \eta_{jet} < 2.5$  cut scenario. Where two numbers are given per column they are to be read as  $+\delta/-\delta$ .

# List of Figures

2.1	CTEQ6 PDF uncertainties . . . . .	9
2.2	Electron-proton scattering . . . . .	9
2.3	Schematic view of dijet production in $ep$ scattering . . . . .	11
2.4	LO diagrams for direct photoproduction . . . . .	12
2.5	LO diagrams for resolved photoproduction . . . . .	12
2.6	Simplified example of the inclusive $k_{\perp}$ algorithm . . . . .	15
2.7	From the hard scattering to detector objects . . . . .	17
3.1	HERA and its pre-accelerators . . . . .	20
3.2	Schematic view of the H1 detector . . . . .	20
3.3	Side view of the LAr calorimeter . . . . .	21
3.4	Backward region with the SpaCal . . . . .	22
3.5	r-z view of the H1 tracking . . . . .	24
4.1	Typical event display . . . . .	28
5.1	Jets in $p_t$ ordering . . . . .	38
5.2	Jets in angular ordering . . . . .	39
5.3	$p_t$ balance as function of the electron $p_t$ . . . . .	40
5.4	$p_t$ balance as function of the hadronic $p_t$ . . . . .	40
5.5	$p_t$ balance as function of the hadronic angle . . . . .	41
5.6	$p_t$ balance as function of the jet angle . . . . .	41
5.7	Jet comparison between data and Monte Carlo before calibration . . . . .	42
5.8	Jet comparison between data and Monte Carlo after calibration . . . . .	43
5.9	Background finder bits in the final selection . . . . .	44
5.10	Background from DIS events . . . . .	45
5.11	Remaining background from DIS events . . . . .	46
5.12	Stability of the event selection . . . . .	48
5.13	Distribution of subtriggers . . . . .	49
5.14	Luminosity weighted trigger prescales . . . . .	50
5.15	Trigger efficiency for the signal trigger combination . . . . .	51
5.16	Trigger efficiency for the individual triggers . . . . .	51
5.17	Preselection quantities . . . . .	53

5.18	Jet pseudorapidity and azimuthal angle . . . . .	54
5.19	Mean jet pseudorapidity and CMS scattering angle . . . . .	54
5.20	Jet $p_t$ and dijet mass . . . . .	55
5.21	Correlations for the forward jet . . . . .	57
5.22	Correlations for the backward jet . . . . .	58
5.23	Hadronisation correction factors for $\bar{p}_t$ , $\bar{\eta}$ and $\cos \theta^*$ . . . . .	59
5.24	Hadronisation correction factors for $x_\gamma$ and $x_p$ . . . . .	59
5.25	Effect of the LAr energy scale variation on the dijet system . . . . .	60
5.26	Effect of the LAr energy scale variation on $x_\gamma$ and $x_p$ . . . . .	61
5.27	Effect of the $y_{JB}$ and $\cos \theta^*$ reweighting . . . . .	62
5.28	Effect of the $y_{JB}$ and $\cos \theta^*$ reweighting on $x_\gamma$ and $x_p$ . . . . .	63
5.29	Jet reconstruction for $\eta$ up to 3.0 . . . . .	64
5.30	Jet reconstruction at $0.32 < x_p < 0.45$ . . . . .	65
5.31	Jet reconstruction at $x_p > 0.45$ . . . . .	66
5.32	Correlations for the backward jet with $\eta_{jet} < 3.0$ . . . . .	67
5.33	$x_p$ reconstruction for different methods . . . . .	68
5.34	Correlations in $x_p$ for different reconstruction methods . . . . .	69
5.35	Reconstructed $x_p$ vs. true $x_p$ . . . . .	70
5.36	$x_p$ distribution of gluon induced events . . . . .	71
5.37	NLO $x_p$ cross section for different beam energies . . . . .	72
5.38	Ratio between the NLO $x_p$ cross section for different cut scenarios . . . . .	73
5.39	Deviations of the 40 CTEQ6 eigenvector sets . . . . .	75
5.40	Gluon uncertainty from CTEQ6.1M eigenvector sets . . . . .	75
5.41	Resulting uncertainties in $x_\gamma$ from the CTEQ6M eigenvector sets . . . . .	76
5.42	Resulting uncertainties in $x_p$ from the CTEQ6M eigenvector sets . . . . .	76
6.1	Cross sections in mean $p_t$ and dijet mass . . . . .	79
6.2	Cross sections in mean pseudorapidity . . . . .	81
6.3	Cross sections in $\cos \theta^*$ . . . . .	82
6.4	Cross sections in $x_\gamma$ . . . . .	83
6.5	Cross sections in $x_p$ . . . . .	85
6.6	Ratio of Data to NLO with uncertainties using CTEQ6M . . . . .	86
6.7	Ratio of the $x_p$ NLO cross sections between other PDFs and CTEQ6 . . . . .	88
6.8	Ratio of Data to NLO with uncertainties for all proton PDFs used . . . . .	89
6.9	Ratio of the $x_\gamma$ NLO cross sections between AFG-HO and GRV-HO . . . . .	91

# List of Tables

2.1	Phase space definition . . . . .	16
5.1	Preselection cuts on HAT level . . . . .	36
5.2	Preselection cuts on MODS and HAT level . . . . .	37
5.3	Selection cuts for the calibration sample . . . . .	39
5.4	Final event selection . . . . .	47
A.1	$d\sigma/d\bar{p}_t$ for $p_{t,2nd} > 15$ GeV, $-0.5 < \eta_{jet} < 2.75$ . . . . .	96
A.2	$d\sigma/dM_{JJ}$ for $p_{t,2nd} > 15$ GeV, $-0.5 < \eta_{jet} < 2.75$ . . . . .	96
A.3	$d\sigma/\bar{\eta}$ for $p_{t,2nd} > 15$ GeV, $-0.5 < \eta_{jet} < 2.75$ . . . . .	97
A.4	$d\sigma/\cos\theta^*$ for $p_{t,2nd} > 15$ GeV, $-0.5 < \eta_{jet} < 2.75$ . . . . .	98
A.5	$d\sigma/dx_\gamma$ for $p_{t,2nd} > 15$ GeV, $-0.5 < \eta_{jet} < 2.75$ . . . . .	99
A.6	$d\sigma/dx_p$ for $p_{t,2nd} > 15$ GeV, $-0.5 < \eta_{jet} < 2.75$ . . . . .	99
A.7	$d\sigma/d\bar{p}_t$ for $p_{t,2nd} > 15$ GeV, $-0.5 < \eta_{jet} < 2.5$ . . . . .	100
A.8	$d\sigma/dM_{JJ}$ for $p_{t,2nd} > 15$ GeV, $-0.5 < \eta_{jet} < 2.5$ . . . . .	100
A.9	$d\sigma/\bar{\eta}$ for $p_{t,2nd} > 15$ GeV, $-0.5 < \eta_{jet} < 2.5$ . . . . .	101
A.10	$d\sigma/\cos\theta^*$ for $p_{t,2nd} > 15$ GeV, $-0.5 < \eta_{jet} < 2.5$ . . . . .	102
A.11	$d\sigma/dx_\gamma$ for $p_{t,2nd} > 15$ GeV, $-0.5 < \eta_{jet} < 2.5$ . . . . .	103
A.12	$d\sigma/dx_p$ for $p_{t,2nd} > 15$ GeV, $-0.5 < \eta_{jet} < 2.5$ . . . . .	103
A.13	$d\sigma/d\bar{p}_t$ for $p_{t,2nd} > 20$ GeV, $-0.5 < \eta_{jet} < 2.75$ . . . . .	104
A.14	$d\sigma/dM_{JJ}$ for $p_{t,2nd} > 20$ GeV, $-0.5 < \eta_{jet} < 2.75$ . . . . .	104
A.15	$d\sigma/\bar{\eta}$ for $p_{t,2nd} > 20$ GeV, $-0.5 < \eta_{jet} < 2.75$ . . . . .	105
A.16	$d\sigma/\cos\theta^*$ for $p_{t,2nd} > 20$ GeV, $-0.5 < \eta_{jet} < 2.75$ . . . . .	106
A.17	$d\sigma/dx_\gamma$ for $p_{t,2nd} > 20$ GeV, $-0.5 < \eta_{jet} < 2.75$ . . . . .	107
A.18	$d\sigma/dx_p$ for $p_{t,2nd} > 20$ GeV, $-0.5 < \eta_{jet} < 2.75$ . . . . .	107
A.19	$d\sigma/d\bar{p}_t$ for $p_{t,2nd} > 20$ GeV, $-0.5 < \eta_{jet} < 2.5$ . . . . .	108
A.20	$d\sigma/dM_{JJ}$ for $p_{t,2nd} > 20$ GeV, $-0.5 < \eta_{jet} < 2.5$ . . . . .	108
A.21	$d\sigma/\bar{\eta}$ for $p_{t,2nd} > 20$ GeV, $-0.5 < \eta_{jet} < 2.5$ . . . . .	109
A.22	$d\sigma/\cos\theta^*$ for $p_{t,2nd} > 20$ GeV, $-0.5 < \eta_{jet} < 2.5$ . . . . .	110
A.23	$d\sigma/dx_\gamma$ for $p_{t,2nd} > 20$ GeV, $-0.5 < \eta_{jet} < 2.5$ . . . . .	111
A.24	$d\sigma/dx_p$ for $p_{t,2nd} > 20$ GeV, $-0.5 < \eta_{jet} < 2.5$ . . . . .	111
B.1	$d\sigma/d\bar{p}_t$ for $p_{t,2nd} > 15$ GeV, $-0.5 < \eta_{jet} < 2.75$ . . . . .	113

B.2	$d\sigma/dM_{JJ}$ for $p_{t,2nd} > 15$ GeV, $-0.5 < \eta_{jet} < 2.75$	114
B.3	$d\sigma/\bar{\eta}$ for $p_{t,2nd} > 15$ GeV, $-0.5 < \eta_{jet} < 2.75$	114
B.4	$d\sigma/\cos\theta^*$ for $p_{t,2nd} > 15$ GeV, $-0.5 < \eta_{jet} < 2.75$	115
B.5	$d\sigma/dx_\gamma$ for $p_{t,2nd} > 15$ GeV, $-0.5 < \eta_{jet} < 2.75$	116
B.6	$d\sigma/dx_p$ for $p_{t,2nd} > 15$ GeV, $-0.5 < \eta_{jet} < 2.75$	116
B.7	$d\sigma/d\bar{p}_t$ for $p_{t,2nd} > 15$ GeV, $-0.5 < \eta_{jet} < 2.5$	117
B.8	$d\sigma/dM_{JJ}$ for $p_{t,2nd} > 15$ GeV, $-0.5 < \eta_{jet} < 2.5$	117
B.9	$d\sigma/\bar{\eta}$ for $p_{t,2nd} > 15$ GeV, $-0.5 < \eta_{jet} < 2.5$	118
B.10	$d\sigma/\cos\theta^*$ for $p_{t,2nd} > 15$ GeV, $-0.5 < \eta_{jet} < 2.5$	119
B.11	$d\sigma/dx_\gamma$ for $p_{t,2nd} > 15$ GeV, $-0.5 < \eta_{jet} < 2.5$	120
B.12	$d\sigma/dx_p$ for $p_{t,2nd} > 15$ GeV, $-0.5 < \eta_{jet} < 2.5$	120
B.13	$d\sigma/d\bar{p}_t$ for $p_{t,2nd} > 20$ GeV, $-0.5 < \eta_{jet} < 2.75$	121
B.14	$d\sigma/dM_{JJ}$ for $p_{t,2nd} > 20$ GeV, $-0.5 < \eta_{jet} < 2.75$	121
B.15	$d\sigma/\bar{\eta}$ for $p_{t,2nd} > 20$ GeV, $-0.5 < \eta_{jet} < 2.75$	122
B.16	$d\sigma/\cos\theta^*$ for $p_{t,2nd} > 20$ GeV, $-0.5 < \eta_{jet} < 2.75$	123
B.17	$d\sigma/dx_\gamma$ for $p_{t,2nd} > 20$ GeV, $-0.5 < \eta_{jet} < 2.75$	124
B.18	$d\sigma/dx_p$ for $p_{t,2nd} > 20$ GeV, $-0.5 < \eta_{jet} < 2.75$	124
B.19	$d\sigma/d\bar{p}_t$ for $p_{t,2nd} > 20$ GeV, $-0.5 < \eta_{jet} < 2.5$	125
B.20	$d\sigma/dM_{JJ}$ for $p_{t,2nd} > 20$ GeV, $-0.5 < \eta_{jet} < 2.5$	125
B.21	$d\sigma/\bar{\eta}$ for $p_{t,2nd} > 20$ GeV, $-0.5 < \eta_{jet} < 2.5$	126
B.22	$d\sigma/\cos\theta^*$ for $p_{t,2nd} > 20$ GeV, $-0.5 < \eta_{jet} < 2.5$	127
B.23	$d\sigma/dx_\gamma$ for $p_{t,2nd} > 20$ GeV, $-0.5 < \eta_{jet} < 2.5$	128
B.24	$d\sigma/dx_p$ for $p_{t,2nd} > 20$ GeV, $-0.5 < \eta_{jet} < 2.5$	128

# Bibliography

- [A<sup>+</sup>97a] I. Abt et al. The h1 detector at herA. *Nucl. Instrum. Meth.*, A386:310–347, 1997. 3.2, 3.2.5
- [A<sup>+</sup>97b] I. Abt et al. The tracking, calorimeter and muon detectors of the h1 experiment at herA. *Nucl. Instrum. Meth.*, A386:348–396, 1997. 3.2
- [A<sup>+</sup>97c] R. D. Appuhn et al. The h1 lead/scintillating-fibre calorimeter. *Nucl. Instrum. Meth.*, A386:397–408, 1997. 3.2.1
- [A<sup>+</sup>01] C. Adloff et al. Measurement and QCD analysis of jet cross sections in deep- inelastic positron proton collisions at  $s^{*(1/2)}$  of 300-GeV. *Eur. Phys. J.*, C19:289–311, 2001. 2.4
- [A<sup>+</sup>02a] G. Abbiendi et al. Measurement of the hadronic photon structure function  $f_2(\gamma)$  at lep2. *Phys. Lett.*, B533:207–222, 2002. 2.2.1
- [A<sup>+</sup>02b] C. Adloff et al. Measurement of dijet cross sections in photoproduction at herA. *Eur. Phys. J.*, C25:13–23, 2002. 2.2.1, 2.2.2, 2.6, 5.7, 5.7.1
- [AGF94] P. Aurenche, J. P. Guillet, and M. Fontannaz. Parton distributions in the photon. *Z. Phys.*, C64:621–630, 1994. 2.2.1, 2.6
- [AP77] Guido Altarelli and G. Parisi. Asymptotic freedom in parton language. *Nucl. Phys.*, B126:298, 1977. 2.2
- [B<sup>+</sup>00] Gerald C. Blazey et al. Run ii jet physics. 2000. 2.4, 2.6
- [Bat99] P. Bate. *High Transverse Momentum 2-Jet and 3-Jet Cross Section Measurements in Photoproduction*. PhD thesis, Univ. of Manchester, 1999. 5.1.7
- [BBDM78] William A. Bardeen, A. J. Buras, D. W. Duke, and T. Muta. Deep inelastic scattering beyond the leading order in asymptotically free gauge theories. *Phys. Rev.*, D18:3998, 1978. 2.1
- [BBM<sup>+</sup>] R. Brun, F. Bruyant, M. Maire, A. C. McPherson, and P. Zancarini. Geant3. CERN-DD/EE/84-1. 2.7

- [BGMS74] V. M. Budnev, I. F. Ginzburg, G. V. Meledin, and V. G. Serbo. The two photon particle production mechanism. physical problems. applications. equivalent photon approximation. *Phys. Rept.*, 15:181–281, 1974. 2.3.2
- [BR97] R. Brun and F. Rademakers. Root: An object oriented data analysis framework. *Nucl. Instrum. Meth.*, A389:81–86, 1997. 4.1.1
- [C<sup>+</sup>98] E. Chabert et al. Qbgfmar: An updated phan package for cosmic and halo muon topological rejection in high  $p_t$  physics analysis. Technical Report H1 internal note 98-556, 1998. 2
- [C<sup>+</sup>01] G. Corcella et al. Herwig 6.4 release note. 2001. 2.7.1
- [Car02] S. Caron. *Jets in Photoproduction at HERA*. PhD thesis, RWTH Aachen, 2002. DESY-THESIS-2002-035. 2.4, 2.5, 2.6, 2.7, 1, 5.1.6, 6.1
- [CDSW93] S. Catani, Yuri L. Dokshitzer, M. H. Seymour, and B. R. Webber. Longitudinally invariant  $k(t)$  clustering algorithms for hadron hadron collisions. *Nucl. Phys.*, B406:187–224, 1993. 2.4
- [CJK04] F. Cornet, P. Jankowski, and M. Krawczyk. A new 5 flavour nlo analysis and parametrizations of parton distributions of the real photon. 2004. 7
- [CSS94] K. Charchula, G. A. Schuler, and H. Spiesberger. Combined qed and QCD radiative effects in deep inelastic lepton - proton scattering: The monte carlo generator djangos6. *Comput. Phys. Commun.*, 81:381–402, 1994. 2.7.2
- [Dok77] Yuri L. Dokshitzer. Calculation of the structure functions for deep inelastic scattering and  $e^+ e^-$  annihilation by perturbation theory in quantum chromodynamics. (in russian). *Sov. Phys. JETP*, 46:641–653, 1977. 2.2
- [E<sup>+</sup>04] S. Eidelman et al. Review of particle physics. *Phys. Lett.*, B592:1, 2004. 5.3
- [FMNR93] Stefano Frixione, Michelangelo L. Mangano, Paolo Nason, and Giovanni Ridolfi. Improving the weizsacker-williams approximation in electron - proton collisions. *Phys. Lett.*, B319:339–345, 1993. 2.3.2
- [FR97] Stefano Frixione and Giovanni Ridolfi. Jet photoproduction at hera. *Nucl. Phys.*, B507:315–333, 1997. 2.5, 2.6
- [Fri97] S. Frixione. A general approach to jet cross sections in QCD. *Nucl. Phys.*, B507:295–314, 1997. 2.6
- [GL72] V. N. Gribov and L. N. Lipatov. Deep inelastic  $e p$  scattering in perturbation theory. *Yad. Fiz.*, 15:781–807, 1972. 2.2
- [GRV92] M. Gluck, E. Reya, and A. Vogt. Photonic parton distributions. *Phys. Rev.*, D46:1973–1979, 1992. 2.2.1, 2.6

- [H1 93] H1 Collaboration. The H1 liquid argon calorimeter system. *Nucl. Instrum. Meth.*, A336:460–498, 1993. 3.2.1
- [Kes60] P. Kessler. *Il Nuovo Cimento*, 17:809, 1960. 2.3.2
- [KS92] Zoltan Kunszt and Davison E. Soper. Calculation of jet cross-sections in hadron collisions at order  $\alpha_s^3$ . *Phys. Rev.*, D46:192–221, 1992. 2.6
- [L<sup>+</sup>00] H. L. Lai et al. Global QCD analysis of parton structure of the nucleon: Cteq5 parton distributions. *Eur. Phys. J.*, C12:375–392, 2000. 2.2.2, 2.6, 6.2
- [Lon92] Leif Lonnblad. Ariadne version 4: A program for simulation of QCD cascades implementing the color dipole model. *Comput. Phys. Commun.*, 71:15–31, 1992. 2.7.2
- [M<sup>+</sup>92] G. Marchesini et al. Herwig: A monte carlo event generator for simulating hadron emission reactions with interfering gluons. version 5.1 - april 1991. *Comput. Phys. Commun.*, 67:465–508, 1992. 2.7.1
- [MRST00] Alan D. Martin, R. G. Roberts, W. James Stirling, and R. S. Thorne. Parton distributions and the lh: W and Z production. *Eur. Phys. J.*, C14:133–145, 2000. 2.2.2, 2.6, 6.2
- [MRST02] Alan D. Martin, R. G. Roberts, W. J. Stirling, and R. S. Thorne. Mrst2001: Partons and  $\alpha(s)$  from precise deep inelastic scattering and tevatron jet data. *Eur. Phys. J.*, C23:73–87, 2002. 2.2.2, 2.6, 6.2
- [MRST03] A. D. Martin, R. G. Roberts, W. J. Stirling, and R. S. Thorne. Uncertainties of predictions from parton distributions. i: Experimental errors. ((t)). *Eur. Phys. J.*, C28:455–473, 2003. 5.7.3
- [MSR] Alan D. Martin, W. James Stirling, and R. G. Roberts. Mrs parton distributions. Talk given at Leipzig Workshop on Quantum Field Theory Theoretical Aspects of High Energy Physics, Bad Frankenhausen, Germany, 20-24 Sep 1993 and at Topical Meeting on QCD at HERA, Durham, Eng., Mar 22-26, 1993. 2.7.2
- [Nis00] Richard Nisius. The photon structure from deep inelastic electron photon scattering. *Phys. Rept.*, 332:165–317, 2000. 2.2.1
- [P<sup>+</sup>02a] J. Pumplin et al. New generation of parton distributions with uncertainties from global QCD analysis. *JHEP*, 07:012, 2002. 2.2.2, 2.1, 2.6
- [P<sup>+</sup>02b] J. Pumplin et al. Uncertainties of predictions from parton distribution functions. ii: The hessian method. *Phys. Rev.*, D65:014013, 2002. 5.7.3
- [Pro03a] H1 OO Project. *The H1 OO Physics Analysis Project*, August 2003. Internal Manual: <https://www-h1.desy.de/icas/ooop/2.3.18/oo.ps.gz>. 4.2.2, 4.2.2, 4.2.2

- [Pro03b] H1 OO Project. *List of HAT variables*, 2003. Internal Webpage: <https://www-h1.desy.de/icas/oop/2.3.18/hatvar.html>. 4.2.2
- [Pro03c] H1 OO Project. *A steering mechanism for the H1 OO analysis environment*, 2003. Internal Webpage: <https://www-h1.desy.de/icas/oop/2.3.18/steering.ps.gz>. 4.2.2
- [PST02] J. Pumplin, D. R. Stump, and W. K. Tung. Multivariate fitting and the error matrix in global analysis of data. *Phys. Rev.*, D65:014011, 2002. 5.7.3
- [Rau02] J. Rauschenberger. *Prozesse des geladenen Stromes in tief- unelastischer Positron-Proton Streuung bei HERA*. PhD thesis, Univ. Hamburg, 2002. 5.1.3
- [S<sup>+</sup>01] Torbjorn Sjostrand et al. High-energy-physics event generation with pythia 6.1. *Comput. Phys. Commun.*, 135:238–259, 2001. 2.7.1
- [S<sup>+</sup>03] Daniel Stump et al. Inclusive jet production, parton distributions, and the search for new physics. *JHEP*, 10:046, 2003. 5.7.3, 5.40
- [Sey95] Michael H. Seymour. Jets in QCD. 1995. 2.4
- [Sjo94] Torbjorn Sjostrand. High-energy physics event generation with pythia 5.7 and jetset 7.4. *Comput. Phys. Commun.*, 82:74–90, 1994. 2.7.1
- [Sjo95] Torbjorn Sjostrand. Pythia 5.7 and jetset 7.4: Physics and manual. 1995. 2.7.1
- [Vee02] C. Veelken. H1nonepbgfinder - rejection of cosmic muon and beam-halo events in the h1oo framework. Technical Report H1 internal note 02-603, Liverpool University, 2002. 2
- [Wit77] Edward Witten. Anomalous cross-section for photon - photon scattering in gauge theories. *Nucl. Phys.*, B120:189–202, 1977. 2.2.1
- [Wob99] M. Wobisch. *Measurement and QCD analysis of jet cross sections in deep-inelastic positron proton collisions at  $s^{*(1/2)} = 300\text{-GeV}$* . PhD thesis, RWTH Aachen, 1999. DESY-THESIS-2000-049. 2.4